



HAL
open science

Development of fibrous cellulosic materials for the production of bio-based 3D printed objects by extrusion

Camille Thibaut

► **To cite this version:**

Camille Thibaut. Development of fibrous cellulosic materials for the production of bio-based 3D printed objects by extrusion. Material chemistry. Université Grenoble Alpes [2020-..], 2020. English. NNT : 2020GRALI005 . tel-02570560

HAL Id: tel-02570560

<https://theses.hal.science/tel-02570560v1>

Submitted on 12 May 2020

HAL is a multi-disciplinary open access archive for the deposit and dissemination of scientific research documents, whether they are published or not. The documents may come from teaching and research institutions in France or abroad, or from public or private research centers.

L'archive ouverte pluridisciplinaire **HAL**, est destinée au dépôt et à la diffusion de documents scientifiques de niveau recherche, publiés ou non, émanant des établissements d'enseignement et de recherche français ou étrangers, des laboratoires publics ou privés.

THÈSE

Pour obtenir le grade de

DOCTEUR DE L'UNIVERSITE GRENOBLE ALPES

Spécialité : **Matériaux, Mécanique, Génie Civil, Electrochimie**

Arrêté ministériel : 25 mai 2016

Présentée par

Camille THIBAUT

Thèse dirigée par **Didier CHAUSSY**, Pr, Grenoble INP, et

codirigée par **Aurore DENNEULIN**, MCF, Grenoble INP

Sabine ROLLAND DU ROSCOAT, MCF (HDR), UGA

Davide BENEVENTI, DR, CNRS

préparée au sein du **Laboratoire de Génie des Procédés**

Papetiers – LGP2, UMR 5518 et du **Laboratoire Sols, Solides,**

Structures et Risques– 3SR, UMR 5521

dans l'**École Doctorale Ingénierie – Matériaux, Mécanique,**

Environnement, Énergétique, Procédés, Production

Développement de matériaux fibreux cellulosiques pour la production d'objets bio-sourcés imprimés en 3D par extrusion

Thèse soutenue publiquement le **8 janvier 2020**,

devant le jury composé de :

Pr. Pierre DUMONT

Professeur à INSA Lyon, Rapporteur et Président

Pr. Roberta BONGIOVANNI

Professeur à Politecnico di Torino (Italie), Rapporteur

Dr. Gilberto DE FREITAS SIQUEIRA

Chercheur scientifique à EMPA (Suisse), Membre

Pr. Didier CHAUSSY

Professeur à Grenoble INP, Directeur de thèse

Dr. Aurore DENNEULIN

Maitre de Conférences à Grenoble INP, Invitée

Dr. Sabine ROLLAND DU ROSCOAT

Maitre de Conférences (HDR) à Université Grenoble Alpes, Invitée

Dr. Davide BENEVENTI

Directeur de Recherche au CNRS, Invité

Dr. Laurent ORGÉAS

Directeur de Recherche au CNRS, Invité



Remerciements

Ainsi, ce travail de 3 ans et un petit peu plus se termine sur ces dernières lignes à écrire...

Ce travail de thèse, financé par Alpes Grenoble Innovation Recherches, est le résultat d'une collaboration efficace entre le Laboratoire de Génie des Procédés Papetiers et le Laboratoire Sols, Solides, Structures et Risques sous la direction de Didier Chaussy et du co-encadrement d'Aurore Denneulin, de Sabine Rolland du Roscoat, de Davide Benvenuti et de Laurent Orgéas. Je tiens donc à vous remercier vivement d'une seule voix pour votre apport, soutien, contribution, accompagnement et encouragement multiformes, chacun à votre manière mais toujours de façon bienveillante.

Je remercie également chacun des membres du jury, Pierre Dumont, président du jury et rapporteur, Roberta Bongiovanni, rapporteur et Gilberto De Freitas Siqueira, membre, pour l'intérêt que vous avez porté à ce travail et pour l'ensemble de vos retours, interrogations et discussions qui ont contribué à l'amélioration de la qualité de ce manuscrit.

Mes remerciements vont aussi à tous ceux qui ont contribué à ce travail et en particulier à : Denis Curtil et Alain Dufresne pour avoir été un œil externe au projet en faisant parti de mon comité de suivi individuel de thèse.

Habib Murtaza et Martine Rueff pour votre collaboration et le développement d'outils indispensable pour l'étude du séchage de mes petits objets (mise au point d'une technique originale d'acquisition rapide d'image par tomographie à rayon X et suivi de la masse de mes échantillons).

Bertine Khelifi pour tes caractérisations au MEB.

Mikael Party et Stéphane Dufrenoy pour vos formations aux différents équipements et appareils. L'équipe du projet DEEP, à savoir Gwendal, Julie, Sophie, Marie et Benjamin, pour avoir bien voulu expérimenter l'impression 3D de votre prototype avec ma formulation et l'imprimante développées.

Je tiens enfin à remercier chaleureusement tous les membres des deux laboratoires qui m'ont témoigné leur sympathie et m'ont permis d'évoluer dans un environnement agréable.

Un grand merci à vous tous et bonne lecture !

Content

Remerciements	2
Content	4
General introduction	8
Chapter 1. State of the art	14
1.1 Additive manufacturing by material extrusion.....	15
1.1.1 Additive manufacturing and generalities	15
1.1.2 Process and material compatibility for additive manufacturing by material extrusion	20
1.1.3 Conclusion.....	38
1.2 Cellulose as a material for additive manufacturing by extrusion.....	39
1.2.1 Cellulose.....	39
1.2.2 The use of cellulose in additive manufacturing	46
1.2.3 Conclusion.....	64
1.3 Conclusion.....	65
1.3.1 Synthesis of the state of the art.....	65
1.3.2 Motivation of the PhD	66
Chapter 2. Material and methods	68
2.1 Introduction.....	69
2.2 Material and paste preparation.....	69
2.2.1 Optimization of the formulations	69
2.2.2 Additives to tailored the paste properties	75
2.3 Additive manufacturing by extrusion.....	75
2.3.1 The used 3D printer	75
2.3.2 Slicing software and AM by extrusion process.....	76
2.3.3 Extrusion flow: calculation, measurement and calibration	77
2.3.4 Printed parts with their printing parameters	79
2.3.5 Drying processes.....	83
2.3.6 Dimension measurements	84

2.3.7	Weight measurements	85
2.4	Characterization.....	86
2.4.1	Rheology of paste.....	86
2.4.2	Deformation after drying.....	87
2.4.3	SEM observation.....	87
2.4.4	Mechanical testing: tensile test	87
2.4.5	Conductivity.....	89
2.4.6	Temporal characterization of the drying.....	89
2.5	Conclusion.....	95
Chapter 3.	Development and characterization of cellulose based formulations with strong potential for AM by extrusion	96
3.1	Introduction.....	97
3.2	The carboxymethyl cellulose, a key component of formulation with strong potential for AM by extrusion.....	98
3.2.1	Characterization of carboxymethyl cellulose.....	98
3.2.2	Optimization of formulations by maximizing the solid content while remaining extrudable	101
3.3	Characterization of the selected formulations	107
3.3.1	Rheological behaviour of the fresh paste	107
3.3.2	Shrinkage during drying.....	109
3.3.3	Microstructure of the extruded filament.....	112
3.3.4	Tensile properties of dried filaments	113
3.4	Toward functionalization of formulation	114
3.4.1	Addition of a wet strength agent: a compromise between easy reuse and wet strength ..	114
3.4.2	Influence of CMC on graphite conductivity	116
3.5	Conclusion.....	118
Chapter 4.	Optimization of the printing parameters and the printer to manufacture accurate 3D parts with the optimized paste.....	119
4.1	Introduction.....	120
4.2	Optimization of the extrusion flow.....	121
4.2.1	Extrusion efficiency	121
4.2.2	Influence of the inner shape of the nozzle and the extrusion flow rate on the aspect of the filament	126
4.2.3	Influence of the extrusion flow rate on the mechanical properties	129
4.3	Optimization of AM by extrusion settings to accurately produce more and more complex parts	131
4.3.1	Influence of the settings on 2D parts.....	131
4.3.2	Influence of the settings on 3D printed parts	135
4.3.3	Printability of a complex model in the fresh state	146

4.4	Conclusion.....	147
Chapter 5.	Study of the drying toward the manufacturing of an accurate dried 3D printed part.	150
5.1	Introduction.....	151
5.2	Toward optimization of ethanol drying conditions	152
5.2.1	Influence of the ethanol concentration during ethanol drying.....	153
5.2.2	Optimization of the immersion time during ethanol drying.....	154
5.2.3	Guideline for ethanol bath.....	157
5.3	Drying of a filament, building block of the 3D printed structure.....	158
5.3.1	Temporal evolution of the filament	159
5.3.2	Influence of the environmental conditions	164
5.3.3	Temporal evolution of the mechanical properties	168
5.4	Drying of a cube, a simple 3D structure.....	172
5.4.1	Validation of the experimental set up	172
5.4.2	Temporal evolution of the cube at macroscopic scale	174
5.4.3	Temporal evolution of the cube at filament scale.....	182
5.5	Dimensional compensation strategy	184
5.6	Conclusion.....	185
General conclusion and perspectives	188
	Conclusions.....	188
	Scientific productions	191
	Perspectives.....	192
Résumé étendu en français.....	194
	Introduction générale.....	194
	Etat de l’art.....	197
	Développement et caractérisation de formulations cellulosiques compatible avec la FA par extrusion	202
	Optimisation des paramètres d’impression et de l’imprimante 3D pour produire des objets 3D conformes au cahier des charges avec la formulation optimisée.....	205
	Etude du séchage en vue de fabriquer un objet 3D imprimé fidèle au modèle à l’état sec	207
	Conclusions et perspectives	210
Abbreviations	212
List of figures	214
List of tables	226
References	228

General introduction

Additive manufacturing (AM), often referred as 3D printing, is regarded as a disruptive technology with many application fields, including the automotive industry, medical field, and leisure sector. This process of joining materials is used to fabricate objects from 3D model data, usually layer upon layer, as opposed to subtractive manufacturing methodologies. Additive manufacturing comprises a wide range of different technologies, as described by the American Society for Testing Materials (ASTM) (2012), each with their own advantages and drawbacks. In a general way, the additive manufacturing process offers new design opportunities for complex and lightweight designs, short manufacturing lead times, and simple design modifications (Huang, Liu, Mokasdar, & Hou, 2013). This technology is compatible with a broad range of materials, such as metals, polymers, ceramics, gels, food, and bio-based materials (Wohlers, Caffrey, & Campbell, 2016). Furthermore, the use of bio-based material and biodegradable materials is currently promoted as their main advantages are the carbon storage from atmosphere, their availability (as a renewable material), their non-accumulation in soils or ocean and the preservation of natural resources such as ore-based material and fuel-based material besides their own interesting characteristics.

Additive Manufacturing by extrusion, one of the ASTM established categories, represents the largest number of 3D printers installed (desktop or industrial) (Wohlers et al. 2016). This process appears as a promising technology because it allows the manufacture of complex and light parts by selectively dispensing a material through a nozzle as a continuous filament with specific flow properties. This process can build parts with more than one material paving the way for smart object manufacturing with resolution of about 0.5 mm. Thermoplastic polylactic acid (PLA), which is a bio-based material derived from starch, degradable only in an industrial composting environment, has been extensively used in AM by extrusion process due to its easy processing (Steinle, 2016; Wittbrodt & Pearce, 2015) and its ability to be charged with fillers such as carbon particles leading to a conductive material (conductivity ranging from 10^2 to 10^3 S.m⁻¹).

Cellulose in the form of fibers, which is the most abundant bio-based polymer on earth with excellent mechanical properties (Dufresne, 2013), could be another very promising candidate as material for producing cheap, lightweight, robust, and compostable 3D structures by AM by extrusion. It may be used not just as an additive for mechanical reinforcement or as a rheological modifier, but also as a bulk material, as discussed in a recent review on 3D printing cellulose and its derivatives (Dai et al., 2019).

To sign up in this strategy, this PhD proposes to evaluate the possibility of developing a cellulose based material for the production of multi-materials objects by AM by extrusion to offer more material choices to this technology in constant evolution. In this context, the decision to set the PLA capabilities towards 3D printing by extrusion as targets for our work regarding resolution, design and mechanical properties as well as economical aspect of the produced part appeared obvious.

At the beginning of this PhD, based on our knowledge, only one study reported the use of cellulose as a bulk material for 3D printing part with AM by extrusion (Markstedt, Sundberg, & Gatenholm, 2014), more than twenty years after the development of this process (US5121329A, 1992). This delay shows the challenges raised by the formulation based on fibrous material such as suspensions and pastes compatible with the AM by extrusion requirements. Nowadays, more than a dozen of studies present 100% cellulose based part printed by AM by extrusion highlighting the interest of the potential of using cellulose as a bulk material for 3D printing. Furthermore, these studies present a wide variety of cellulose used, solid content, resolution (nozzle size), shape of the successfully printed part as proof of concept, post-treatment (e.g cross linking and drying) and applications (medical, 1 m long part). This variety of cellulose based formulations comes from the various challenges raised by the AM by extrusion process and the multiple assets of cellulose to meet some of the requirements. To be 3D printed, the cellulose must flow homogeneously through the nozzle and then “set” immediately to facilitate shape retention (J. A. Lewis, 2006). This behavior cannot be obtained by temperature variation as it is done for thermoplastic materials, which are compatible with AM by melt extrusion. A liquid vehicle must be used to achieve the specific flow properties for extrusion. This liquid addition can result in incompatibility with an immediate “set” of the material without sudden viscosity change due for example to crosslinking, rapid evaporation or coagulation. Moreover, it can raise issue during the vaporization of the liquid: shrinkage and delamination.

Several challenges have to be overtaken in order to achieve the main objective of this project. These challenges spanned from part design, mechanical properties, resolution, cost and applications. We based our study on parameters summed up in the fish bone diagram of Figure I-1 *i.e.* the material

composition, the design of the 3D part, the used 3D printer, the selected printing settings, the environmental factors and the post processing of the part.

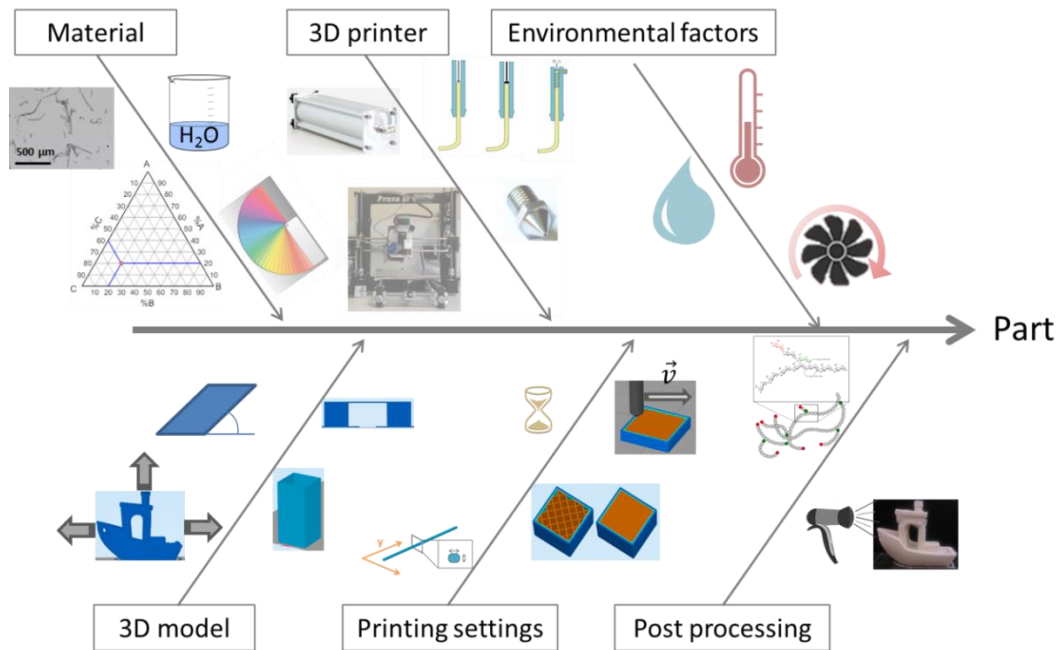


Figure I-1. Summary of the main studied parameters of this project to obtain the 3D printed part as accurate as possible.

The study of these parameters results in a multidisciplinary work which covered different disciplinary fields such as formulation, rheology, process engineering, material characterization and drying process. On the basis of the covered fields, this manuscript is divided into five chapters, as shown in Figure I-2.

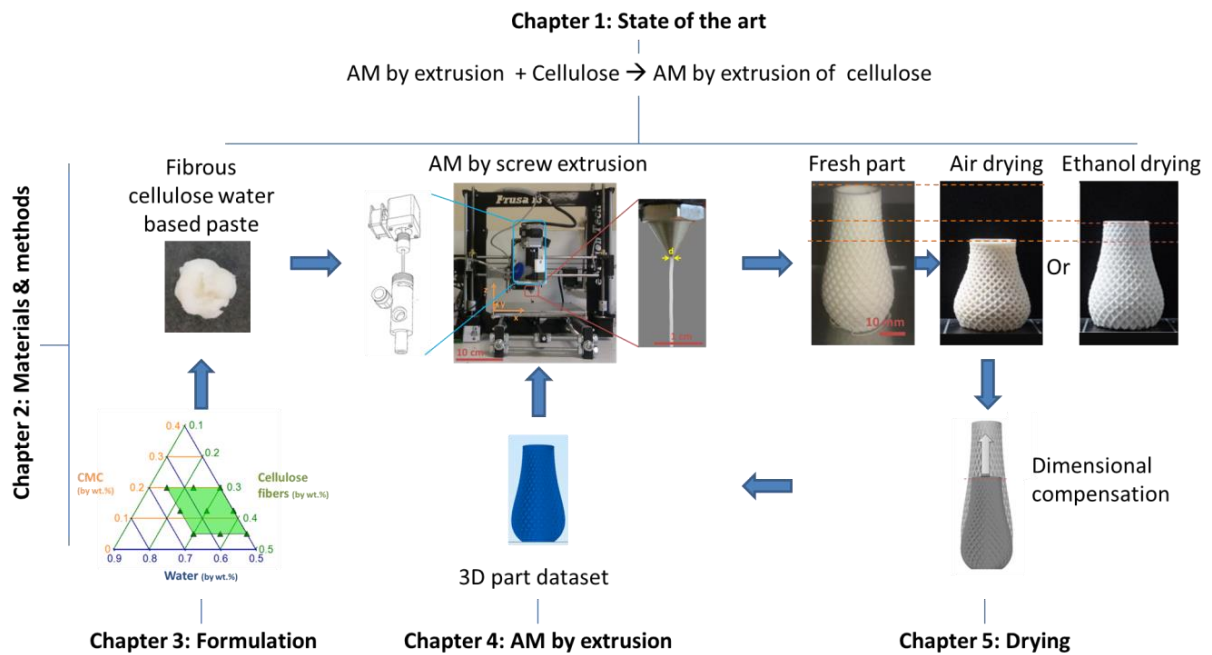


Figure I-2. Schematic representation of the manuscript organization.

Chapter 1 is dedicated to a literature review in the context of the project combining both the AM by extrusion process and the ‘cellulose’ as raw material. This chapter ends with an extensive overview of the use of cellulose in AM by extrusion and a discussion of the main strategies implemented to overcome the challenges.

Chapter 2 is dedicated on an accurate description of the materials and used or developed methods to obtain the results presented in the three following chapters.

Chapter 3 is dedicated to the development and characterization of cellulose based formulations with strong potential for AM by extrusion (extrusion of filament without clogging, viscosity of the material large enough to maintain the 3D shape and limited strain with air drying) achieved by a high solid content paste. The influence of additive to tailor the formulation properties (conductivity, water resistance) is also presented.

Chapter 4 is dedicated to the evaluation of the influence of the main identified printing parameters such as material extrusion quantity or layer height and the influence of the printer technology choices such as the tank or the inner shape of the nozzle on the accuracy of AM by extrusion parts. These parts were broken down into elementary features to suggest a printing settings guideline for paste compatible with AM by extrusion.

Chapter 5 is dedicated to understand the drying mechanism of 3D printed parts through the study of the influence of the drying conditions such as relative humidity or solvent exchange. A focus is done on the temporal evolution of the deformation of a filament and of a simple printed part

(cube). Such analysis resulted in the implementation of a compensation strategy to obtain a 3D printed part that is as close as possible to the CAD model.

Conclusions and perspectives end up this manuscript.

Chapter 1. State of the art

1.1	Additive manufacturing by material extrusion.....	15
1.1.1	Additive manufacturing and generalities	15
1.1.1.1	Definition and terminology	15
1.1.1.2	Additive manufacturing processes.....	17
1.1.1.3	Material availability.....	18
1.1.1.4	Opportunities and restrictions	18
1.1.2	Process and material compatibility for additive manufacturing by material extrusion	20
1.1.2.1	Composition and formulation of compatible material for AM by extrusion	21
1.1.2.2	Extrusion step	24
1.1.2.3	Deposition step	30
1.1.2.4	Drying.....	34
1.1.3	Conclusion.....	38
1.2	Cellulose as a material for additive manufacturing by extrusion.....	39
1.2.1	Cellulose.....	39
1.2.1.1	General description.....	39
1.2.1.2	Cellulose fibers	41
1.2.1.3	Nanocellulose: microfibril and nanocrystal.....	42
1.2.1.4	Cellulose derivative	44
1.2.2	The use of cellulose in additive manufacturing	46
1.2.2.1	Cellulose as an additive in the printed part by extrusion.....	47
1.2.2.2	Cellulose as the main component in the printed part	56
1.2.3	Conclusion.....	64
1.3	Conclusion.....	65
1.3.1	Synthesis of the state of the art.....	65
1.3.2	Motivation of the PhD	66

1.1 Additive manufacturing by material extrusion

1.1.1 Additive manufacturing and generalities

1.1.1.1 Definition and terminology

Additive manufacturing (AM), often referred as 3D printing and less often to solid freeform fabrication, consists in a joining materials process which allows the production of objects from 3D model data, usually layer upon layer, as opposed to subtractive manufacturing methodologies (ASTM International 2012). The printed part can require post processing. A scheme illustrated the key steps of an additive manufacturing process is presented in Figure 1-1.

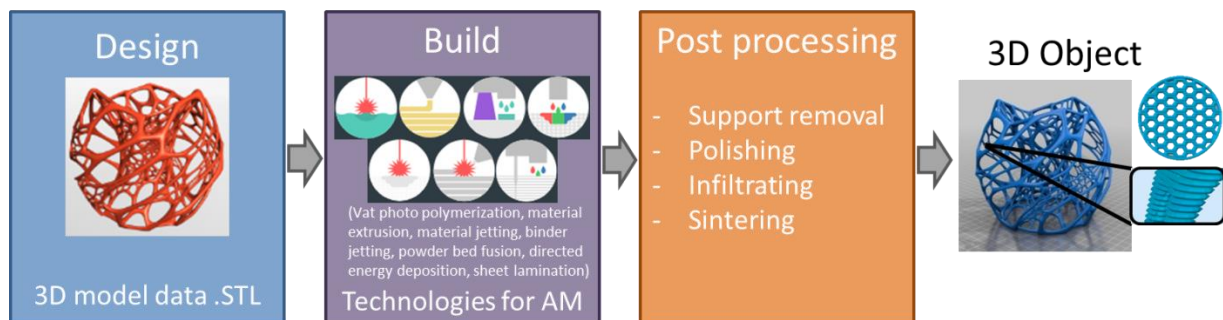


Figure 1-1. The additive manufacturing process steps adapted from (3D Hubs website, 2018).

Additive manufacturing is a technology having less than 40 years old. The first patents related to the major additive manufacturing processes such as stereolithography (1987), fused filament fabrication (1991) and selective laser sintering (1992) (Wohlers et al. 2016) had now expired, leading to the improvement and the diversification of these processes. The rapid expansion of new additive manufacturing processes (Wohlers et al. 2016) leads the American Society for Testing and Materials (ASTM) to write the standard terminology for Additive Manufacturing Technologies in 2012 (ASTM International 2012). The ASTM sorted additive manufacturing processes in seven categories linked to the process as illustrated in Table 1-1. These AM processes can shape a broad range of materials which are specific to the technology used such as resins which can only be processed by vat photo polymerization and material jetting.

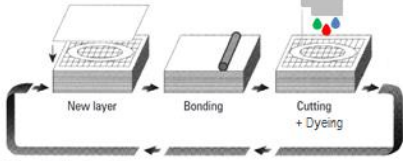

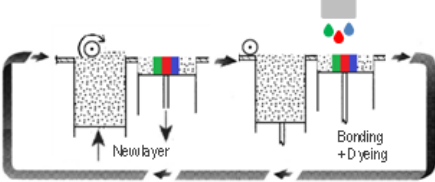

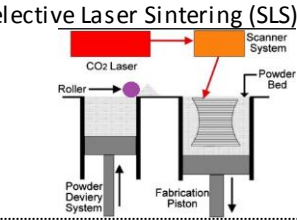

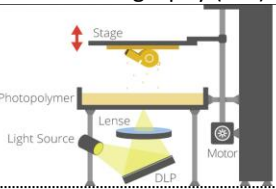

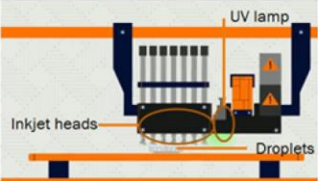

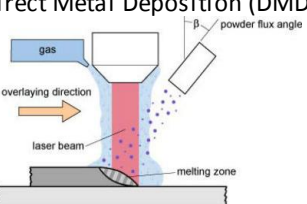

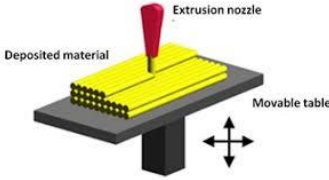

ASTM processes category	Process principle of an example	Compatible Materials	Parts example
	Laminated Object Manufacturing (LOM)		
Sheet lamination	 <p>Source: Helisys Inc. (nd)</p>	Paper Metal Polymer	
Binder jetting		Metal Sand	
Powder bed fusion		Metal Thermoplastic	
Vat photo polymerization		Resin	
Material jetting		Metal Wax Resin	
Directed energy deposition		Metal	
Material extrusion		Thermoplastic Ceramic	

Table 1-1. The seven categories of additive manufacturing processes according to the American Society for Testing and Materials (ASTM).

1.1.1.2 Additive manufacturing processes

The sorting strategy of ASTM was based on the process used for material addition to produce parts. Other sorting decisions based on the material implemented or structure that can be printed could have been used. The different AM processes as defined by ASTM and their main characteristics are presented in the following paragraphs:

- **AM by sheet lamination** is a process in which sheets of material such as paper or polymer films are cut and bonded together through the use of glue or ultrasound for example to form an object. This process is considered as fast as only the outline of the part are cut and so it can be used for quite large part. However, it is necessary to peel the part off the surrounding sheets which limit the design and the surface finish of the part and create waste (Pham et Gault, 1998).
- **AM by binder jetting** is a process in which a liquid bonding agent is selectively deposited to join powder material such as sand, ceramics or metal powder. The produced parts do not require support for overhang features. However, the produced 3D printed part presents a rough surface finish, the part has to be cleared of dust and might require a post treatment step for reinforcement and decreasing porosity (Pham et Gault, 1998).
- **AM by powder bed fusion** is a process in which a source of thermal energy selectively fuses regions of a powder bed. Materials such as semi-crystalline thermoplastics or metal powder can be implemented. It shows the same properties as binder jetting process as it does not require support for overhang and the part presents a rough surface finish that has to be cleared of dust. However, unlike parts produced by AM by binder jetting, these 3D printed parts present high strength and stiffness and a risk of thermal distortion (Pham et Gault, 1998).
- **AM by vat photopolymerization** is a process in which liquid photopolymer in a vat is selectively cured by light-activated polymerization. The produced part has a smooth surface finish after the removal of uncured resin during a post treatment step. However, the part has to be carefully designed in order to avoid trapped volume of uncured resin that cannot drain which can impact the part resistance (Pham et Gault, 1998).
- **AM by material jetting** is a process in which droplets of build material such as photopolymer and wax are selectively deposited. The produced part has a smooth surface and can be made of multiple materials with different stiffness. However, this process is quite expensive and also requires support for overhang features.
- **AM by direct energy deposition** is a process in which focused thermal energy is used to fuse materials (metal) by melting as they are being deposited. This process can be used

for repairing part or producing parts of few mm³. However, the surface quality and the dimensional accuracy are limited (White, 2001).

- **AM by material extrusion** (US5121329A, 1992) is a process in which material with specific flow properties such as amorphous thermoplastic or ceramic paste is selectively dispensed through a nozzle or an orifice. It allows a cost effective manufacturing of complex and light parts with potentially more than one material. However, the supporting material has to be printed for overhang features and the resolution, dictated by the nozzle size and the layer height is generally more coarse than with other processes (Pham et Gault, 1998).

Our project is focus on the development of materials compatible with AM by material extrusion processes. A focus on this last category is presented in the following parts of this chapter.

1.1.1.3 Material availability

The large panel of technologies used in additive manufacturing makes it compatible with a broad range of materials. Metal, thermoplastic, resin, ceramic, sand, concrete, wax, gel, biological tissue and food can be mentioned as potential material for AM and this is not an exhaustive list (Wohlers et al. 2016). However, all these materials are not compatible with the seven categories of additive manufacturing processes illustrated in Table 1-1. For each category, the material compatible with the process has to fit some specifications. Moreover, some manufacturers of 3D printers, especially the first companies present in the AM market, limited the use of material to their proprietary material due to an intern development of the printer, the software and the material. This latter approach is now tempered in particular for printers using metal and desktop printers as the customers asked for multiple source of raw material (Wohlers et al. 2016).

In the recent years, the range of material available for additive manufacturing increased considerably. For example, for fused filament fabrication process, in 2012, only ABS (acrylonitrile butadiene styrene) and PLA (polylactic acid) were available on the market. Now, the offer has increased with (i) other polymers such as nylon, PC (polycarbonate), PET (polyethylene terephthalate), PVA (polyvinyl acetate) and (ii) composites such as PLA filled with wood fibers (Duigou et al. 2016) or conductive graphene-PLA (D. Zhang et al. 2016).

1.1.1.4 Opportunities and restrictions

The major assets of AM processes are to offer new design opportunities and the availability of customized parts. The efficient use of material in the AM approach allows the production of complex and intricate designs which may lead to lightweight and robust parts. The complexity of the parts produced has no impact on the production cost and lattice structures with honeycomb for instance,

or topologically optimized part can be printed as well as solid part. Moreover, in a single printing step, it is technically possible to produce assembled part and/or moving part with different materials according to the additive manufacturing process used. This might be the most important benefit from additive manufacturing as it reduces the number of parts and therefore simplifies production logistics, decrease documentations (e.g. product reference, inventory list) and assembling operations (Wohlers et al. 2016). The short manufacturing lead time (few hours) and the low cost of the first parts in the AM approach allows customization, quick loops of design optimization (for parts or molds) as well as the on-demand production that reduces warehousing and inventory. Moreover, the availability of low cost 3D printers (<2 000€), mostly fused filament fabrication printers, enables individuals to access the technology and print their own objects. Coupled with this availability of printer for the general public, a broad open source data on part designs, printer and process settings for example are available in the Internet sphere such as the Reprap project (Jones et al. 2011).

Nevertheless, AM also has some limitations particularly regarding the productivity, the product dimensions and the surface finish of the printed part. Indeed, the dimensions of the printed part are a significant limiting factor: the cycle time of a 3D printed part may represent hours of manufacturing whereas a plastic injected part, once the mold is ready for production, is manufactured in seconds or minutes for the larger one. The dimensions of the part are restricted to the volume of the building chamber. Moreover, as additive manufacturing parts are built layer by layer (or at least by addition of material), the surface finish of produced parts will be generally unsmooth compared to the same material implemented with another process such as injection molding for instance and its mechanical properties will be negatively impacted in the built direction in comparison with the raw material mechanical properties.

That is why, AM is regarded as a disruptive technology with many application fields, including the automotive industry, medical field, and leisure sector as illustrated by the circle chart (Figure 1-2). However, one of the key challenges reported by (Wohlers et al. 2016) for the next years will be the qualification of new process and materials as well as new design for highly regulated industries such as aerospace and medical industries.

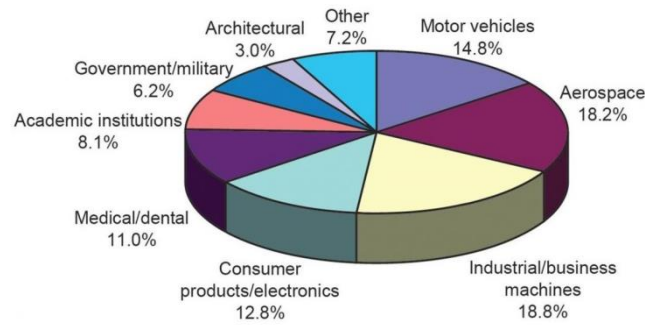


Figure 1-2. Circle chart of the industrial sectors applying additive manufacturing (Wohlers Associates, 2017).

1.1.2 Process and material compatibility for additive manufacturing by material extrusion

Additive Manufacturing (AM) by material extrusion, one of the ASTM established categories consists in the extrusion of a continuous filament of material to build 3D part as described previously (section 1.1.1.2 p.17). This AM category comprises the well-known Fused Filament Fabrication process (or Fused Deposition Modeling, a tradename given by Stratasys), bio-printing, robocasting (Cesarano, 1998), direct ink writing (Jennifer A Lewis et Gratson, 2004) and liquid deposit modeling. It represents the largest number of 3D printers installed (desktop or industrial), mainly due to printers using the Fused Filament Fabrication process (Wohlers et al. 2016). The interest in this technology came from (i) its low cost (printer available for less than 400€), (ii) its office friendly environment, (iii) its ease of use and light post processing operations and, (iv) its ability to produce complex and lattice parts with one or more extruder head (multi-materials approach).

All of these processes have the particularity to be composed of three key steps, each raising several material challenges: extrusion, deposition and post treatment, as illustrated in Figure 1-3. A description of formulations compatible with AM by extrusion is detailed in this section, followed by the three key steps of this process.

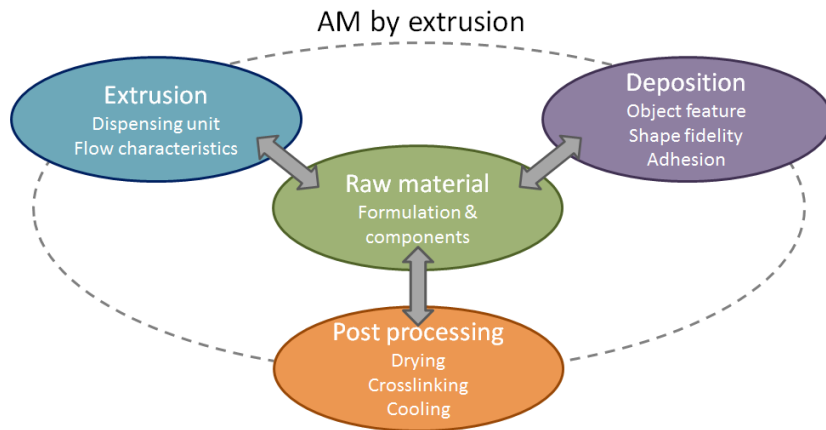


Figure 1-3. Dependence of the raw material with the key steps of AM by extrusion: extrusion, deposition and post processing.

1.1.2.1 Composition and formulation of compatible material for AM by extrusion

In Table 1-2, different kind of materials that were developed to be compatible with an AM process by extrusion are presented. The list proposed is not exhaustive but try to cover the main category of materials (gel, suspensions, composite, thermoplastic).

Material category	Composition	References
Gel	- 4.5 wt.% of alginate and 0.5wt.% TEMPO*-oxydized cellulose nanofibrils, 50 wt.% of glycerin and 45 wt.% of water.	Leppiniemi et al. 2017
	- 15 wt.% of potato starch with 85 wt% of lemon juice.	Yang et al. 2018
Colloidal suspension	- 47 vol.% of lead zirconate titanate powder with water and additive.	Smay, Cesarano, et Lewis 2002
Highly concentrated suspension or pastes	- 58 to 61 vol.% of alumina powder with water and additives.	J. I. Cesarano, Baer, et Calvert 1997
	- 31-35 vol.% of yttria-doped zirconium oxide powder with water and organic additive.	Peng et al. 2018
	- Sugar cookies recipe (flour, butter, sugar, egg yolk)	Lipton et al. 2010
Composite ink	- Fresh pasta (mainly flour and water)	Barilla and TNO
	- 20wt.% of cellulose nanocrystal with 2-hydroxyethyl methacrylate monomer, polyether urethane acrylate and photoinitiator.	G. Siqueira et al. 2017
Thermoplastic	- Polylactic acid (PLA).	Wohlert et al. 2016
	- Acrylonitrile butadiene styrene (ABS).	

Table 1-2. Examples of material compatible with AM by extrusion.

It can be noticed that most of the materials quoted in Table 1-2 were formulated by combining spherical and solid particles with a liquid vehicle, such as water or thermosetting polymers for example. To avoid nozzle clogging issues, it has been reported that the maximum diameter of the

solid particles loaded in the formulation must not exceed one-hundredth to one-tenth of the nozzle diameter (J. Benbow et Bridgwater, 1993; Jennifer A Lewis et Gratson, 2004; Truby et Lewis, 2016). Furthermore, in order not to be subject to irregular flow and nozzle clogging, the suspension must show a high colloidal stability (J. A. Lewis, 2006; J. Benbow et Bridgwater, 1993). This high colloidal stability is promoted by a large viscosity of the liquid vehicle and a closer density between the solid particles and the liquid vehicle (Coussot, 2012). The resistance to deformation of the paste was tailored by the amount of liquid contained in the formulation, its particles size distribution, its packing propensity and its mixing process. The amount of liquid should be sufficient to fill the inter-particles voids related to their packing and to separate the solid particles to allow deformation to be extruded (J. J. Benbow, Blackburn, et Mills, 1998). The larger the inter-particle distance is, the lower the resistance to deformation is, including the shrinkage phenomenon after drying (Cesarano, 1998).

To obtain a homogeneous matter composed of solid particles and liquid, an appropriate mixing is a key step to obtain a material that will generate an homogeneous flow rate (Mason et al. 2009). Several steps are required to warrant a efficient mixing as described by (J. Benbow et Bridgwater, 1993):

- (i) Dry mixing of the solid particles: the dispersion is more efficient at this stage.
- (ii) Wet mixing: the liquid is uniformly incorporated. The viscosity of the bulk material increases. The shearing force due to the mixing are transmitted to the bulk material enabling good consolidation of the particles without clumps.
- (iii) High shear mixing: agglomerates are broken down to avoid perturbation during extrusion.
- (iv) Degazing: removal of gaz bubble in the paste to avoid defect during extrusion.

(Jennifer A Lewis et Gratson, 2004; Compton et Lewis, 2014; M'Barki, Bocquet, et Stevenson, 2017; Feilden, 2017; G. Siqueira et al. 2017) described that the adequate rheological behavior to be compatible with AM by extrusion is a material presenting a strong shear thinning behavior with a yield stress, σ_y , that can be modeled as a Herschel-Bulkley fluid (Cf. equation 1). Three parameters characterize the Herschel-Bulkley model: the consistency index K , the flow index n , and the yield stress.

$$\sigma = \sigma_y + K\dot{\gamma}^n \quad (1)$$

Where σ is the stress [Pa],

σ_y is the yield stress [Pa],

K is the consistency index [Pa.sⁿ],

$\dot{\gamma}$ is the shear rate [s⁻¹],

n is the flow index.

In the considered papers, the developed materials compatible with AM by extrusion at ambient temperature with a pneumatic technique shows (i) an apparent viscosity at ambient temperature that goes from approximately 10^4 Pa.s at 0.1 s^{-1} to 10 Pa.s at 10^2 s^{-1} , (ii) a yield stress about 10^2 - 10^3 Pa and (iii) an elastic modulus comprised between 10^4 and 10^5 Pa, as illustrated in Figure 1-4. It is important to point out that the order of magnitudes proposed above could be moderately modulated to perfectly fit with (i) the specificities of the selected dispensing unit (nature of the driven technology, upper limit of the applied pressure, tips shape and nozzle size as presented in the following sections), (ii) the printing parameters (printing speed, layer thickness, etc.), (iii) the 3D object specifications (shape of the produced part, mechanical properties, etc) and (iv) the drying phase (type and kinetics of drying).

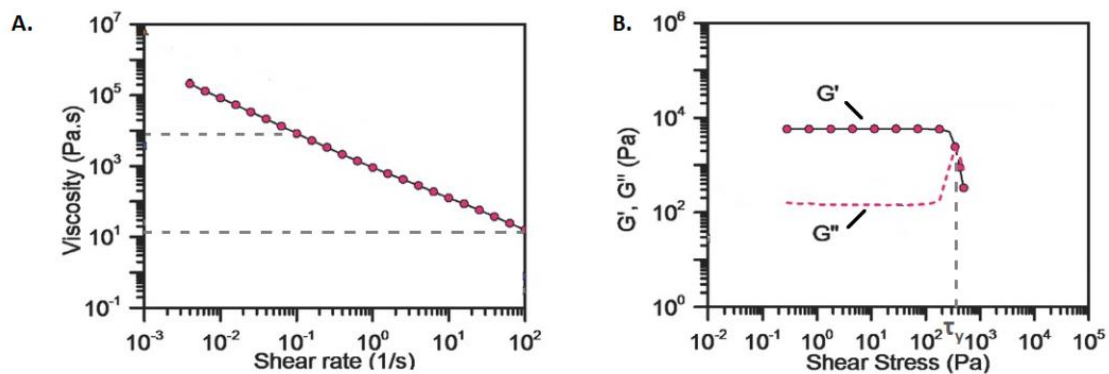


Figure 1-4. Rheological behavior of a compatible material for AM by extrusion. (A) the apparent viscosity, (B) the viscoelastic properties and the yield stress (G. Siqueira et al. 2017)

Amorphous thermoplastics materials are also quoted in Table 1-2. Their long polymer chains form a homogeneous material. Their resistance to deformation is tailored by the temperature: (i) below the glass temperature, the thermoplastic remain solid and (ii) above the glass transition temperature, the viscosity of the thermoplastic material decreases with the increase of temperature until the melting temperature is reached. The high thermal conductivity allows a rapid viscosity change after heating that makes it compatible with AM by extrusion.

To conclude, all the materials quoted in Table 1-2 formed a homogeneous material with a viscosity that can be tailored by liquid vehicle addition or temperature increase to present a rheological behavior compatible with AM by extrusion. This specific rheological behavior will have meaning after the explanation of the extrusion, deposition and post treatment steps developed in the following sections.

1.1.2.2 Extrusion step

The first objective during the extrusion phase for AM by extrusion is to obtain a continuous and homogeneous material flow through a small nozzle without any clogging during deposition. Moreover, during printing, sometimes, the extruder head have to move to the next deposition point without filament deposition: a stop of the flow and a filament breakage must occur. All of these requirements make the development of a material for AM by extrusion rather complex. For a more complete understanding of the phenomenon governing the extrusion step, in each subsection, the influence of formulation and of the equipment will be described: The 1st sub-section will be dedicated to the basics principle of the extrusion process and for the 2nd one, an overview of the various dispensing unit available on the market was proposed.

1.1.2.2.1 Basics principle of the extrusion phase

The extrusion phase during AM by extrusion is a crucial phase in which the printed material will undergo high physical stresses. Three major steps affecting the material state during the extrusion phase can be described. Indeed, during this phase the material will be subject to (J. Benbow et Bridgwater, 1993; J. A. Lewis, 2006):

- (i) an extensional flow at the die entry due to a constriction,
- (ii) a shear flow through the constant diameter circular channel of the extrusion head,
- (iii) a relaxation once released from the die.

Extrusion of a material through a circular channel of radius R and a length L along z direction can be characterized by the 2nd law of Newton with the use of several assumptions such as the no slip boundary condition as a first approximation (Michaeli 2003). This approach leads to equation (2):

$$\tau(r) = \frac{r\Delta P}{2L} \quad (2)$$

where, τ is the shear stress [Pa]

ΔP is the pressure difference between outlet and inlet (negative) of the channel [Pa]

L is the length of the channel [m]

r is the radius from the center line of the channel [m]

Equation (3) and (4) defines the concept of shear stress and shear rate.

$$\tau(r) = -\eta_{app}\dot{\gamma} \quad (3)$$

$$\dot{\gamma} = \frac{dv_z}{dr} \quad (4)$$

Where, η_{app} is the apparent viscosity [Pa.s]

$\dot{\gamma}$ is the shear rate or velocity gradient [s^{-1}]

v_z is the velocity along z direction, the channel direction [m.s⁻¹]

By combining equation (2), (3) and (4), the following equivalence can be achieved (Cf. Equation (5)):

$$\frac{r\Delta P}{2L} = -\eta_{app}\dot{\gamma} = -\eta_{app}\frac{dv_z}{dr} \quad (5)$$

The objective during extrusion is to obtain the largest flow by minimizing ΔP which can be limited by the dispensing unit used (section 1.1.2.2.2 p.27). As we assume that $v_z(R) = 0$ (no slip boundary condition), the larger $\frac{dv_z}{dr}$, the larger the flow rate. So equation (5) emphasizes the important impact of the tip design (minimum length and maximum radius) and the interest to have a material with a low viscosity at the shear rate experienced during the extrusion phase.

However, the assumption of no slip boundary is not valid for some materials such as colloidal suspension or some rubber compounds (Meijer et Verbraak, 1988). Firstly, a true slip at the wall can occur when a critical shear stress is reached (Coulomb's law of friction of a solid body on a wall). Secondly, an apparent slip can occur for mixture with a phase separation and migration of solid particles away from the wall (Cloitre et Bonnecaze, 2017). This phenomenon creates a peripheral thin layer of liquid, the thickness of whom is of the order of magnitude of the solid particle diameter. The viscosity of the liquid itself is usually lower than the composite's one; the formed thin film of liquid at the periphery acts as a lubricating layer resulting in a reduction of the shear stress applied to the material. This wall slip could be considered as an advantage since a lower pressure is required to produce a similar extrusion flow than without the presence of wall slip phenomenon. Moreover, a faster recovery of the material elasticity is observed as the material is less sheared which is an important parameter for the second step of AM by extrusion: the deposition (section 1.1.2.3 p.30).

A side objective during extrusion of material with fibers as component can be the alignment of these fibers to tailor the properties of the printed part (Sydney Gladman et al. 2016; G. Siqueira et al. 2017). This fiber alignment is induced by shear and extensional flow. To be sheared, the material must not slip at the wall and the yield stress of the material has to be overcome to avoid plug flow. This is for this reason that (G. Siqueira et al. 2017) limited the yield stress of its developed formulation at the value of the maximum shear stress experienced by the material at the wall calculated from Equation (2). According to their experimental specification, (a 410 μm nozzle diameter, 1.27 cm long tips and a pressure applied at the nozzle of 4 bars), the maximum shear stress at the wall was about 3 200 Pa. With an ink yield stress of 349 Pa, the critical radius above which the ink is expected to undergo shear was found to be 22.2 μm . Thus for a 410 μm nozzle diameter, 98.8 vol% is expected to undergo shear force and lead to fiber alignment.

At the exit of the nozzle, different phenomena can occur:

- (i) Nozzle swelling which is a viscoelastic phenomenon as presented in Figure 1-5. A and B. The diameter of the extruded filament can increase up to 30% of the die diameter (Carrot et Guillet, 2000). This is a well-known phenomenon in polymers extrusion (Carrot et Guillet, 2000). This is caused, among others, by a relaxation of the polymer chains after being stretched in the flow direction. The addition of inelastic fillers tend to reduce die swelling (A. Gold, Strong, et N. Turner 2014). Die swelling phenomenon is not present in suspension. The presence of this swelling phenomenon has a clear impact on AM by extrusion track width.
- (ii) Surface fracture, a phenomenon presented in Figure 1-5.C and D that can be generated with numerous material such as ceramic, food or viscoelastic material (J. Benbow et Bridgwater, 1993). The extrudate shows a rough and uneven surface. This phenomenon may be influenced by three identified factors: paste formulation, die shape and operating conditions.

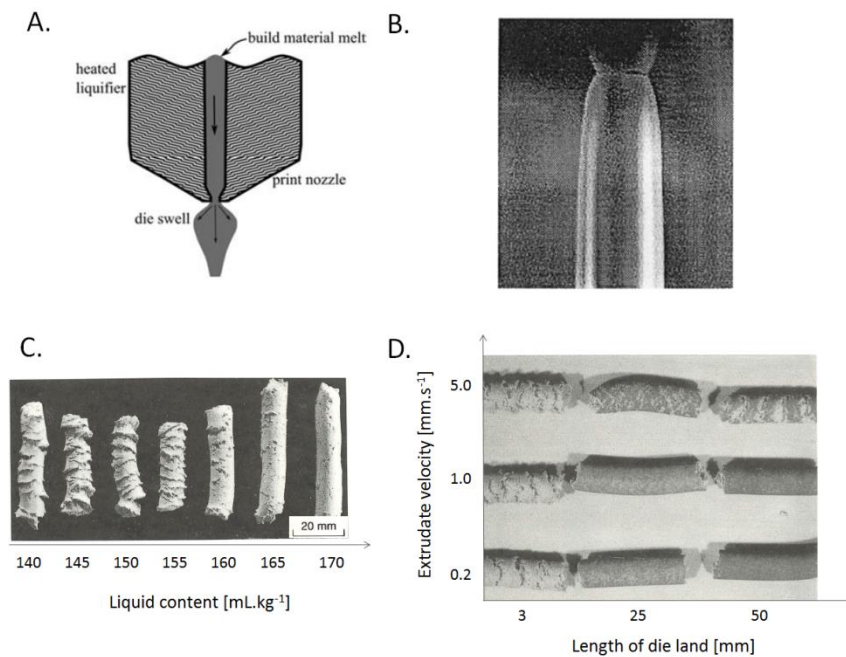


Figure 1-5. Flow defects – Illustration (A) and picture (B) of die swelling phenomena (A. Gold, Strong, et N. Turner 2014; Carrot et Guillet, 2000). Surface fracture phenomenon influenced by the composition (C) and die shape and operating conditions (D) (J. Benbow et Bridgwater, 1993).

To conclude, the pressure applied at the inlet of the nozzle as well as the nozzle design (shape and dimensions) are critical to obtain an accurate extrusion flow and are linked to the material chosen. The different dispensing units in the AM systems by extrusion available are presented in the following section.

1.1.2.2.2 Dispensing units in the AM systems by extrusion

To dispense material in AM by extrusion, several systems operating either at room temperature or involving a temperature conditioning can be considered. Figure 1-6 synthesizes the different dispensing units that are classically embedded in the AM systems by extrusion. The dispensing units can be characterized by their operating temperature, the driven device technology, the inner shape of the tip and the nozzle diameter.

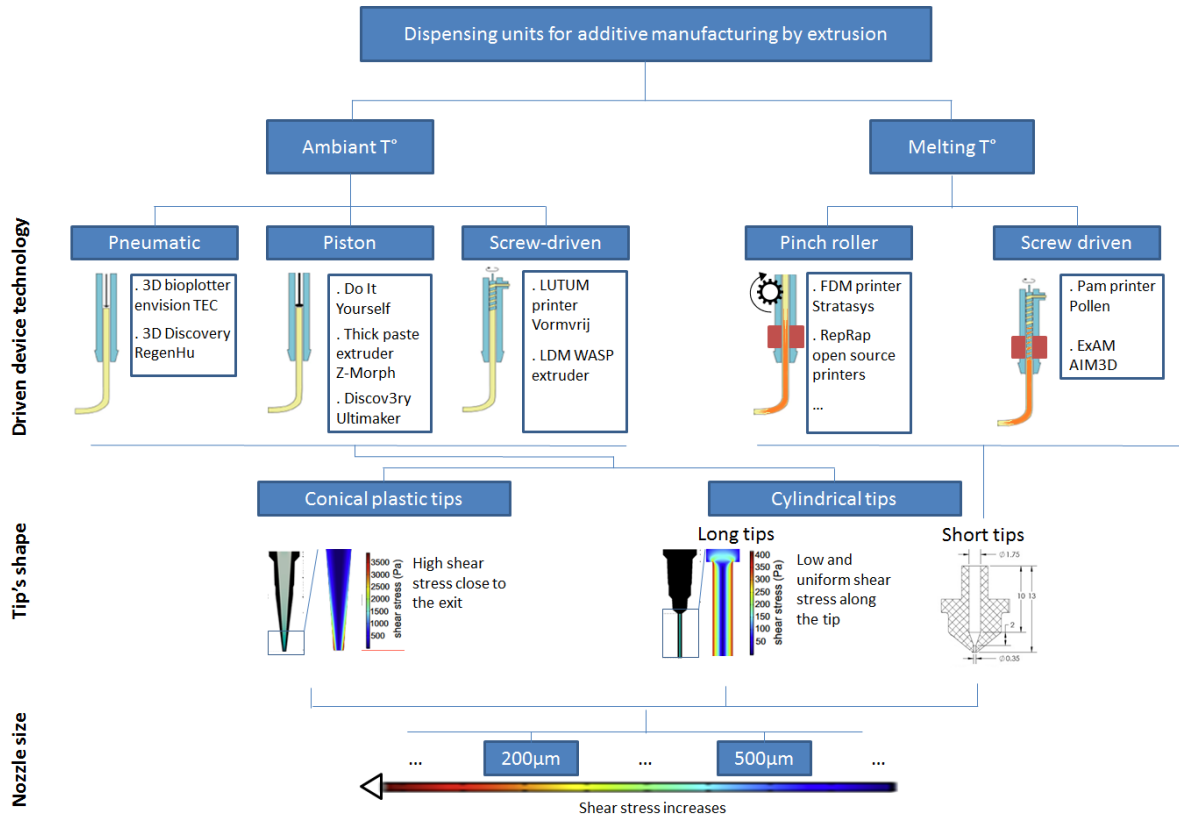


Figure 1-6. Dispensing devices for additive manufacturing by extrusion. Driven device technology were adapted from (Hölzl et al. 2016) and tips shape adapted from (Billiet et al. 2014).

Four criteria of differentiation regarding dispensing unit for AM by extrusion can be identified, as illustrated in Figure 1-6. More detailed about these criteria are given in the following paragraphs:

(a) Temperature conditioning:

Depending of the material involved in the AM process by extrusion, the extruded material can be either extruded at ambient temperature or heated up to its melting temperature in order to allow its extrusion as for traditional extrusion. Table 1-3 gives a non-exhaustive list of materials requiring a temperature conditioning to be extruded. Most of commercially printers limit the heating of the extrusion head at 230°C for technical and low cost issues which limits the number of compatible material for hot extrusion process. To extrude at larger temperature, the 3D printer needs to

integrate a closed building chamber that will be heated from the building platform and an effective cooling system to constrain the melting zone close to the nozzle.

Material	Extrusion temperature	Reference
Polylactic acid (PLA)	180-230°C	Commercial
Acrylonitrile butadiene styrene (ABS)	210-250°C	Commercial
Polycarbonate (PC)	260-310 °C	Commercial
Polyamide (PA)	220-270°C	Commercial
Suspension of alumina	Room temperature (22°C)	(Wang et al. 2015)
Zirconate titanate gel-based ink	22°C	(Smay, Cesarano, et Lewis, 2002; J A Lewis, 2002)
Aqueous colloidal ink of silicon carbide	Room temperature	(Cai et al. 2012)
Cellulose nanocrystal aqueous ink	Room temperature	(G. Siqueira et al. 2017; V. C.-F. Li et al. 2017)
Screen printing silver ink	Room temperature	(Tricot et al. 2018)

Table 1-3. Non exhaustive list of materials compatible with 3D printing by extrusion with their working temperature required to allow extrusion.

(b) Driven device technology:

At ambient temperature, three different kind of driven device technologies to push the material through the nozzle were developed (Sun et al. 2018):

- The pneumatic technique: A controlled air pressure pushes the material to flow through the nozzle. The pressure has to be adjusted to obtain the flow corresponding to the printing parameters (printing speed, layer height, extrusion track width). It is compatible with material that exhibit (i) a low viscosity at the shear rate experienced during the extrusion phase (about $10 \text{ Pa}\cdot\text{s}^{-1}$ for example (G. Siqueira et al. 2017)) and (ii) a limited yield stress to be able to initiate and maintain the flow through the nozzle. This method is typically implemented on bio-printers (such as 3D Bioplotter, 3D discovery) as cleaning is easier than for other technologies and contamination risk and cell death are reduced. However, this time-pressure dispensing technique does not allow an immediate stop of the flow.
- The piston technique (or ram extruder): In this case, it is the control of the plunger movement and the applied force that regulates the flow of material. According to the system used for the plunger motion, material with viscosity similar to the pneumatic technique should be used. However, as the pneumatic technique, it does not allow an accurate start and stop of the flow (W. Li et al. 2017; Mason et al. 2009). This technique

that does not require air pressure can be used by individual consumer on low cost printers.

- The screw-driven technique (or auger): With this technology, this is the rotation of the screw that regulates the flow of material. An air pressure syringe is often added to the system for material storage and replenishment of the supply chamber located upstream to the screw. This technology can be used with materials showing higher level of viscosity than what is permitted with both of the previous technologies described. Moreover, an effective start and stop of the extrusion flow can be achieved by activating rotation, reverse rotation or no rotation of the screw (W. Li et al. 2017). Clay printers (WASP and LUTUM printer) used this technique.

The 3D printers embedding heating systems can drive material to the nozzle thanks to two different techniques:

- The pinch roller system: in this approach, a pinch roller pushes the material which is pre-shaped as a filament in the direction of the heaters where it will be melted to easily flow through the nozzle. This technique is quite similar to the piston one where the piston is here represented by the pinch roller and the solid filament. The maximum pressure applied is related to (i) the adhesion without slipping between the roller and the filament and, (ii) the filament resistance to buckling (A. Gold, Strong, et N. Turner, 2014). The filament must have a constant cross section to allow a precise control of the quantity of the extruded material. Most of the available AM by extrusion printers used this technology (Wohlers et al. 2016).
- The screw driven technique: in this case, the material is forming into pellets that are introduced into a barrel in which they will be melted and pushed thanks to the screw driven unit. This approach is quite similar to the screw driven technique at ambient temperature. This well-known process in industry for extrusion and injection process has been developed by very few manufacturers (Pollen, AIM3D).

(c) Tips shape:

Today, two main kinds of tips commercially available for AM at ambient temperature can be distinguished: (i) conical plastic tips and (ii) short and long cylindrical tips. Short cylindrical tips are around 1 mm long whereas long cylindrical tips can be 6 to 40 mm long. The geometry of the tip is crucial because it may imply different stresses to the material resulting in different flow behaviors. (Billiet et al. 2014) tried to quantify this different level of stresses by developing a simulation program on COMSOL, a multiphysics simulation software, to compare the impact of the shape of the

tips on cell viability as cells are highly sensitive to shear stress. In their study, the diameter of the tips and the inlet pressure were set at 200 μm and 1 bar, respectively. The material properties such as the zero shear viscosity, the flow behavior index and the consistency coefficient were empirically measured to simulate the stress with a fluid power law. The overall results of the study revealed that superior stresses with one order of magnitude were obtained for the conical tips in comparison with the cylindrical ones. It was also emphasized that the stress was localized close to the fluid outlet (1 mm) for the conical tips whereas for the 16 mm long cylindrical tips, shear stress was uniform along the tips as illustrated in Figure 1-6. It means that a same material will show a larger flow in the conical tips than in the 16 mm long cylindrical tip with the same inlet pressure.

(d) Nozzle size:

Whether in literature or on commercial equipment, most of the nozzles implemented on 3D printing devices have a diameter ranging from 200 to 800 μm (Eqtesadi et al. 2013; Shao et al. 2015). For a constant applied pressure, the nozzle size will directly affect the achievable resolution, the printing time and the exit material flow.

1.1.2.3 Deposition step

The objective during the deposition step of material in AM by extrusion is to obtain accurate free standing structures with good adhesion between layers. To better understand the requirements regarding material to achieve different level of 3D structure complexity, this section will be divided into two sub-sections: the first one will be dedicated to the features of 3D parts and the second one to the adhesion between successive layers or filaments.

1.1.2.3.1 Feature of 3D parts and material properties

All the 3D parts design can be broken down into a series of fundamental structures for AM by extrusion: cube, cylinder, overhang, bridge, negative and positive space, long and high wall structure. Open source test models were designed to evaluate the material, the printer and the printing settings. Few examples of these referenced models are shown in Figure 1-7. Other test models were made of a single feature as presented by (Yang et al., 2014).

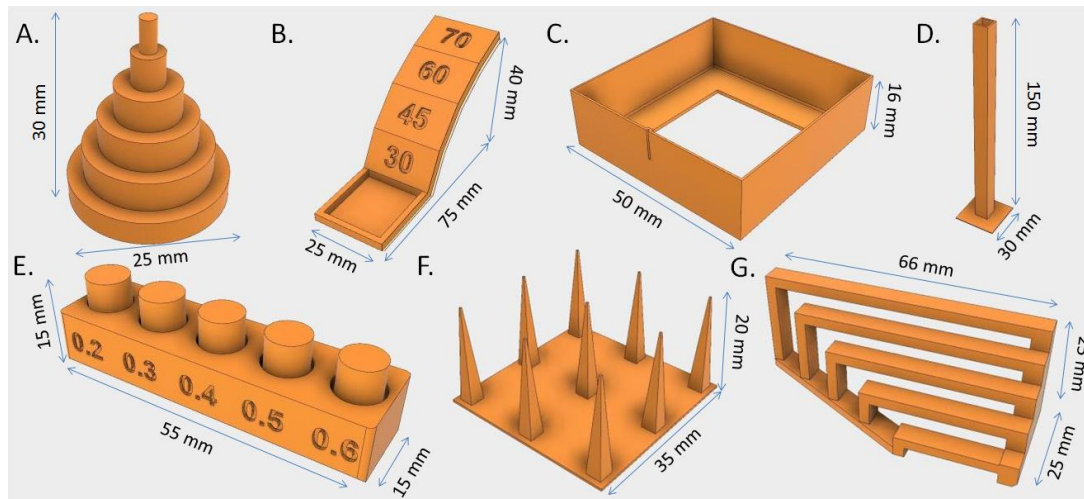


Figure 1-7. Test models for AM by extrusion: (A) dimensional accuracy, (B) overhang performance, (C) mechanical resonance in XY, (D) mechanical resonance in Z, (E) negative space tolerance, (F) fine positive space features performance, (G) bridging performance. Adapted from (Bastian, 2001).

To obtain accurate printing of these parts, the material should exhibit specific properties such as (i) keep its (flatten) filament shape without spreading after deposition on a previous layer or without support (Figure 1-7), (ii) stick fast to the previous printed layer and to the juxtaposed filament (Figure 1-7.B), (iii) allow a precise stop and go of the extruded flow with sharp filament breaking (Figure 1-7.F), (iv) offer an enough solid layer of the part for supporting the filament flattening during its deposition above it (Figure 1-7.C) and (v) resist to the weight of the above layers (Figure 1-7.D). These qualitative properties of material mostly related to its rheological behavior give a general overview of the material challenges raised by the test models.

For materials that are 3D printed without heating, some of these qualitative properties (i, iv and v) were quantified either by extensive characterization of the rheological behavior of the extruded material or by theoretical modeling of the stress applied on the material such as for the bridge (Figure 1-7.G):

- Lewis et Gratson, 2004; Compton et Lewis, 2014; M'Barki, Bocquet, et Stevenson, 2017; Feilden et al. 2016; Siqueira et al. 2017 performed extensive characterization of the rheological behavior of the studied material by describing its apparent viscosity at ambient temperature, its yield stress under shear and compression and its viscoelastic properties (shear loss and elastic moduli) as previously described (section 1.1.2.1 p.21)
- Smay, Cesarano, et Lewis, 2002 modeled the bridging by the simple bending equation (6) that came from beam theory and the involved assumptions. The span filament was modeled as a beam of length L based on two supported beams. The beam bears a

distributed load (its weight) of density, W , on the length, L , as it can be seen on Figure 1-8.

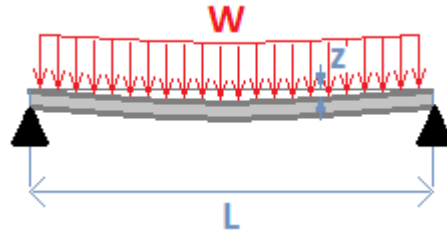


Figure 1-8. Simple bending

$$z_{max} = - \frac{5}{384} \frac{WL^4}{EI} \quad (6)$$

Where, $W = \pi\rho g \frac{D^2}{4}$ is the distributed load [Pa.m] with ρ , the density [$\text{kg}\cdot\text{m}^{-3}$]

g , the standard gravity [$\text{m}\cdot\text{s}^{-2}$]

D , the filament diameter [m]

L is the span distance [m]

$E = 2G'(1 + \nu)$ is the Young's modulus [Pa] where $\nu = 0.5$, the Poisson's ratio for an incompressible material.

$I = \frac{\pi D^4}{64}$ is the area moment of inertia of a circular section of diameter D [m^4].

The guideline limit of the authors was based on the maximum deflection, $|z_{max}|$ which must not exceed 0.5% of the filament diameter. It gives a lower limit for the elastic modulus G' : $G' > 1.4 \frac{\rho g L^4}{D^3}$ or a minimum normalized infill density of one layer of the part (D/L).

The bridging approach could also be modeled by a straight beam clamped at its extremities and subjected to its own weight (Thibaut et al. 2019). In that case, the guideline limit can be based on the maximal tension-compression stresses in the filament calculated from the Euler-Bernoulli beam theory. These maximal stresses must not exceed the yield stress of the material to avoid deformation and vertical sagging.

Regarding the case of thermoplastics materials, the challenges raised by the printing of the test models presented previously remain relevant only for a short time, when the temperature of the thermoplastics material is close to its melting temperature. Indeed, their rheological behavior is mainly governed by temperature change; below the glass transition temperature, the thermoplastic remains solid. Once the material is flowing through the nozzle, the latter will cool down and harden quickly thanks to its high thermal conductivity. The complex structures are therefore more easily reproducible with thermoplastic materials.

1.1.2.3.2 Adhesion between successive layers and juxtaposed filaments

As described previously, the AM by extrusion process consists in the deposition of a filament to manufacture 3D parts. The main strategy employed consists in manufacturing parts one layer at a time. One layer consisted in a filament deposited along a path. To produce a cohesive part, the filament has to bond juxtaposed filaments belonging to intra layer as well as those belonging to the previous and next layer. The adhesion between filaments is known as being a weak point in the approach of AM by extrusion (Wohlers et al. 2016). Indeed, for example, the PLA tensile specimens printed in the horizontal direction exhibit a tensile strength two times larger than the one of specimen printed in the vertical direction (Laureto et Pearce 2018). This observation can be explained by two main factors, as illustrated in Figure 1-9: (i) the first factor is that a porosity will be induced by the shape of the extruded filament resulting in the emergence of gap between juxtaposed filaments (Gordeev, Galushko, et Ananikov, 2018); (ii) the second factor will be linked to the adhesion strength. The adhesion between juxtaposed filaments is the results of both a squeeze flow and an interfacial healing. It consists in a partial coalescence of the two deposited filaments. In the case of thermoplastic material, the adhesion strength is tailored by the temperature of extrusion and the temperature in the chamber (Reddy, Reddy, et Ghosh, 2007). In this case, a limited coalescence can be due to a rapid cooling of the thermoplastics material that limits the polymer chain diffusion and entanglement (Gurralla et Regalla, 2014). For colloidal suspensions, this is a too fast recovery of the disrupted structure (gel, suspension or paste) after extrusion that can lead to a poor cohesion between filaments (Gurralla et Regalla, 2014; Smay, Cesarano, et Lewis, 2002).

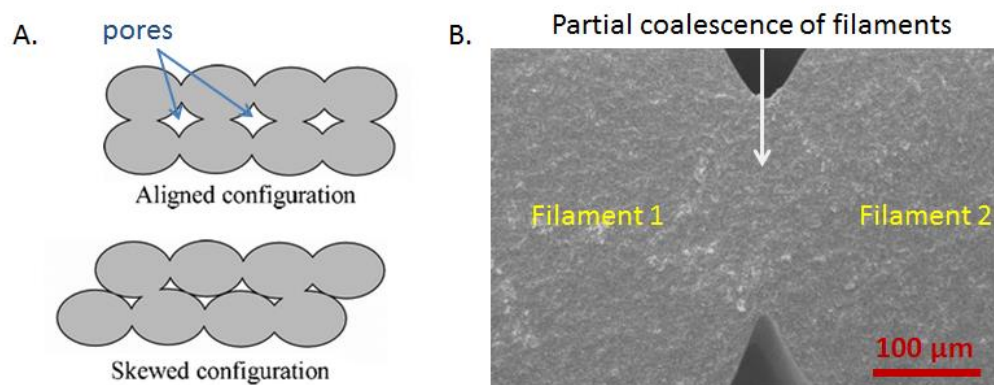


Figure 1-9. Filament bonding – (A) Porosity in AM by extrusion (adapted from Reddy, Reddy, et Ghosh, 2007) and (B) Micrograph of contact between two filaments deposited.(adapted from Shor, Bellini, et Guceri, 2005).

A compromise has to be found between the flow properties of the 3D printing material to ensure both an accurate printing of the part and a good adhesion between juxtaposed filaments.

1.1.2.4 Drying

After the manufacturing of the 3D part, the main challenge regarding material is to maintain the structure stable overtime while preserving the details present in the original model as the printed part is not in a final solid state when printing is over. Depending on the used material, different solidification phenomena and therefore different strain can occur such as for example (i) inhomogeneous crystallization of thermoplastics material which induces a limited shrinkage or (ii) cross linking of material using a liquid vehicle which induces a reasonable shrinkage or (iii) water removal which may induce large deformation depending on the drying process.

1.1.2.4.1 *Inhomogeneous crystallization of thermoplastics materials*

During and after printing with fused filament fabrication (FFF) process, the part cools down. This is an important step for semi crystalline thermoplastics material. Indeed, it is during cooling that semi crystalline thermoplastic crystallizes leading to shrinkage. Moreover, the crystallization rate is linked to the cooling rate. Yet, for fused filament fabrication, the cooling rate is inhomogeneous over time and space. It can lead to an inhomogeneous crystallization and warpage of parts due to shrinkage (see Figure 1-10). That is why, most of plastics used for FFF are amorphous. The volume shrinkage for injection molding of plastics used for FFF is generally less than 1%. However, for injection molding, the cooling is well controlled in order to minimize it (Alsoufi et El-Sayed, 2017; Spoerk, Arbeiter, et al. 2018; Schumacher, Schöppner, et Fels, 2019).



Figure 1-10. 3D printed part with warpage in ABS. According to Simplify 3D troubleshooting guide, ABS material can shrink up to 1.5%.

1.1.2.4.2 *Cross linking of material using a liquid vehicle*

The cross linking consists in linking one polymer chain to another one by covalent or ionic bond. It can be initiated by heat, UV exposure, pH change or contact with salt solution for instance. The cross linking can occur during or after the AM by extrusion process. It is mainly used to enhance mechanical properties and to maintain the 3D structure in open air (Markstedt et al. 2017) or in a liquid (Leppiniemi et al. 2017). The cross linking can result in a strain of the structure about 5 to 15% of the initial dimensions (Markstedt et al. 2015; Leppiniemi et al. 2017).

1.1.2.4.3 Drying of water based material

1.1.2.4.3.1 Drying

Generalities: as presented in Figure 1-11.A, a wet porous solid is described as a solid with liquid inside its pores and around its surface. Above the surface, a boundary layer of air is saturated in liquid vapor. Liquid adheres to the surface of the solid by its superficial forces and it adheres to the pore thanks to complex capillarity phenomenon. For hygroscopic solid, this adhesion can be large enough so that after drying in ambient condition, the liquid can stay bounded to the surface (Figure 1-11.C).

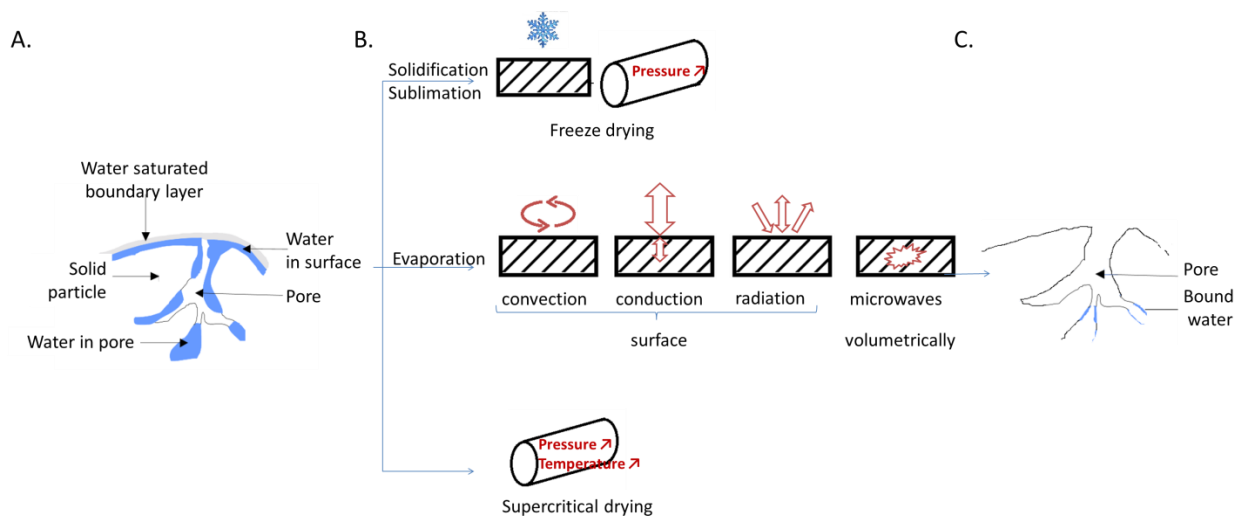


Figure 1-11. The different techniques for drying a wet solid – (A) Wet porous solid, (B) variety of the drying processes and (C) dried porous solid adapted from <https://eduscol.education.fr>

Three routes to remove a liquid from a solid part exist:

- freeze-drying
- supercritical drying
- air-drying

Freeze-drying: in this process, the liquid first solidifies in solid and then sublimates in gaz. The first step of this technique which is the solidification might alter the internal structure and impact the all solid shape: ice crystal grows and expenses the pore as the density of ice is lower than the one of water. The second step which is the sublimation of the solidified liquid has almost no impact on the structure of the solid. This technique is expensive. (Gupta et al. 2018).

Supercritical drying: in this process, no phase change are crossed, liquid and vapor coexist and cannot differ from each other. The supercritical point of moisture is passed and there is no more surface tension. However, passing this point for water leads to extreme pressure and temperature

(218 bar-374°C) that is why, solvent replacement is used for hydrogel in order to replace water by a low critical parameter solvent such as carbon dioxide (CO₂). This technique is also expensive.

Air-drying: this process is the combination of two phenomena that are evaporation and liquid diffusion inside the part toward the surface. The energy required for drying by evaporation came from the heat. This heat is supplied to the surface of the object by convection, conduction or radiation and inside the volume by microwaves (Figure 1-11.B). The mesoporous structures might not be preserved and the shrinkage is enormous. To minimize this huge deformation upon drying, solvent exchange techniques (Håkansson et al. 2016) or polymerization techniques (Einarsrud 1998) might be used to replace water.

1.1.2.4.3.2 Physics of air-drying

Water evaporation

As presented in Figure 1-12, liquid turns into gaz under two conditions: gaz around the liquid is too dry (liquid partial vapor pressure < liquid saturation vapor pressure at a given temperature) or the temperature and pressure for phase changes are reached. The largest the temperature, the fastest the phenomenon of evaporation is for a given liquid partial vapor pressure.

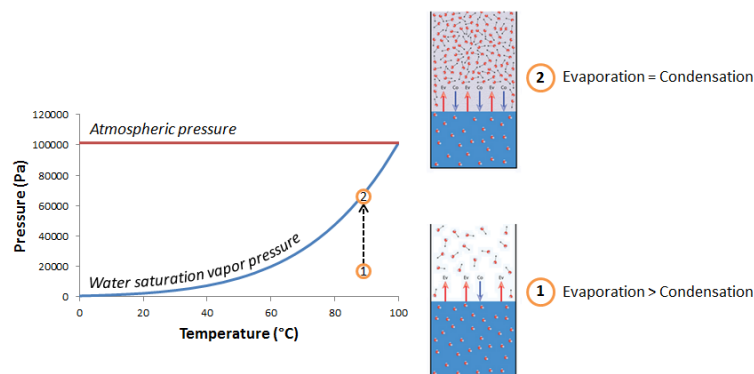


Figure 1-12. Evaporation of water adapted from www.meteobell.com

Main steps of drying of a wet porous solid

The diffusion inside the part toward the surface is mainly driven by Darcy's law (cf. Equation 7) in response to a pressure gradient in the liquid. Indeed, evaporation leads to several stresses such as capillarity pressure (cf. Equation 8), osmotic pressure, disjoining pressure and moisture stress (Scherer, 1990). The stress often mentioned in articles as a cause of shrinkage when wet solid dries is the capillarity pressure, P_c (Einarsrud, 1998). This pressure P_c comes from a minimization of energy: the liquid vapor interface is less energetic than the solid vapor interface. So when liquid evaporates, instead of decreasing the liquid level with flat surface, it creates meniscus inside the pore. Yet, the

smaller the radius of curvature of the meniscus, the larger the capillarity pressure (cf. Equation 8). As the capillarity pressure increases, the flux of liquid toward the surface increases. Equilibrium between diffusion and evaporation rate can be reached. However, after a while, the flux of liquid will be lower than the evaporation rate. It is the end of the constant evaporation rate period (explain one paragraph below) and shrinkage of the porous solid. Besides, from the equation (8) of the capillarity pressure, it can be noticed that the larger the surface tension is, the larger the capillarity pressure is. Similarly, the smaller the pores are, the larger the capillarity pressure is. Water surface tension is considered large with a surface tension γ_{LV} of 0.073 N.m⁻¹. For example, (Håkansson et al. 2016) who worked on the solidification of nanocellulose hydrogel, exchange water with another solvent that exhibited a lower surface tension (hexane $\gamma_{LV} = 0.018$) in order to increase the shape fidelity of the solid after drying.

$$\vec{j} = -\frac{D}{\eta_L} \overrightarrow{grad}(P) \quad (7)$$

Where, \vec{j} is the flux of liquid [m.s⁻¹],

D is the permeability [m²],

η_L is the viscosity of liquid [Pa.s],

P is the pressure in the liquid [Pa].

$$P_c = -\frac{2\gamma_{LV}}{r} \quad (8)$$

Where, P_c is the capillarity pressure [Pa],

γ_{LV} is the liquid/vapor surface tension [N.m⁻¹],

r is the radius of curvature of the meniscus [m].

It is possible to distinguish 3 to 4 steps for the drying of a wet porous solid (Scherer 1990; Bonazzi et Bimbenet 2003) at temperature and pressure below the vaporization line (Figure 1-13):

1. Increase of the wet solid temperature: this step occurs when the wet solid is surrounded by hot air. The available heat flow is large compared to the heat flow required for the evaporation as the liquid saturation vapor pressure (at the solid temperature) is low. The heat flow surplus is used to increase the temperature of the wet solid which impact positively the liquid saturation vapor. At one point, a balance between energy required for evaporation and energy required to keep or increase the material temperature is reached.
2. Constant rate period: the evaporation rate per unit of the drying surface area is equal to the one of bulk liquid without solid particles. It means that the solid is surrounded by a thin layer of liquid and the diffusion from inside the solid to the surface is fast enough compared to the evaporation rate in order to let this thin layer of liquid intact. During this period, drying

stresses reach a maximum and shrinkage occurs. Measuring the volume of liquid evaporated during this period is equivalent to measure the volumetric shrinkage.

3. First falling rate period: the shrinkage stops; air enters the pore of the wet solid. Liquid evaporates inside the pore and then the vapor is removed by diffusion or the liquid still flow until the surface where it evaporates. The outer surface of the porous media hardens and the temperature of the solid increases. This phenomenon does not occur with micro wave drying.
4. Second falling rate period: the liquid evaporates before reaching the surface. Then, vapor is removed by diffusion inside the pore. It is a slower process than the first falling rate period.

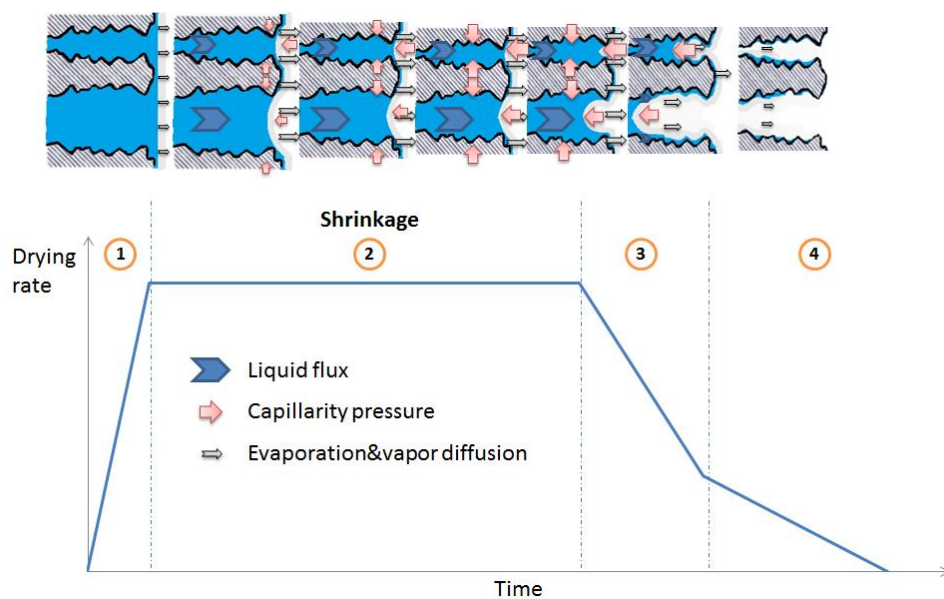


Figure 1-13. Drying steps and drying phenomena coupled inspired from (Scherer, 1990).

- To sum up, a large surface tension and a small pore size dimension of the solid are the main factors that lead to huge strains upon shrinkage with air drying.

1.1.3 Conclusion

To conclude, additive manufacturing is an interesting process which differs from traditional shaping process and opens new opportunities. The development of new materials is challenging. The material had to fit several requirements linked to the steps of the AM by extrusion process: material preparation, extrusion, deposition, and hardening. These requirements are generally based on the rheological behaviour of the material. Moreover, these new materials must also be in agreement with environmental challenges such as their renewability and biodegradability to have a future.

1.2 Cellulose as a material for additive manufacturing by extrusion

Cellulose is the main component of plant cell wall. It is the most abundant and available material around the world. Indeed, every year, about $1.5 \cdot 10^{12}$ tons are produced by photosynthesis on the Earth (Klemm et al. 2005) against the $3.3 \cdot 10^8$ tons of plastics production in 2016 (Aeschelmann et Carus, 2017). Moreover, this bio-based and biodegradable material has several well-known characteristics such as its lightweight (bulk density about $1.50\text{-}1.55 \text{ g}\cdot\text{cm}^{-3}$), low cost, high specific strength and modulus (due to its structural function in plant cell) and its broad chemical modifying capacity (presence of a large number of side hydroxyl groups along a linear polymer with a degree of polymerization from 2 000 to 27 000) (Dufresne, 2017). The cellulose used today in industry is mainly dedicated to the production of paper and cardboard, textile fibers, isolation material, films and cellulose derivatives for coating applications for instance (Klemm et al. 2005) as well as the production of biofuel (Golecha et Gan, 2016).

1.2.1 Cellulose

1.2.1.1 General description

1.2.1.1.1 *Different sources, localizations and treatments leading to cellulose fibre with different properties*

Raw materials such as wood, bast fibers, agricultural residues, leaf fibers, bacterial cellulose, shell of some fruits and vegetables or tunicates are sources of cellulose. However, according to its source, cellulose can be (i) pure with only cellulose chains (bacterial, seed hair of cotton) or (ii) in a composite form with lignin and hemicelluloses present around cellulose fibers (wood). To isolate the cellulose present in this composite, as illustrated in Figure 1-14, different treatments like chemical pulping separation and purification process are used (Arnoul Jarriault, 2015; Perrin, 2016; Curmi, 2018). Such processes provide cellulose fibers with different lengths, widths, degrees of fibrillation and purity. These characteristics being also dependent on the species, it affects the chains length (degree of polymerization) and its distribution, the degree of crystallinity and the intermolecular interactions. At a macro level, it influences mechanical, thermal and chemical properties.

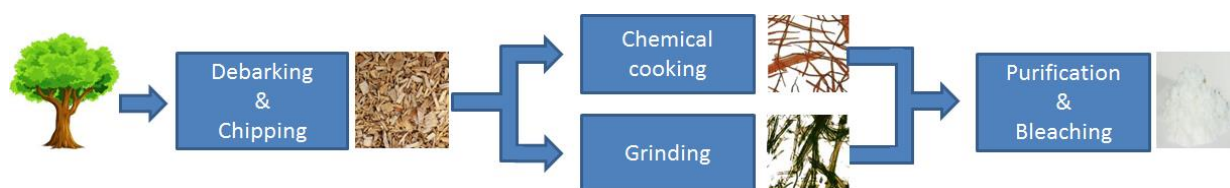


Figure 1-14. Schematic process for producing cellulose fiber from wood.

1.2.1.1.2 Supramolecular organization of cellulose

The supramolecular organization of cellulose is illustrated by Figure 1-15. The plant cell wall corresponds to the cellulose fiber. It is shaped as a rectangular tube where lifeblood circulates inside during its “lifetime”. It is constituted of a combination of microfibrils aligned with different angles and embedded with hemicellulose and lignin. These microfibrils are also named nanofibrils justified by their width which is about 10 to 30 nm. A microfibril of cellulose is formed by parallel strings of microcrystal structure called crystallites linked together by amorphous domains (Dufresne, 2017). These crystallites are constituted of cellulose chains aggregated together by Van der Waals forces and hydrogen bonding.

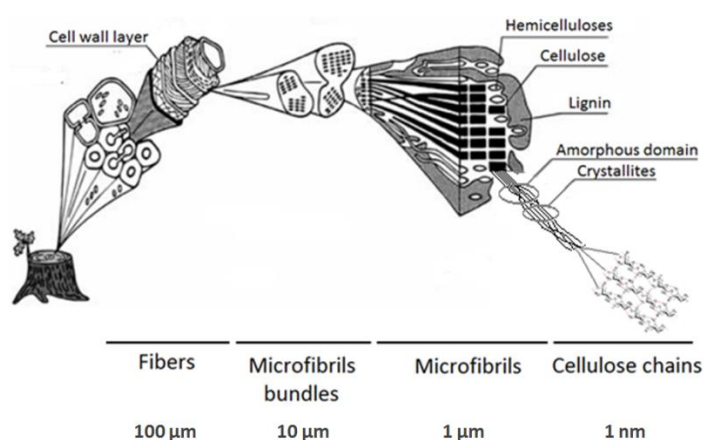


Figure 1-15. Schematic illustration of the supramolecular organization of cellulose adapted from (Sixta, 2006).

1.2.1.1.3 Molecular structure of cellulose

The description of the molecular structure of cellulose was the results of long investigations of several scientists such as Sponser et Dore, 1926; Meyer et Misch, 1937; Haworth, 1940 and in recent year by Nishiyama, Langan, et Chanzy, 2002. Cellulose polymer consists in a linear homopolysaccharide composed of β -D-glucopyranose units linked together by β -1-4-linkages. One side of the chain ends by a C4-OH group, a non-reducing end whereas the other side is a reducing end as it is presented in Figure 1-16. These two different ends confer chemical polarity to cellulose chain and orientation. Each monomer of the cellulose chain bears three hydroxyl groups on carbon atom number 2, 3 and 6. The bond of these hydroxyl groups is polarized as well as water molecule (H_2O). As a consequence, these hydroxyl groups have the ability to form intra and intermolecular hydrogen bond. The hydroxyl group on carbon atom number 3 and oxygen atom number 5 are linked by hydrogen bonding (cf. Figure 1-16). Yet, this hydrogen bonding inhibits rotation between the monomer and stiffer the cellulose chain. Indeed, the strength of a hydrogen bond is about one tenth

of an average covalent bond and it has effect up to 0.25 nm (β -D-glucopyranose units is 0.52 nm long). The two other hydroxyl groups play a key role in cellulose crystallinity structure. Indeed, the several combinations of hydrogen bonding between two celluloses chains leads to different crystalline structures and so different mechanical, thermal and chemical properties.

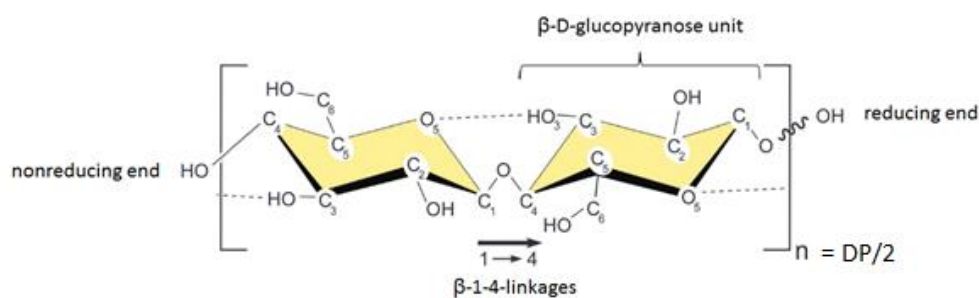


Figure 1-16 : Molecular structure of cellulose adapted from (Moon et al. 2011).

1.2.1.2 Cellulose fibers

Physical, thermal and chemical properties are governed by the molecular structure of cellulose, its packing organization, its source and its treatments. The following paragraphs propose an overview of the main properties of cellulose fibers sorted by the nature of properties:

- Structural properties: The average dimension of a cellulose fiber in length, in diameter and in wall thickness is 1-5 mm, 10-50 μm and 1-5 μm respectively, as illustrated in Table 1-4 (Niskanen, 1998).

Source	Fiber length, l_f	Fiber width, w_f	Aspect ratio
	[mm]	[μm]	l_f / w_f
Hardwood (Eucalyptus)	1.1	20	53
Softwood (Spruce)	3.5	27	130
Non wood plant (Wheat)	1.5	13	115

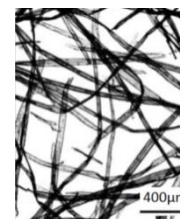


Table 1-4. Structural properties of cellulose fiber with an image of kraft pulp fibers of Spruce (Niskanen, 1998)

- Mechanical properties: Cellulose fiber exhibits good mechanical properties. A typical tensile strength of a single wood fiber is in the range of 100 to 200 mN with a breaking stress in the range of 400 to 500 MPa (Sixta, 2006). The Young's modulus of fibers is in the range of 10 to 70 GPa according to the angle of the microfibrils that constitute the fiber (Niskanen, 1998).

- Thermal properties: The degradation of cellulose is around 330°C although its depolymerization starts at 100°C. Unlike numerous polymers, the calculated melting temperature of cellulose is beyond its degradation temperature. Therefore, the shaping processes of cellulose material are different from thermoplastics polymers.

- Chemical properties: Cellulose fibers are insoluble in several organic solvents and in water. It shows good resistance to dilute acid, alkali, oil and grease (INRS, 2018) and can be dissolved in only few solvents (ex: DMSO used for nanocrystal of cellulose manufacturing). Cellulose presents a broad chemical modification capacity due to the presence of hydroxyl groups (cf. section 1.2.1.1.3 p.40).

- Hygroscopic properties: Cellulose is a hygroscopic material. An indicator named Water Retention Value (WRV)(ISO 23714 2014) is often used to determine the ability of the fiber to retain water. For example the WRV of cotton linter is around 50% compared to the 60-90% of pulps and regenerated cellulose fiber due to a lower accessibility of the hydroxyl group caused by a larger crystallinity of cotton linter cellulose. The more the cellulose fibers are refined (the refining process is a mechanical process where the fibers are under compression and shear forces (Gharehkhani et al. 2015)), the larger the specific surface of cellulose fiber is and the larger the WRV is. In presence of water, the cellulose fiber swells in diameter (20 to 30%) whereas its length remains the same (1% of expansion) (Wainwright, 1976) and holds water by hydrogen bonding. When cellulose fiber dries, the fiber contracts and pores collapse due to the capillarity forces. Parts of these collapses are irreversible due to the strong bonds that result from the drying even when rehydrated. This phenomenon is called hornification. It affects the solvent accessibility of the fiber and its flexibility. The hornification can be reduced by adding a solvent exchange step. When water is substitute by ethanol then acetone and other solvents that are less and less polar, it reduces the formation of new hydrogen bonds between approaching cellulose chains and preserve the pore structure of the cellulose fiber in the dry states (Sixta, 2006; Merchant, 1957). Furthermore, cellulose can be crosslinked to increase its absorbent properties to superabsorbent properties or increasing stiffness and strength of the material. It can results from the addition of chemical cross linking agent (Young, 2002) or from heating and radiation for example.

1.2.1.3 Nanocellulose: microfibril and nanocrystal

Behind the term nanocellulose, two kinds of particles can be identified: Micro-Fibrillated Cellulose (MFC) and Cellulose NanoCrystals (CNC). As presented in Figure 1-17.B, microfibrils, a structural component of a cellulose fiber (Figure 1-17.A), is composed of both amorphous and crystalline parts whereas nanocrystals are only composed of crystalline parts (Figure 1-17.C). In the recent years, nanocellulose fibers gain interest due to their outstanding properties linked to their nanometric dimensions with a diameter ranging from 2 to 60 nm (Dufresne, 2017). Microfibrils presents a high aspect ratio due to a length that can reach few micrometers leading to flexibility whereas nanocrystals are rigid rod like particles with a length ranging from 150 to 500 nm as illustrated in Figure 1-17.B and C.

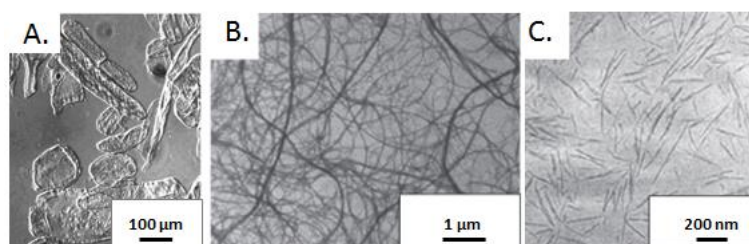


Figure 1-17. Micrograph of sugar beet (A) cell wall (Dufresne, Cavaillé, et Vignon, 1997), (B) microfibrils (Dufresne, Cavaillé, et Vignon, 1997) and, (C) nanocrystals (Saïd Azizi Samir et al. 2004).

The main highlighted properties of nanocelluloses are their:

- Outstanding mechanical properties compared to natural cellulose fiber. This difference comes from the absence of structural defect coming from the source of cellulose or the microfibrils arrangement of the cell wall layer. For a single fibril, the Young Modulus is around 100 GPa (Dufresne 2015).
- Broad chemical modification capacity due to an increase accessibility of OH group compared to cellulose fiber which has interest in medical applications for example.
- Gel like behavior at low concentration in water with a pseudoplastic rheological behavior as presented in Figure 1-18 with thixotropic properties (Hubbe et al. 2017; X. Jia et al. 2014; Nechyporchuk, Belgacem, et Pignon, 2016).

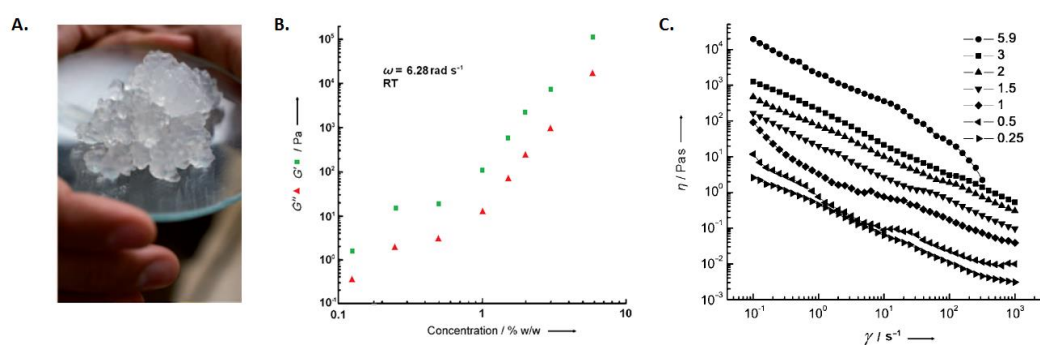


Figure 1-18. The gel like behavior of nanocellulose adapted from (Klemm et al. 2011) (A) macroscopic image of nanocellulose hydrogel, (B) storage, G' and loss modulus, G'' of nanocellulose suspension of different concentration at a frequency of 6.28 rad.s^{-1} , (C) viscosity of different concentration of nanocellulose suspension as a function of the shear rate.

The production process of nanocelluloses requires a high energy consumption as the natural fiber need to undergo a high shear to destructure its wall. To reduce this energy consumption and to adjust the obtained properties of the gel, different pre-treatments (mechanical, biological or chemical), mechanical treatments and post treatments are applied as illustrated in Figure 1-19. Due to the manufacturing process, this material is more than 100 times the price of the natural cellulose

fiber. That is why, nowadays it is used in small quantities and in high added value applications. A list of its potential applications sort by sector of activity can be found in the review (Dufresne, 2015).

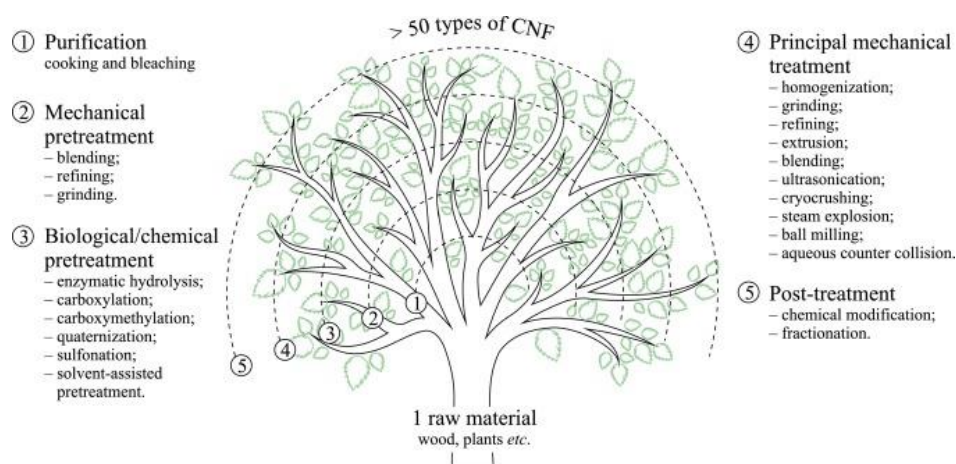


Figure 1-19. Overview of the broad treatments used to produce various type of nanocellulose suspensions (Nechyporchuk, Belgacem, et Bras 2016).

1.2.1.4 Cellulose derivative

Due to the presence of three hydroxyl groups per monomer of cellulose, it gives numerous opportunities to chemically modified cellulose and produce cellulose with different properties. The cellulose derivatives are characterized by their Degree of Substitution (DS) of hydroxyl groups (OH). It is the number of substituted OH groups over the number of OH groups before the chemical modification. Then, this number is ranging from 0 to 3. The two main categories of cellulose derivatives are ester and ether of cellulose. Cellulose esters are used as explosives, coatings, cigarette filter, membranes and plastics whereas cellulose ethers which are often soluble in water can be used as a thickener or as an adhesive (Ganster et Fink, 2013). Only the ester acetate of cellulose and the ether carboxymethyl cellulose are presented.

1.2.1.4.1 Cellulose acetate

It is produced by esterification of cellulose: OH groups are replaced by acetate groups as presented in Figure 1-20. The most common form of cellulose acetate shows a Degree of Substitution (DS) of 2.4 and 3 for diacetate and triacetate, respectively. These degrees of substitution influence the properties of cellulose acetate such as the density, the solubility and the thermal properties.

- The density increases from 1.22 to 1.35 g.cm⁻³ with the degree of substitution.
- The diacetate is soluble in acetone whereas an appropriate solvent of the triacetate is the methylene chloride combined with 20% of alcohol (Champetier, 1954).
- The melting temperature (T_m) is lower than the decomposition temperature (T_d) only for the diacetate (DS = 2.4)(Kamide et Saito 1985). However T_m and T_d are still too close to allow

melt processing as thermoplastics. Plasticizer to reduce T_m and increase flexibility can be added ranging from 15 to 35 wt.% (Ganster et Fink, 2013) to increase their melt processibility to behave as thermoplastics.

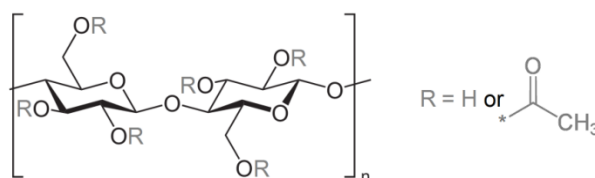


Figure 1-20. Molecular structure of cellulose acetate based on its degree of substitution (from Sigma Aldrich).

1.2.1.4.2 Carboxymethyl cellulose

Carboxymethylcellulose (CMC) is produced by etherification of cellulose: OH groups are replaced by carboxymethyl groups as presented in Figure 1-21. The degree of substitution is ranging from 0.3 to 1.4 for commercialized CMC. With a degree of substitution larger than 0.4, CMC is soluble in water unlike cellulose fiber. However, the full solubility of CMC with a DS <1.06 was challenged by the presence of aggregated crystalline domains in aqueous solution of CMC (Lopez et al. 2015; Xiquan, Tingzhu, et Shaoqui, 1990) due to a probable irregular substitution of $-\text{CH}_2\text{CO}_2\text{Na}$. The presence of these colloids affects the rheological behavior of the suspension. The aqueous solution is stable with a pH ranging from 5 to 9.

Furthermore, CMC offers a broad range of viscosity levels from 10 to 50,000 mPa s at 2 wt.% in aqueous solution with a thixotropic and pseudoplastic behavior (Edali, Esmail, et Vatistas, 2001). It was reported that the viscosity of aqueous CMC solution was influenced by the degree of polymerization of cellulose. This statement might be linked to a greater probability of irregular substitution of carboxymethyl groups. The viscosity decreases with an increase of temperature.

CMC has been used in a broad range of sectors such as the food industry, oil industry, textile industry and paper industry for its safe thickening properties and high water retention, to keep particles in suspension, for its binding properties, its filmogenic properties and its oil resistance (Drisch et Chêne 1967). Moreover, its use has improved the global performance of battery whereas it has been first used as a thickening agent to prevent graphite particles to settle out (Lee et al. 2005).

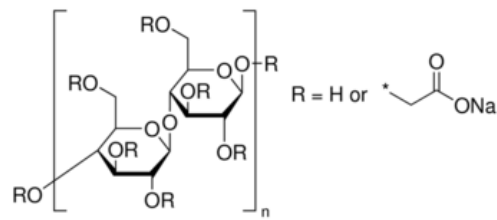


Figure 1-21. Molecular structure of sodium carboxymethyl cellulose based on its degree of substitution (from Sigma Aldrich).

To conclude, cellulose is an abundant and available material with a broad range of characteristics linked to its source and its extraction process. Its specific molecular organization allows obtaining a wide range of material with distinct properties such as cellulose fiber, nanocellulose, cellulose ether and ester.

1.2.2 The use of cellulose in additive manufacturing

Since the 90's, cellulose has been used in additive manufacturing whether as an additive or as a bulk material for producing parts. Two very recent review articles described the use of cellulose in additive manufacturing processes by following two distinct approaches: Wang et al. built its synthesis according to the additive manufacturing process and its requirements (Q. Wang et al. 2018) whereas (Dai et al. 2019) presents data according to the nature of the contribution of cellulose in the material developed for AM. Both reviews give an extensive overview on the subject. Four other interesting reviews on the topic were also considered to improve and widen the overview (Liu et al. 2019; Li T et al. 2016; Xu et al. 2018; Billiet et al. 2012).

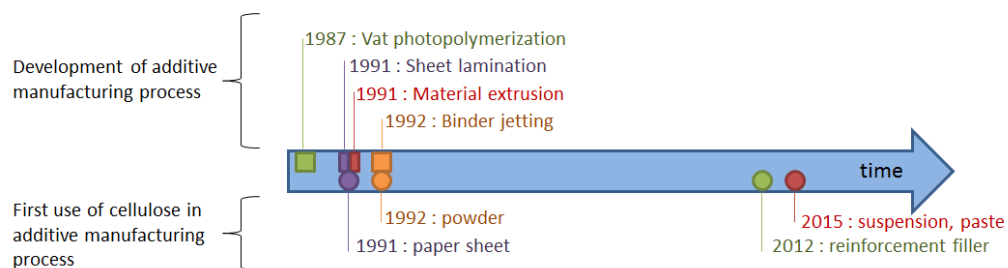


Figure 1-22. Historical review of development of additive manufacturing processes and the first use of cellulose of those processes.

As illustrated in Figure 1-22, the first uses of cellulose dates from the 90's with two processes belonging to the sheet lamination category (Feygin et Hsieh, 1991) and to the binder jetting category (Sachs et al. 1992).

More recently, in the past 5 years, cellulose was used with the vat photopolymerization (only as additive) (Kumar et al. 2012; Palaganas et al. 2017) and the material extrusion categories. For both of

these AM categories (vat photopolymerization and material extrusion), the time duration recorded between the development of the process and the first use of cellulose whether as an additive or as a bulk material shows the complexity or the non-evidence of its use with the process.

The main challenges raised by the development of cellulose based formulation compatible with AM by extrusion and the motivation to the rapid expansion of publications dealing with it are presented in the following sections. These sections start with the use of cellulose as an additive in the printed part by extrusion and finishes by its use as a bulk material.

1.2.2.1 Cellulose as an additive in the printed part by extrusion

As reported by (Dai et al. 2019) and (Q. Wang et al. 2018) , cellulose and its derivative were added in the composition of material for AM by extrusion. These 3D printed materials by extrusion can be (i) thermoplastics, (ii) resins, (iii) other polysaccharides such as alginate, chitin and chitosan, (iv) lignin, (v) starch, (vi) solid particles such as glass fiber and graphite and (vii) other materials. The role of the addition of cellulose can be sorted in seven categories as mentioned by (Dai et al. 2019): fillers, reinforcing aid, viscosity modifiers, matrix, binders, plasticizers and excipient. In this section, few examples are being presented. The selected examples were chosen to illustrate the different roles of cellulose in material compatible with AM by extrusion. They also illustrate the wide range of materials compatible with AM by extrusion as well as the use of different structures of cellulose (fiber, microfibrils and nanocrystals) and its derivatives. These examples are summed up in Table 1-5.

Role of cellulose	Material	Cellulose content (wt.%)	Solvent content (wt.%)	3D printed structures	References
- Filler	PLA+ MCC	3			(Murphy 2018)
- Reinforcement	PLA+ wood fiber	5-40		tensile specimen	(Tao et al. 2017)
- Substitution of thermoplastic	PLA+PHA+ recycled wood fiber	15	-	+ 3D structures as the material was commercialized	(Duigou et al. 2016)
- Woody aspect	PVOH+ CNC	2-10			(Cataldi et al. 2018)
	PP+ CNF	10			(Kaynak et al. 2018)
- Solid particles	Starch ether + wood flour +water	8	79	rectangular cuboid	(Gardan et al. 2016; GARDAN et Roucoules 2010)
- Anisotropic reinforcement	Acrylamid+clay + NFC	3	78	2D structures	(Sydney Gladman et al. 2016)
	HEMA+PUA + CNC	10-20	-	Rectangular cuboid	(G. Siqueira et al. 2017)
- Matrix	Montmorillonite + NFC + Methylcellulose	2.4	96.5	Cube	(Voisin et al. 2018)
- Rheological modifier	sodium lignosulfonate + MFC	2	48	Rectangular cuboid	(Shao et al. 2015)
	T-Xylan + MFC	2.7	86.5	Chess piece	(Markstedt et al. 2017)
	Alginate+glycerin + MFC	0.5	45	Cube	(Leppiniemi et al. 2017)
- Gelling agent	Bioglass fiber+ CMC	1	55 vol.%	Cube, cylinder	(Eqtesadi et al. 2013)
	Graphite powder + CMC	4	50	Cylinder	(Martínez-Vázquez, Pajares, et Miranda 2018)
	Lithium active material+AgNW + CMC	3.8	60	2D structures	(Park, Kim, et Kim 2017)

Table 1-5. Overview of a panel of example that highlight the wide range of materials compatible with AM by extrusion, the use of different structures of cellulose (text bold) and derivatives with their solid content, the different roles of cellulose in the formulation as well as the shapes of the printed parts.

AgNW: silver nanowire, CMC: carboxymethyl cellulose, CNC: cellulose nanocrystal, CNF: cellulose nanofiber MCC: microcrystalline cellulose, MFC: micro fibrillated cellulose, NFC: nano fibrillated cellulose, PHA: Polyhydroxyalkanoates, PLA: polylactic acid, PP: polypropylene, PVOH: polyvinyl alcohol

1.2.2.1.1 Cellulose fibers as filler in thermoplastics matrix

Thermoplastics materials are 3D printed by hot extrusion of a filament with a constant diameter size such as 1.75 and 2.85 mm. L. Wang, Gardner, et Bousfield 2017; Tao et al. 2017; Murphy 2018; Cataldi et al. 2018 and two companies (CC-Products and ColorFabb) added cellulose whether in the

form of wood flour (5-40 wt.%), recycled wood fibers (15 wt.%), microcrystalline cellulose or as nanocelluloses (3-10wt.%) to a thermoplastic matrix (PLA, PP) for AM by fused filament fabrication. The motivations displayed were (i) to replace one part of the matrix by a more eco-friendly material, (ii) to improve the mechanical properties in a preferential direction and (iii) to reduce shrinkage and warping for PP matrix. After succeeding in the complex addition of a hygroscopic material such as the cellulose with those matrixes with different techniques, the authors mentioned above studied the impact of cellulose addition on the microstructure, the mechanical and thermal properties and the hygroscopic behavior of the composite. However, not all the studies showed a printed part with the developed material. Duigou et al. 2016 characterized one of the two PLA filled with cellulose fiber available on the market that comprise 15 wt.% of cellulose fiber. They showed that the porosity inside such filament before printing was about 16% and the sensitivity to water uptake increased which leads to a more fragile material. A cross section of such a filament is presented in Figure 1-23.A. Figure 1-23.B and C shows printed parts with the two commercially available PLA filled with wood.



Figure 1-23. 15 wt.% of wood filled PLA: (A) SEM micrograph of a section of the raw filament (Duigou et al. 2016), (B) printed part with WoodFill filament from ColorFabb – 40% of wood filled PLA: (C) Printed part with Laywoo-3D filament from CC-Products (Li T et al. 2016).

- To conclude, cellulose was used as a filler for reinforcement, to reduce warping and to increase the proportion of eco-friendly material in the thermoplastic polymer. It was proven that a polymeric matrix loaded with up to 40 wt.% and more generally up to 15 wt.% of cellulose filler, a hygroscopic material, remains compatible with AM by hot extrusion. As a consequence, by converting these weight fractions in volume fraction, a volume filling of 36 v.% and more generally 13 v.% of cellulose filler in a matrix could be considered as processable by AM by extrusion.

1.2.2.1.2 Nanocellulose for reinforcement along the printing filament

Cellulose fiber in its nanostructured form was added to liquid resin for preferential reinforcement in printed part with ambient extrusion system. Two examples are presented.

G. Siqueira et al. 2017 selected monomers with good compatibility with Cellulose Nano Crystals (CNC) (aspect ratio 8): 2-hydroxyethyl acrylate and polyether urethane acrylate. Without acetylated modification of CNC, the CNC solid content in the ink cannot exceed 10 wt.% due to (i) the high hydrogen bonding forces, (ii) a lower dispersibility and (iii) a lower interface bonding with the resin compared to acetylated CNC. The solid content of acetylated CNC could have been increased up to 20 wt.%. This ink exhibits a strong shear thinning (10^4 Pa to 10 Pa for a shear rate of 0.01 to 50 s^{-1}) and a yield stress exceeding 100 Pa. These rheological properties combined with the use of a micronozzle ($410\text{ }\mu\text{m}$) for extrusion with an applied pressure of 3-4 bar indicate that a large volume of the ink experienced shear force during extrusion leading to fibers alignment. This fibers alignment was observed by polarized light microscopy and Atomic Force Microscopy (AFM) measurement. A slight misalignment of CNC between two adjacent printed filaments was observed. It was explained by the drag exerted by the passage of the nozzle during the deposition of the next line. This misalignment should be beneficial to increase adhesion between two adjacent deposited filaments. The tensile tests of 2D printed films with different CNC contents show, compared to the neat matrix, a more prominent strain hardening behavior after the yield point, an increase of the Young's modulus from 30 to 80% with decrease of the strain at break and a constant stress at break value of 45 MPa.

4D printing (or shape morphing system) is a process where the structure evolves over time as a response to a stimulus such as temperature or humidity. Sydney Gladman et al. 2016 printed 2D shape that turned in 3D shape actuated by a controlled anisotropic swelling of the filament after immersion of the structure in water as presented in Figure 1-24. The few quantity (3 wt.%) of nanocellulose added to their ink was enough to succeed the 4D printing experiment while avoiding clogging issue. The high aspect ratio (~ 100) of the nanocellulose combining with printing parameters such as the printing speed and the diameter of the nozzle allow a control of the alignment of these fibers induced by shear, through the extrusion nozzle. This alignment conferred an anisotropic stiffness to the material leading to an anisotropic swelling strain of the printed filament. The longitudinal and transversal strains along the filament length are 10 and 40%, respectively as illustrated in Figure 1-24.

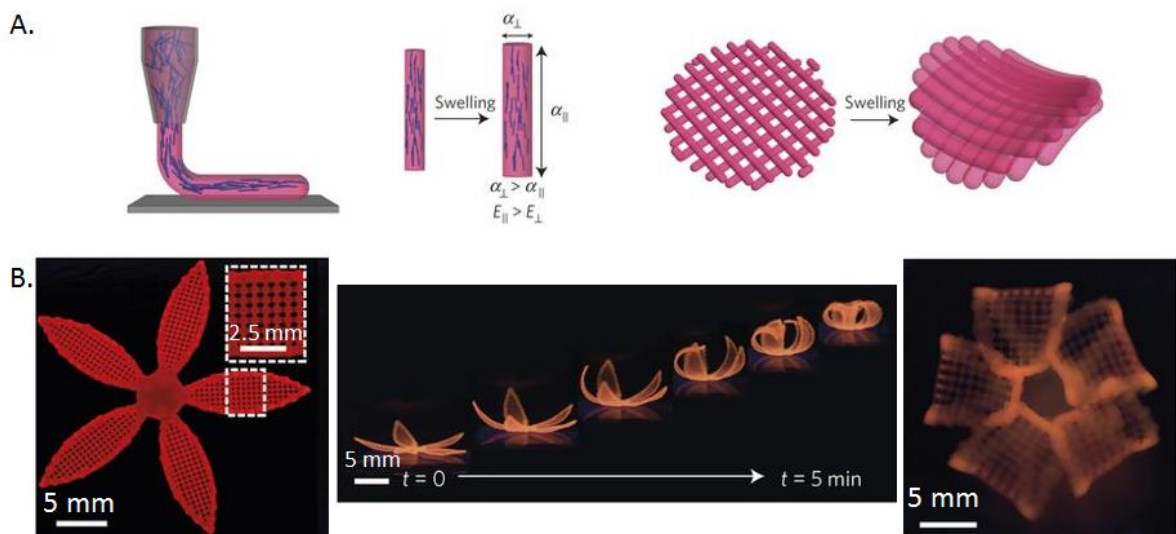


Figure 1-24. 4D printing – (A) schematic illustration of the 4D process induced by an anisotropic swelling behavior – (B) Flower 4D printed. (Sydney Gladman et al. 2016)

- To conclude, cellulose in its nanocellulose form was used for anisotropic reinforcement along the printing track. It was shown that the use of particles with a high aspect ratio in a liquid matrix induced an alignment of the elongated particles along the printing direction during the extrusion step. This alignment led to an anisotropic behavior of the printed material that can affect its mechanical properties and its swelling behavior.

1.2.2.1.3 Nanocellulose and methylcellulose as a matrix for stable foam

Voisin et al. 2018 developed a formulation for stable cellulosic based foam suitable for additive manufacturing by extrusion with optimal properties (mechanical and density) after drying. The highly charged carboxylated nanocellulose, an entangled network and the methylcellulose, a surface active molecule at 0.4 and 2 wt.%, respectively, formed a stable aqueous foam. However, other components were added to the formulation: (i) Montmorillonite at 1.1 wt.% as a rheological modifier and strengthening of the dry foam, (ii) a limited amount of polyphenol (tannic acid) at 0.02 wt.% that tuned the properties and the structures of the foam such as a stabilization of small bubble ($<10 \mu\text{m}$) and decreasing the bubble size (92 ± 54 to $52 \pm 34 \mu\text{m}$) without formation of aggregate and (iii) a paper strength agent, glyoxal, for crosslinking cellulose during drying at 80°C and increase the water resilience. The foam exhibited a pronounced shear thinning in the same range as the CNC filled resin of (G. Siqueira et al. 2017) (10^4 to 4 Pa for a strain rate of 0.01 to 100 s^{-1}). However, the yield stress was larger with a value of 800 Pa. As illustrated in Figure 1-25, they successfully extruded filament through a 0.84 mm nozzle and print a 3D structure with honeycomb. However, the side view of the printed 3D structure shows a collapse of the structure on its own weight. After drying at 80°C , the

filament showed a limited shrinkage of 8% in its diameter contrary to the ambient drying process that shows a larger shrinkage. This difference in drying inducing shrinkage behavior was explained by an increase of the loss and storage moduli of the foam by one order of magnitude due to the thermogelation of methylcellulose, increasing the strength resistance to the drying forces. The density of the dried foam, the Young's modulus and the yield strength are $21\text{kg}\cdot\text{m}^{-3}$, $2.8\pm 1.2\text{ MPa}$ and $113\pm 14\text{ kPa}$, respectively.

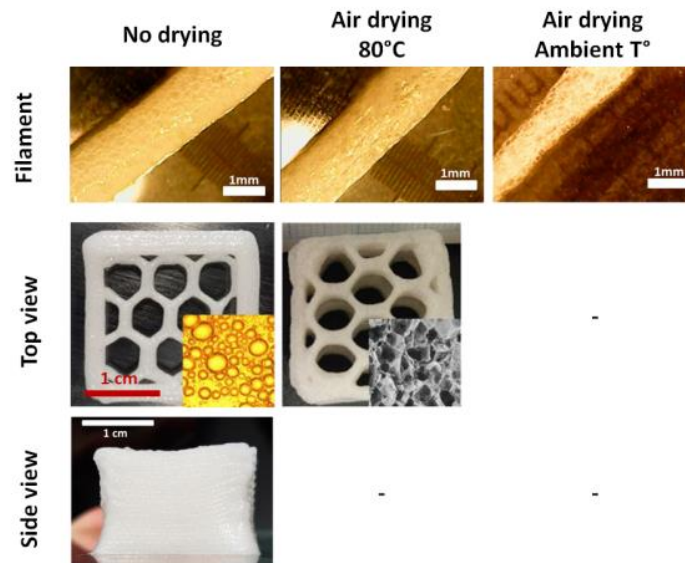


Figure 1-25. Images of extruded filament and 3D structure with honeycomb before drying, after air drying at 80°C and ambient condition with insert micrograph of the fresh and dried foam.

(Voisin et al. 2018)

- To conclude, cellulose (nanocellulose and methylcellulose) was used to produce a stable foam with a low solid content ($<5\text{ wt.}\%$), that is processable by AM by extrusion. It was shown that by reducing the drying strength (presence of bubble) and increasing the loss and storage moduli (thermogelation of methylcellulose), a dried part with limited shrinkage can be obtained.

1.2.2.1.4 Nanocellulose as a rheological modifier

As exposed in previous section (section 1.1.2 p.20), a material for AM by extrusion should exhibit a strong shear thinning to be extruded through small nozzle ($\sim 500\ \mu\text{m}$) and after extrusion, at zero shear, this material should exhibit a high viscosity and behave as a solid to keep shape fidelity. This rheological behavior corresponds roughly to the rheological behavior of nanocellulose suspension. (Shao et al. 2015; Markstedt et al. 2017; Leppiniemi et al. 2017) added nanocellulose to their ink to change its rheological behavior and to meet the requirements to obtain a printable formulation.

Shao et al. 2015 developed a formulation composed of (i) 50 wt.% of sodium lignosulfonate as a water-soluble carbon precursor (solubility up to 55 wt.%) and a large part of the solid-phase content to limit shrinkage during air drying and (ii) 2 wt.% of enzymatic MFC as a rheological modifier for 3D printability. As illustrated in Figure 1-26.A, sodium lignosulfonate dissolved at 50 wt.% in water displays a Newtonian behavior whereas MFC suspension at 2 wt.% displays typical shear thinning behavior. The blend of the two components displays a shift of the MFC curve to larger viscosity. It allows the printing of a square cuboid ($2 \times 2 \times 1 \text{ cm}^3$) without major deformations after printing except the rounded profiles of the edges indicating a balance made between the high viscosity and the pronounced thixotropic behavior of the ink (rebuild time $\sim 27 \text{ s}$). After air drying, the part displayed limited deformation of the square face and 40% shrinkage along the vertical axis (Figure 1-26.B).

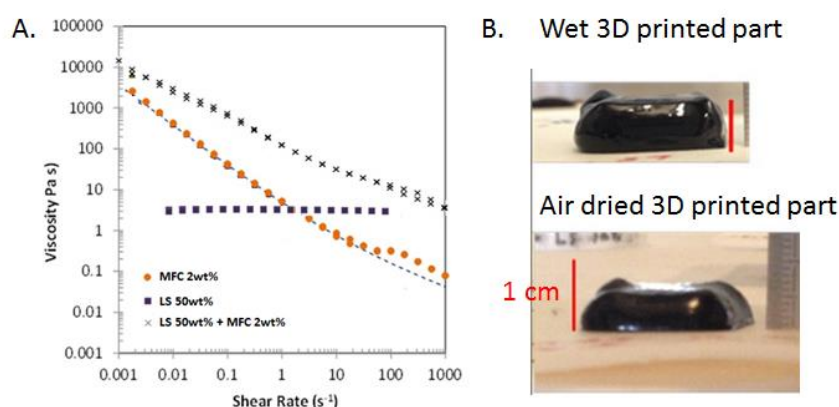


Figure 1-26. (A) Viscosity curves of MFC at 2 wt.%, lignosulfonate (LS) at 50 wt.% and the blend of the two. (B) 3D printed part with 2 wt.% of MFC blend with 50 wt.% of LS before and after air drying.

(Shao et al. 2015)

Markstedt et al. 2017 optimized an ink composed of:

- (i) 10.7 wt.% of modified xylan with tyramide (degree of substitution of 19%). Xylan was extracted from hemicellulose. Yet, hemicellulose and xylan present a natural affinity with cellulose as they form a natural composite before their extraction. Tyramide was added to xylan for irreversible and fast ($\sim 10 \text{ min}$) enzymatic cross linking with horseradish peroxidase (HRP) and hydrogen peroxide (H_2O_2) to obtain a stable handled hydrogel as illustrated in Figure 1-27.
- (ii) 2.7 wt.% of enzymatic nanocellulose with low charge. It was added as a rheological modifier for printability. However, without the addition of xylan that improve the homogeneity of the ink, bulk nanocellulose aqueous suspension can lead to phase separation.
- (iii) 0.01 wt.% of HRP. It was added to facilitate the cross linking after printing.

After being printed at a pressure of 0.7 bar through a nozzle diameter of 420 μm and cross linked, this formulation, with high water content (87 wt.%), can be used for tissue engineering or wound dressing as suggested by the author.

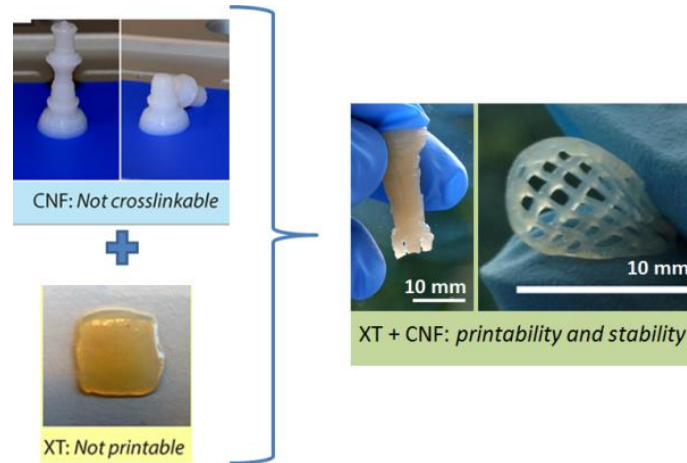


Figure 1-27. 3D printed part with CNF, modified Xylan with Tyramide (XT) and XT+CNF after crosslinking. (Markstedt et al. 2017)

Leppiniemi et al. 2017 optimized a pasty ink with (i) 50 w/v% of glycerin to increase the share of non-solvent material to minimized shrinkage and keep the shape fidelity of the part after curing (ii) 0.5 w/v% of tempo oxidized nanocellulose (TCNF) with width of 3-10 nm in a suspension concentrated at 1.06 wt.% (iii) 4.3 w/v% alginate. This formulation was successfully printed in a 20 layers high 3D structure with dimensional stability at room temperature. The goal of the study was to develop a biocompatible hydrogel for medical application: the 3D printed sample should keep its dimensions when soaked in a Phosphate-Buffered Saline (PBS) buffer. After printing, the addition of a cross linking step (immersion in a 90 mM CaCl_2 bath during 3 min) doubled the line width of the grid (1.1 to 1.9 mm) and resulted in a small shrinkage of the outer edges from 34 to 32 mm. However, after the immersion in PBS buffer during 24 h, only a slight swelling was observed whereas the non-cross linked sample turned into jelly.

- To conclude, cellulose as nanocellulose suspension at low solid content (about 1 wt.%) was added to different formulations as a rheological modifier to meet the requirements for AM by extrusion printability of the developed formulations. The addition of nanocellulose suspension changed the Newtonian behavior of the formulation into a shear thinning behavior.

1.2.2.1.5 CMC as a gelling agent

Carboxymethyl cellulose (CMC) with Molecular weight (M_w) ranging from 35 000 to 250 000 $\text{g}\cdot\text{mol}^{-1}$ was added in formulations that reached a solid content ranging from 33 to 45 vol% at a content lower than 5 wt.% for its multifunctionality: viscosity thickening agent, dispersant, binder and water processability.

Eqtesadi et al. 2013 developed a formulation for tissue engineering applications with the possibility to customize the external geometry and the pore architecture of scaffold. It was composed of (i) 45 vol.% bioglass fibers milled down at 1-10 μm and (ii) 1 wt.% CMC with a $M_w = 250\,000\text{ g}\cdot\text{mol}^{-1}$. This paste exhibited a shear thinning behavior with viscosity decreasing from 800 to 200 Pa for a strain rate varying from 1 to 100 s^{-1} , a storage modulus about 10^5 Pa, two orders of magnitude larger than the paste without CMC and a yield stress around 10 Pa. These rheological properties were compatible with a well-defined 3D scaffold structure of 60 layers as shown on Figure 1-28.

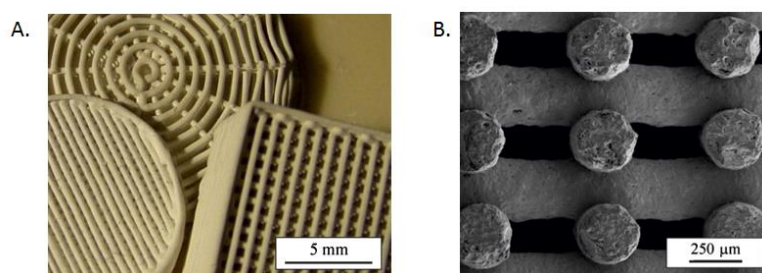


Figure 1-28. (A) 3D printed porous scaffold (B) SEM image of the well-defined cross section after sintering. (Eqtesadi et al. 2013)

Martínez-Vázquez, Pajares, et Miranda, 2018 developed a fugitive ink formulation adapted to 3D printed ceramics part; the fugitive ink exhibited a drying induce shrinkage similar to the printed ceramic part (3-10%) during air-drying and debound at high temperature during sintering of ceramics. The developed formulation was composed of 47 wt.% of graphite powder with particles size below 20 μm and 4 wt.% CMC with a $M_w = 35\,000\text{ g}\cdot\text{mol}^{-1}$. The low charge of CMC and the apolar nature of graphite facilitated the CMC adsorption onto graphite allowing this large dry content. The paste exhibited a yield stress of 6 Pa which was sufficient for maintaining the filament circularity without sagging even when spanning underlying gaps as experienced by Eqtesadi et al. 2013.

Park, Kim, et Kim 2017 designed a highly conductive ink (conductivity $1.2\cdot 10^2\text{ S}\cdot\text{cm}^{-1}$) for battery application. The highly conductive ink at 25 wt.% of dry content for 3D printability was composed of (i) 1.9 vol% of silver nanowire (AgNW) with metallic electrical conductivity of $1.6 \times 10^{-6}\ \Omega\cdot\text{cm}$ and a high aspect ratio (133~200) for percolated network formation and (ii) 98.1 vol%

of CMC with a molecular weight of $250\,000\text{ g}\cdot\text{mol}^{-1}$ and a degree of substitution of 0.7. A lithium active material (density $3.6\text{ g}\cdot\text{cm}^{-3}$ with particle size $< 5\ \mu\text{m}$) was added to the formulation for cathode and anode application while maintaining the CMC/AgNW volume ratio. The formulation had to reach 40 wt.% to minimize the volume shrinkage of the printed part upon drying. The weight proportions for the paste with AgNW, CMC and lithium active material were 2.4 wt.%, 3.8 wt.% and 33.8 wt.%, respectively. The conductivity of this paste was lower than the AgNW/CMC ink. The lithium active material might have disturbed the percolation network formation. The estimated viscosity of the paste during extrusion through a 0.84 mm sized nozzle was about $6\text{ Pa}\cdot\text{s}^{-1}$ which allows them to print a battery as shown on Figure 1-29.

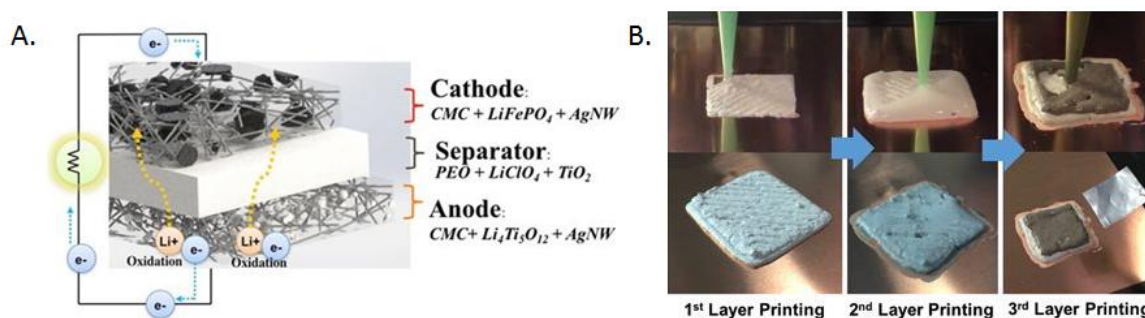


Figure 1-29. (A) Schematic overview of the printed electrode with composition of each layer. (B) the 3D printed electrode being 3D printed. (Park, Kim, et Kim 2017)

- To conclude, a cellulose derivative, carboxymethyl cellulose (CMC) was added to a water based formulation with small solid particles. It was shown that these formulations form a paste compatible with AM by extrusion even with the addition of a low solid content of CMC (about 1 wt.%).

To conclude, the addition of cellulose as a component in an ink for AM by extrusion was beneficial for all the examples presented. However, 3D printing cellulose as the main bulk material presents challenges as the contribution of the other components should be brought by the cellulose itself.

1.2.2.2 Cellulose as the main component in the printed part

Recently, several scientific articles were published on formulations compatible with AM by extrusion where cellulose was the main building block, as well as designer project (paper pulp printer from B. Holthuis). However, they present a wide variety of cellulose used, dry content, resolution (nozzle size), shape of the successfully printed part as proof of concept, post treatment and applications. The cellulose used can be sorted in four categories: (i) thermoplastics derived from

cellulose, (ii) dissolved cellulose, (iii) a blend of short fiber and wood flour and (iv) nanocellulose obtained by different treatments. Through the following examples, the current advances and limitations regarding the use of cellulose as main component are presented.

1.2.2.2.1 Poly(ethylene-2,5-furandicarboxylate), a 3D printed thermoplastic derived from cellulose

The poly(ethylene-2,5-furandicarboxylate) (PEF) is defined by Kucherov et al. 2017 as a “completely biomass-derived green polymer” as it is derived from cellulose as presented in Figure 1-30 A. Kucherov et al. 2017 studied the 3D printability of PEF by hot extrusion. PEF showed excellent compatibility with the AM by extrusion process as it did not require specific set up, it shows a negligible thermal shrinkage, between the 1.8% of PLA and the 3.4% of ABS (Figure 1-30.B) and the printed part can be recycled and printed again after filament fabrication without degradation as presented in Figure 1-30.C. Moreover, Kucherov et al. 2017 compared the quality of the 3D printed object with PEF to those printed with standard PLA. Its quality was found superior in term of fusion of the layer and smoothness of the surface. This new developed material compatible with AM by extrusion also shows excellent resistance to aggressive liquid phase unlike traditional thermoplastics used in FFF such as PLA, ABS and PETG, paving the way for numerous applications.

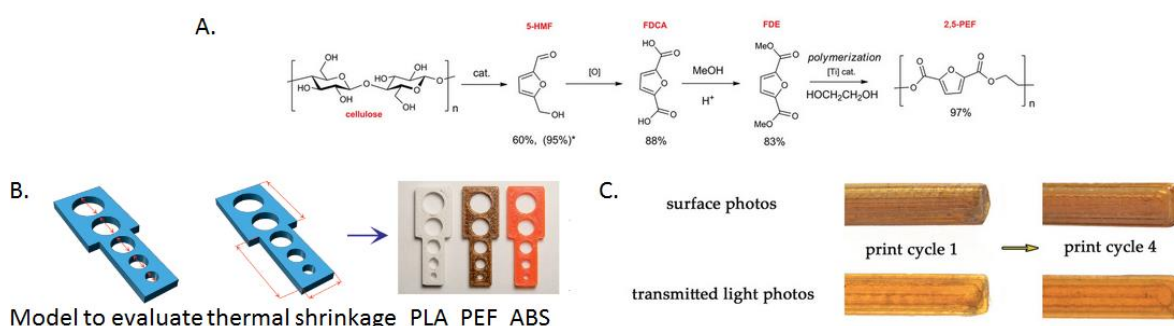


Figure 1-30. (A) reaction scheme for the synthesis of PEF from cellulose. (B) Model and printed part in PLA, PEF and ABS for thermal shrinkage evaluation. (C) No apparent change between printed part with fresh and 4 time recycled PEF. (Kucherov et al. 2017)

- The poly(ethylene-2,5-furandicarboxylate) (PEF), a thermoplastics polymer derived from cellulose is well adapted for AM by extrusion as the commercial polylactic acid thermoplastic (PLA). Few challenges were raised by its use.

1.2.2.2 AM by extrusion of dissolved cellulose

Markstedt, Sundberg, et Gatenholm, 2014; L. Li, Zhu, et Yang, 2018; Pattinson et Hart, 2017 3D printed dissolved cellulose. However, the dry content, the post treatment and the successfully printed part as proof vary between the three authors.

Based on our knowledge, Markstedt, Sundberg, et Gatenholm, 2014 were the first to use cellulose as a main bulk material for AM by extrusion. Cellulose fibers were dissolved in an ionic liquid (EmimAc (1-ethyl-3-methylimidazolium acetate)) with varying degrees of polymerization ranging from 150 to 8000. One limitation was the dry content of their solutions (4 wt.%), which limited the pressure for the extrusion to 6 bars for their operating parameters (12.7 mm long needle with an inner diameter of 0.41 mm at a flow rate of 10 $\mu\text{L}/\text{min}$). Subsequently, they had to balance the rate of coagulation with water replacing the ionic liquid. If the coagulation occurred too quickly, there was poor adhesion between printed layers. However, if the coagulation occurred too slowly, there was a height limitation of the printed part to avoid its collapse. For low structure with a maximum height of 8 mm, the solution was printed onto agar water based gel that allows a slow diffusion of water through the part from the bottom up as presented in Figure 1-31.A and for high structure, vertical agar water based gel structure (with vertical imperfections) were used to ensure a constant and continuous coagulation of the printed part as presented in Figure 1-31.B and C. The amorphous cellulose gel printed part after the replacement of the ionic liquid by water can be freeze-dried to obtain an interconnected porous structure as presented in Figure 1-31.D.

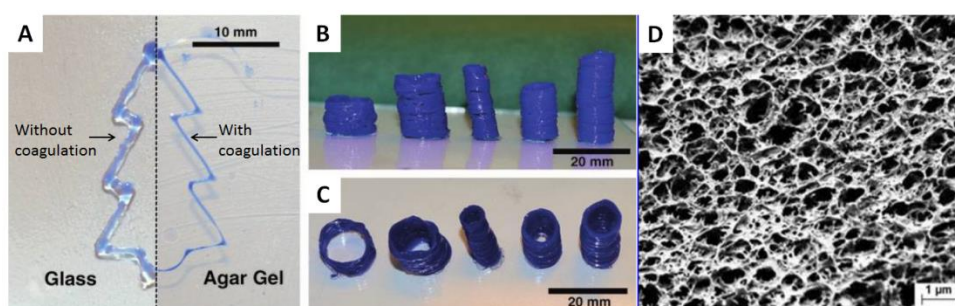


Figure 1-31. (A) Low structure printed with or without coagulation of the dissolved cellulose. (B) side view (C) top view of high structure printed with imperfectly vertical agar gel structure. (D) SEM image of the microstructure of the freeze-dried coagulated part. (Markstedt, Sundberg, et Gatenholm 2014)

L. Li, Zhu, et Yang, 2018 dissolved cellulose fibers (dissolving pulps) in N-methylmorpholine N-oxide (NMMO) at less than 10 wt.%. Their solution was printed at 70 °C and solidified after the extrusion, similar to the fused filament fabrication (FFF) method. Parts were successfully printed with heights around 2 cm. As presented in the last example, the printed part was then immersed into

Milli-Q water to form a gel that was freeze-dried to maintain the interconnected porous structures in the final product.

Pattinson et Hart, 2017 used cellulose acetate at 25-30 wt.% in acetone. The quasi-immediate evaporation of the acetone (~1 min) during the printing (cf. Figure 1-32.A and B) allowed (i) the hardening of the part as it was printed and, (ii) the shrinkage compensation of every printed layer to maintain dimensional stability of the part. A complex flower was printed (cf. Figure 1-32.C and D) that illustrates the good compatibility of their formulation with AM by extrusion process and its expectation. The main drawback of this approach was the speed limitation due to the acetone evaporation process.

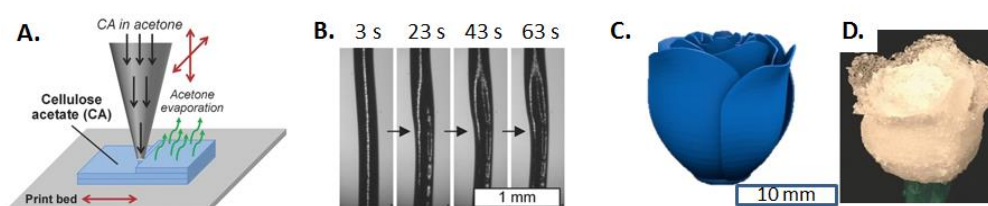


Figure 1-32. (A) Illustration of the AM by extrusion process of cellulose acetate and acetone. (B) Optical image of extruded filament during acetone evaporation. (C) 3D model of flower (D) 3D printed flower.

(Pattinson et Hart, 2017)

- The dissolved cellulose up to 30 wt.% (equivalent to 18 v.%) showed good compatibility with AM by extrusion thanks to (i) the possibility to increase the rheological properties of the last deposited layer (coagulation, hardening or solvent evaporation) and (ii) a drying process that preserves the interconnected porous structure after drying (freeze-drying) or induced enough fast shrinkage that can be compensated during the printing.

1.2.2.2.3 Short cellulose fiber, wood flour and chitosan: a fungal-like adhesive material (FLAM) for AM by extrusion

Sanandiya et al. 2018 developed a low cost cellulose based material for large -scale 3D printing. It was bioinspired from oomycetes (eukaryotic organism) to form a solid composite. The FLAM consisted in (i) high purity cellulose fiber (length < 200 μm) or wood flour (grain size < 500 μm) at 19 wt.% for shrinkage limitation and (ii) 2.4 wt.% of chitosan that presents a low degree of acetylation compared to chitin and enough protonable groups to enable dispersion at 3 wt.% in an acetic acid solution at 1 v.%. to form a colloidal dispersion of cellulose fibers. After drying, the chitosan crystallized in between fibers and bind it leading to a solid composite as presented in Figure 1-33.A. This material shows excellent bonding properties with wood (hold $33.5 \pm 7.3 \text{ kg.cm}^{-2}$) as well as with itself, a key property for being 3D printed. It was 3D printed by supplying the material

with air pressure (12 bars) to the auger screw until the 7 mm diameter nozzle as well as hot air focus on the extruded layer to increase the drying speed. As this material exhibit a low density of 0.4 g.cm^{-3} , tensile strength of 11 MPa and a Young's modulus of 240 MPa, a lightweight 1.2 m long wind turbine blade was 3D printed in two parts with the FLAM, fused in one part, manually coated with 3 mm height of FLAM to removed imperfections and finally polished. The processing stages are presented in Figure 1-33.

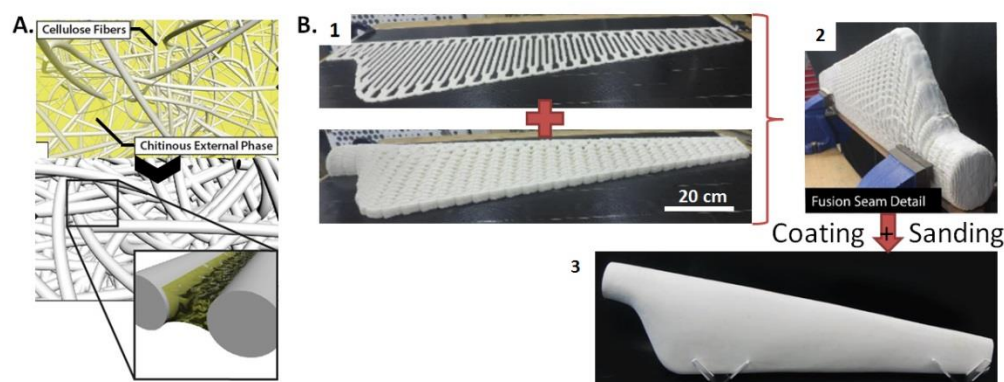


Figure 1-33. (A) Schematic illustration of the wet (up) and dry (down) fungal-like adhesive material.

(B) Processing stage of the 3D printed 1.2m long wind turbine blade (1) 3D printing in two parts (2) assembly (3) final part after coating and sanding. (Sanandiya et al. 2018)

- The paste made of less than 20 wt.% of short cellulose fiber or wood flour has shown great compatibility with AM by extrusion to produce large and simple parts with an intensive post treatment (coating and sanding) to obtain the final part. However, no comment on the strain induced deformation was presented whereas the dry content was quite low suggesting an important deformation upon drying.

1.2.2.2.4 Nanocellulose suspension for AM by extrusion

Nanocellulose suspensions were optimized to be compatible with AM by extrusion. The studies can be divided in two categories : low solid content (< 4 wt.%) with surface charged microfibrils such as TEMPO microfibrils (Rees et al. 2015; V. C. F. Li et al. 2018; Håkansson et al. 2016; Chinga-Carrasco et al. 2018) or high solid content (around 20 wt.%) with cellulose nanocrystals (Klar et al. 2019; G. Siqueira et al. 2017; V. C.-F. Li et al. 2017). Only one study (C. Jia et al. 2017) was in between with a cellulose nanocrystal concentration of 15 wt.%. They all used an air pressure extrusion system except (Klar et al. 2019) who used a piston driven by a motor. Moreover, compared to acetone, the water evaporation rate at ambient conditions is low. Yet, the hardening and main deformation begins after completion of the 3D printed part. In general, these printed parts were used either in their wet states

after cross-linking with solutions, such as CaCl_2 solutions, or were freeze-dried to produce porous media and preserve the 3D structure of the printed part.

- *Low solid content* : (Rees et al. 2015) printed a grid on a nanocellulose film with TEMPO nanocellulose at 0.95 wt.%. They report collapse of the tracks while they could not increase the solid content by centrifugation due to the already large viscosity. At a larger consistency, 2 wt.% of TEMPO or highly charged nanocellulose, (Chinga-Carrasco et al. 2018; Håkansson et al. 2016) succeeded to print well defined parts such as a nozzle, ear scaffold and a 1 cm^3 grid cube with high resolution (nozzle size < 0.6 mm). Likewise, with larger solid content of 2.8 wt.% but a lower resolution (nozzle size = 0.8 mm) (V. C. F. Li et al. 2018) successfully printed larger (4-5 cm long and > 2 cm high) and complex parts such as an ear, a pyramid and a boat. Other kinds of nanocellulose were used such as the one obtained with enzymatic pretreatment (with lower charge density) (Markstedt et al. 2015) or shorter nanofibrils with C-periodated pre-treatment (< 200 nm) (Rees et al. 2015). However, Markstedt et al. 2015 added 0.5 wt.% of alginate to its enzymatic cellulose. The resulted printed parts are presented in Figure 1-34.



Figure 1-34. 3D printed part with nanocellulose at low solid content. (A) TEMPO or highly charged nanocellulose with increasing solid content from left to right (Rees et al. 2015; Håkansson et al. 2016; V. C. F. Li et al. 2018) (B) enzymatic nanocellulose (Markstedt et al. 2015) and (C) C_Periodate nanocellulose (Rees et al. 2015).

For the studies that go further in the AM by extrusion process, all the printed parts were freeze-dried to keep the structure and the dimensions intact. It was often (i) preceded with a CaCl_2 cross linking that stabilized the structure by forming ionic link between carboxyl group (COO^-) and the divalent cation Ca^{2+} (Håkansson et al. 2016; Rees et al. 2015) or (ii) followed by thermal treatment to cross linked the nanocellulose due to the addition of 0.06 wt.% Kymene in the initial nanocellulose suspension (V. C. F. Li et al.

2018). Håkansson et al. 2016 had also evaluated less expensive drying techniques such as the solvent exchange, the addition of surfactant and the simple air drying techniques with low solid content nanocellulose; The air-drying technique did not preserve the 3D structure and dimensions whereas the solvent exchange or addition of surfactant, which added a post treatment step, preserved the 3D structures of the parts as presented in Figure 1-35. The mechanical properties of the obtained freeze-dried structure were evaluated by (i) tensile test with an ultimate tensile strength and a mean stiffness of 3.9 ± 2.7 MPa and 0.031 ± 0.019 GPa, respectively (Håkansson et al. 2016) and by (ii) compression test with a Young's Modulus of 2-3 MPa and a densification of the structure at 96-97% with a corresponding stress of 1-6 MPa (V. C. F. Li et al. 2018). As these developed formulations are compatible with AM by extrusion and freeze-drying, an expensive drying technique, they are dedicated for high added value applications such as scaffold for medical applications.

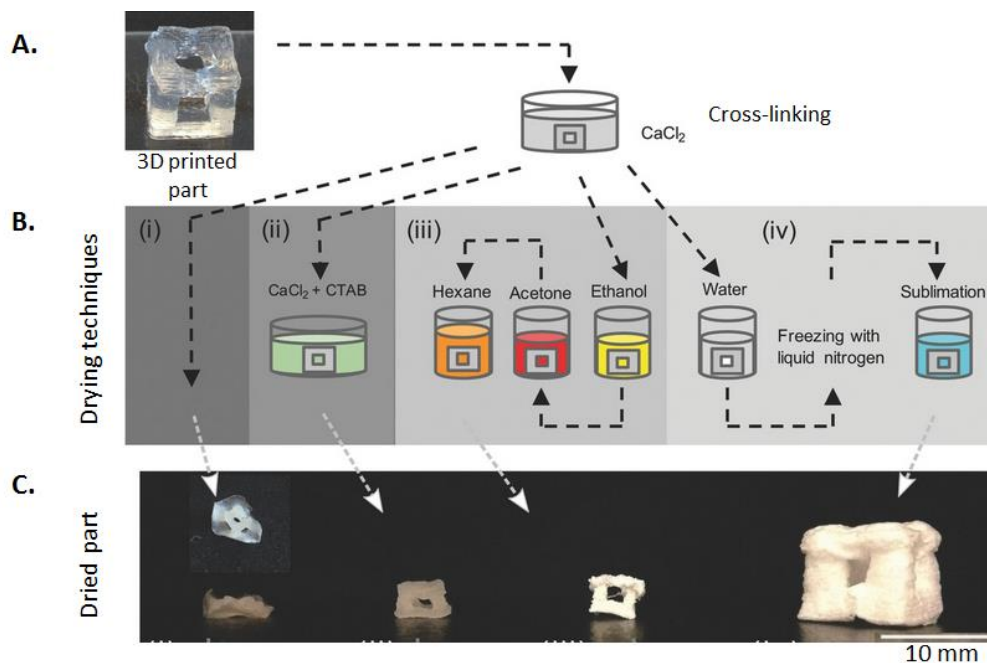


Figure 1-35. Evaluation of the drying technique on a 1cm^3 grid cube made of 2 wt.% of nanocellulose and 98 wt.% of water. (Håkansson et al. 2016)

- *High solid content* (around 20 wt.%): The limitation to 20 wt.% (or tested until 30 wt.%) of CNC content for AM by extrusion with nozzle size below 0.5 mm was justified by (i) a limitation of the power of the homogenizer to obtain a homogeneous gel and the air pressure controller for extrusion (V. C.-F. Li et al. 2017) and (ii) a plug flow experienced in the nozzle that limit the CNC alignment (aspect ratio ~ 18) and so the isotropic

reinforcement for targeted applications (G. Siqueira et al. 2017). For the enzymatically fibrillated cellulose nanofibers, the limitation to 20 wt.% was motivated by a lower clogging propensity and a more stable extrusion pressure with 1.2 or 0.84 mm large nozzle.

This high solid content allows the maintaining of the printed edges without sagging even after few minutes while a larger pressure is required for extrusion (x4 from a solid content of 15 wt.% to 20 wt.%) (V. C.-F. Li et al. 2017). (G. Siqueira et al. 2017; Hausmann et al. 2018) studied the rheological behavior of the printed suspensions. The CNC ink exhibits a pronounced shear thinning behavior with a well-defined dynamic yield stress of 350 Pa and an elastic behavior at low shear characterized by a storage modulus of $5.8 \cdot 10^3$ Pa that exceed the loss modulus by one order of magnitude.

(V. C.-F. Li et al. 2017; Klar et al. 2019) characterized their dried part obtained by freeze or air drying. For the freeze-dried structure (V. C.-F. Li et al. 2017), no shrinkage or damage was observed whereas the air-dried structure shrank up to 21% of the original model (Klar et al. 2019, 201) (cf. Figure 1-36). They both studied the microstructure and the mechanical properties.

Both observed macropores from 20 to 800 μm with scanning electron microscopy (SEM) images or with X-ray tomography. The distribution was shifted to smaller pore for the freeze-dried structure as most of the pores are smaller than 200 μm whereas they count for only 40% for the air-dried structure. Moreover, the density of the dried part was $1.2 \text{ g}\cdot\text{cm}^{-3}$ for air-dried against $0.3 \text{ g}\cdot\text{cm}^{-3}$ for the freeze-dried structure.

For the mechanical properties, (Klar et al. 2019) studied its tensile properties. The obtained material was brittle with a stiffness, a stress and an elongation at break of 500 MPa, 25 MPa and 9%, respectively. V. C.-F. Li et al. 2017 studied the compression of the freeze-dried nanocellulose suspension with the addition of Kymene (2.5 wt.% in the suspension before printing and immersion in a 2.5 wt.% of Kymene solution during 3 h). The aerogel was less brittle than without Kymene addition and exhibit a Young's modulus of 9 MPa with a densification of the structure of 78% and a corresponding stress of 22 MPa.

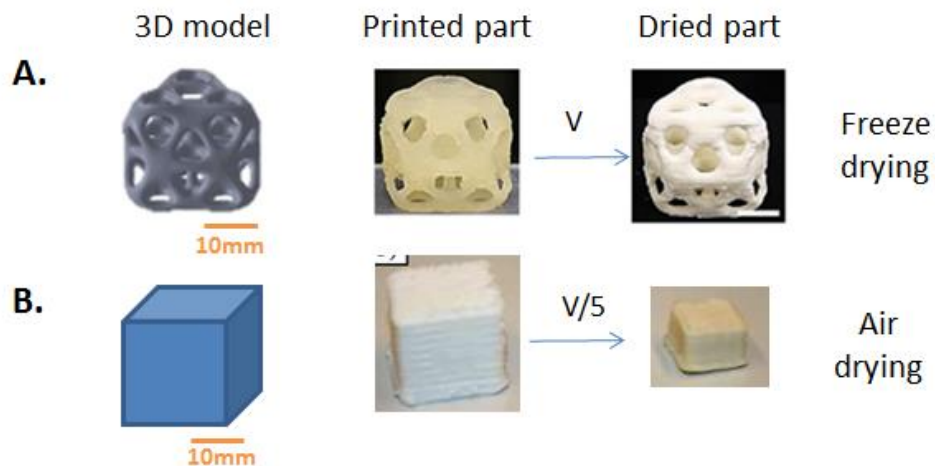


Figure 1-36. 3D models printed with high solid content (20wt.%) and dried with (A) freeze-drying without shrinkage (V. C.-F. Li et al. 2017) or (B) air drying with a volume shrinkage by 5 (Klar et al. 2019).

- By tuning the charge and the solid content of nanocellulose, complex 3D printed structures were obtained with pneumatic extruder head. The preservation of the porosity of the 3D structures after drying was primordial as the objective was to use it as scaffold for medical applications. As a consequence, cross linking and freeze-drying process are common uses as drying by solvent exchange or by air induced too large strain with less porosity.

1.2.3 Conclusion

To conclude, cellulose is a versatile renewable and biodegradable polymer due to its specific molecular organization. It can be in the form of natural fiber, nanocellulose suspension, solution of dissolved cellulose, thermoplastic like or gel. These multiple forms make it often present as key additive in composition of ink for AM by extrusion. It was also used as the main bulk material showing interesting results with still numerous challenges to face.

1.3 Conclusion

1.3.1 Synthesis of the state of the art

Additive manufacturing (AM) and in particular AM by extrusion presents numerous opportunities and is in constant evolution with new developed materials and printing devices. AM by extrusion is composed of three key steps: extrusion, deposition and post processing. Cellulose is a bio-based and biodegradable material with numerous specific properties, which makes it promising for a common use in AM by extrusion. However, only few studies demonstrated that cellulose can be actually used as a bulk material with AM by extrusion. The overview of these studies is presented in Table 1-6.

Type of cellulose	Cellulose derivatives		Cellulose short fibers	Nanocelluloses		
	PEF	Dissolved cellulose		Charged NFC	Enzymatic NFC	NCC
Dry content	-	4 to 30 wt.%	20 wt.%	1 to 4 wt.%	20 wt.%	15 to 20 wt.%
Driven device technology	Hot extrusion Pinch roller system	Pneumatic technique	Screw driven technique	Pneumatic technique	Piston technique	Pneumatic technique
Part 3D printed	Rectangular cuboid	2 cm high cylinder to complex flower model	Internal structure of a wind turbine blade	Disk, cube, to complex model	Cube to complex model	Cuboid to highly complex model
Resolution	0.5 mm	0.5 mm	7 mm	0.5 mm	0.8-1.2 mm	0.5 mm
Drying method	-	Freeze-drying or evaporation during printing	Air drying	CaCl ₂ cross linking and freeze-dried	Air drying	Freeze-drying
Dried part 3D printed	Dense Dimension and 3D structure preserved	Porous structure to dense structure Dimension and 3D structure preserved	Intense post processing (coated and polished)	Porous structure Dimension and 3D structure preserved	Dense Volume reduced by 5, structure preserved, few cracks	Porous structure Dimension and 3D structure preserved
References	Kucherov et al. 2017	Markstedt, Sundberg, et Gatenholm 2014; L. Li, Zhu, et Yang 2018; Pattinson et Hart 2017	Sanandiya et al. 2018	Rees et al. 2015; Chinga-Carrasco et al. 2018; Håkansson et al. 2016; Markstedt et al. 2015; V. C. F. Li et al. 2018	Klar et al. 2017, 2019	G. Siqueira et al. 2017; Hausmann et al. 2018; V. C.-F. Li et al. 2017; C. Jia et al. 2017

Table 1-6. Overview of the studies published on formulations compatible with AM by extrusion where cellulose was the main building block.

Table 1-6 highlights the different challenges and strategies developed:

- A chemical conversion of cellulose in an amorphous thermoplastic to be process exactly like PLA with the fused filament fabrication process.
- The addition of a solvent to cellulose material to be shaped by AM by extrusion.
- A cellulose dissolution at 30 wt.% of dry content in a highly volatile solvent to immediately compensate deformation induced by drying and to allow an immediate “set” of the material to facilitate shape retention. Challenges faced are linked to the layer adhesion, a slow printing process and solvent recyclability.
- A maximum solid content about 20 wt.% for colloidal suspension to be compatible with pneumatic technique or piston technique and a resolution about 0.5-1.0 mm. To maintain the dimensions upon drying, an expensive freeze-drying technique must be used. If not, with air-drying technique, the volume dimensions are reduced by at least 5. Freeze-dried part showed low mechanical properties compared to dense part. One challenge is linked to the large viscosity of the suspension that reached the limit of range of the operating devices (mixing and AM by extrusion with pneumatic technique) in order to maintain shape fidelity. Another one is linked to a possible phase separation, which can induce nozzle clogging or produce inhomogeneous filaments.

1.3.2 Motivation of the PhD

The summary presented in the previous sections (section 1.3.1) shows that the developed formulations with cellulose as the main component raised several questions: can cellulose be a new, cheap, lightweight, robust, renewable, and biodegradable material compatible for AM by extrusion similar to PLA? What form of cellulose (natural cellulose fiber, nanocellulose, cellulose derivative) should be used and with which solvent? Which proportion of cellulose fibers is required to limit deformation after drying and the cost of the drying process while being an extrudable material? Are there any design restrictions or new design opportunities compared to fused filament fabrication processes with thermoplastic materials, such as the bio-based PLA? Can a functional cellulose based ink be implemented similar to conductive graphene-PLA for 3D pattern?

To deal with these challenges, in this project, we focus our strategy on the development of a 100% cellulose based material and a functional one compatible with AM by extrusion to produce complex and multi-material parts such as smart objects. The objective was to develop a cellulose based material with the same capabilities as PLA toward 3D printing by extrusion:

- resolution up to 0.4-0.8 mm,
- printing speed up to 10-50 mm.s⁻¹,

- complex part design,
- mechanical properties (Young's modulus about 2-3 GPa),
- safety aspect by using non-hazardous material,
- economical aspect of the material and the produced part down to 30 €/kg.
- conductivity of about 10^2 - 10^3 S.m⁻¹ for PLA/carbon composite

To reach this objective, this work focused on:

- concentrated aqueous paste formulations based on short cellulose fibers and CMC or graphite and CMC,
- 3D printer customization to be compatible with such pastes,
- air-drying of 3D dense parts with the possibility of the addition of a solvent exchange step before air-drying to reduce shrinkage after drying.

The material and process choices were based on the state of the art and the targeted objective. Indeed, the freeze-drying process was too expensive and lead to low mechanical properties compared to air-drying although it preserves the dimension of the part after drying.

To ensure a minimum shrinkage, the solid content of the formulation should be as large as possible while being compatible with AM by extrusion. Nanocelluloses are quite expensive and increasing their solid content up to 30 wt.% is challenging unlike short cellulose fibers, that still meet the resolution requirement and keep the reinforcement aspect of fibers. As presented in the state of the art (section 1.2.2.1.5 p.55), CMC can be added as gelling agent in formulation based on solid particles to form a paste compatible with AM by extrusion. Functional inks compatible with screen printing can be deposited with 3D printing by extrusion process as a 2D pattern on a surface of a 3D printed part. However, they cannot be used to manufacture conductive 3D part unlike graphite and CMC formulation that was developed as a support material for 3D printing ceramics. The conductivity of this kind of formulation must be tested and compared to conductive PLA blend.

The 3D printer can be customized to be adapted to the developed material such as the extrusion head which must be adapted to the viscosity of the material.

Such developments will extend the possibilities offered by AM by extrusion from a paste point of view.

Chapter 2. Material and methods

2.1	Introduction.....	69
2.2	Material and paste preparation.....	69
2.2.1	Optimization of the formulations.....	69
2.2.2	Additives to tailored the paste properties.....	75
2.3	Additive manufacturing by extrusion.....	75
2.3.1	The used 3D printer.....	75
2.3.2	Slicing software and AM by extrusion process.....	76
2.3.3	Extrusion flow: calculation, measurement and calibration.....	77
2.3.4	Printed parts with their printing parameters.....	79
2.3.5	Drying processes.....	83
2.3.6	Dimension measurements.....	84
2.3.7	Weight measurements.....	85
2.4	Characterization.....	86
2.4.1	Rheology of paste.....	86
2.4.2	Deformation after drying.....	87
2.4.3	SEM observation.....	87
2.4.4	Mechanical testing: tensile test.....	87
2.4.5	Conductivity.....	89
2.4.6	Temporal characterization of the drying.....	89
2.5	Conclusion.....	95

2.1 Introduction

The main objective of this PhD is the development of a new cellulose based formulation compatible with AM by extrusion to produce complex object. As mentioned in the previous chapter (**Erreur ! Source du renvoi introuvable.**), the shape and size distribution of the particles in the paste composition, the paste rheology, the extruder head design, the part design and the drying process are key parameters in AM by extrusion. The objective of this chapter is to provide an accurate description of the used material and its mixing process to prepare three different pastes with different types of fillers (section 2.2), the setups of the AM by extrusion process (section 2.3) and the tools developed to characterize and evaluate the paste compatibility with AM by extrusion, in particular the temporal characterization of samples during drying (section 2.4).

2.2 Material and paste preparation

2.2.1 Optimization of the formulations

The three studied pastes were composed of:

- (i) One type of fillers: natural cellulose fibers, natural cellulose powder or graphite powder,
- (ii) Carboxymethyl cellulose (CMC),
- (iii) Distilled water.

2.2.1.1 Description of the components

(i) *Fillers:*

- The cellulose fibers (Carl Roth) consisted of a mix of milled hardwood and softwood natural fibers, as illustrated in Figure 2-1.A. The fiber length and width distributions were measured using the Morfi[®] approach (Techpap[®], Grenoble, France) (Passas et al. 2001). Figure 2-1.B and C show that (i) 90% of the fibers were shorter than 200 μm and (ii) fibers longer than 100 μm had a mean fiber width of 27 μm . The moisture content of these cellulose fibers was about 10%, measured using standard to determine the dry content of paper, board and pulps (ISO 638:2008).

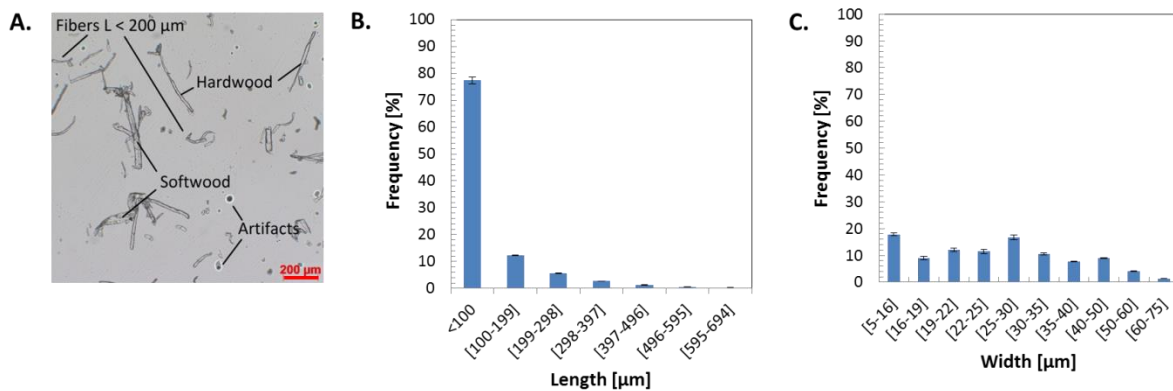


Figure 2-1. Optical characterization of cellulose fibers – (A) Image of natural cellulose fibers in suspension taken with an optical microscope. (B) Length distribution of cellulose fibers. (C) Width distribution of cellulose fibers with lengths greater than 100 μm .

- The cellulose powder (Sigma Aldrich T50) consisted of microcrystalline powder of cotton linter (Figure 2-2.A). The size of the particles was measured using a granulometer (Cilas particle size analyzer 1190) based on the Fraunhofer method to confirm the supplier specifications that at least 50 wt.% of the particles are smaller than 50 μm . Figure 2-2.B shows that 90% of the analyzed particles had a diameter below 43 μm . The moisture content of this cellulose powder was about 10%, measured using standard to determine the dry content of paper, board and pulps (ISO 638:2008).

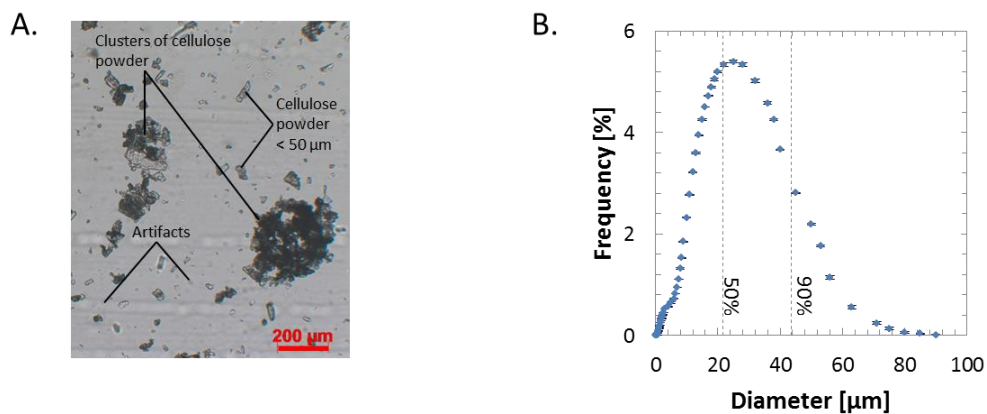


Figure 2-2. Optical characterization of cellulose powder – (A) Image of microcrystalline cellulose powder in suspension taken with an optical microscope. (B) Diameter distribution of cellulose powder.

- The graphite powder (TIMCAL TIMREX SLP 30) consisted of more than 99.5% of graphite with a bulk density of $2.2 \text{ g}\cdot\text{cm}^{-3}$. Likewise for the cellulose powder, the size of the particles was measured using the granulometer based on the Fraunhofer method. Figure 2-3.B shows that 90% of the analyzed particles had a diameter below 39 μm .

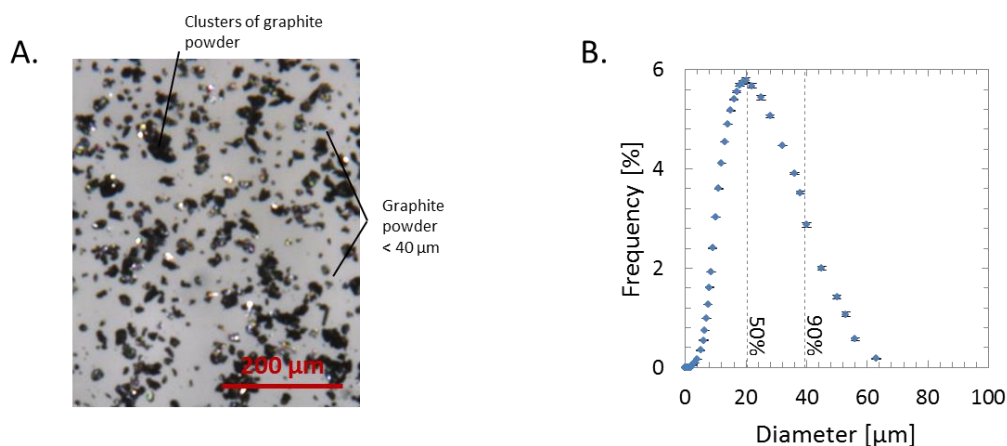


Figure 2-3. Optical characterization of graphite powder – (A) Image of graphite powder in suspension taken with an optical microscope. (B) Diameter distribution of graphite powder.

(ii) *Sodium carboxymethyl cellulose (CMC):*

Sodium carboxymethyl cellulose (CMC) with an average molecular weight of $90\,000\text{ g}\cdot\text{mol}^{-1}$ and 0.7 carboxymethyl groups per anhydroglucose unit was purchased from Sigma Aldrich. Figure 2-4 shows the CMC powder before its use.

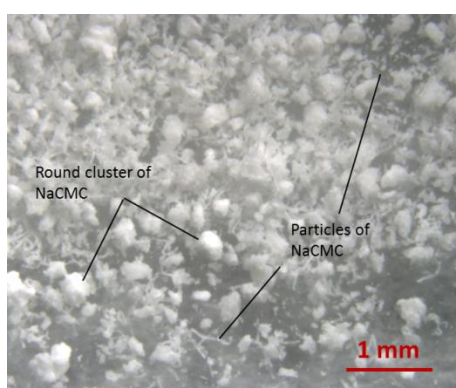


Figure 2-4. Image of dry sodium carboxymethyl cellulose powder taken with a binocular magnifier.

2.2.1.2 Paste preparation and composition

Preliminary remarks

The different dry contents, that are the CMC content and fillers content, were chosen after preliminary testing (Figure 2-5.A) to achieve a balance between:

- the extrusion processability of the paste by maintaining enough CMC and water content to avoid fiber-water phase separation by increasing the viscosity of the water and to keep enough liquid phase between fibers to obtain a paste.
- the shrinkage limitation upon drying by increasing the filler solid content.

Paste preparation

- Batches of 100 g and 500 g of paste were prepared by dry mixing the fillers with the CMC and then adding distilled water to adjust the dry solid contents. The paste was homogenized for 5 to 10 min at 120 rpm using a planetary mixer (Proline RP10). The paste was stored for 24 h in the fridge at 4–5 °C before printing.

Composition of the pastes

Different dry contents, CMC contents and fillers contents were evaluated for the three studied pastes composition (Figure 2-5.A):

- The fiber cellulose paste formulations had overall dry contents varying from 35 to 50 wt.%, cellulose fiber contents varying from 15 to 45 wt.% and CMC contents varying from 5 to 20 wt.% as represented in the ternary diagram (Figure 2-5.B) and detailed in Table 2-1.

N° formulation	Water (by wt.%)	CMC (by wt.%)	Cellulose fiber (by wt.%)	Water (by vol.%)	CMC (by vol.%)	Cellulose fiber (by vol.%)
1	65.0	5.0	30.0	73.6	3.8	22.6
2	57.5	5.0	37.5	67.0	3.9	29.1
3	50.0	5.0	45.0	60.0	4.0	36.0
4	65.0	12.5	22.5	73.6	9.4	17.0
5	57.5	12.5	30.0	67.0	9.7	23.3
6	50.0	12.5	37.5	60.0	10.0	30.0
7	65.0	20.0	15.0	73.6	15.1	11.3
8	57.5	20.0	22.5	67.0	15.5	17.5
9	50.0	20.0	30.0	60.0	16.0	24.0

Table 2-1. Fibrous cellulose formulations in weight and volume contents of water, CMC and cellulose fiber. The conversion weight to volume was performed based on a cellulose fiber and CMC density of 1.5 g.cm⁻³.

- The powder cellulose paste formulations had overall dry contents varying from 42.5 to 57.5 wt.%, cellulose powder contents varying from 22.5 to 52.5 wt.%, and CMC contents varying from 5 to 20 wt.% as represented in the ternary diagram (Figure 2-5.C) and detailed in Table 2-2.

N° formulation	Water (by wt.%)	CMC (by wt.%)	Cellulose powder (by wt.%)	Water (by vol.%)	CMC (by vol.%)	Cellulose powder (by vol.%)
1	57.5	5.0	37.5	67.0	3.9	29.1
2	50.0	5.0	45.0	60.0	4.0	36.0
3	42.5	5.0	52.5	52.6	4.1	43.3
4	57.5	12.5	30.0	67.0	9.7	23.3
5	50.0	12.5	37.5	60.0	10.0	30.0
6	42.5	12.5	45.0	52.6	10.3	37.1
7	57.5	20.0	22.5	67.0	15.5	17.5
8	50.0	20.0	30.0	60.0	16.0	24.0
9	42.5	20.0	37.5	52.6	16.5	30.9

Table 2-2. Powder cellulose formulations in weight and volume contents of water, CMC and cellulose powder. The conversion weight to volume was performed based on a cellulose fiber and CMC density of 1.5 g.cm^{-3} .

- The graphite paste formulations had overall dry contents varying from 24.1 to 43.3 wt.%, graphite contents varying from 42.3 to 67.8 wt.% and CMC contents varying from 5.7 to 12.6 wt.% as represented in the ternary diagram (Figure 2-5.C) and detailed in Table 2-3. These mass ratios differ from the ones of the cellulose pastes mentioned above to keep the CMC mass concentration in water varying from 15 to 25 wt.% and to obtain a dry content of 40 to 50 vol.%. This is due to the difference in bulk density between the graphite (2.2 g.cm^{-3}) and the cellulose (1.5 g.cm^{-3}).

N° formulation	Water (by wt.%)	CMC (by wt.%)	Graphite (by wt.%)	Water (by vol.%)	CMC (by vol.%)	Graphite (by vol.%)
1	41.9	7.4	50.7	60.0	7.1	32.9
2	36.8	6.5	56.7	55.0	6.5	38.5
3	32.1	5.7	62.3	50.0	5.9	44.1
4	42.6	10.6	46.8	60.0	10.0	30.0
5	37.3	9.3	53.4	55.0	9.2	35.8
6	32.4	8.1	59.5	50.0	8.3	41.7
7	43.3	14.4	42.3	60.0	13.3	26.7
8	37.8	12.6	49.6	55.0	12.2	32.8
9	32.8	10.9	56.2	50.0	11.1	38.9

Table 2-3. Graphite formulations in weight and volume content of water, CMC and graphite. The conversion weight to volume was performed based on a CMC density of 1.5 g.cm^{-3} and graphite density of 2.2 g.cm^{-3} .

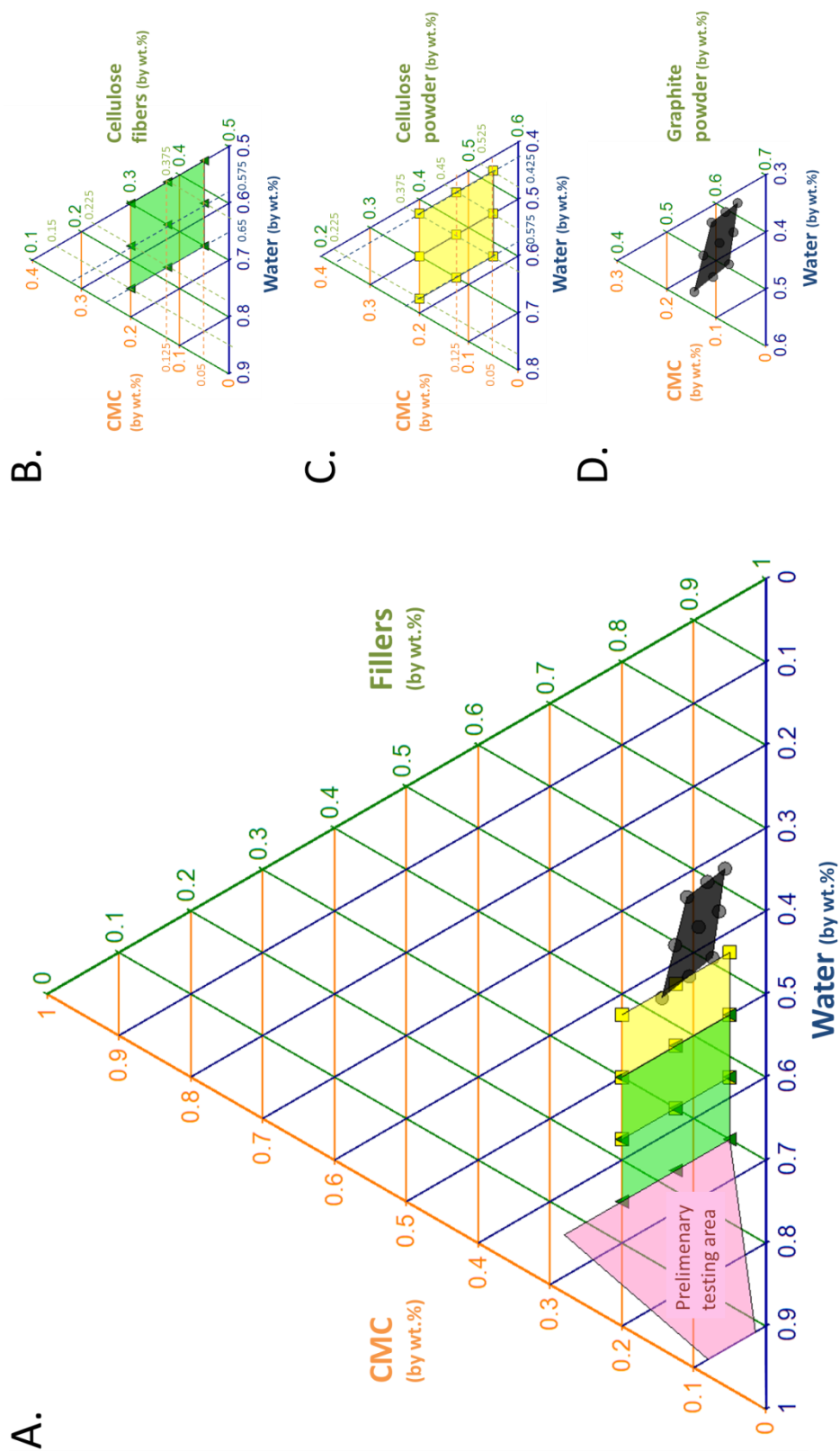


Figure 2-5. Ternary diagrams indicating the weight fractions of CMC, fillers, and water for the tested formulations: (A) global overview; Zoom on (B) cellulose fiber pastes, (C) cellulose powder pastes and (D) graphite powder pastes.

2.2.2 Additives to tailored the paste properties

Once the fiber cellulose paste was optimized, extra components such as a wet strength agent or dye were added to distilled water before its mixing with the dry components.

- Wet strength agent: Kymene 16 X-CEL (Ashland) at a concentration of 16 wt.% in water was added to the formulation from 0 to 10 wt.% of the dry content as described in Table 2-4. It was added to increase the wet properties of the optimized paste.
- Dye: few drops of food dye (Violet icing color from Wilton) were added to the water in the formulation to color the white paste. It was added to produce colored parts to show the wide color possibilities of printed parts with the optimized paste.

Formulation	Water (by wt.%)	CMC (by wt.%)	Cellulose fiber (by wt.%)	Kymene at 16 wt.% (by wt.%)
Ref	57.5	12.5	30.0	0.0
Kymene 0.5	56.2	12.5	30.0	1.3
Kymene 1	54.8	12.5	30.0	2.7
Kymene 3	49.3	12.5	30.0	8.2
Kymene 5	43.5	12.5	30.0	14.0
Kymene 10	28.0	12.5	30.0	29.5

Table 2-4. Formulations to evaluate the influence of the wet strength agent from 0 to 10 wt.% of the dry content.

2.3 Additive manufacturing by extrusion

2.3.1 The used 3D printer

The commercial 3D printer Prusa i3 is a Cartesian 3D printer with a build platform that moves in Y axis and the extruder head moves in X and Z axis. This printer was upgraded with a liquid deposit modeling (LDM) WASP extruder (Figure 2-6.A and B). To feed the cavity of the LDM extruder (caption 1 of Figure 2-6.A) with the paste described in section 2.2, two sizes of air pressure tanks were used:

- a 15 cm³ syringe designed on a CAD software (123D Design) and 3D printed by stereolithography to allow extrusion of small batches of paste with a pressure of 1 to 3 bars carried by the extruder (caption 2 of Figure 2-6.A).
- a 3L tank (3D WASP) pressurized at 5.5 bars which is connected to the extruder by a 60 cm long tube in PTFE (polytetrafluoroethylene) as the tank stands on the table with only translation and rotation allowed in its longitudinal direction.

The cavity was placed in the device just before the paste entered the LDM extruder. The extruder consisted of a screw-driven device (3) in a barrel (4) and a steel nozzle (5) with an outlet

diameter d varying from 0.5 to 0.9 mm. The inner shapes of the nozzles were designed with two successive constrictions from a diameter of approximately 5 mm to the final outlet diameter d (Figure 2-6.D). This extruder device could apply up to 40 bars of pressure to the paste, a significantly larger pressure than the typical 7 bars pressure achieved by pneumatic extruders. So, this LDM extruder allowed the use of highly viscous pastes at printing speeds of the same order of magnitude as those of the FFF process, ranging from 10 to 50 mm.s⁻¹. It was possible to quickly interrupt the flow by changing the direction of rotation of the screw to release the pressure applied to the paste. To compensate for the pressure loss due to the nozzle, the rotational velocity of the screw was set 2 to 3 times larger than the theoretical velocity to achieve the flow required for accurate 3D printing. The rotation velocity of the screw was approximately 10 rpm for most of the printed parts analyzed in this manuscript.

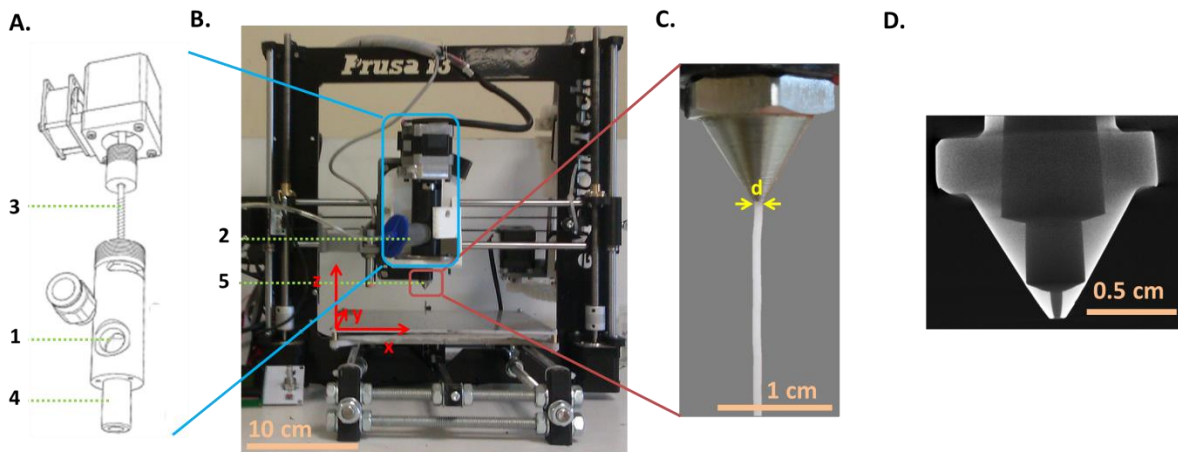


Figure 2-6. 3D printer Prusa i3 upgraded with a Liquid Deposit Modeling WASP Extruder – (A) Close-up and exploding drawing of the LDM extruder(www.3dwasp.com), (B) Picture of the printer used in this work, (C) Close-up of nozzle with an inner diameter of 0.7 mm and (D) 2D view of an X-ray Computed Tomography (XCT) scan of the nozzle .

(1) Cavity, (2) Air pressure syringe, (3) screw-driven device, (4) barrel, and (5) steel nozzle.

2.3.2 Slicing software and AM by extrusion process

In general, to 3D print a part, a CAD model is first sliced orthogonally in the Z direction in thin layers, which are then divided into tracks by a slicing software (Simplify 3D in this study) using several key parameters: (i) the track width (width of the track laid down), (ii) the layer height (thickness of each layer), (iii) the infill (density of rectilinear pattern in one layer), and (iv) the number of perimeter shells (solid wall of the model). These parameters are illustrated in Figure 2-7. This dataset and the printing speed are converted to a programming language compatible with the printer named G-code (C. Y. Huang 2018). The main parameters defined in this programming language are the X,Y,Z

coordinates, the speed of the print head and the quantity of material to consume. This quantity of material to consume is calculated from the layer height, the track width, the length of the track and an extrusion multiplier in order to be able to easily tailor it for over-extrusion for example. Its unity is expressed in length of a filament of 1.75 mm of diameter. This parameter as well as the speed of the print head and the length of the track defined the rotation velocity value of the screw. One layer at a time, the extruder head (and/or the build platform on which the part is manufactured) moves in the (x,y) plane and extrudes material shaped as a flatten filament in order to create one cross-section of the part. After completing the layer, the extruder head lifts (or the building plate lowers) to the height of a layer thickness to build the next layer of the part on top of the previous layer, and this process continues until the part is completed.

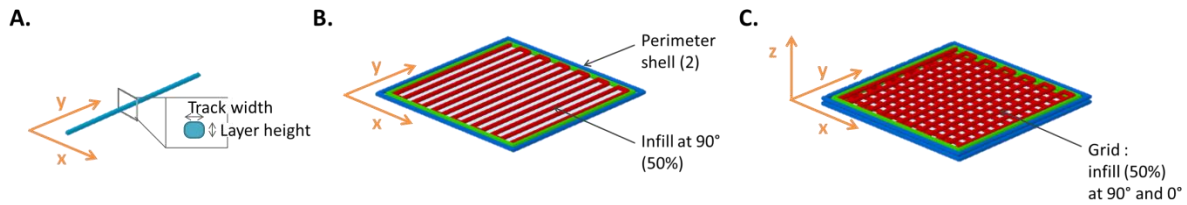


Figure 2-7. Visualization obtained using Simplify 3D of (A) one track, (B) one layer, and (C) two layers of a cube.

2.3.3 Extrusion flow: calculation, measurement and calibration

As mentioned previously, the 3D printer was upgraded with a screw-driven extruder. The rotation velocity of the screw Ω [rpm] was calculated from the section of the track, $S_p = hw$ [m²] (where h is the height and w is the width of the track), the printing speed, v_p [m.min⁻¹] and the quantity of material conveyed for one rotation of the screw, $V_{2\pi}$ [m³] as follows by the 3D printing software:

$$\Omega = \frac{S_p v_p}{V_{2\pi}} \quad (9)$$

By assuming that this extruder behaves as a volumetric pump, for one rotation of the screw, the quantity of material conveyed, $V_{2\pi}$ can be calculated with equation (10) (Vergnes et Puissant 2002).

$$V_{2\pi} = ZWH \quad (10)$$

Where $Z = \frac{B}{\sin(\theta)}$ is the length of one revolution of the screw [m]

$W = B \cos(\theta) - e$ is the channel width [m]

$H = \frac{D-d}{2}$ is the channel depth [m]

With, as illustrated in Figure 2-8.A and B,

$B = 2.6 \text{ mm}$, the screw thread

$\theta = \tan^{-1}\left(\frac{B}{\pi 0.5(D+d)}\right)$, an approximation of the angle between the thread and a perpendicular plan to the axis of the screw as it depends of the distance from the central axis of the screw.

$D = 6.0 \text{ mm}$, the internal diameter of the barrel

$d = 3.7 \text{ mm}$, the internal diameter of the screw

$e = 0.1 - 0.8 \text{ mm}$, the thickness of the thread, the mean of these values was chosen for $V_{2\pi}$ calculation.

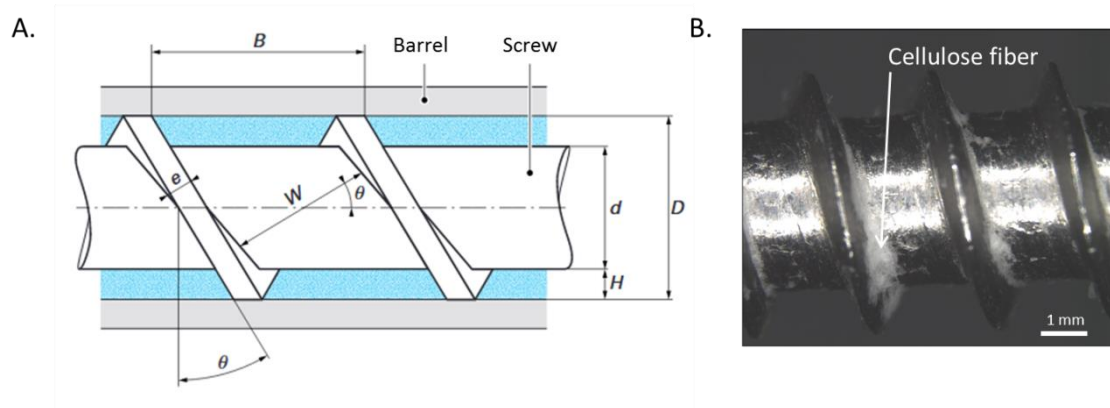


Figure 2-8. Screw extruder geometry – (A) Illustration (Vergnes et Puissant 2002) and (B) picture of the screw used without a proper cleaning.

In this particular case, with data from the screw (Figure 2-8.B), $V_{2\pi}$ was about 46 mm^3 which is equivalent to the volume of 19 mm of a filament of 1.75 mm of diameter whereas the supplier value was about 7% lower than the calculated one. The supplier value was easily calculated from the number of rotation of the screw measured for an instruction of extrusion of 300 mm of filament of 1.75 mm of diameter.

Without calibration, the actual extrusion flow rate, Q_{exp} , (that can be measured) is lower than the set flow rate, $Q_{th} = \Omega V_{2\pi} = S_p v_p$ leading to an inaccurate 3D printing part. A calibration is needed to overcome this problem. The calibration was performed before every printing session and depends on the paste and the used nozzle.

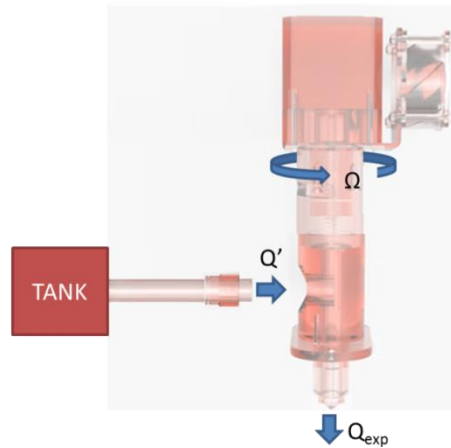


Figure 2-9. Schematic view of the extruder with the three flows: the measured outlet flow of the tank, Q' , the rotation speed of the screw, Ω , and, the experimental flow measured at the outlet of the nozzle, Q_{exp} (inspired from www.3dwasp.com).

The calibration consisted in measuring Q_{exp} and compared it to Q_{th} to obtain the calibration factor referred as C . To calculate Q_{exp} , the length of the extruded filament and its extrusion time were measured with a graduated ruler and a timer, respectively and the filament diameter was assumed to be equal to the nozzle diameter. The sampling length and the sampling time were around 25 cm and 30 s, respectively, to minimize measurement errors due to timer start and stop, filament sampling and length measurement with graduated ruler. The calibration factor was calculated as $C = \frac{Q_{th}}{Q_{exp}}$.

To evaluate the influence of the variation of the outlet flow rate of the tank, Q' , on the flow at the exit of the nozzle Q_{exp} , we measured Q' with a 10 cm long tube in PTFE at 1.5, 1.7, 2 and 2.5 bar. For each Q' , we measured Q_{exp} after stabilization (extrusion flow rate variation < 2%) at rotation velocity of the screw varying from 3 to 70 rpm. A similar procedure was applied to evaluate the influence of the rotation speed on Q' .

2.3.4 Printed parts with their printing parameters

Nine geometrical parts were selected and printed on glass plates. They exhibit an increasing complexity. The objective was to determine a guideline in term of CAD design and printing settings for one of the paste developed due to (i) the printing challenges detailed in chapter 1 (section 1.1.2.3.1 p.30) such as the bridging and overhang performance and (ii) the post processing challenges such as the drying of the paste. The first seven parts were drawn on a CAD software (123 Desk) and the two last parts were downloaded from the Thingiverse database (Thingiverse.com, March 2018) :

- Single filament (Figure 2-10.A): a single filament represents the building block of the 3D printing structures. The filaments were extruded at different linear flows (3 to 30 mm.s⁻¹), with different nozzle sizes (0.5, 0.7 and 0.9 mm) and at a distance between the nozzle and the building table larger than the length extruded to avoid filament winding on the surface. Most of the filaments were printed with a linear extrusion flow of about 6 mm.s⁻¹ through a nozzle, the diameter of whom was 0.7 mm. Different lengths were tested depending on the objectives of the characterization:
 - characterization of the fresh state *i.e.* about 1 minute after the filament extrusion : the length was about 20, 40, 60 and 80 cm to evaluate the rheological behavior of the paste
 - characterization of the dried state *i.e.* about 1 hour after the filament extrusion : the length was about 20 cm to evaluate the mechanical properties and about 10 and 20 cm to evaluate the longitudinal strain of the filament.
 - characterization during drying: the length was about 7 cm for diameter and length measurement and 20 cm for mass measurement and evaluation of the mechanical properties.
- Rectangular 2D forms (Figure 2-10.B): two layers height rectangles of $L \times l = 15.0 \times 1.5 \text{ cm}^2$ were printed to evaluate the influence of the main printing settings : *i.e.* the layer height, the track width and the extrusion rate on the mechanical properties. The printing settings were: a layer height of 0.35, 0.45 and 0.55 mm, a track width of 0.65 and 0.71 mm, no perimeter shell, 100% rectilinear infill with an extrusion multiplier of 1.0 and 1.2 times the calibration factor, C and a printing speed of 15 mm.s⁻¹. The build time was about 7 min.

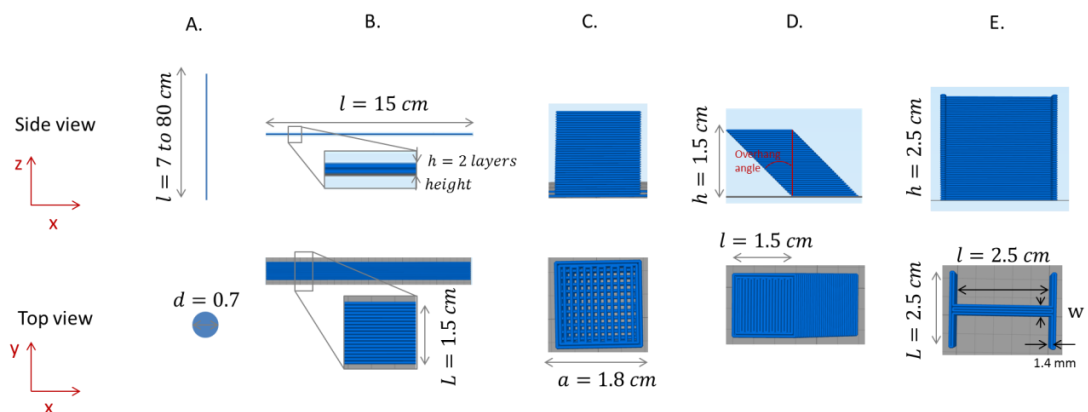


Figure 2-10. Side and top view of 3D model sliced with their printing parameters – (A) Single filament with various lengths, (B) rectangular 2D form, (C) cube, (D) parallelepiped with overhang angles to respect to the vertical plane and (E) H beam.

- Cubes (Figure 2-10.C): two cubes of different sizes were printed: 9 and 15 mm of sides. The printing settings between these cubes were different.
 - (i) Cube 1: the cube of 15 mm side was printed to evaluate the influence of few main printing settings (i.e. the layer height (0.35, 0.45 and 0.55 mm), the extrusion multiplier (1.0 C and 1.2 C where C is the calibration factor) and the infilled percentage (35 and 100% of the infill area)) on the qualitative accuracy of the printed parts. The sharing printing parameters were: a track width of 0.71 mm, 2 perimeter shells, 2 bottom and top layers, a rectilinear infill pattern rotated at 90° every layer and a printing speed of 15 mm.s⁻¹. The main printing settings are detailed in Table 2-5. The build time varied from 6 to 16 min with the different printing settings tested.
 - (ii) Cube 2: the cube of 9 mm side was printed to quantify the structural properties (shape and mass) during drying. The printing settings were: a track width of 0.71 mm, a layer height of 0.45 mm, 2 perimeter shells, a 50% and rectilinear infill pattern rotated at 90° every layer, an outline overlap of 60% of the track width of one outline perimeter shell, a printing speed of 10 mm.s⁻¹ and an extrusion multiplier of 2.35, equal to the calibration factor. It gives a solid volume of 592 mm³. The main printing settings are presented in Table 2-5. The build time was about 3 min. The two perimeter shells and an infill percentage of 50% of the infill area or below are typical settings for 3D printing as in general, only the apparent external shape of the printed part is important.
- Parallelepiped with a 30 and 45° overhang angles to the vertical plane (Figure 2-10.D): like the rectangular 2D part and the cube of 15 mm side, these parts were printed to evaluate the influence of few main printing settings (i.e. the layer height (0.35, 0.45 and 0.55 mm) and the extrusion multiplier (1.0 C and 1.2 C where C is the calibration factor)) on the qualitative accuracy of the printed parts. The sharing printing parameters were: a track width of 0.71 mm, 2 perimeter shells, 2 bottom and top layers with an infill percentage of 35% of the infill area and a printing speed of 15 mm.s⁻¹. The main printing settings are detailed in Table 2-5. The build time varied from 6 to 10 min.
- H beam (Figure 2-10.E): it was composed of a square wall of $hxL = 2.5 \times 2.5$ cm² with 3 different thicknesses, w to evaluate the ethanol diffusion time in the part: (i) 1.42 mm which is equivalent to the width of two printed filaments side by side, (ii) 2.84 mm which is equivalent to four printed filaments side by side and, (iii) 5.68 mm which is equivalent to two times the width of two printed filaments side by side separated by a 50% infilled part and

two perpendicular rectangular walls to the square wall in z direction. This part was printed to evaluate the influence of the duration of the ethanol bath in the ethanol drying process on the qualitative accuracy of the printed parts after drying. The main printing settings are detailed in Table 2-5. The build time was about 12, 17 and 25 min for the 3 models.

3 D model name	Rectangular 2D form	Cube 1	Cube 2	Parallelepiped overhang angle	H beam
Nozzle diameter [mm]	0.71	0.71	0.71	0.71	0.71
Track width [mm]	0.71-0.65	0.71	0.71	0.71	0.71
Layer height [mm]	0.35-0.45-0.55	0.34-0.45-0.55	0.45	0.35-0.45-0.55	0.45
Printing speed [mm.s ⁻¹]	15	15	10	15	10
Extrusion multiplier	1.0 C-1.2 C	1.0 C-1.2 C	C	1.0 C-1.2 C	C
Infill [%]	100	35-100	50	35	50
Perimeter shell	0	2	2	2	2

Table 2-5. The Main 3D printing settings of the tested printed parts where *C* is the calibration factor.

- 4.0 cm high monofilament rectangular cuboid with a 4.00 cm² square cross-section (Figure 2-11.A). It was printed to evaluate the main printing settings on the vertical stacking performance. The printing parameters are identical to those of the parallelepiped and detailed in Table 2-6.
- 1.5 cm long bridge with a 1 cm high pillar and rectangular cross-section of 0.5 × 1.0 cm² (Figure 2-11.B). It was printed to evaluate the main printing settings on the bridging performance. The printing parameters are identical to those of the parallelepiped and detailed in Table 2-6.

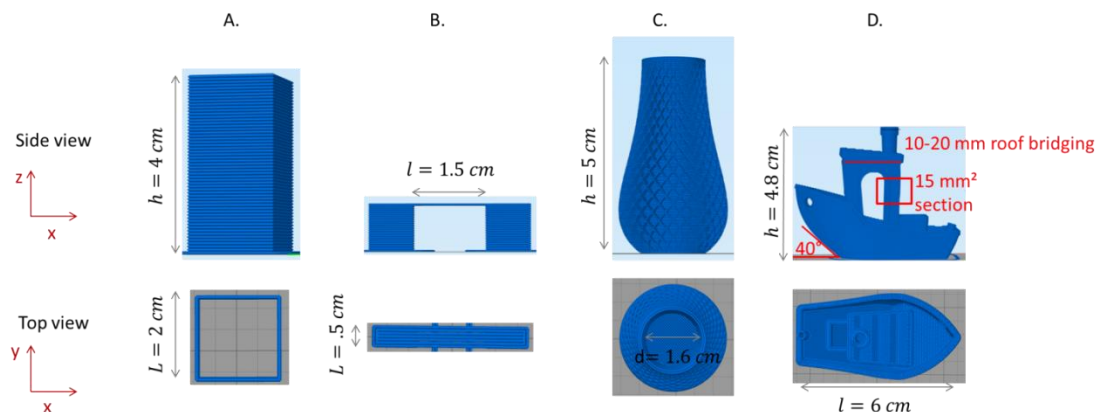


Figure 2-11. Side and top view of 3D model sliced with their printing parameters – (A) 4 cm high monofilament rectangular cuboid, (B) 1.5 cm long bridge, (C) 5 cm high double spiral vase and (D) 3DBenchy.

- 5.0 cm high double spiral vase with an opening diameter of 1.6 cm (Figure 2-11.C). It was printed to evaluate the height compensation multiplication on the dimension accuracy of the dried part. The main printing parameters are detailed in Table 2-6.
- 3DBenchy model composed of complex 3D printing shapes, including a 40° overhang angle to respect to the horizontal plane, 1.0–2.0 cm long bridge, and 1 cm high narrow pillars with a 0.15 cm² cross-section (Figure 3-11.D). The main printing parameters are detailed in Table 2-6.

3 D model name	4 cm high cuboid	1.5 cm long bridge	Double spiral vase	3DBenchy
Nozzle diameter [mm]	0.71	0.71	0.51	0.51
Track width [mm]	0.71	0.71	0.51	0.51
Layer height [mm]	0.35-0.45-0.55	0.34-0.45-0.55	0.30	0.30
Printing speed [mm.s ⁻¹]	15	15	15	20
Extrusion multiplier	1.0 C-1.2 C	1.0 C-1.2 C	C	C
Infill [%]	0	100	0	50
Perimeter shell	1	2	2	2

Table 2-6. The main 3D printing settings of the tested printed parts where *C* is the calibration factor.

2.3.5 Drying processes

2.3.5.1 General drying processes

Once printed, the samples were dried at 30±3% or 50±2% of Relative Humidity (RH) at a temperature of 22°C using two different methods:

- the first one, called “air drying” consisted in simply letting the sample dry in a conditioned room
- the second one, called “ethanol drying” consisted in plunging the printed part in an ethanol bath (95% and purchased from Révol) followed by air drying as in the first method.

The cube of 9 mm side, the filament and the double spiral vase were immersed in an ethanol bath for 15 min, 30 min and 120 min, respectively. For the ethanol drying condition, samples were immersed in an ethanol bath less than 30 s after their manufacturing unless a fresh measurement had to be performed such as a weight measurement or laboratory X-ray micro-tomography as described in the following section.

2.3.5.2 Optimization of the ethanol drying

The optimization of the ethanol drying was based on the:

- Ethanol concentration: distilled water was added to the as received ethanol at 95% with the following weight proportions: [water/ethanol at 95%], 50/50, 30/70, 20/80, 10/90 and 0/100 which is considered as the reference to evaluate the influence of the ethanol bath concentration on the parts dried with the ethanol drying process.
- Duration of ethanol bath: different durations of ethanol bath at 95% (10, 20, 30, 120 and 1440 min) were evaluated to characterized the influence of the ethanol bath duration on the parts dried with the ethanol drying process.

2.3.6 Dimension measurements

After drying, the dimensions of the printed filaments and 3D parts were measured.

2.3.6.1 Dimension measurements of dried filaments

To measure the filament diameters, three images per filament were taken with a binocular magnifier at $\times 100$ (ZEISS SteREO Discovery V20 with an AxioCam ICc 5) with a pixel size of $0.54 \mu\text{m}$, two centimeters apart all along the filament length. The diameter analysis was performed after binarization of the 8 bit grey scale pictures (Figure 2-12.A) with a lower and upper thresholds, manually chosen (Figure 2-12.B-D). The binarized pictures (Figure 2-12.C) were analyzed using the imageJ “Analyze stripes v2.4.5.b” plugin (Copyright 2013 Justin R. Bickford) to measure the distance between the edges of the filament, which was considered to be the filament diameter. The final diameter is the mean value between the diameters obtained with the upper and lower thresholds.

The filament length was measured with a graduated ruler ($\pm 0.05 \text{ cm}$).

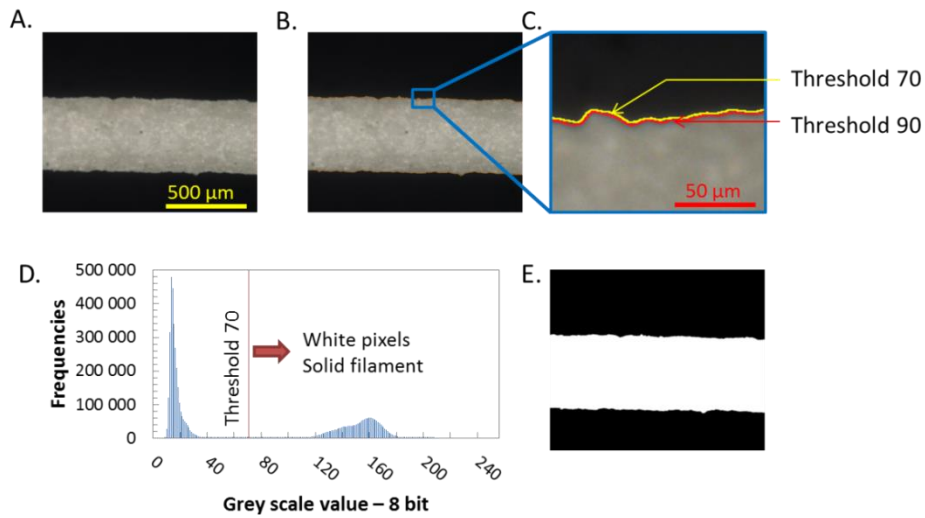


Figure 2-12. Automatic procedure for diameter measurement: (A) 8 bit grey scale image, (B) Selection of the upper and lower thresholds on the grey scale image zoom in (C), (D) Histogram of the 8 bit grey scale image and (E) the obtained binarized image.

2.3.6.2 Dimension measurement of dried printed parts

The height of the monofilament cuboid was measured with a digital caliper (± 0.01 mm) at the four edges of the cuboid and at the four central points between two consecutive edges to obtain the mean value and the standard deviation. Likewise, the height, h , and the thickness, w , of the H beam were measured at three different locations to obtain a mean value. The height and outlet diameter of the dried double spiral vase were measured with the same digital caliper.

2.3.7 Weight measurements

Parts or pieces of paste were weighed with a precision scale to have access to the following properties:

- Density measurement: after the filaments were dried and their dimensions were measured, three filaments were stored for 48 h in a conditioned room at 23 °C and 50% RH, after which they were weighed to within ± 0.0001 g.
- Initial dry content of the paste (ISO 638:2008): 2 g sample of fresh paste was weighed and then placed in an oven at 105°C during 48h for removing all the water content of the sample followed by a weight measurement. The dry content of the paste was calculated as the ratio between these two weights.

2.4 Characterization

2.4.1 Rheology of paste

To characterize the rheology of the cellulosic pastes in the “fresh” state, *i.e.*, at the nozzle exit, lubricated squeeze flow tests were performed using a universal tension-compression testing machine equipped with a 2 kN load cell (Instron 5944). These tests are well-suited to study the rheology of highly viscous pastes reinforced with fibers of finite lengths. Indeed, characterizing the rheology of such (fiber-reinforced) pastes using standard shear or high pressure capillarity rheometers may be difficult due to (i) the size of fibers (Chalencon et al. 2010; Laurent Org  as et al. 2008) and (ii) their marked shear thinning, which often causes to undesirable wall slippage and shear banding (Martoia et al. 2015; L. Org  as et al. 2003).

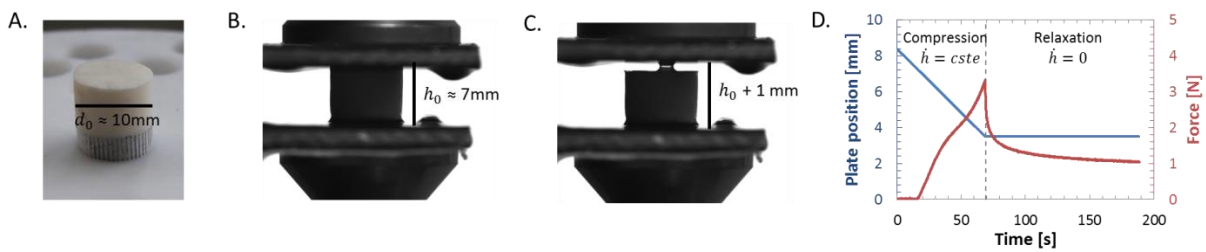


Figure 2-13. Lubricated squeeze flow testing – (A) Cylindrical sample preparation by casting, (B) Contact of the two compression plates with the sample for initial height, h_0 , measurement, (C) Sample positioning before compression started and (D) Plot of the measured data: plate position and force as a function of time.

We prepared cylindrical samples from the pastes with initial heights $h_0 = 7$ mm and diameters $d_0 = 10$ mm (Figure 2-13.A and B). The diameter d_0 was measured by image analysis with the same method as described in this chapter (2.3.6.1 p.84). Each sample was placed between two parallel compression plates that were lubricated with thin layers of a mixture of silicon oil and grease to ensure a homogeneous compression flow of the sample. The test started with a distance of $h_0 + 1$ mm between the two compression plates (Figure 2-13.C). The samples were monitored with a video camera. The recorded videos showed that samples flowed at nearly constant volume (less than 2% of volume variation of the cylinder at the end of the tests). Using the compression force F measurements and the actual sample height, h , we plotted the evolution of the compression Cauchy stress, $|\sigma| = \frac{4|F|h}{\pi h_0 d_0^2}$, as a function of time t and as a function of the compression Hencky strain, $|\varepsilon| = \left| \ln\left(\frac{h}{h_0}\right) \right|$. As illustrated in Figure 2-13.D, the tests were first carried out at constant compression velocity \dot{h} and with initial compression strain rates $|\dot{\varepsilon}_0|$ ranging from 0.01 to 1 s^{-1} , up to a compression strain $|\varepsilon| = 0.8$. Subsequently, the compression ended and the stress relaxation was

recorded for 2 mins, *i.e.*, up to steady-state regimes with approximately constant stresses. Three samples were used for each testing condition, and the error bars given in the strain stress curves (Figure 3-6) correspond to the min and max values recorded during these tests.

2.4.2 Deformation after drying

The deformation was calculated as the absolute value of the engineering strain $|e| = \left| \frac{X_{dried}}{X_{fresh}} - 1 \right|$, where X_{dried} corresponds to the measurements obtained using the methods described in this chapter (section 2.3.6 p.84) and X_{fresh} corresponds to (i) the dimensions of the 3D model given in section 2.3.4 p.79 or (ii) the nozzle diameter for radial strain of the filament, as no apparent swelling was observed.

The longitudinal and radial strains of the filament were calculated on three or five samples. The strain of the 4 cm high monofilament cuboid was calculated on two air-dried samples. The strain of the vase was calculated on a single sample.

2.4.3 SEM observation

To characterize the microstructures of the extruded filaments, two types of samples were recorded: (i) dried filaments with cross-sections cut using a razor blade perpendicular to its length and (ii) air-dried filaments after the tensile tests. Samples cut with the razor blade were metalized with a thin layer of gold and palladium (around 1 nm) and the tensile tested sample was metalized with carbon. Then, SEM images of the surface and cross-section of the filament were recorded on a FEI Quanta 200.

2.4.4 Mechanical testing: tensile test

2.4.4.1 Sample preparation

Tensile tests were performed on three different types of samples:

- Dried filaments composed of a fibrous cellulose paste formulation produced as described previously in this chapter (section 2.3.4 p.79). They were extruded through different nozzle sizes and inner geometry at a linear output flow rate of 5, 15 and 30 mm.s⁻¹ and with different drying process: air and ethanol drying processes.
- Filaments after water immersion during 30 min composed of fibrous cellulose paste formulations with the addition of Kymene, a wet strength agent. These formulations are summed up previously in this chapter (section 2.2.2 p.75). They were produced as the dried filaments. However, before their immersion in water, these filaments were air-dried at 50%RH and 23°C, then cured at 110°C during 1h and stored during 1 month at

23°C and 50%RH to ensure a complete curing of the Kymene agent (E. J. Siqueira 2012). It should be noticed that the wet filament diameter was not measured. The Cauchy stress was calculated with the dried diameter of the filament.

- Dried casting films of CMC. CMC solutions were casted at 5 wt.% for an even distribution of the solution in plastic Petri dishes or in aluminum mold. The two batches of casting films had a thickness about 0.2 mm (0.22 and 0.16 mm) measured with micrometer (Adamel Lhomargy MI20). The tensile specimens were cut with paper cutter to obtain a width of 1.5 cm. The gage lengths (L_0) of these samples were 5 cm and 10 cm respectively.

2.4.4.2 Tensile test

To characterize the mechanical properties of the paste after drying in dried and wet conditions and of the CMC, we performed tensile tests partially based on ISO 1924-3:2005. We used samples described above (section 2.4.4.1), the gage of whom was $L_0 = 5$ or 10 cm and a universal tensile testing machine (Instron 5965 equipped with a 5 kN load cell) in a conditioned room (23 °C, 50% RH) (Figure 2-14.A and B). The initial diameters of the dried filament were measured by an image analysis (section 2.3.6 p.84) and the thickness of the CMC films with a micrometer (Adamel Lhomargy MI20). Using the tensile force measurements F , the actual sample length L (Figure 2-14.C) and the section area of the tested sample S , we plotted the evolution of the tensile Cauchy stress, $\sigma = \frac{F}{S}$, as a function of the engineering strain, approximation of the Hencky strain for small deformation, $\frac{L-L_0}{L_0}$ (Figure 2-14.D), as previously discussed in this chapter (section 2.4.1 p.86). The tests were carried out at a constant stretch velocity of $1\%L_0 \cdot \text{min}^{-1}$ (equivalent to $10 \text{ mm} \cdot \text{min}^{-1}$ for a gage length of 10 cm) until sample breakage. From these strain stress curves, the Young's modulus, the strain at break and the tensile strength can be extracted. The Young's Modulus was calculated as the slope of the linear fit of the strain stress curves (Figure 2-14.D). Five samples were measured for each batch of samples.

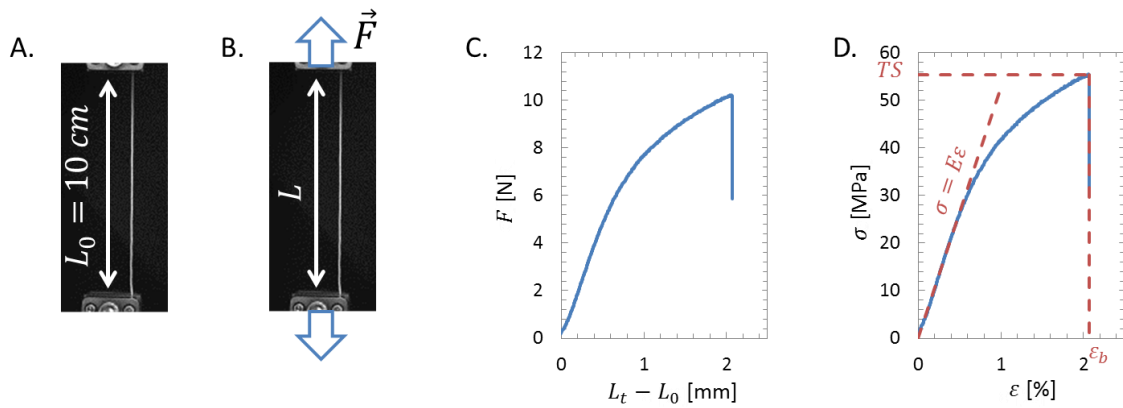


Figure 2-14. Tensile test – (A) Filament positioning with the 10 cm gage length before (B) the beginning of the tensile test. (C) The plotted curve with the record data: force and displacement of the clamp and (D) the strain-stress curve with the Young's Modulus, E , the tensile strength, TS , and the strain at break, ϵ_b , represented.

2.4.5 Conductivity

To characterize the conductivity of CMC and graphite blend, the electrical resistance of dried extruded filament stored at 50%RH was measured using an ohmmeter (HP 34401A multimeter). Current clamps were carefully used to measure the electrical resistance between the two ends of the 5 to 10 cm long filament without breaking it. The conductivity, was calculated as $\frac{L}{RS}$ with L , the length between the two clamps, R , the electrical resistance and S the cross section area of the filament calculated from the measured diameter (section 2.3.6.1 p.84).

2.4.6 Temporal characterization of the drying

2.4.6.1 Weight measurement

Figure 2-15.A shows the Mettler Toledo MS204 scale with a 0.0001 g precision that was used to record the temporal evolution of the weight of the analyzed sample during its drying on a glass slide for the cube or suspended between the two edges of a beaker for the filament (Figure 2-15.B). The weight measurement was recorded every 5 s until a steady state was reached. To decrease the weight measurement noise, the temporal measurement, w_t , was averaged using the mean of the recorded weight over 1 min as illustrated in Figure 2-15.C. The equilibrium weight, w_e , was measured after more than two hours of weight stabilization. The dry weight, w_d , was measured after placing the sample during 48 h in an oven at $105 \pm 5^\circ\text{C}$. The Moisture Content at time t (MC_t) was defined by the ratio between the water content and the dry content of the sample ($MC_t = \frac{w_t - w_d}{w_d}$) and the Relative Moisture content (RM) which is defined by $\frac{MC_t}{MC_0}$ with MC_0 , the initial moisture content of the paste. Both magnitudes can be obtained from the measurements described in the paragraph. MC_0

was measured on three samples of about 2 g of paste. The drying rate, R was defined as $R = \frac{w_d dMC_t}{A_t dt}$ with A_t , the exposed surface area for drying at time t , and discretized as $R = \frac{w_d MC_{t+1} - MC_t}{A_t \Delta t}$ with the time step, $\Delta t = 1$ min. For each type of samples and drying conditions, the measurements were carried out for 3 samples.

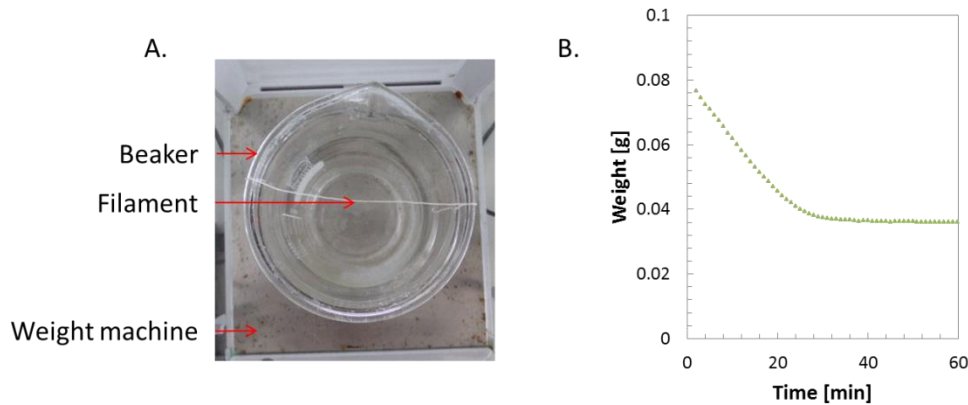


Figure 2-15. Monitoring of the temporal weight evolution – (A) Top view of the weight machine during filament drying and (B) the plotted recorded weight data as a function of time.

2.4.6.2 Dimension measurement of the filaments during drying

The filament is characterized by its diameter, d and its length, l . The temporal evolution of these two dimensions, d_t and l_t was followed by pictures analysis with automatic developed procedures to quantify them.

- Diameter: the filament was placed on a sample holder (Figure 2-16.A) with a portative USB camera (Dino-Lite Premier) on the top (Figure 2-16.B) or the filament was placed on the top of the portative USB camera (Figure 2-16.C and D). Pictures were taken with the camera every 30 s during 1 h at a pixel size of $0.73 \mu\text{m}$. As the USB microscope did not allow an automatic focus, some edges of the filament on the picture over time became less focused as shown by images presented in Figure 2-17. The diameter analysis was performed as previously described in this chapter (2.3.6.1 p.84). For a diameter that measured about $450 \mu\text{m}$ after drying, its mean deviation between the two manually selected thresholds was around $10 \mu\text{m}$ but can reach $20 \mu\text{m}$. As in the case of the weight measurements, the diameter measure d was average over 1 min.

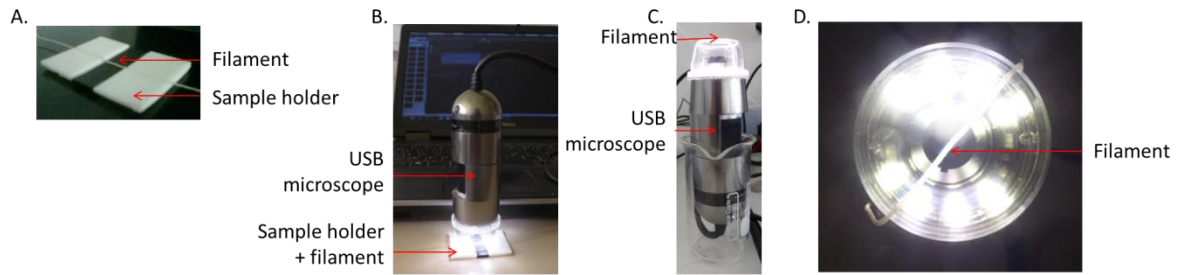


Figure 2-16. Optical set up to monitor the temporal evolution of the filament – (A) Sample holder (B) Positioning of the camera on the top of the filament and (C) side and (D) top view of the positioning of the filament on the top of the camera during images acquisitions.

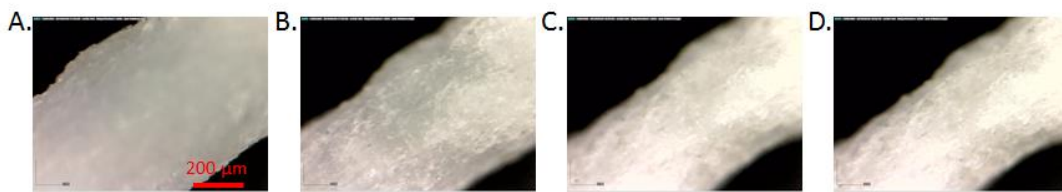


Figure 2-17. Temporal evolution of the filament images focus with (A) the first snapped image, (B), (C) and (D), snapped images after 20, 40 and 60 min, respectively.

- **Length:** the evolution of the length of the filament suspended in the air was imaged with a JAI camera at a pixel size of $41 \mu\text{m}$ every minute with a field of view of $100 \times 84 \text{ mm}^2$ (Figure 2-18.A). The recorded images were binarized using a threshold. The skeleton of the filament was obtained using the plugin Skeltonize from ImageJ developed by (T. Y. Zhang et Suenn 1984). Based on a thinning approach, the skeleton corresponded to the median line of the filament. The length of this median line was obtained by taking into account about 20% of its coordinates, equally spaced to avoid an overestimation of the length due to discretisation effects (Laurencin et al. 2016).

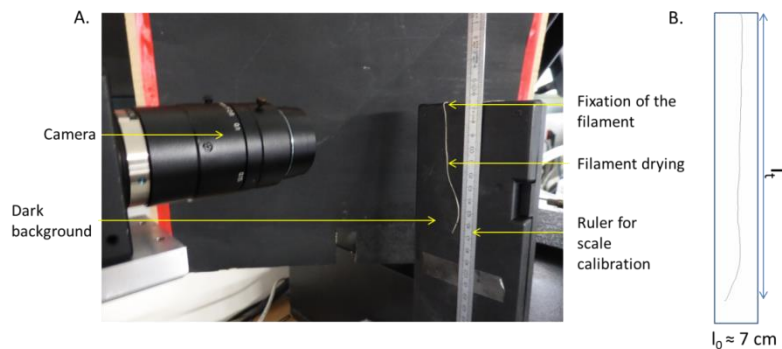


Figure 2-18. Length measurement – (A) Test implementation and (B) skeleton of the binarized image.

The temporal evolution of both the diameter and the length of the filament were evaluated on 3 different samples.

2.4.6.3 Dimension of the cube during drying

To follow both inner and outer modifications of the cube during drying, laboratory X-ray micro-tomography was performed using a RX solutions apparatus (Annecy, France). This technique gives access to the 3D inner structure of the sample in a non-invasive and non-destructive ways: the sample placed on a rotation stage was irradiated by a polychromatic beam source (100 kV, 300 μ A), the transmitted beam was recorded using a flat panel (binning 4, reducing the pixels on the detector to 480x384 from original pixels 1920x1536) for 720 different angular positions leading to a 36 s scan. This test was performed one time with air drying and ethanol drying conditions at 30%RH and 23°C. The recorded radiographs were used to reconstruct the 3D structure with a filterbackprojection algorithm. We obtained a stack of slices along X, Y or Z directions corresponding to the edges of the cube. A 3D scan was recorded every 4 minutes during 8h00, leading to the acquisition of 120 scans with a voxel size of $28^3 \mu\text{m}^3$. Extra scans, before ethanol bath or after 24h of drying were recorded.

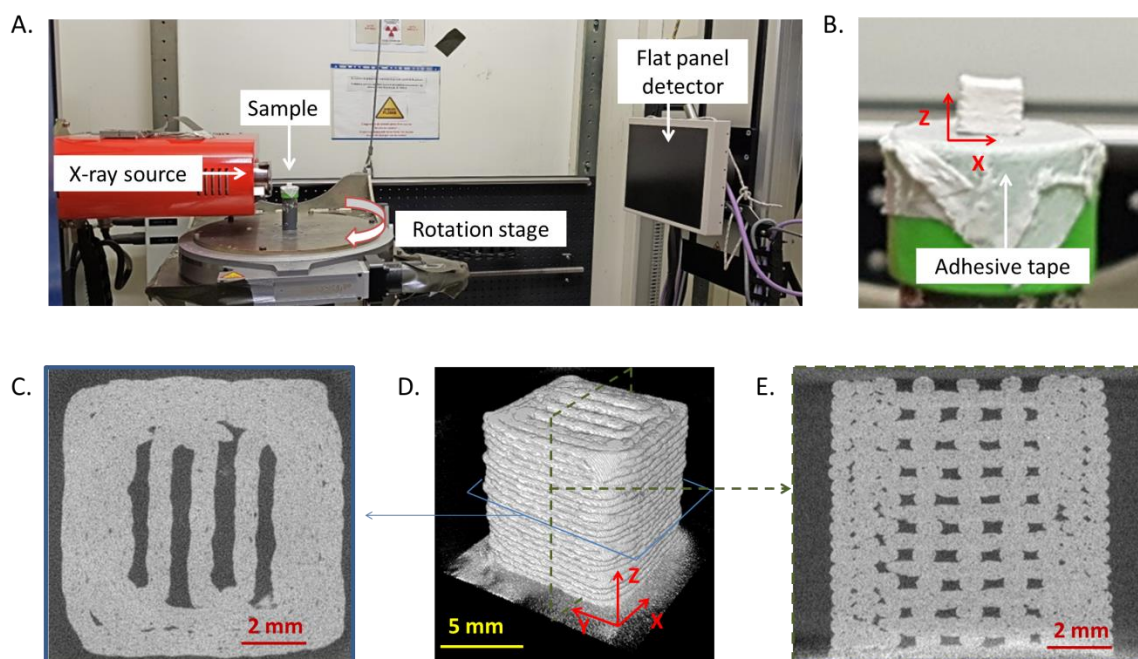


Figure 2-19. (A) Experimental set up with a laboratory X-ray micro-tomography to monitor the inner and outer modifications of the cube during drying. (B) Zoom in of the cube fixed on the platform. (D) Stack of slices composed of whether Z slices (C) or Y slices (E).

The obtained scans were analyzed with Fiji. A manually chosen threshold was applied to the stack of the 16 bit slices that composed the scan as shown on Figure 2-20 and resulted in a binarized stack

with the white voxels that represent the solid volume and the black voxels that represent the outer and pores volume.

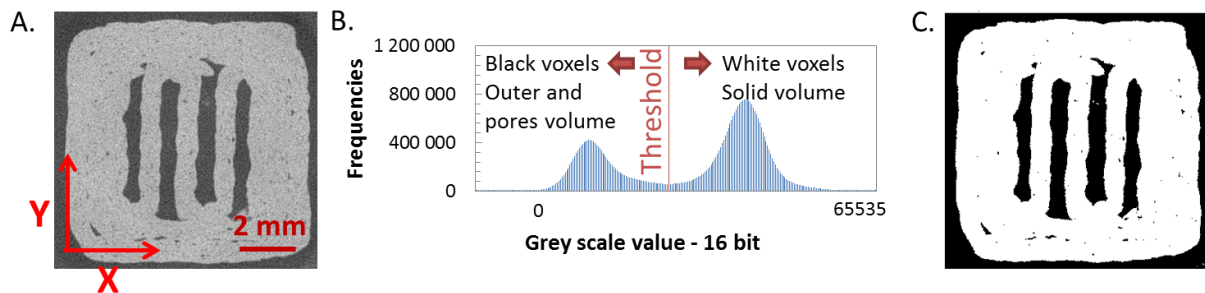


Figure 2-20. Threshold determination of the scans of the cube – (A) 16 bits slice, (B) histogram of the 16 bits stack and (C) binarized slice.

Figure 2-21.A shows that the lower part of the scans was noisy due to the support on which the cube was printed on. From the binarized stack of slices, the temporal evolution of several data can be extracted as presented in Figure 2-21:

- Solid volume, V : it corresponds to the volume generated by the printing settings of the CAD model. It was calculated as the number of white voxels multiplied by the voxel size (Figure 2-21.A).
- Apparent volume, V_a : it corresponds to the volume of the CAD model. It was calculated as the number of white voxels obtained after filling the holes of parallel slices to the (x,y) plane with white voxels multiplied by the voxel size (Figure 2-21.E).
- Height, h_z : it corresponds to the length in z direction of the 3D model. It was calculated as the number of slices between the lower and the upper part of the cube converted in length with the pixel size (Figure 2-21.H).
- Apparent section area, S_a : it corresponds to the area of the cross section of the 3D model in (x,y) plane (Figure 2-21.F). It was calculated from above calculated values as followed: $\frac{V_a}{h_z}$
- Filament section area, S_f : it corresponds to the cross-section area of unsupported filaments. It was calculated as the mean surface area of the cross section of the central filament of each layer in pixels multiplied by the pixel size (Figure 2-21.C).
- Volume of macro pore, V_{mp} : it corresponds to the volume of pore generated by the 3D printing settings such as the interior fill percentage. The addition of the volume of macro porosity and the solid volume of the 3D model gave the apparent volume of the cube. It was calculated thanks to the 'analysis 3D' plugin developed by (Boulos et al. 2012) which identified each closed pores in a 3D volume. The macro porosity was labelled and the

number of voxels was measured by the plugin and then multiplied by the voxel size (i.e. $28^3 \mu\text{m}^3$). In some cases, the macro porosity was connected to the outer volume of the cube, V_o (Figure 2-21.H). The volume of the macro porosity was obtained by removing the outer volume of the cube, which was calculated from the number of black voxels multiplied by the voxel size obtained when the apparent volume was calculated.

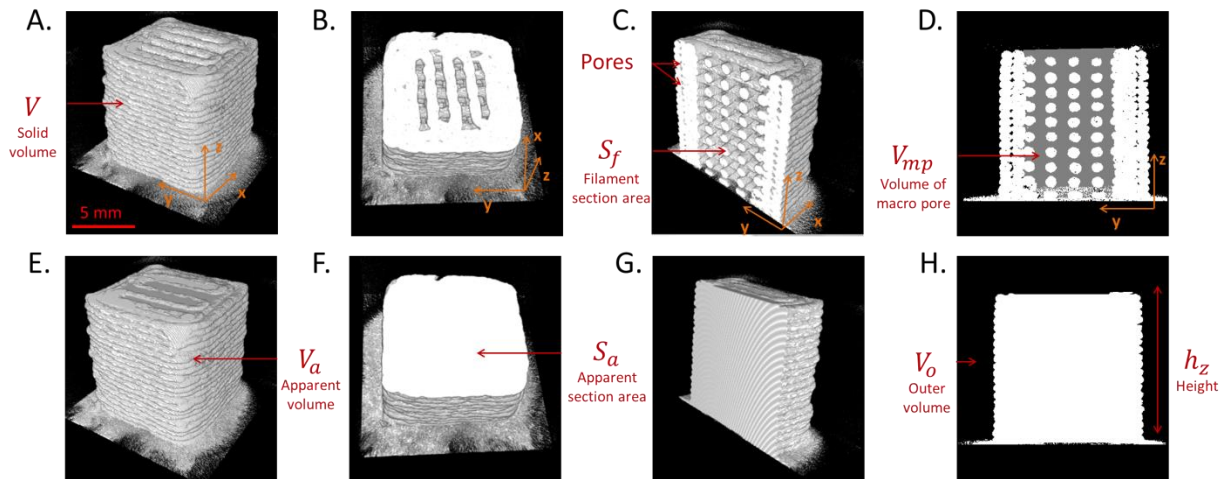


Figure 2-21. 2D and 3D views of a X-ray Computed Tomography (XCT) scan of the 3D printed cube (upper row) and the same XCT scan filled by image processing to extract apparent data (lower row). (A and E) 3D view of the whole scan, (B and F) 3D view of the scan cropped horizontally in (xy) plane, (C and G) 3D view of the scan cropped vertically in (yz) plane and, (D and H) 2D view of a cross section in (yz) plane.

2.4.6.4 Mechanical characterization of the paste during drying

Tensile test : to characterize the mechanical properties of the paste during drying, we performed tensile tests on single filaments, the gage of whom was $L_0 = 10$ cm, using a universal tensile testing machine (Instron 5944 and 3365 equipped with a 10 N or 10kN load cell) at $10 \text{ mm} \cdot \text{min}^{-1}$ in a conditioned room (23°C , 30%HR). Tensile tests were performed 2, 10, 15, 20, 30, 40, 50, 60 min after the beginning of the sample extrusion that lasted 30 s. The filament immersion in the ethanol bath was considered as a one-off action without duration. As described in section 2.4.4 p.87, we plotted the evolution of the tensile Cauchy stress as a function of the engineering strain. Only the Young's Modulus, E_t , and the yield stress, σ_{yt} were extracted from the obtained data due to a large amount of filament breakage near the clamps for samples air-dried less than 20 min. Indeed, the manual clamping was a key parameter: a too tight clamping result in a weak area leading to filament breakage close to the clamp and a too loose clamping result in slipping between the clamps. The yield stress is equated to the proportionality limit of the strain stress curves, calculated as a deviation of 10% between the linear fit and the stress-strain curve. 5 samples were tested for each drying time.

Drying strength: this test consisted in recording the temporal evolution of the force F during the drying of a filament without any displacement of the clamp during 60 min. A preload of about 1/5 of the yield stress of the filament obtained in the previous section at 10 mm.s^{-1} was applied to stretch the fresh filament (2 min after the beginning of extrusion). However, as fresh samples without ethanol bath broke after 10 min in the clamps, tests were carried after 10 minutes of drying without constraints. Tests were conducted under controlled environmental conditions at 30%RH and 23°C. At least 3 samples per drying conditions were tested.

2.5 Conclusion

In this chapter, the components of the paste formulation were described, in particular the particle size of the fillers (cellulose powder and fiber and graphite powder) as well as the composition and preparation of the paste evaluated for Additive Manufacturing (AM) by extrusion. The setups of this AM by extrusion process were detailed by the description of the printer used, the calibration of the extrusion flow, the printing parameters applied on 3D models and the post processing of the printed part. Due to the characteristics of the pastes and of the 3D printed parts, standard measurements had to be adapted by the development of structural, rheological and mechanical characterizations. These developed methods were used:

- in chapter 3 to optimize and characterize the paste made of one type of fillers (cellulose fiber, cellulose powder or graphite powder), CMC and distilled water.
- in chapter 4 to optimize the AM process by extrusion (printer and process settings) to manufacture 3D part with the bio-based paste optimized in chapter 3.
- in chapter 5 to study the drying process in details (moisture content, dimensional strain, mechanical properties) on filaments and simple 3D parts and to suggest a dimensional compensation strategy.

Chapter 3. Development and characterization of cellulose based formulations with strong potential for AM by extrusion

3.1	Introduction.....	97
3.2	The carboxymethyl cellulose, a key component of formulation with strong potential for AM by extrusion.....	98
3.2.1	Characterization of carboxymethyl cellulose	98
3.2.2	Optimization of formulations by maximizing the solid content while remaining extrudable	101
3.3	Characterization of the selected formulations	107
3.3.1	Rheological behaviour of the fresh paste	107
3.3.2	Shrinkage during drying.....	109
3.3.3	Microstructure of the extruded filament.....	112
3.3.4	Tensile properties of dried filaments.....	113
3.4	Toward functionalization of formulation	114
3.4.1	Addition of a wet strength agent: a compromise between easy reuse and wet strength ..	114
3.4.2	Influence of CMC on graphite conductivity	116
3.5	Conclusion.....	118

3.1 Introduction

As describe in chapter 1 (section 1.2.2 p.46), it was only twenty years after the development of Additive Manufacturing (AM) by extrusion process (US5121329A, 1992), that cellulose was used for the first time as a bulk material to 3D print part by this process (based on our knowledge, Markstedt, Sundberg, & Gatenholm, 2014). It comes from the various challenges raised by the properties of cellulose and of this process (Chapter 1). Unlike thermoplastic materials, which are compatible with AM by melt extrusion, cellulose cannot be melted to be processed (extrusion and deposition steps) and so recover its stiffness when cool down, a solvent must be added.

Recently, several articles were published on formulations compatible with AM by extrusion composed of nanocellulose suspension or dissolved cellulose as the main building block as reported in chapter 1 (1.2.2.2 p.56). The main limitations were (i) succeeding in printing accurate fresh part, (ii) the expensive freeze-drying process to maintain accuracy of the dried part leading to part with low density and mechanical properties due to a solid content limitation of 20 wt.% and (iii) a slow AM process in order to allow the solvent evaporation during the printing process. However, no formulation with cellulose fiber with diameter in the μm range and resolution of 0.5 mm were reported while this form of cellulose seems to show the best properties for producing cheap, lightweight, robust, and recyclable 3D structures, within the spirit of 3D printed part with PLA. The average dimensions of a cellulose fiber used in the paper making industry in length, in diameter and in wall thickness are 1-5 mm, 10-50 μm and 1-5 μm respectively (Niskanen, 1998). The diameter of the cellulose fiber is compatible with a printing resolution of 0.5 mm: a 500 μm large nozzle diameter is more than 10 times the cellulose fiber diameter. However, the lengths of these cellulose fibers must be shortened to 0.5 mm to maintain the targeted resolution. Preliminary testing with formulations that comprise these cellulose fibers reduced in powder as fillers and enzymatic MFC in suspension as a rheological modifier presented phase separation that could lead to nozzle clogging in particular when the fillers content was increased for limiting shrinkage. Yet, a cellulose derivative, CMC, a well-known additive for its thickening and large water retention properties, its ability to keep particles in suspension and its binding properties must be added to limit phase separation.

This chapter proposes to study the development and characterization of cellulose based formulations with strong potential for AM by extrusion as well as the influence of additive to tailor the formulation properties.

As mentioned in chapter 2, the rheological behavior of CMC in water at concentration ranging from 5 to 25 wt.% and the mechanical properties of dried CMC films were evaluated to better understand the influence on this component in formulations composed of fillers (cellulose fiber,

cellulose powder or graphite powder), CMC and water. Nine formulations for each filler were assessed to identify an optimal formulation with strong potential for AM by extrusion: constant and homogeneous flow, a large viscosity for low strain rate characterized by a filament that does not flow under its own weight and a limited strain after drying. The influence of the fillers dimensions as well as its nature was evaluated and discussed.

The optimal formulations were characterized by their rheological behavior, their mechanical properties from extruded filament, their microstructure and their strain after drying to compare with other characterized formulations compatible with AM by extrusion found in the literature and with the PLA, one of the material references in AM by extrusion. To enhance and tailor the wet strength properties of the material, the influence of the addition of a wet strength agent on the dry and wet properties as well as the strain were evaluated. Likewise, to enhance and tailor the conductive properties of the paste, the influence of the CMC content ranging from 14 to 33 vol.% on graphite conductivity was evaluated.

3.2 The carboxymethyl cellulose, a key component of formulation with strong potential for AM by extrusion

3.2.1 Characterization of carboxymethyl cellulose

3.2.1.1 Rheological behaviour

The rheological behaviour of low viscosity of carboxymethyl cellulose (CMC) grade (50 to 200 mPa.s at 4 wt.% in water at 25°C (Sigma Aldrich specifications)) was qualitatively evaluated for concentrations ranging from 5 to 25 wt.% in distilled water. This grade was used in the paste formulations.

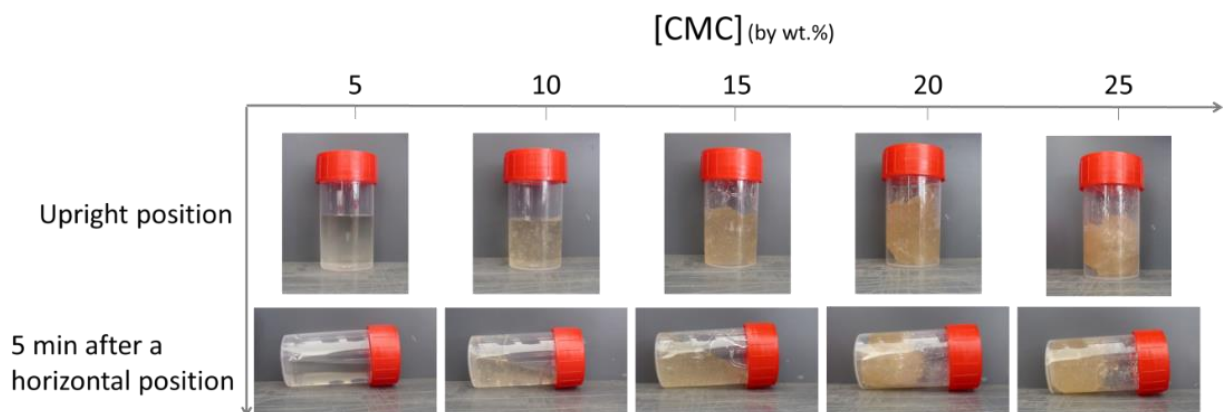


Figure 3-1. Images of CMC at different concentrations (5 to 25 wt.%) in water in an upright jar and in a laying jar after 5 min in that position

Figure 3-1 shows the obtained mixture of water and CMC at different concentrations in a small container in an upright position and after 5 min in a horizontal position. The change of position from upright to horizontal allows qualitatively evaluating the flowing ability of the material. We can observe that the dry and white CMC powder with the addition of water give a yellow mixture and all the CMC seems to have been hydrated. For CMC at a concentration from 5 to 15 wt.%, 5 minutes after the horizontal position, the material started to flow. However, the slope formed by the transition line between the CMC mixture and the air increased with the CMC concentration highlighting its thickening ability. From a concentration of 20 wt.%, we cannot observe any deformation of the material under its own weight. The rheological behaviour of CMC was not quantitatively evaluated with a cone plate rheometer as the highly viscous materials (> 15 wt.%) presents bubbles that could not be removed by degassing with vacuum or ultrasound equipment. We can find in the literature studies on the rheological behaviour of medium and high viscosity CMC grade at concentration ranging from 4 to 8 wt.% considered as high (Edali, Esmail, et Vatisas, 2001; Benchabane et Karim, 2008). The viscosity specifications of these two grades are ranging from 400 to 800 mPa.s at 2 wt.% and from 2500 to 6000 at 1 wt.% in water at 25°C, respectively. From these studies, no yield stress was measured, it shows a shear thinning behaviour and above a critical concentration the elastic behaviour predominates over the viscous behaviour. This critical concentration might be between 15 and 20 wt.% in our case of low viscosity CMC grade.

This broad range of viscosities obtained by tailoring the concentration of CMC in water can be beneficial to limit phase separation and allows the addition of fillers in the formulation.

3.2.1.2 Mechanical properties

The mechanical properties (Young's modulus, tensile strength and elongation at break) of dried CMC films (casting at initial concentration of 5 wt.%) were evaluated by tensile tests for two different dimensions of samples (chapter 2, section 2.4.4 p.87).

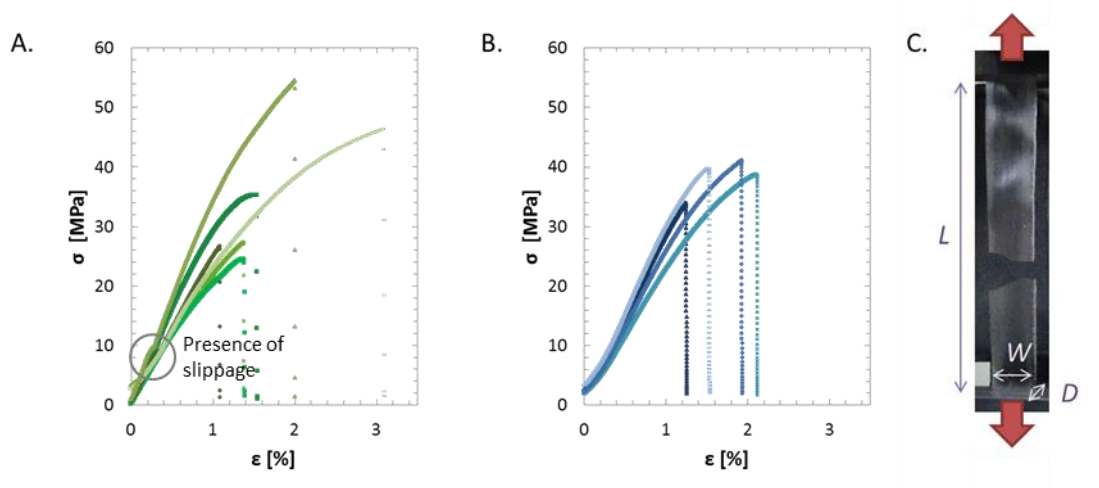


Figure 3-2. Mechanical properties of CMC films – Strain-stress curves of samples with dimensions ($L \times W \times D$) of (A) $50 \times 15 \times 0.22 \text{ mm}^3$ and (B) $100 \times 15 \times 0.16 \text{ mm}^3$ and (C) picture of a tensile specimen after fracture.

Figure 3-2. A and B show the obtained stress strain curves of CMC tensile specimens that break between the two clamps (Figure 3-2.C). We can observe a quite good reproducibility of the results. The dispersion might come from the sample preparation and also from the presence of a small slippage (0.1 mm) of the sample between the clamps as it can be observed in Figure 3-2.A for a stress around 10 MPa. However, all the CMC strain stress curves present a typical behavior of a brittle material confirmed by the sharp fracture of the sample. From these curves the Young's modulus, the tensile strength and the elongation at break were extracted as presented in Table 3-1.

Batch	Young's modulus [GPa]	Tensile strength [MPa]	Elongation at break [%]
$50 \times 15 \times 0.22 \text{ mm}^3$	2.9 ± 0.7	36 ± 12	1.7 ± 0.7
$100 \times 15 \times 0.16 \text{ mm}^3$	2.7 ± 0.3	38 ± 3	1.7 ± 0.4
Gao et al. 2018 $20 \times 2.5 \times 0.5 \text{ mm}$	2.03 ± 0.01	120 ± 10	17 ± 1
Suderman, Sarbon, et Mohamad Isa, 2016	-	10.0 ± 0.5	-

Table 3-1. Mechanical properties of two batches of CMC films and results from literatures.

The CMC used in our study presented a Young's modulus, tensile strength and elongation at break of $2.8 \pm 0.6 \text{ GPa}$, $37 \pm 9 \text{ MPa}$ and $1.7 \pm 0.6\%$, respectively. The Young's modulus and the tensile strength are in line and in between those found with CMC films with lower and larger molecular weight (Gao et al. 2018; Suderman, Sarbon, et Mohamad Isa, 2016), which validates our measurements.

3.2.2 Optimization of formulations by maximizing the solid content while remaining extrudable

3.2.2.1 Optimization of a fibrous cellulose paste

To identify an optimized fibrous cellulose-based paste formulation compatible with 3D printing by extrusion, several pastes with varying solid contents and proportions of compounds (chapter 2, section 2.2.1.2 p.71) were evaluated.

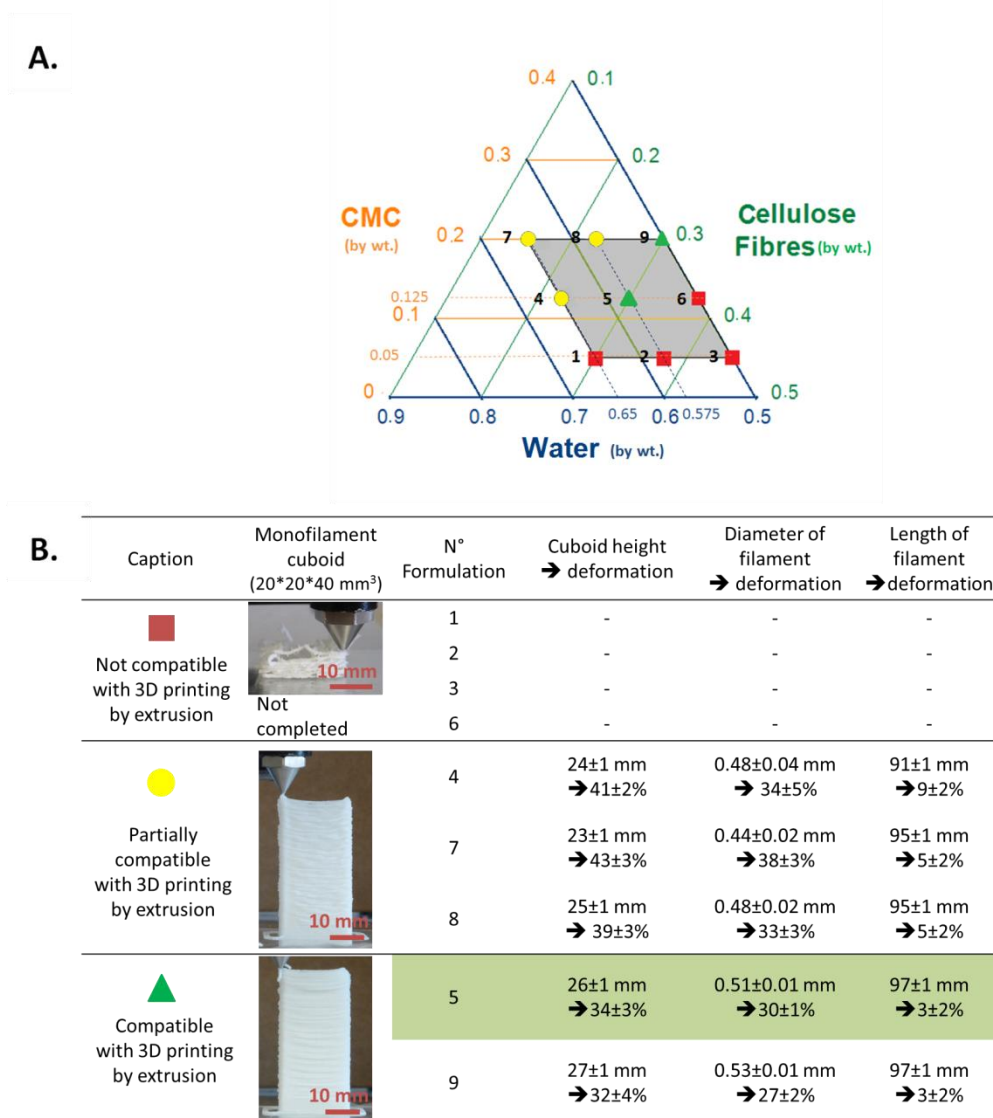


Figure 3-3. (A) Ternary diagram indicating the weight fractions of CMC, cellulose fibers, and water for the tested formulations. (B) Qualitative and quantitative characterization of the nine different tested formulations for compatibility with AM by extrusion.

Figure 3-3.A shows the compositions of the nine tested formulations with overall dry contents varying from 35 to 50 wt.%, cellulose fiber contents varying from 15 to 45 wt.%, and CMC contents varying from 5 to 20 wt.%. These formulations were assessed according three main criteria, which

ensured the accuracy of the printed part relative to the 3D model: (i) extrusion of an adequate filament, as defined in the section 3.1; (ii) production of undried and accurate 3D printing parts that do not collapse; and (iii) limiting and forecasting the deformation after drying. These criteria were applied to a 10 cm long filament and the monofilament cuboid part that was extruded, printed, and air-dried using the parameters specified in chapter 2 (2.3.4 p.79).

Figure 3-3.B shows the typical results obtained with the nine tested formulations, which were as follows:

- The tested formulations with cellulose fiber contents of 37.5 wt.% or with a CMC content at 5 wt.% did not allow the extrusion of smooth and regular filaments with a nozzle diameter of 0.7 mm, as the extruded filaments were friable and irregular, which led to filament breakage. Furthermore, these characteristics did not allow the complete printing of a regular monofilament wall cuboid, as can be seen in Figure 3-3.B. These formulations were found to be incompatible with 3D printing by extrusion, as they did not meet criteria (i) based on filament extrusion, and (ii) based on the accuracy of the undried 3D printed part.
- The five remaining tested formulations with cellulose fiber contents of 30 wt.% or less and a CMC content of 12.5 wt.% or more yielded smooth and regular filaments extruded through a 0.7 mm diameter nozzle, allowing the manufacture of a monofilament cuboid as high as 4 cm with a wall thickness of the size of the nozzle outlet, as no die swelling was observed. These parts did not collapse under their own weights, as can be seen in Figure 3-3.B. Indeed, the lower region of the 3D part did not widen. These five formulations were found to be compatible with 3D printing by extrusion to manufacture wet parts, as they met criteria (i) based on adequate filament extrusion, and (ii) based on the accuracy of the undried 3D printed part.

Figure 3-3.B also summarizes the strain of the extruded filament and the height of the cuboid after drying.

- For formulations with a cellulose fiber content lower than 30 wt.%, the strains of the filaments were larger than 30% and 5% for the diameters and lengths, respectively, and the height strain of the cuboid was larger than 35%. Therefore, these formulations with cellulose fiber contents lower than 30 wt.% were found to be partially compatible with 3D printing by extrusion because of the high strain observed after drying (criteria (iii)). By comparison, the formulations containing 30 wt.% of cellulose fibers and CMC contents of 12.5% or 20 wt.% exhibited better strain behaviors during the drying phase. These two

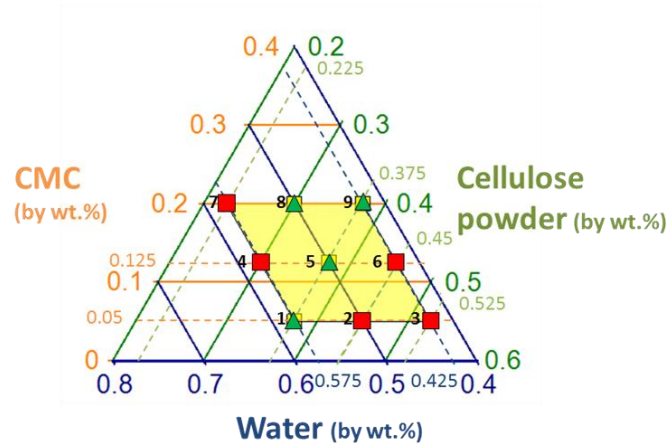
last formulations were found to be compatible with 3D printing by extrusion, as they fulfilled criteria (i) based on adequate filament extrusion, (ii) based on the accuracy of the undried 3D printed part and, and (iii) based on limitation of the deformation after drying.

To conclude, the formulation with a dry content of 42.5 wt.%, a cellulose fiber content of 30 wt.%, and a CMC content of 12.5 wt.% was selected as the optimized formulation, because its cost was lower than a similar formulation in which 7.5 wt.% of distilled water was replaced by CMC, and because the paste that was formed was easily processed (lower viscosity), facilitating simple filling of the syringe.

3.2.2.2 Optimization of formulation based on other fillers

The same assessments were performed to identify an optimized cellulose powder paste and graphite powder paste for AM by extrusion. The results are summed up in Figure 3-4 and Figure 3-5, respectively. Formulation were found not compatible with AM by extrusion for two main reasons: (i) a paste too dry that was friable and brittle in the screw or at the exit of the nozzle and (ii) a paste that flew too much after extrusion leading to large collapse of the monofilament cuboid or large deviation for diameter measurement and no measurement of the length of the filament as the filament broke on its own weight during drying.

A.



B.






Caption	N° formulation	Diameter of filament → deformation	Length of filament → deformation	Monofilament cuboid
 Not compatible with AM by extrusion	2	-	-	
	3	-	-	
	6	0.53±0.01 mm → 27±1%	-	
	4	0.46±0.02 mm → 36±2%	18.8±0.4 cm → 6±2%	
	7	0.46±0.01 mm → 36±2%	19±0.2 cm 5±1%	
	 Compatible with AM by extrusion	1	-	-
5		0.49±0.01 mm → 31±1%	18.5±0.1 cm → 8±1%	
8		0.50±0.01 mm → 30±1%	18.4±0.02 cm → 8±1%	
9		0.52±0.01 mm → 28±1%	18.7±0.1 cm → 7±1%	

Figure 3-4. (A) Ternary diagram indicating the weight fractions of CMC, cellulose powder, and water for the tested formulations. (B) Qualitative and quantitative characterization of the nine different tested formulations for compatibility with AM by extrusion.

For cellulose powder paste, the formulations that were not compatible with AM by extrusion were: (i) formulations with a cellulose powder content equal to or larger than 45 wt.% which were friable and (ii) formulations with a solid content of 37.5 wt.% and a cellulose powder content equal to or lower than 30 wt.% which present partial collapse of the monofilament cuboid.

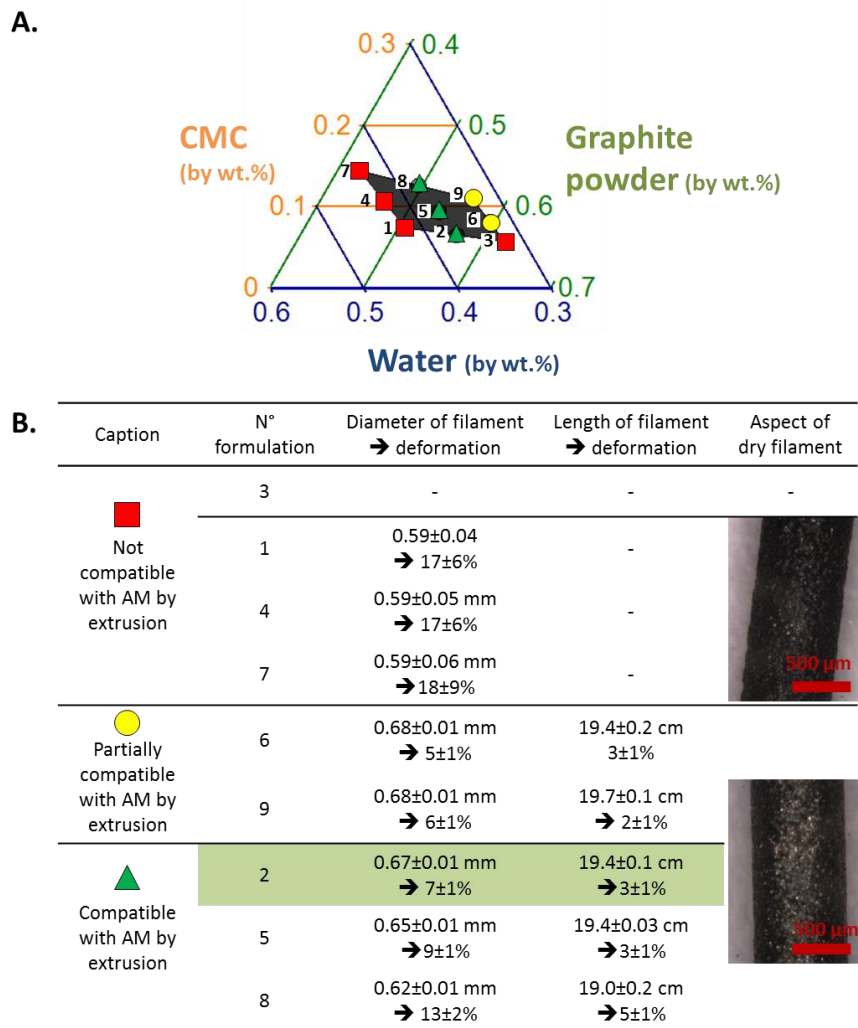


Figure 3-5. (A) Ternary diagram indicating the weight fractions of CMC, graphite powder, and water for the tested formulations. (B) Qualitative and quantitative characterization of the nine different tested formulations for compatibility with AM by extrusion.

For graphite powder paste, formulations not compatible with AM by extrusion were: (i) the formulation with a graphite powder content larger than 60 wt.% which was too friable and (ii) formulations with a solid content lower than 60 wt.% which flew under their own weight and present, as a consequence a large deformation of the filament diameter.

3.2.2.3 Comparison of the optimized pastes with the different fillers

The composition of the identified formulations of fiber and powder cellulose pastes and graphite paste in weight and in volume (based on cellulose and CMC density of $1.5 \text{ g}\cdot\text{cm}^{-3}$ and graphite density of $2.2 \text{ g}\cdot\text{cm}^{-3}$) were:

- 30 wt.% of cellulose fiber, 12.5 wt.% of CMC and 57.5 wt.% of water which is equivalent to 23.3 vol.% of cellulose fiber, 9.7 vol.% of CMC and 67.0 vol.% of water.

- 37.5 wt.% of cellulose powder, 12.5 wt.% of CMC and 50 wt.% of water which is equivalent to 30 vol.% of cellulose powder, 10.0 vol.% of CMC and 60.0 vol.% of water
- 56.7 wt.% of graphite powder, 6.5 wt.% of CMC and 36.8 wt.% of water which is equivalent to 38.5 vol.% of graphite powder, 6.5 vol.% of CMC and 55.0 vol.% of water.

We can notice that the composition of the optimized cellulose powder paste corresponds to a formulation not compatible with AM by extrusion when cellulose powder is replaced by cellulose fiber. The paste was too friable. The differences between these two cellulose particles were the cellulose source (wood or cotton) and the particle geometry (length). As mentioned in the chapter 1 (1.2.1.2 p.41), the water retention value of wood is larger than the one of cotton with 60 to 90% against 50%, respectively. It might influence the water availability in the paste which is used as a medium to tailor the rheology of the paste. Moreover, the friction between elongated particles is larger than the one between round particles, which affects the rheological behavior of the paste.

Likewise, the optimized cellulose powder paste corresponds in volume to a formulation not compatible with AM by extrusion when cellulose powder is replaced by graphite powder. The paste was too liquid and could not resist to its own weight. Indeed, although the size distribution of graphite and cellulose powder are similar (section 2.2.1 p.69), their water interactions (e.g. hydrogen bonding or hygroexpansion) are different and influence the rheological behavior of the paste.

These three optimized formulations had a solid particles content of 23.3 to 38.5 vol.% in a CMC gel at 0.17 to 0.25 g mL⁻¹. The particles solid content of the fibrous cellulose paste was up to two times lower than the solid content used in two other pastes successfully formulated for AM by extrusion at ambient temperature with a nozzle diameter smaller than 500 µm: (i) 45 vol.% of glass powder with up to 2 wt.% of CMC (Eqtesadi et al., 2013) and (ii) 47 vol.% of lead zirconate titanate and a cellulose concentration of 5 mg mL⁻¹ (Smay, Cesarano, & Lewis, 2002). As discussed, this difference in solid content might arise from the components used. The glass powder and lead zirconate titanate were different from cellulose fibers, as they had smaller dimensions (< 10 µm), round geometries, and low interactions with water (e.g. hydrogen bonding or hygroexpansion). The difference in solid content reduce with the cellulose and graphite powder paste as these particles present less difference in dimension, geometry and interaction with water for the graphite one than cellulose fiber. Using an elongated cellulose mat, V. C. F. Li et al., 2018 and Siqueira et al., 2017 also successfully formulated a paste at high solid content with 20 wt.% of freeze-dried cellulose nanocrystals (CNCs) as received or modified CNC in suspension. They limited their solid content to 20 wt.% owing to limitations of the devices used for mixing and/or printing, which did not allow proper homogenization of the paste or sufficient extrusion flow or alignment of the CNCs. These solid

contents were lower than the optimized formulations proposed herein. These differences were due to the use of a screw-driven device instead of a pneumatic device and the addition of CMC, which reduced the friction between particles due to its filmogenic property.

3.3 Characterization of the selected formulations

3.3.1 Rheological behaviour of the fresh paste

The rheological behaviour of fresh cellulose based pastes was evaluated by lubricated squeeze flow (chapter 2, section 2.4.1 p.86).

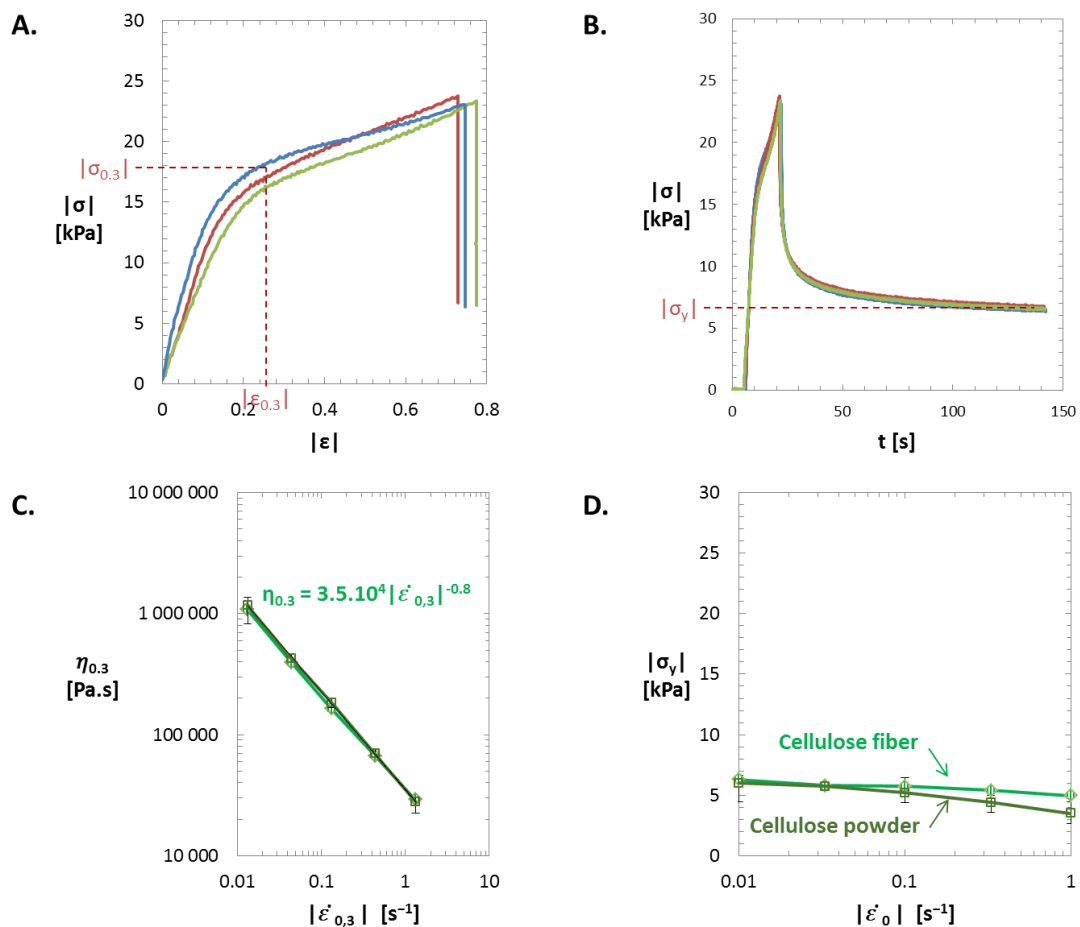


Figure 3-6. Rheological properties of the optimized cellulose based formulations (30 wt.% cellulose fiber, 12.5 wt.% carboxymethyl cellulose (CMC), 57.5 wt.% distilled water and 37 wt.% of cellulose powder, 12.5 wt.% CMC and 50 wt.% of distilled water). Three lubricated squeeze flow tests (compression at constant speed followed by 2 min of relaxation) were performed at an initial compression strain rate of 0.033 s^{-1} . (A) Stress-strain curves. (B) Stress during the lubricated squeeze flow test. During the relaxation time, the stress reached a plateau, which corresponds to the yield stress $|\sigma_y|$. (C) Viscosity curve fit with a power law, $\eta_{0.3} = k|\epsilon'_0|^{n-1}$. (D) Yield stress, $|\sigma_y|$ as a function of the initial strain rate.

Figure 3-6.A and B show typical stress-strain and stress-time curves recorded with the optimized fiber cellulose formulation during three compression tests, which were obtained at a first compression flow of $3.33 \cdot 10^{-2} \text{ s}^{-1}$. Similar curves were obtained for the optimized powder cellulose formulation. High reproducibility of the stresses was observed, with deviations of less than $\pm 10\%$. After a quasi-linear and sharp increase of the stresses, the samples flowed more easily, exhibiting stress hardening behaviors that are typical of fiber-reinforced paste materials (Chalencon et al., 2010; Orgéas et al., 2008).

We arbitrarily characterized the transition between these two regimes using the compression stress $|\sigma_{0.3}|$ recorded at a compression strain $|\varepsilon| = 0.3$. As shown in Figure 3-6.C, the compression viscosity $\eta_{0.3} = \frac{\sigma_{0.3}}{\dot{\varepsilon}_{0.3}}$ decreased with the strain rate $|\dot{\varepsilon}_{0.3}|$ and followed a power-law function, *i.e.*, $\eta_{0.3} = k|\dot{\varepsilon}_{0.3}|^{n-1}$. The value obtained for the power-law exponent, $n = 0.2$, indicates the optimized pastes exhibited a pronounced thinning behavior, which is similar to those obtained for similar fiber-reinforced paste materials. The stress levels recorded here one order of magnitude larger than those reported under shear for other 3D printing formulations (Compton & Lewis, 2014; Lewis, 2006; Siqueira et al., 2017; Smay et al., 2002).

When the compression flow stopped, the compression stress rapidly decreased to reach a steady and constant stress (Figure 3-6B), which corresponds to the yield stress $|\sigma_y|$ after the paste flow. Figure 3-6.D shows that $|\sigma_y|$ achieved finite values that were quasi-independent of the initial strain rate $|\dot{\varepsilon}_{0.3}|$ and about 4 to 6 kPa (Figure 3-6.D). The yield stress $|\sigma_y|$, which was measured for the “fresh” state, is one of the most critical parameters for AM by extrusion from a mechanical standpoint (as the paste liquid phase evaporates, the yield stress is expected to increase). If the stress state in a “fresh” printed filament remains below the yield stress, the filament should behave as an elastic solid and maintain its printed shape. Above this value of yield strength, the dimensional stability may be lost, as the paste can flow.

We can observe that the rheological behavior of both of the optimized cellulose based pastes was similar although the yield stress of the powder base paste seems to be less independent of the initial strain rate.

To confirm the presence of this yield stress, the diameter of the upper and lower part of filament of length from 20 to 80 cm of the optimized cellulose fiber based formulation extruded and dry in vertical position were measured and are plotted in Figure 3-7.

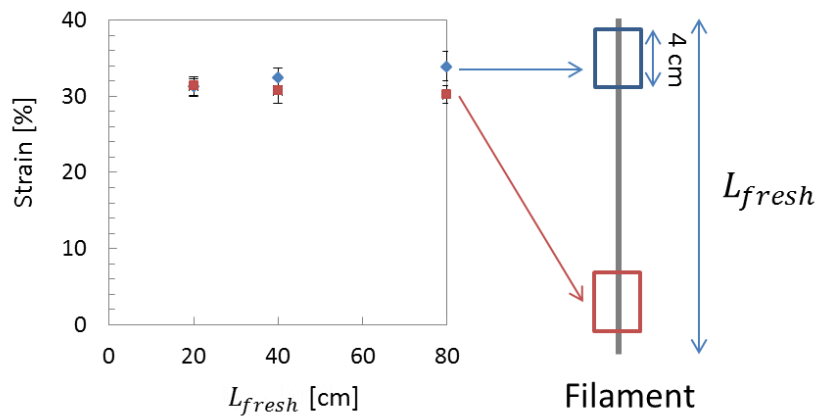


Figure 3-7. Plot of the diameter strain of the lower and upper part of the dry filament as a function of its extrusion length, L_{fresh} , for the optimized fiber cellulose paste. The diameter engineering strain was

calculated as followed: $\left| \frac{d_{dried}}{d_{nozzle}} - 1 \right| * 100$ and the errors bars represent the standard deviation

between the 5 tested samples for each extrusion length.

Figure 3-7 shows the deformation of the lower and upper part of the dry filament for different length. We can observe that for a filament length of 20 cm, there is no difference between the mean diameter of the upper and lower part of the filament. However, for a 80 cm long filament, we can observe a larger deformation of the upper part of the filament compared to its lower part. Indeed, if we consider that the fresh density of the paste, ρ , is about 1.2 g.cm^{-3} , the strain applied on the upper part, σ , is about 9.1 kPa ($\sigma = L_{fresh}\rho g$ with $g = 9.8 \text{ m.s}^{-2}$, the standard gravity), which is larger than the yield stress measured by lubricated squeeze flow (about 6 kPa): the filament starts to flow under its own weight. The flow was not enough fast in comparison with the yield stress increase due to the drying as the filament did not break.

These two techniques allow an evaluation of the rheological behaviour of the optimized pastes. The rheological behaviour observed should be compatible for AM by extrusion to manufacture parts with dimensions that induced an applied stress on the material lower than its yield stress.

3.3.2 Shrinkage during drying

The longitudinal and radial strains of filaments made up of the three identified pastes were assessed, compared with each other and compared to their water volume content which corresponds to the maximal strain that could be observed if we assume the absence of air bubble in the paste in its wet state.

As illustrated in Figure 3-3.B, Figure 3-4.B and Figure 3-5.B, after drying, the filament dimensions of all the water based formulations decreased. These strains were summed up in Table 3-2.

For the optimized cellulose fiber paste, the filament diameter decreased from 0.72 to 0.49 ± 0.1 mm, and its length decreased from 200 to 193 mm (Figure 3-3.B). Thus, the strain was primarily radial and about 33%. These dimensional changes were due to the 67 vol.% of distilled water in the optimized paste. During the drying phase, the water evaporates and in parallel is transported from the inside to the outside of the printed part, leading to high drying stresses, such as the capillarity pressure (Scherer, 1990). The capillary forces tend to bring the flexible cellulose fibers embedded in dissolved CMC closer together (i.e. mainly in their longitudinal direction), resulting in strain. Moreover, the hygroexpansion of a cellulose fiber is larger in the transversal direction than in the longitudinal direction: over the relative humidity range from 0% to 100% at 23 °C, a single cellulose fiber roughly expanded by 1% in the longitudinal direction, whereas it expanded about 20 to 30% in the radial direction (Wainwright, Biggs, & Currey, 1982). Moreover, Sampson et Yamamoto, 2011 considered that about half of the thickness variability of an isotropic paper sheet during drying was attributable to fiber width variability ranging from 0.3 to 0.8 depending of the mechanical treatment of the cellulose fiber for a moisture loss of 80%. Thus, as the strain of filament is mainly a radial strain (33%), it suggests that most of the cellulose fibers were aligned in the extrusion flow direction, as shown in Figure 3-8.A. Figure 3-8.B shows the SEM image of the inner structure of a dried filament, a porous phase was present. This porosity is the result of a volumetric strain lower than the water volume content of the paste in the wet state (56% vs. 67%). This suggests that the deformation ends before the end of the drying phase. Thus, the stiffness of the partially dried paste was sufficient to resist the drying forces.

Formulation (dry content)	Cellulose fiber paste (33 vol.%)	Cellulose powder paste (40 vol.%)	Graphite paste (45 vol.%)
Radial strain	$33 \pm 1\%$	$31 \pm 1\%$	$7 \pm 1\%$
Longitudinal strain	$4 \pm 1\%$	$8 \pm 1\%$	$3 \pm 1\%$
Volumetric strain	$56 \pm 2\%$	$56 \pm 2\%$	$16 \pm 3\%$

Table 3-2. Filament strains results for the three identified pastes.

For the optimized cellulose powder paste, the filament diameter presented roughly the same decrease as the optimized cellulose fiber paste and a larger length decrease, from 200 to 185 mm whereas the paste was composed of less water (60 vol.% vs. 67 vol.%). Indeed, the cellulose powder presented the same cross section as a cellulose fiber one, only their length was different. Moreover, in the previous section (3.3.1 p.107), we observed that both of the optimized cellulose fiber and powder pastes exhibited the same rheological behavior. Their resistance to drying strength should be the same. That is why, the radial strain was roughly the same. However, as the characteristic length of cellulose powder was about one third of the length of cellulose fiber (Figure 2-1 and Figure 2-2),

the extruded filament comprises more cellulose powder in its longitudinal direction than cellulose fiber. So, in proportion, more liquid phase is present in the longitudinal direction, resulting in a larger longitudinal strain of the filament.

For the optimized graphite powder paste, the radial and longitudinal filament strains were 7 and 3%, respectively. Compared to the 100% cellulose based formulation, the volumetric strain of the filament was more than 3 times smaller. Indeed, the water volume content in the graphite formulation was also smaller (55 vol.%) leading to a lower theoretical strain (without taking into account the pore formation). Moreover, the solid filler volume content was larger (less CMC in proportion) and particles presented a rigid spherical frame leading to more pores formation due to the packing. Furthermore, the graphite presents a non-hygroscopic behavior.

The shrinkage of a material shape as a filament after drying is a negative aspect for its AM by extrusion compatibility for manufacturing part as it can lead to non-accurate 3D printed part. However, as the shrinkage is anisotropic and the longitudinal strain is small for the optimized cellulose fiber and graphite pastes (<4%) and the AM by extrusion process is a layer by layer process along Z direction, these pastes can present potential for AM by extrusion as soon as the radial strain is controlled.

3.3.3 Microstructure of the extruded filament

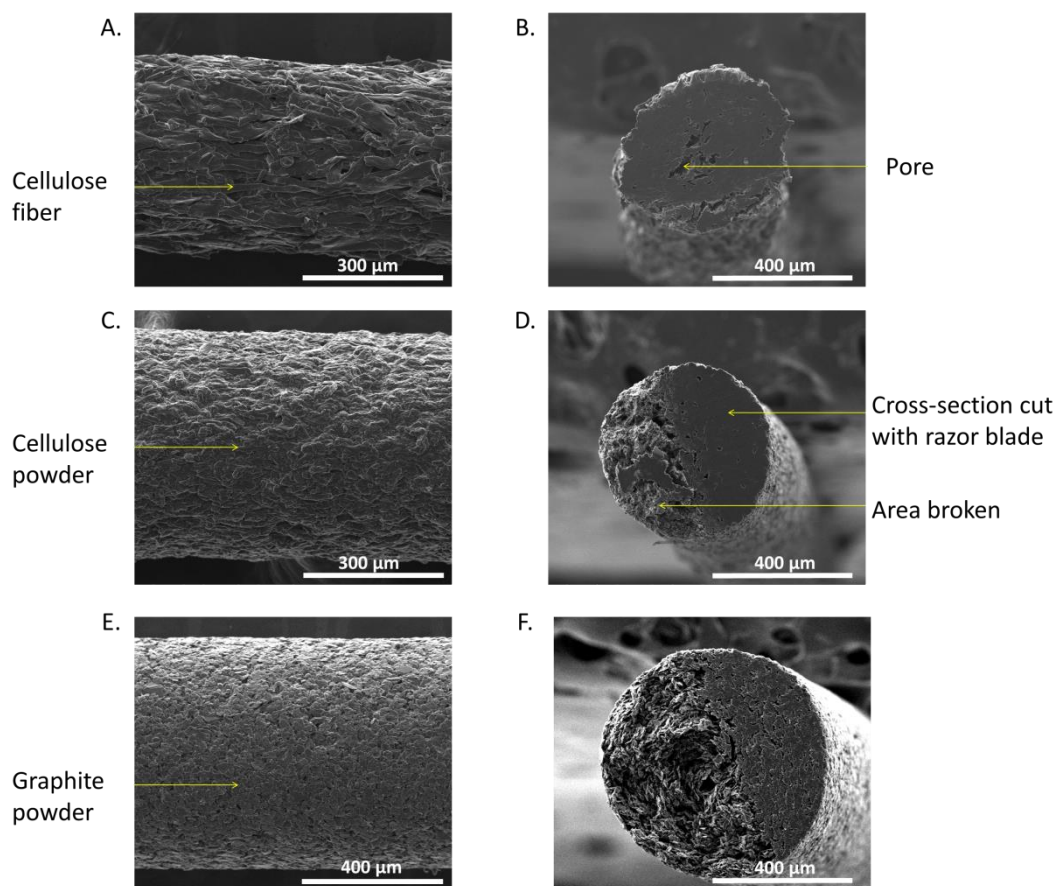


Figure 3-8. SEM images of the surface and cross-section of air-dried filament with (A, B) short cellulose fiber, (C, D) cellulose powder and (E, F) graphite powder.

As shown in Figure 3-8.A, C and E, the fillers seem glued together and form a well-defined surface. The powder based filament showed a smoother surface than the fiber based filament. Due to their aspect ratio, we can observe an alignment of the cellulosic fibers in the extrusion direction at least on the surface. An in depth study of the alignment could be performed with X-ray diffraction measurement for example. This alignment and the packing of the fillers may have been enhanced by the capillary forces during the drying process.

The filament cross-sections are shown in Figure 3-8.B, D and F, showing homogeneous solid phases with pores. The pores seem larger for the cellulose fiber paste than for the graphite paste. However, the air-dried graphite filament presents a large number of small pores due to the 55 vol.% of water and a volume strain of 16%. This is not in favor of a highly conductive material.

Both of these observations confirmed the following: (i) The initial paste was homogeneous due to the mixing process that kept the fillers dispersed in this gelatinous matrix, forming a single phase paste. (ii) The flow through the 0.7 mm nozzle was homogeneous even for the cellulose fiber paste,

as no fibers aggregation or detachment was observed, despite a mean cellulose fiber width of $27\ \mu\text{m}$ for cellulose fibers with lengths larger than $100\ \mu\text{m}$. This may have been owing to the CMC. Indeed, the addition of CMC dissolved in water in the formulation acted as a gelation agent by increasing the water viscosity (Edali, Esmail, & Vatistas, 2001) and allowed the cellulose fibers to be embedded, which reduced the friction between fibers. (iii) High stresses developed in the nozzle due to the elongational strain and shear rate were caused by the successive constrictions inside the nozzle and its small outlet diameter. For instance, the apparent shear rate value was about 10^1 to $10^2\ \text{s}^{-1}$ for a flow rate of $5\ \text{mm s}^{-1}$ through nozzles with outlet diameters of $0.5\text{--}0.7\ \text{mm}$. These high stresses might be the main factor that induced the cellulose fiber alignment.

3.3.4 Tensile properties of dried filaments

Only the tensile properties of the optimized cellulose fiber formulation was evaluated as the dried filament of powder based formulations were brittle (cannot be cut by a razor blade without breaking as shown on Figure 3-8.D and F) and the fillers in a powder form have no mechanical enhancement functions.

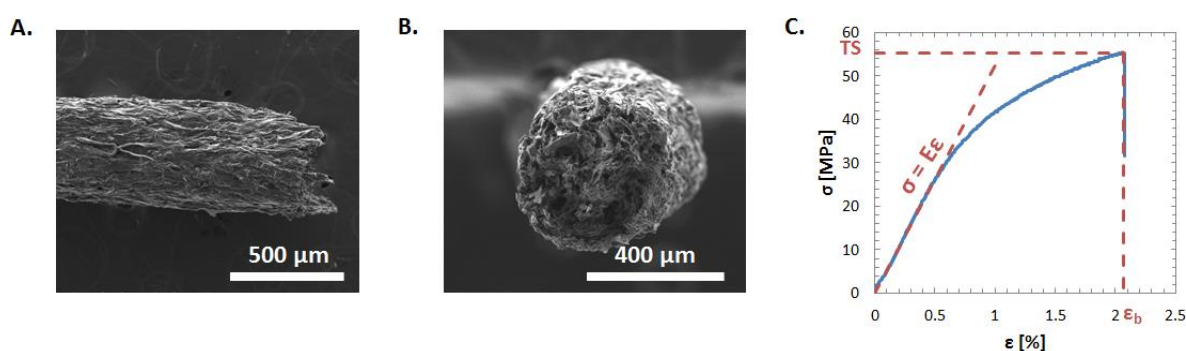


Figure 3-9. SEM images of a fractured air-dried filament extruded through a $0.7\ \text{mm}$ nozzle diameter: (A) surface and (B) cross-section. (C) Typical stress-strain curve obtained for a tested air-dried filament.

Figure 3-9.A and B show the fractured surfaces in the rupture zone of an air-dried filament after the tensile test. The cross-section of the filament after fracture was not sharp as those shown in Figure 3-8.B, indicating that some fibers broke away from the surrounding fibers. The strain stress curve obtained from the tensile test of a dried filament shown in Figure 3-9.C is typical of the behavior of a brittle material without a strain-hardening region. From this strain-stress curve, the Young's modulus can be determined. The Young's modulus was $5.4 \pm 0.5\ \text{GPa}$, two times the CMC Young's modulus ($2.8 \pm 0.6\ \text{GPa}$, section 3.2.1.2 p.99). Indeed, as presented in chapter 1 (1.2.1.2 p.41), the Young's modulus of single cellulose fiber is about 10 to 70 GPa which reinforce the

composite. Moreover, the cellulose fiber adhesion with the filmogenic CMC might be enhanced by the cellulose fiber-fiber bonding which result in a stiffer material than pure CMC matrix.

The Young's modulus of the dried filament was of the same order of magnitude as tensile test specimens of PLA using the Fused Filament Fabrication process, which range from 2 to 3 GPa according to the PLA data sheet of Stratasys, Ltd. This reinforces the hypothesis that this new cellulosic paste is compatible with the market expectations.

3.4 Toward functionalization of formulation

3.4.1 Addition of a wet strength agent: a compromise between easy reuse and wet strength

3.4.1.1 Influence of the wet strength agent on the dry properties

The influence of the addition of a wet strength agent (Kymene in this case) on the shrinkage after drying and the dry mechanical properties were evaluated for concentration ranging from 0 to 10 wt.% in a dry content basis (chapter 2, section 2.2.2 p.75).

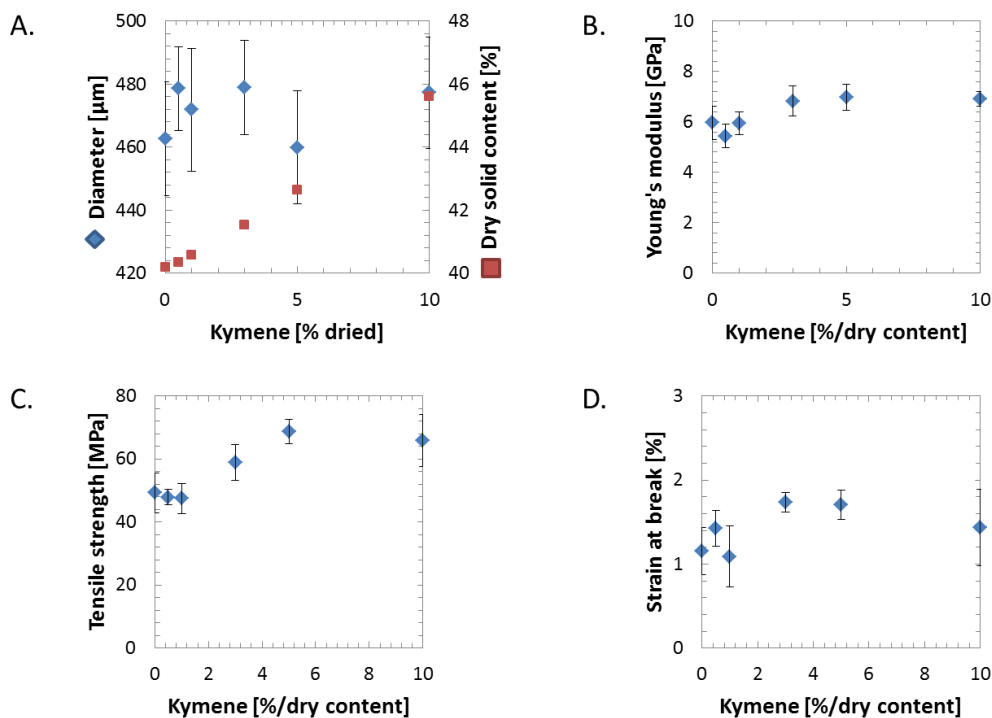


Figure 3-10. Influence of the wet strength agent (Kymene) on the dry properties: (A) diameter, (B), Young's modulus, (C) Tensile strength and (D) Strain at break.

Figure 3-10.A shows that we were able to process all the paste with increasing Kymene concentrations as well as the dry solid content of the paste that goes from 40 to 46 wt.%. We can observe that the diameter of the dried filament vary from 460 to 480 μm independently of the dry

solid content. The addition of Kymene which reduce the dry solid content does not seem to have a clear influence on the radial strain of the dry filament.

Figure 3-10. B, C and D show the influence of the wet strength agent on the mechanical properties of dried filament. For a Kymene concentration up to 1 wt.%, the wet strength agent does not seem to influence the mechanical properties whereas from 3 to 10 wt.%, the Young's modulus, the tensile strength and the strain at break show an increase of their value up to 17, 40 and 48%, respectively. Indeed, in the paper industry, Kymene can be added up to 1 wt.% of the cellulose fibers content with CMC that form a complex that improve the dry strength of paper (E. J. Siqueira 2012). The cross-linking of the resin lead to resin-resin bonding as well as resin-fiber bonding as Kymene can be absorb on the cellulose fiber surface.

3.4.1.2 Influence of the wet strength agent on the wet properties

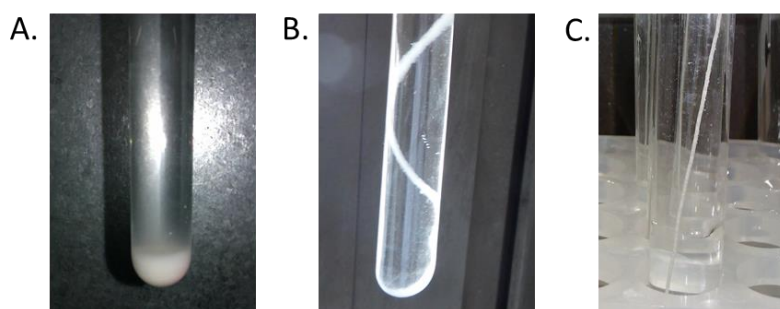


Figure 3-11. Filament made of cellulose fiber paste after 30 min in water with a dry Kymene concentration of (A) 0 wt.%, (B) 0.5 wt.% and (C) 5 wt.%.

Figure 3-11 shows a filament after 30 min in water with dry Kymene concentration ranging from 0 to 5 wt.% in the cellulose fiber paste. After 30 min in water without addition of a wet strength agent in the formulation, we can observe the sedimentation of cellulose fibers that composed the dry filament whereas with 5 wt.% of Kymene, the filament maintain its shape. At 0.5 wt.% of Kymene addition, we can observe a filament dilatation. Moreover, this filament cannot support handling. In a qualitative point of view, the addition of Kymene presents a strong impact on the wet properties as it prevents the destructure of the filament and therefore the sedimentation of cellulose fiber in water due to a simple immersion of the part in water. This fibers dispersion in contact of water is an interesting result for material reuse from one part to another. However, the part should not be in contact of water to maintain its shape.

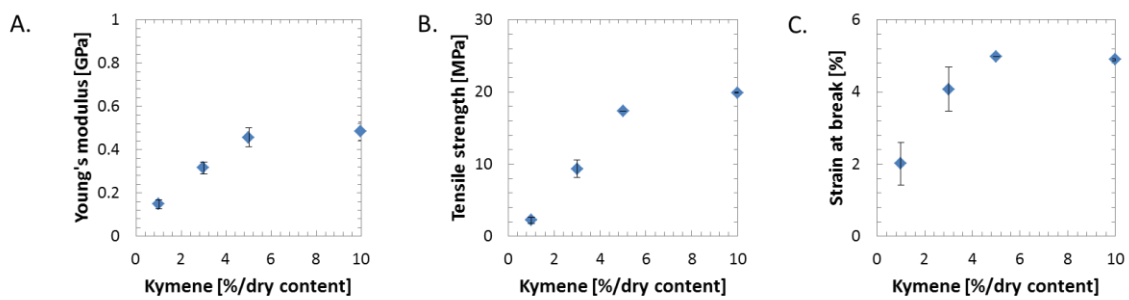


Figure 3-12. Influence of the wet strength agent (Kymene) on the wet properties: (A) Young's modulus, (B) Tensile strength and (C) Strain at break.

Figure 3-12 shows the influence of the wet strength agent on the wet mechanical properties of filament immersed in water during 30 min. We can observe that the Young's modulus and the tensile strength increased from 0.15 to 0.48 GPa and from 2 to 20 MPa, respectively with the increase of Kymene concentration until reaching a plateau for concentration larger than 5 wt.%. Moreover, the maximum wet Young's modulus and tensile strength are about 15 and 3 times lower than the dried ones, respectively whereas the strain at break which reaches 5% is about 2 to 3 times larger. Indeed, after cross linking, the Kymene has built a network between fibers to maintain their adhesion while the strong and effective hydrogen bonding between fiber in dry conditions and the filmogenic adhesion of CMC lose its strength in water.

According to the condition of use of the part that will be 3D printed, Kymene at 1 wt.% or more can be added to improve the wet properties and maintain the part shape in case of water immersion. However, it can be noticed that the use of the paste without Kymene for AM by extrusion part show very interesting properties for reuse as the shape of the printed part will not be maintained when immersed in water. The addition in the right proportion of dry cellulose fiber and CMC to the former dried part immersed in water allows the obtention of paste that can be reuse to produce new parts.

3.4.2 Influence of CMC on graphite conductivity

AM by extrusion can be used for manufacturing smart objects composed of a conductive and a non-conductive material for example. The conductive material can be used as a 2D tracks or 3D patterns. (Tricot et al. 2018) show that highly conductive screen printing ink can be used for 2D tracks with a dispensing unit mounted on a Cartesian 3D printer. For 3D patterns, few commercial conductive thermoplastics with carbon based fillers are available on the market. We were interested in developing a carbon based conductive material for 3D pattern. Yet, the conductivity of graphite within a CMC matrix was evaluated on air-dried extruded filament with the composition described in chapter 2, section 2.2.1 p.69. It corresponds to 14 to 33 vol.% of CMC in dry basis. A broader interval

of CMC/graphite blend ratio would have been evaluated if the casting of dilute CMC and graphite blend for homogeneous thickness did not lead to graphite sedimentation (Lee et al. 2005) and therefore, inconsistent results with the 4 points probe method.

CMC content [vol.%/dry vol.%]	Initial dry content [vol.%]	Volumetric strain [%]	Conductivity [S.m ⁻¹]
14.4	45.0	16	3.4 10 ⁻¹
16.7	50.0	13	4.0 10 ⁻¹
17.6	40.0	-	3.7 10 ⁻¹
20.4	45.0	18	3.2 10 ⁻¹
22.2	50.0	12	4.5 10 ⁻¹
27.2	45.0	30	3.5 10 ⁻¹
33.3	40.0	-	2.7 10 ⁻¹

Table 3-3. Conductivity of extruded filament made of graphite paste with different CMC contents in dry basis, initial dry contents and measured volumetric strain.

Table 3-3 shows the conductivity of the formulation evaluated for AM by extrusion compatibility. Besides the CMC filmogenic properties, we can observe that the CMC content does not influence the conductivity of the filament for solid content varying from 14 to 33 vol.%. The average measured conductivity (0.4 S.m⁻¹) is 9 orders of magnitude larger than the CMC conductivity which is around 10⁻¹⁰ S.m⁻¹ (Moteleb 1992) and 5 orders of magnitude lower than the bulk graphite conductivity which is about 2.5.10⁴ S.m⁻¹. Two main mechanisms of electron conductivity can be considered: (i) electron conductivity by mechanical contact if the CMC does not cover completely the graphite particles and (ii) electron conductivity by tunnelling effect (conductivity mechanism of composite made of conductive fillers in insulative matrix). This second assumption was verified by Park, Kim, et Kim, 2017 with a conductive silver ink with low percolation ratio made of silver nanowires in a CMC matrix that represent 98 vol.% of the dried formulation. Moreover, unlike silver nanowire, the aspect ratio of graphite is close to one which influences the particles packing and is less in favour of good conductivity by mechanical contact. Furthermore, the volumetric strain of all the filaments was low compared to the initial volumetric water content (Table 3-3) which imply the presence of numerous pores as observed in the previous part on the microstructure of the filament (section 3.3.3 p.112).

The obtained conductivity of graphite extruded filament is 3 to 4 order(s) of magnitude lower than thermoplastic filaments designed for 3D printing by Protopasta, Graphene 3D lab, F electric, Carbomorph or Nanocyl with carbon black, graphene or carbon nanotubes in PLA or PCL (Polycaprolactone) matrix.

The composition of the CMC/graphite formulation should be enhanced to be competitive with the commercial conductive filament by optimizing the particle shape and its packing. The presence of

CMC avoids graphite sedimentation and is compatible with conductive ink as studied by Park, Kim, et Kim, 2017.

3.5 Conclusion

In this chapter 3, we identified three formulations with strong potential for AM by extrusion. They are composed of (i) fillers that vary in shape, in nature and in concentration in the matrix: cellulose fiber (30 wt% - 23 vol.%), cellulose powder (37.5 wt% - 30 vol.%) and graphite powder (57 wt.% - 38 vol.%) and, (ii) a matrix made of CMC at a concentration from 17 to 20 wt.% in water. This matrix presents (i) a large viscosity before drying as it does not seem to flow after 5 min after a vertical to horizontal position change of a half filled 100 mL container, (ii) a Young's modulus, tensile strength and elongation at break of 2.8 GPa, 37 MPa and 1.7%, respectively after drying and (iii) a conductivity about 0.3 S.m^{-1} when added to graphite at 14 to 33 vol.% in a dry basis. These formulations were identified based on specific criteria that should ensure accuracy between the cellulose printed part and the 3D model: (i) filament extrusion, (ii) shape fidelity before drying, and (iii) limiting deformation after drying.

These identified pastes exhibited a pronounced thinning behavior and a yield stress after relaxation, which are critical parameters for 3D printing parts. Moreover, they all present homogeneous filaments with anisotropic shrinkage: a larger radial strain than the longitudinal strain. The radial strain was about 33% for the cellulose based paste whereas it was about 8% for the graphite paste leading to more or less porosity. The fibrous cellulose based filament that exhibited high Young's moduli ($\sim 5 \text{ GPa}$) in a dry state were produced by a screw-driven device with nozzle diameters of 0.7 mm. When immersed in water, the filament shape was not maintained allowing the reuse of paste. However, to keep the filament shape and increase mechanical properties, a wet strength agent (Kymene) should be added at least 1 wt.% in a dry basis. Another possibility could be to crosslink CMC to cellulose with high temperature condition (180°C). Preliminary tests have shown a strong and positive impact of this high temperature treatment on part made of the cellulose fibrous based paste to avoid a rapid disintegration of the 3D printed part.

For the following chapters, we have selected the cellulose fibrous based paste to work with to optimize the 3D printing process and the drying. However, the same studies can be performed with the two other identified pastes.

Chapter 4. Optimization of the printing parameters and the printer to manufacture accurate 3D parts with the optimized paste

4.1	Introduction.....	120
4.2	Optimization of the extrusion flow.....	121
4.2.1	Extrusion efficiency.....	121
4.2.2	Influence of the inner shape of the nozzle and the extrusion flow rate on the aspect of the filament.....	126
4.2.3	Influence of the extrusion flow rate on the mechanical properties.....	129
4.3	Optimization of AM by extrusion settings to accurately produce more and more complex parts.....	131
4.3.1	Influence of the settings on 2D parts.....	131
4.3.2	Influence of the settings on 3D printed parts.....	135
4.3.3	Printability of a complex model in the fresh state.....	146
4.4	Conclusion.....	147

4.1 Introduction

As described in chapter 1, among the Additive Manufacturing (AM) process, AM by extrusion represented the process with the largest number of 3D printers installed in 2015 (Wohlers et al. 2016). The interest in this technology comes from (i) its low cost (printer available for less than 400€), (ii) its office friendly environment, (iii) its ease of use and light post processing operations and, (iv) its ability to produce complex and lattice parts with one or more extruder head (multi-materials approach). The process consists in selectively dispensing material through a nozzle or an orifice as a first step. This material must present specific flow properties such as amorphous thermoplastic, ceramic paste or nanocelluloses suspension. Then, as a second step, this process consists in depositing the material usually layer upon layer as a flatten filament shape to join materials along a path to produce objects from 3D model data, (ASTM International 2012). To do so, a 3D printer and a slicing program are used to guarantee a precise control of the extrusion flow rate and the printing path for manufacturing accurate 3D parts.

- The 3D printer is basically constituted of an extrusion head adapted to the rheology of the material, a moving system in the X, Y and Z directions, a building plate, a controller and a power supply.
- The slicing program converts a 3D model saved in STL format (Standard Triangle Language) in a G code, a programming language to control the 3D printer by instructions such as the coordinates of the point to reach, the displacement speed and the amount of material to extrude.

The first commercial AM by extrusion printers could not be customized, proprietary material must be used and the choice of the printing settings to generate the G-code by the user was limited by predefined limits. All the equipment was internally developed by the companies such as Stratasys. This technology benefits, now, from a large open source community that shares, for instance, part designs, helpful tips on printer customization or process settings. The well documented RepRap project (Jones et al. 2011) illustrates the open source community with the development of open sourced hardware and software for AM by extrusion. It opened a full control over the process options to the user that can lead to the use of a troubleshooting guide, exploitation of printing error (Takahashi et Miyashita, 2017), high quality printing but also to maintenance and calibration of the 3D printer (perfectly horizontal build plat, accurate extrusion flow, motion of the extruder head...). The process options can be linked to the extrusion (track width, extrusion multiplier, oozing parameters), the layer (number of perimeter shell, layer height), the infill of the part (interior fill percentage, internal fill pattern), the temperature, the printing speed, the part placing, the addition

of support material and so on. These settings were broadly studied with thermoplastics to optimize for example, the bond adhesion between layers (Kuznetsov, Tavitov, et Urzhumtcev, 2019), the accuracy or the surface quality (roughness)(Dey et Yodo, 2019), the support generation for overhang (Dumas, Hergel, et Lefebvre, 2014; Jiang, Lou, et Hu, 2019). Such studies are rare for paste or suspension. For paste or suspension, articles mainly deals with the formulation adjustment and their rheological behavior before concluding on a successful printing with one set of printing parameters as in chapter 3.

This chapter aims at studying the influence of the main printing parameters and the printer technology choices on the accuracy of AM by extrusion in order to suggest a printer setting guideline. Moreover, this study was based on the results of the previous chapter, where a fibrous cellulose paste formulation was developed for manufacturing 3D solid parts. The major objective of this chapter is to confirm the 3D printing compatibility of the developed paste and its limits.

The main parameters that affect the extrusion step were identified and evaluated on criteria such as the extrusion efficiency (effective quantity of material extruded over the set value (Kuznetsov, Tavitov, et Urzhumtcev, 2019)) as a function of the extrusion flow rate, the filament aspect and its mechanical properties. Likewise, the main parameters that affect the deposition step (the 90° turn of the extruded filament and its deformation) were identified and evaluated on the 2D and 3D parts selected to test the printing accuracy of the main elementary features that composed any 3D part.

4.2 Optimization of the extrusion flow

4.2.1 Extrusion efficiency

As described in material and method (section 2.3.1 p.75) and showed in Figure 4-1.A, the paste is provided through an air pressurized tank to the inlet cavity of the extruder. Without the connection, the paste flows from the tank at a flow rate, Q' , that can be adjusted by the tank pressure. The rotation of the screw with a defined screw thread convoys the paste at a set rotation velocity, Ω until the nozzle. The paste is extruded through the nozzle at an experimentally measured flow, Q_{exp} which is a key parameter for accurate printing. The extrusion efficiency is the effective quantity of paste extruded over the set value. All these magnitudes are schematically represented Figure 4-1.A.

4.2.1.1 Influence of the rotation speed

The influence of Ω on Q_{exp} through a nozzle with a diameter of 0.7 mm was evaluated for Ω ranging from 3 to 50 rpm. Q' was about $20 \text{ mm}^3 \cdot \text{s}^{-1}$.

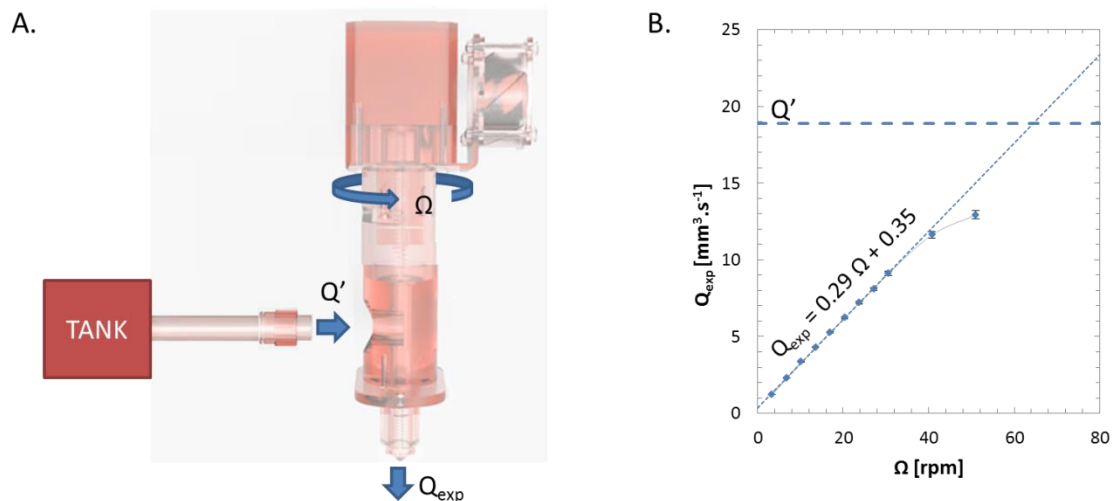


Figure 4-1. Influence of the rotation velocity on the outlet flow of the extruder for a given outlet flow of the tank – (A) Schematic view of the extruder with the outlet flow of the tank, Q' , the rotation velocity of the screw, Ω , and, the experimental flow measured at the outlet of the nozzle, Q_{exp} (www.3dwasp.com). (B) Plot of Q_{exp} as a function of Ω for a given Q' .

Figure 4-1.B shows Q_{exp} as a function of Ω for a given Q' . We can observe that while Q_{exp} is small enough compared to Q' , Q_{exp} and Ω can be linearly fitted by $Q_{exp} = 0.29\Omega + 0.35$. If we neglect the small intercept compared to the range of flow studied, Q_{exp} is proportional to Ω with a proportionality coefficient of 0.29. But when Q_{exp} approaches Q' , its maximum limit, we can observe that Q_{exp} levelled off. To explain this level off, we can make out several hypothesis : (i) the pressure loss in the nozzle is equal or larger than the one that the screw can deliver leading to the presence of backpressure, (ii) cavitation occurred, the air pressure applied on the material to feed the screw is not enough for larger extrusion flow. This second hypothesis is discussed in section 4.2.1.3 p.125.

The first hypothesis may be cause by a too large pressure loss in the nozzle or a plateau of pressure reached by the conveyance of the paste due to slippage between the paste and the screw or a limit of the motor power for example. The pressure loss in the nozzle can be evaluated by:

- Modeling the nozzle by a circular channel with an inner diameter about 0.72 mm and a length about 1.4 mm (Figure 4-4.A)
- Assuming that there is non-slip boundary condition as described in chapter 1 (section 1.1.2.2.1 p.24)
- Using the coefficients of the power law describing the rheological behaviour of the paste (section 3.2.1.1 p.98), besides the range of shear rates required for the following calculation might be out of range,

By using the equation 11, for a rotation velocity varying from 30 to 50 rpm, the pressure loss in the nozzle goes from 9 to 10 bars whereas the extruder head used should be able to deliver up to 40 bars (supplier data). As a consequence, the increase of the pressure loss in the nozzle could not be the main explanation.

$$\Delta P = \left(\frac{Q_{exp}}{\pi} \frac{1 + 3n}{n} \right)^n \frac{2KL}{R^{1+3n}} \quad (11)$$

Where ΔP is the pressure loss [Pa],

Q_{exp} is the flow rate measured at the outlet of the nozzle [$m^3.s$],

n is the power-law exponent,

K is the flow consistency index [$Pa.s^n$],

L is the length of the nozzle [m],

$R = \frac{D}{2}$ is the radius of the nozzle [m],

- To guarantee a constant flow rate for various printing speed, the rotation speed from which Q_{exp} began to level off should not be exceeded. This constant flow rate is a key parameter to favor a potential success of the AM by extrusion process to produce accurate parts. However, this threshold limits the choice of the maximum printing speed, layer height and filament width, increasing the printing time of the part.

As described in chapter 2 (section 2.3.2 p.76), in the hardware of the printer, the supplier set the relation between the quantity of the paste to extrude, $V_{E\theta}$ and the angle of rotation of the screw, θ . For one rotation of the screw, $V_{E2\pi} = 42 \text{ mm}^3$. The theoretical set flow, Q_{th} can be calculated as follow: $Q_{th} = V_{E2\pi} \Omega$. Therefore, the proportionality coefficient between Q_{exp} and Q_{th} can be calculated thanks to the one measured between Q_{exp} and Ω (Figure 4-1.B). It was found to be about 0.41 which is below 1. This is mainly due to pressure losses in the nozzle as observed in single screw extrusion process (Vergnes et Puissant 2002).

- To achieve the flow rate required for accurate 3D printing (Q_{th}), the rotation speed of the screw must be multiplied by a calibration factor, C of 3.4. It should be highlighted that this proportionality between Q_{exp} and Q_{th} allows variation of the flow rate (such as a variation of the printing speed during AM to print small details at slow rate) with the same calibration factor.

4.2.1.2 Influence of the nozzle

The extrusion efficiency was evaluated for three different nozzles (Figure 4-4.A) with Ω ranging from 3 to 20 rpm.

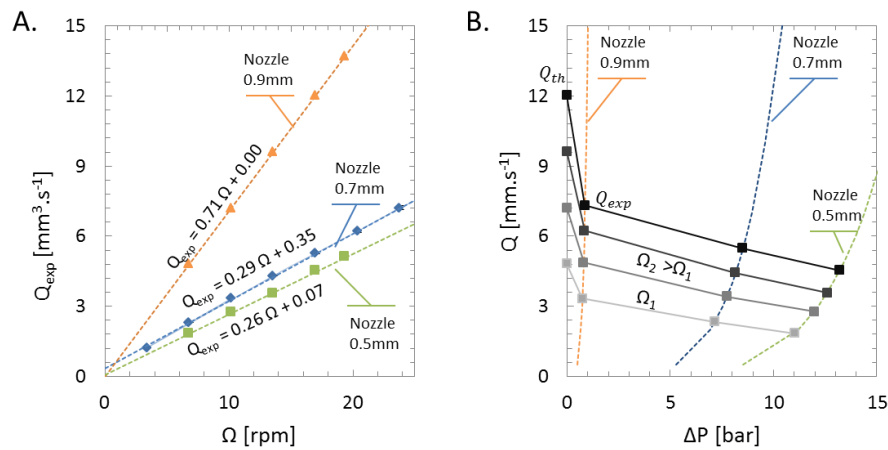


Figure 4-2. Influence of the nozzle (diameter and inner shape) on the extrusion efficiency, nozzle with diameter of 0.9, 0.7 or 0.5 mm – (A) Plot of Q_{exp} as a function of Ω for the three nozzles, (B) Plot of the extrusion flow through the three nozzles as a function of the main pressure loss in the nozzle and plot of Q_{th} and Q_{exp} through different nozzles for different rotation speeds as a function of the pressure loss in the nozzle.

Figure 4-2.A shows that regardless the nozzles, the relation between Q_{exp} and Ω was linear. However, the proportionality coefficient between Q_{exp} and Ω depends on the used nozzle. The calibration factor is therefore specific to the used nozzle.

Figure 4-2.B shows:

- the theoretical evolution of the extrusion flow through three nozzles as a function of the main pressure loss in the nozzle calculated from equation (11),
- Q_{th} and Q_{exp} through different nozzles for different rotation speeds as a function of the pressure loss in the nozzle for various operating conditions.

As expected, for less restrictive nozzle (*i.e.* short and large nozzle), the extrusion flow was larger. The evolution of the operating point for a set rotation velocity was quasi linear. This quasi straight line was shifted for different rotation speeds. We can observe that Q_{th} was not aligned with the three operating points for the same rotation speed. Yet, this supplier theoretical set flow was found to be close to the one calculated with the assumption that the extruder head behaves as a volumetric pump (section 2.3.3 p.77). The too large Q_{th} compared to Q_{exp} through the nozzles

means that the volumetric pump model was not valid, slippage between the paste and the screw must occur to explain these results.

Likewise, the evolution of the flow rate in the screw extruder as a function of the pressure loss could not be fitted by a linear equation in the range of pressure loss studied with the Couette model. This model was applied (no slip boundary conditions) at the unwound channel defined by the thread of the screw and the barrel with the thinning behaviour of the paste studied in chapter 3 (section 3.3.1 p.107). A linear evolution of the flow as a function of the pressure loss by applying the Couette model is valid for a Newtonian behaviour.

- Simple model cannot be applied to model this paste extrusion in the extruder head.

4.2.1.3 Influence of the outlet flow of the tank

The influence of Q' , the outlet flow of the tank on Q_{exp} through a nozzle with a diameter of 0.7 mm was evaluated for Q' ranging from 5 to $50 \text{ mm}^3 \cdot \text{s}^{-1}$.

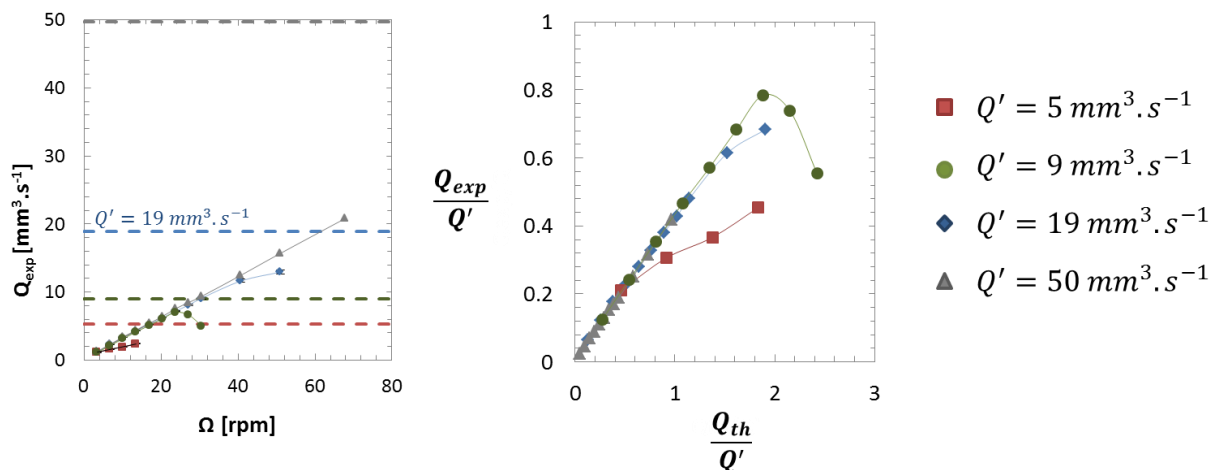


Figure 4-3. Influence of the outlet flow of the tank, Q' for different rotation speeds, Ω on the extrusion flow of the nozzle, Q_{exp} – (A) Plot of Q_{exp} as a function of Ω for different Q' and (B) plot of $\frac{Q_{exp}}{Q'}$ as a function of $\frac{Q_{th}}{Q'}$.

Figure 4-3.A shows that for an outlet flow of the tank (Q') ranging from 9 to $50 \text{ mm}^3 \cdot \text{s}^{-1}$ the coefficient of proportionality between Q_{exp} and Ω remains constant for the same nozzle until at least $\frac{Q_{exp}}{Q'} = 0.5$. However, we can notice that for a lower Q' ($Q' = 5 \text{ mm}^3 \cdot \text{s}^{-1}$), from $\frac{Q_{exp}}{Q'} = 0.3$, the proportionally coefficient decreases from 0.29 to 0.12. Indeed, the resulting pressure due to the slow outlet flow from the tank might not be enough to produce an enough large pressure with the screw conveyance of the paste to overcome the pressure loss of the nozzle.

To conclude, to guarantee a constant extrusion multiplier between Q_{exp} and Ω for the extrusion flow range required due to the chosen printing settings, the outlet flow of the tank should be larger than the measured extrusion flow ($\frac{Q_{exp}}{0.5}$ in the case of the nozzle tested). It should be highlighted that this outlet flow of the tank, Q' is mainly tailored by the used paste, the used pressure and the dimensions of the tank (length and diameter) including those of the tube of connection (and its matter). In our case, the upper limit of the outlet flow of the 3L tank ($15 \text{ mm}^3 \cdot \text{s}^{-1}$) limits the printing speed of parts to around $20 \text{ mm} \cdot \text{s}^{-1}$ with our printing settings whereas for the 15 mL tank, the outlet flow can be much larger allowing printing at larger speed. An optimization of the extruder head (screw, barrel, stepper motor, nozzle) and maximizing the outlet flow of large tank to increase the printing speed range could be addressed. For example, the implementation of a fix extruder head and a moving X and Y build platform can allow the fixation of a large tank with a short connection tube from the tank to the extruder head.

4.2.2 Influence of the inner shape of the nozzle and the extrusion flow rate on the aspect of the filament

The influences of the inner shape of the nozzle and the extrusion flow were evaluated on the aspect of the filament for (i) three nozzles characterized by the dimensions of their outlet channel: a diameter varying from 0.5 to 0.9 mm and a length varying from 0.3 to 1.5 mm (Figure 4-4.A) and for (ii) three linear extrusion flows varying from 5 to $30 \text{ mm} \cdot \text{s}^{-1}$. With these testing parameters, the maximum shear stress experienced by the paste (hypothesis of non-slip boundary condition) were ranging from 110 to 230 kPa, much larger than the yield strength of the paste which was about 6 kPa (section 3.3.1 p.107).

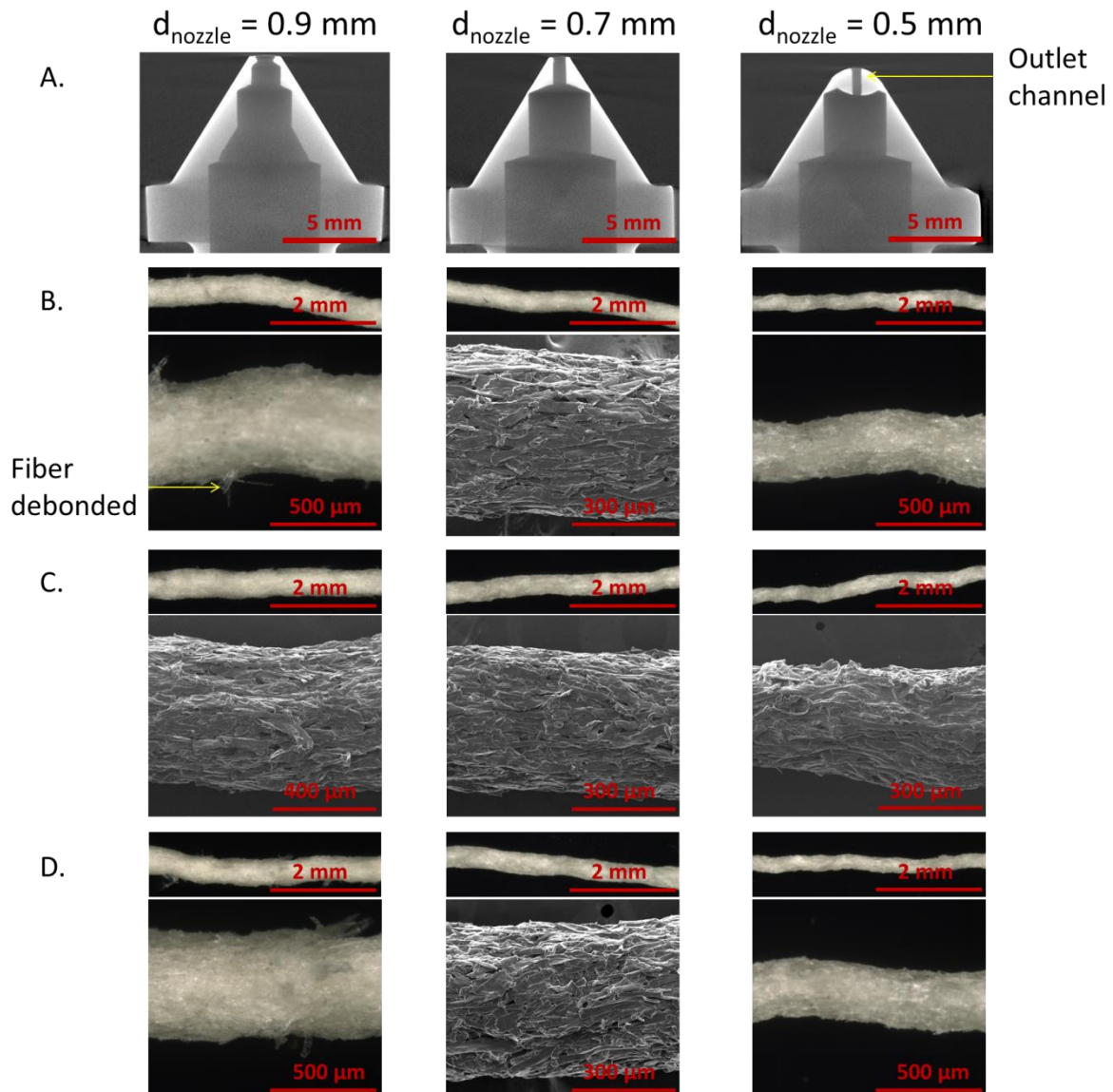


Figure 4-4. Influence of the inner shape of the nozzle and the extrusion flow on the aspect of the filament – (A) 2D view of a X-ray Computed Tomography (XCT) scan of the 3 tested nozzle: 0.9, 0.7 and 0.5 mm large nozzle. SEM images and snapped images with a binocular magnifier (x25 and x100) of the surface of a dried filament extruded through the 3 nozzles at a linear extrusion flow of (B) $5 \text{ mm}\cdot\text{s}^{-1}$ (C) $15 \text{ mm}\cdot\text{s}^{-1}$ and (D) $30 \text{ mm}\cdot\text{s}^{-1}$.

Figure 4-4.B-D show the surface of dried filaments extruded through the 3 tested nozzles (Figure 4-4.A) at 3 linear extrusion flows: 5, 15 and $30 \text{ mm}\cdot\text{s}^{-1}$. First, we can observe that whatever the linear flow rate, all the dried filaments present (i) fibers alignment in the longitudinal direction on their surface (as mentioned in section 3.3.3 p.109), (ii) surface roughness due to the fibers dimensions and, (iii) tortuosity. In particular, filaments extruded through the 0.9 mm diameter nozzle show fibers debonding and those extruded through the 0.5 mm large nozzle present more tortuosity. By focusing

on the length of the outlet channel of the 0.9 mm large nozzle, we can observe that its length is (i) in the same order of magnitude (about 0.3 mm) than the length of a part of fibers used (section 2.2.1 p.69) and, (ii) shorter than the exit diameter of the nozzle. On the contrary, the two other tested nozzles show an outlet channel length about 10 times longer than the cellulose fiber length and more than two times larger than the exit diameter. As a consequence, in addition to being a short outlet channel that can lead to surface fracture (see section 1.1.2.2.1 p.24), the 0.9 mm large nozzle allows the extrusion of fibers that present one end out of the nozzle and the other end before the constriction and not always in the outlet channel extension as cellulose fibers are flexible. In this case, the fiber is pulled outside of the nozzle without an enough long residence time to stick the other fibers. After its exit, the upper part of the fiber debonds from the extruded filament. This can happen for a bundle of fibers as illustrated in Figure 4-4.B. The diameter of the 0.5 mm large nozzle was about 10 times larger than the diameter of a part of the cellulose fibers used which was in the lower limit range to be compatible with fillers extrusion (section 1.1.2.1 p.21). Moreover, the inner shape of the 0.5 mm large nozzle is unusual with an inverted truncated cone before the outlet channel due to its manufacturing process: welding and drilling of an initial larger nozzle. These can lead to a non-optimal packing of the fibers in the outlet channel due to a dead zone too close to the screw. This non-optimal fiber packing might cause brief and localized filament diameter variations quite large regarding its diameter leading to tortuosity.

The quality of the extruded filament with the fibrous cellulose paste developed was affected by the inner shape of the nozzle. In the literature, conical nozzle or long cylindrical nozzles (6 to 40mm long) were used with cellulose based formulation for AM by extrusion (section 1.2.2.2 p.56). No fiber debonding was highlighted; moreover these nozzle shapes should promote a homogeneous flow. However, with these nozzles, the flow interruption by screw retraction was delayed as the paste between the end of the screw and the outlet of the nozzle was still pressurized with a pressure that overcomes the pressure loss of the nozzle, resulting in a residual paste flow. Yet, the flow interruption is crucial for accurate printing of parts that required extruder head travelling during the printing (oozing performance, section 1.1.2.3.1 p.30).

The inner shape of the 0.7 mm large nozzle seems to be the most suited nozzle for the fibrous cellulose paste developed. Therefore this latter is going to be used for most of the following printed parts, except when the part required a better resolution. In this case, the 0.5 mm large nozzle was used.

The tested flow rate does not seem to influence the microstructure of the dried filament. This statement was confirmed by results of Figure 4-5 that do not show any obvious evidence of a

correlation between the linear extrusion flow and the deformation after air drying of the filament, whatever the diameter of the nozzle is.

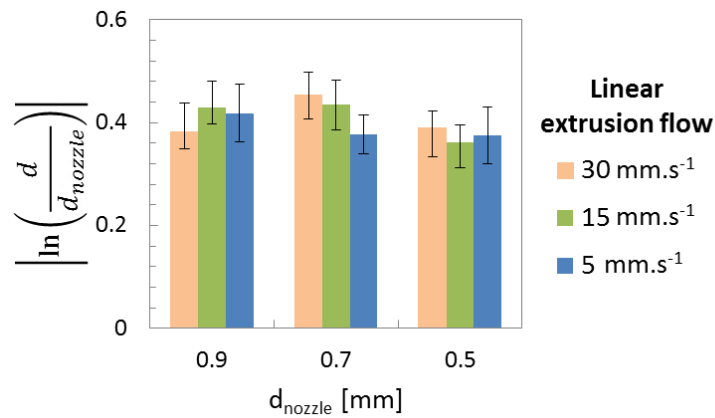


Figure 4-5. Influence of the nozzle shape and the linear extrusion flow on the diameter deformation of the dried filament. The error bars represent the standard deviation between the 15 diameters measurements performed on 5 tested samples for each condition.

4.2.3 Influence of the extrusion flow rate on the mechanical properties

To complete the influence of the extrusion flow rate and the inner shape of the nozzle on the microstructure of the filament, the influence of these parameters was evaluated on the mechanical properties of the dried filament.

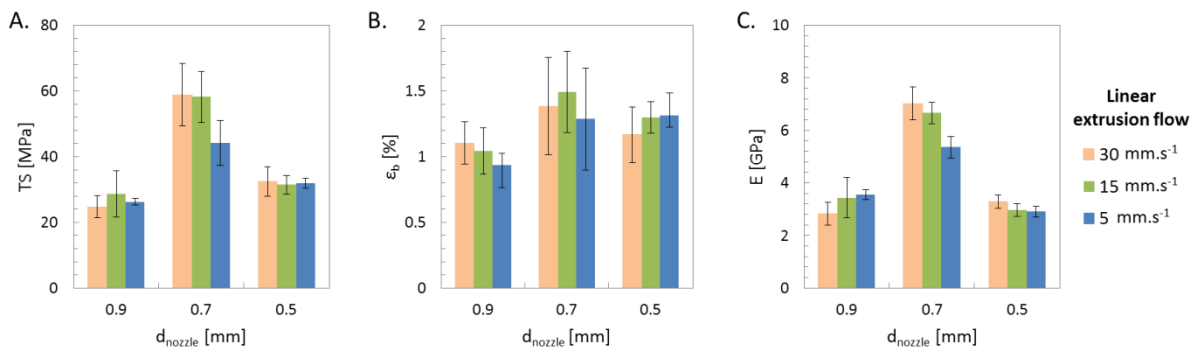


Figure 4-6. Influence of the extrusion flow rate and the inner shape of the nozzle on the mechanical properties – (A) Tensile strength, TS, (B) strain at break, ϵ_b and (C) Young's modulus, E.

Figure 4-6 shows the tensile strength, the strain at break and the Young's modulus obtained from tensile test on dried filament extruded at linear flow from 5 to 30 mm.s⁻¹ and through the three nozzles characterized by their inner shape (see Figure 4-5.A). As previously mentioned (section 3.3.4 p.113), the filament showed a brittle material strain stress curve. The same behavior was found for all the tested filaments.

The tensile strength of filament extruded through the 0.9 and 0.5 mm large nozzle was found to be around 27 and 32 MPa, respectively whereas, the tensile strength of the filament extruded through the 0.7 mm large nozzle was found to be two times larger than the smallest one, with a mean value around 54 MPa. The elongation at break was roughly the same ($\approx 1.2\%$) for every conditions tested (inner shape of the nozzle or the extrusion flow rate). However, the standard deviation was quite large. For the Young modulus, we obtained the same trend as the tensile strength (as we obtained the quasi same elongation at break and the filament present a typical behavior of a brittle material), with a Young's modulus about 3.3 and 3.1 GPa, for the 0.9 and 0.5 mm large nozzle, respectively and a Young's modulus twice as large as the previous ones for filament extruded through the 0.7 mm large nozzle with a mean value about 6.4 GPa.

An increase of the tensile strength and the Young's modulus with a decrease of the nozzle diameter was expected for the same linear flow rate since the shear stress increases with smaller nozzle diameter and longer outlet channel and favors the fibers alignment. However, as observed previously (section 4.2.2 p.126), the surface aspect of the filament was influenced by the inner shape of the nozzle. For the 0.9 and 0.5 mm large nozzle, the dried extruded filament present variation of the section due to the debonding of bundle of fibers or large tortuosity due to the small nozzle size compared to the cellulose diameter. This section reduction and tortuosity are weak points that can lower mechanical properties of the dried filament. Moreover, Figure 4-5 shows that the diameter deformation was about 0.32 for the 0.5 mm large nozzle whereas the deformation was larger for filaments that showed the best mechanical properties with a value of 0.36. This lower deformation was related to a larger porosity and maybe less fiber alignment that must lower the mechanical properties as well.

The linear extrusion flow rate does not seem to influence the mechanical properties of the 0.9 and 0.5 mm large nozzle whereas for the 0.7 mm large nozzle, the tensile strength and the Young's modulus of the filament extruded at a linear flow of $5 \text{ mm}\cdot\text{s}^{-1}$ are 44 MPa and 5.4 GPa respectively whereas they are about 30% larger for filament extruded at 15 and $30 \text{ mm}\cdot\text{s}^{-1}$. A larger extrusion flow rate and so larger shear stress should increase the fibers alignment and as a consequence improve the mechanical properties. Unlike the 0.7 mm large nozzle, this improvement was not noticed for filament extruded through the 0.5 and 0.9 mm large nozzle as the filament aspect was already damaged.

The parameters that affect the first step of AM by extrusion process, the extrusion step, were identified and assessed on the extrusion flow and the quality of the extruded filament (aspect and mechanical properties). What about the parameters that influence the deposition step?

4.3 Optimization of AM by extrusion settings to accurately produce more and more complex parts

The influence of the main extrusion settings was evaluated on the apparent accuracy and mechanical performance of different parts, from 2D to complex 3D parts in order to identify the best settings. Major variables were the layer height, the filament width, the extrusion multiplier and the infilled percentage.

For all the printing conditions, the same batch of paste colored with a dye was used. Moreover, the calibration factor remained constant as the required flows were in the range of its stabilization. In our analysis, we consider that the volume of the deposited filament (track) after extrusion, a 90° turn and deformation, was identical to the theoretical volume of paste calculating using the calibration factor.

4.3.1 Influence of the settings on 2D parts

The influence of the layer height, the filament width and the extrusion flow was assessed on the surface aspect of 2D parts (Figure 4-7.A) and their mechanical properties after air-drying. Only the longitudinal path orientation was tested since the poor adhesion between the deposited filaments after drying does not allow testing the adhesion force among juxtaposed filaments (transversal path orientation). The layer height, the filament width and the extrusion multiplier were evaluated for values ranging from 0.35 to 0.55 mm, 0.65 to 0.72 mm and 100 to 120% of the calibration factor, C , respectively with two or three levels of values.

These layer height values were equivalent to:

- 76 to 50% of the nozzle diameter
- 97% and 62% of the area of the outlet cross section of the nozzle with a filament width of 0.72 mm.

The filament width corresponds to 90 and 100% of the nozzle diameter. A larger filament width was not considered as we did not observe die swelling due to the large amount of inelastic fillers in the paste as Feilden, 2017 with its developed alumina paste.

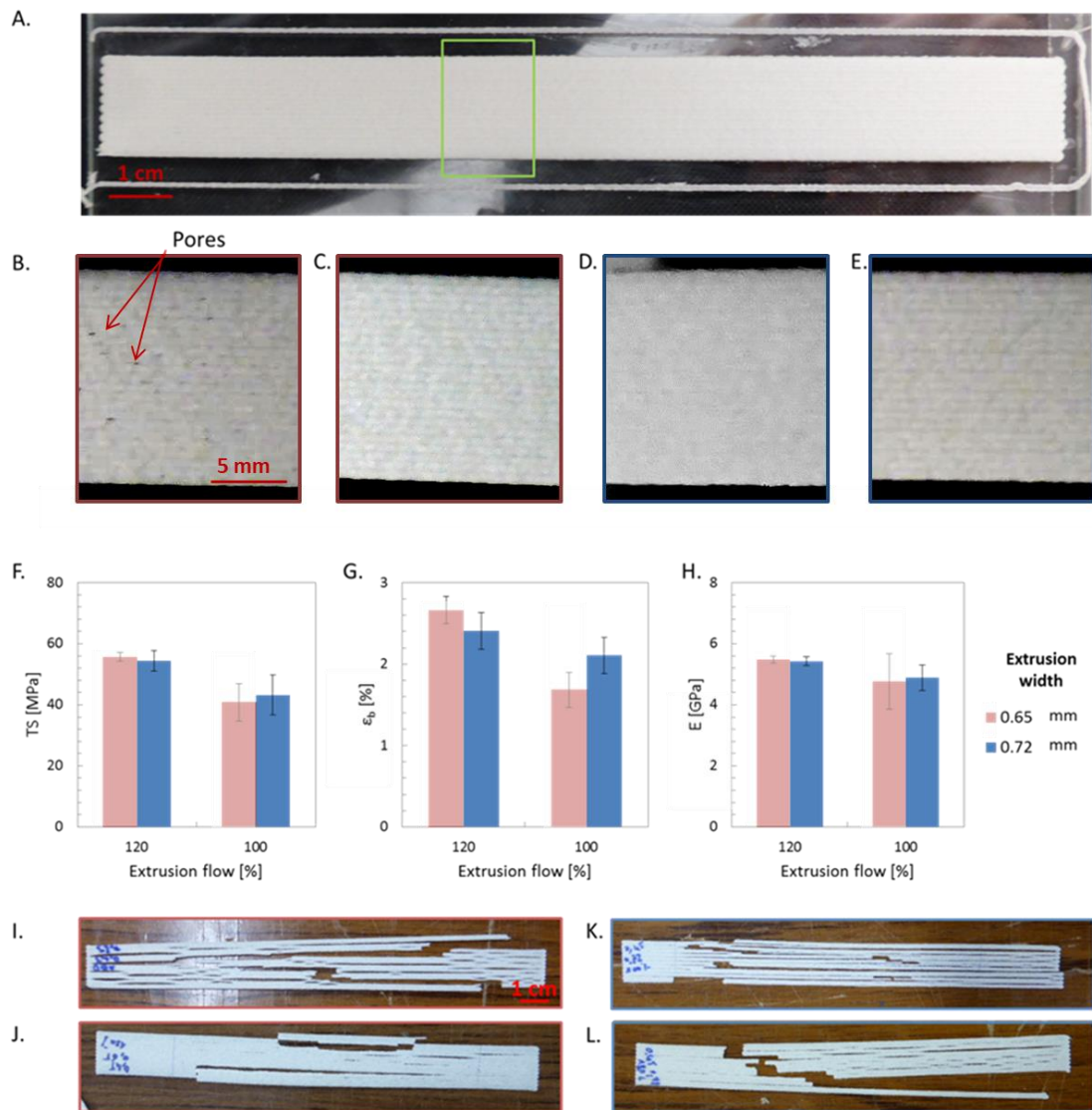


Figure 4-7. Influence of the filament width and extrusion flow on tensile test specimens: aspect and mechanical properties – (A) Whole fresh tensile test specimen ($1.4 \times 15.0 \times 0.1 \text{ cm}^3$) with longitudinal infill pattern and zoom of the sample printed with a filament width of 0.65 mm, 90% of the nozzle diameter (B,C) and 0.72 mm, the nozzle diameter (D,E) and an extrusion flow of 100% (B, D) and 120% (C and E). Plots of the tensile strength (F), elongation at break (G) and Young's modulus (H) obtained from tensile test on 3 dried specimens for each filament width (0.65 and 0.72 mm) and extrusion flow (100 and 120% of the calibrated one). Images of the specimen after performing the tensile test: filament width of 0.65 mm (I, J) and 0.72 mm (K, L) and extrusion flow of 100% (I, K) and 120% (J, L).

Figure 4-7. B-E show images of a part of the surface of a fresh tensile specimen (rectangular 2D form) printed with a layer height of 0.45 mm with different filament widths and extrusion flows. The tensile specimen was composed of 2 layers of 23 and 21 tracks in the longitudinal direction for the 0.65 and 0.72 mm filament width, respectively and was printed at $15 \text{ mm} \cdot \text{s}^{-1}$ which corresponds for the tested condition to a linear extrusion flow about $11 \text{ mm} \cdot \text{s}^{-1}$. Besides a low photo quality, pores

and filament tearing can be observed in the horizontal plane of the fresh 2D part printed with a filament width of 0.65 and a calibrated extrusion flow, whereas the 2D part with a larger extrusion flow and/or filament width does not show any of these pores. Indeed, since the flow was calculated for a filament width of 0.65 mm for a 0.72 mm large nozzle, the filament was stretched due to the under extrusion (-10%). It was found that the developed paste in its fresh filament state showed a tensile strength of 0.02 MPa and an elongation at break of at least 3% as the sample often broke in/near the clamps (section 5.3.3.1 p.168) at a constant stretch velocity 90 times lower than the printing speed, after 2 min of extrusion. However, no breakage during the printing was observed. This stretching due to under extrusion only weakens the filament by reducing its width at different locations leading to pores Figure 4-7.B. For the 2D part also printed with a filament width of 0.65 mm but with an over extrusion of 120%, the filament was not stretched anymore as the extrusion flow was larger than the one required for the nozzle size. Moreover, the filaments overlapped due to an actual deposited filament width of 0.72 mm and a rectilinear printing pattern with a width spacing of 0.65 mm. No pores can be observed in the horizontal plane. For the 2D parts printed with a filament width equal to the nozzle diameter and an extrusion flow equal or superior to the one required, the filaments were not stretched but juxtaposed without porosity in the horizontal plane in the wet state.

Figure 4-7. F-H show the mechanical properties (tensile strength, elongation at break and Young's modulus) of the dried tensile specimen printed with the settings described in the previous paragraph. The tensile curves are characteristics of a reinforced composite that shows a brittle material behavior and exhibits multiple ruptures. As expected, the samples that present pores before drying show the lowest apparent mechanical properties with a tensile strength, elongation at break and a Young's modulus of 41 ± 6 MPa, $1.7 \pm 0.2\%$ and 4.8 ± 0.9 GPa, respectively. The best apparent mechanical properties were reached by samples with the less apparent porosity after drying (filament width of 0.65 mm and an extrusion multiplier of 1.2 C) with a tensile strength, elongation at break and a Young's modulus of 56 ± 1 MPa, $2.7 \pm 0.2\%$ and 5.5 ± 0.1 and not for the samples with the largest shearing (filament width of 0.72 mm and an extrusion multiplier of 1.2 C). This lower apparent porosity for sample printed with an extrusion multiplier of 1.2 C is due to a filament that is more flatten when deposited than with an extrusion multiplier equal to the calibration factor (Serdeczny et al. 2018). While few pores are visible, these last values are similar to those obtained with tensile tests on filament extruded through the same nozzle while the elongation at break was a bit larger and the Young's modulus lower (section 4.2.3 p.129). No extensometer or camera monitoring were used to check the non-slip condition from the clamp that may occur during tensile tests.

- Among the two printing settings tested with the paste developed, an over extrusion flow was found beneficial to flatten the deposited filament, lower the apparent porosity and increase the shear rate and the mechanical properties. Whereas, a filament width lower than the nozzle diameter without an extrusion flow compensation can lead to filament breakage during the printing. So to assess the influence of the layer height, a filament width of 0.72 mm and an extrusion multiplier of 1.2 C was selected.

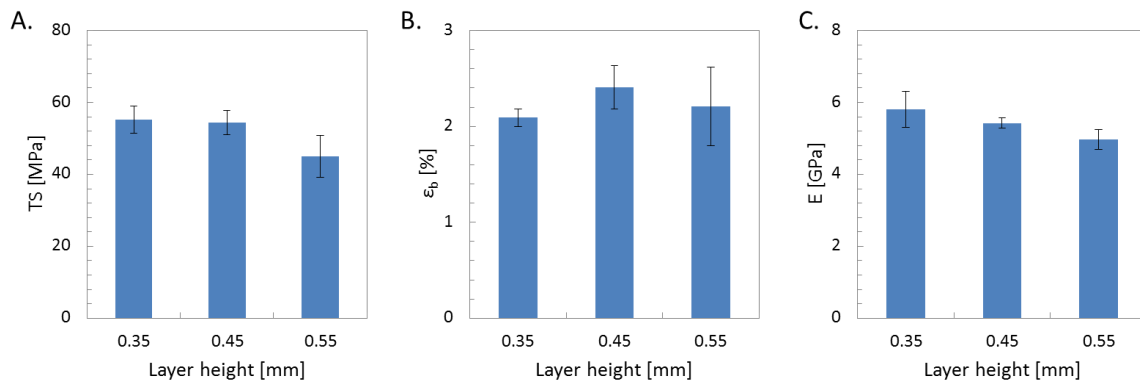


Figure 4-8. Influence of the layer height on the mechanical properties of 2 layers high tensile specimens ($1.4 \times 15 \text{ cm}^2$) with a filament width of 0.72 mm and an extrusion flow about 120% of the calibrated one – Plot of the tensile strength (A), elongation at break (B) and Young's modulus (C) obtained from tensile tests on 3 dried specimen for each layer height tested ranging from 0.35 to 0.55 mm.

Figure 4-8 shows the plot of the tensile strength, elongation at break and Young's modulus as a function of the layer height of a 2 layers high tensile specimen. The influence of the layer height on mechanical properties was less pronounced than the extrusion flow with a variation about -16% for the 0.55 mm layer height compared to the tensile strength and the Young's modulus of the 0.35 mm layer height. With fused filament fabrication, the influence of the layer height on mechanical properties varies as reported by Kuznetsov, Tavitov, et Urzhumtcev, 2019 due to absence of a common methodology to assess FFF printed parts strength and a broad range of parameters. It might come from a better filament squeezing of the second layer on the first one by the nozzle which might not be perfectly perpendicular to the build table and not by the flow rate which is proportional to the layer height. Indeed, a slightly larger resistance of the tensile specimen with a layer height of 0.55 mm was expected as the extrusion flow was larger for the same printing speed.

The layer height shows low influence on the mechanical properties of 2D parts. What about its influence on 3D part accuracy?

4.3.2 Influence of the settings on 3D printed parts

The influence of the layer height, the extrusion multiplier and the infill percentage were assessed on the accuracy of few 3D models selected to test the printing accuracy of the main elementary features that composed any 3D part such as described in chapter 1 (section 1.1.2.3.1 p.30). The selected 3D models studied herein are a 1.5x1.5x1.5 cm³ cube, a parallelepiped with an overhang angle of 35 and 45° to respect with the vertical plane, 4 cm high monofilament rectangular cuboid and 1.5 cm long bridge as presented in chapter 2 (section 2.3.4 p.79). Their accuracy was visually evaluated in the fresh state, just after printing and after air drying. However, as mentioned in chapter 3 (section 3.3.2 p.109), the filament shrink after air drying, the same result was expected for 3D part. The accuracy after drying deals with the absence of damage rather than the dimension stability (studied in chapter 5).

4.3.2.1 1.5x1.5x1.5 cm³ cubes for simple object printability

This part was designed for testing the printability of a simple object. However, a low infill percentage resulting in short spanning can be challenging. Figure 4-9 shows side and top images of two filaments thick walls cubes printed with a layer height of 0.45 mm, an extrusion multiplier of 1.0 and 1.2 times the calibration factor, C and an interior of the part filled at 35 and 100%. This range of infilled percentage was often advice in 3D printing websites to guarantee a successful printing with a solid apparent exterior and enough large mechanical properties. The lower the infill percentage, the faster the part is printed and the lighter the part is.

In the fresh state, all the printed cubes looked accurate and well printed apart the corners that were not as sharp as part manufactured by injection molding. It was due to the round and large nozzle exit (diameter of 0.7 mm). Only the cube printed with an infill of 35% and an extrusion multiplier equal to the calibration factor shows spacing between the top parallel deposited tracks. Indeed, the filaments that formed the top solid layer had to span across the hollow air pocket due to the 35% infill (with our settings, 1.34 mm spacing between two successive deposited filaments belonging to the same layer) without solid foundation to help squeezing the filament throughout its deposition to obtain a deposited filament with a height of 0.45 mm and a width of 0.72 since the paste remains in a fresh state. As a consequence, the filament was stretched throughout its spanning between the two filaments belonging to the previous layer, resulting in a thinner width and spacing between the top parallel deposited tracks.

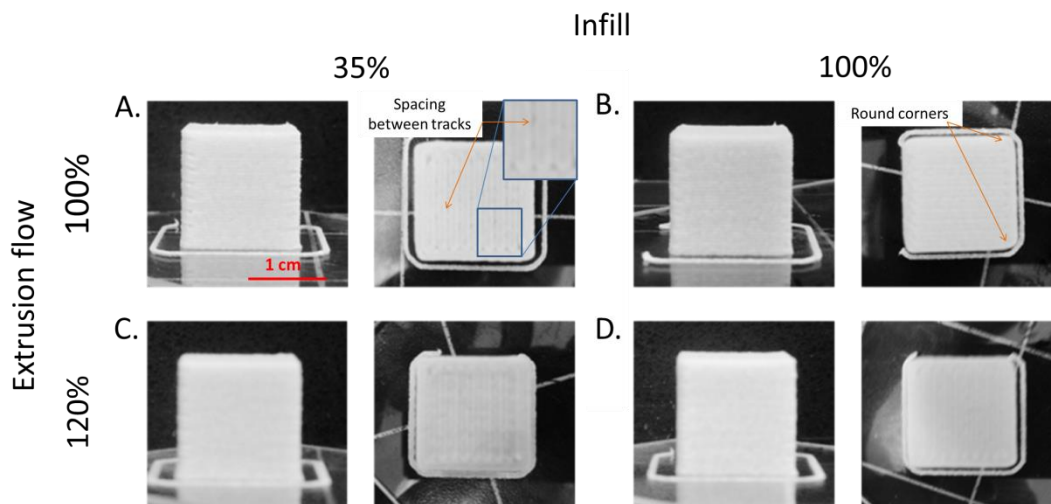


Figure 4-9. Influence of the extrusion flow on the accuracy of a 2 filaments thick wall cube with edges of 1.5 cm filled at 35 and 100% with a layer height of 0.45 mm to test printability of simple object – Side and top grey scale images of 3D parts printed with an extrusion flow of 100% (A and B) and 120% (C and D) of the calibrated one.

The same result was obtained with the 0.35 mm layer height cubes with a larger stretching of the filament that composed the two top solid layers of the cube printed with an infilled of 35% and an extrusion multiplier equal to the calibration factor (Figure 4-10.A). On the opposite, a collapse of the top solid layers was observed for the partially filled cube printed with a 0.55 mm layer height and an extrusion multiplier of 1.2 times the calibration factor (Figure 4-10.F). Indeed, as explained in the previous section (4.3.1 p.131), with a layer height of 0.55 mm and a filament width of 0.72 mm, equal to the nozzle diameter, the section of the deposited filament corresponds to 97% of the cross-section area of the nozzle, which means that with a calibrated extrusion flow, the filament was not stretched without support to squeeze it whereas with 1.2 time the calibrated extrusion flow, too much filament was extruded which filled the gap between the filaments of the 35% infilled layer leading to an apparent collapse of the two top layers.

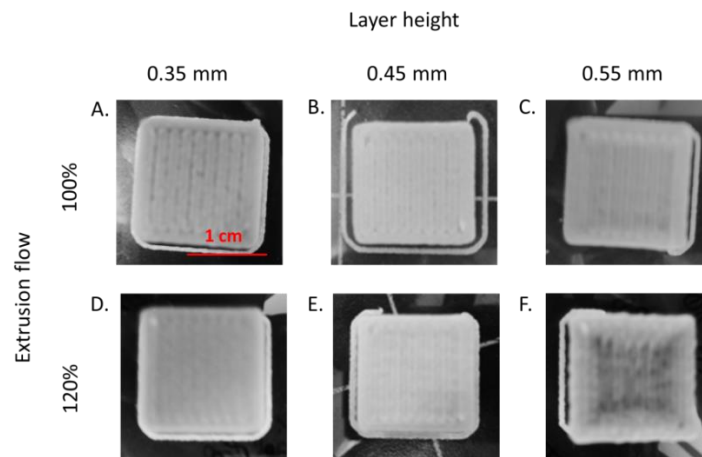


Figure 4-10. Influence of the layer height and the extrusion flow on the accuracy of a 2 filaments thick wall cube with edges of 1.5 cm filled at 35% to test printability of simple object – Top grey scale images of 3D parts printed with an extrusion flow of 100% (A, B and C) and 120% (D, E and F) of the calibrated one.

After air drying, Figure 4-11 shows that with an infill percentage of 35%, the part does not show any damage whereas with a 100% infill, at least three over the six printed cubes present large delamination with layer separation and splitting. Among these 100% infilled cubes, it seems that the cube with larger layer height and a 100% infill are likely to present delamination. It might come from the drying process gradient that induce an anisotropic strain and can lead to failure in bond adhesion. This drying process gradient is more important for 100% solid parts. However, with an over-extrusion (extrusion multiplier about 1.2 the calibration factor), the bonding between layers was larger and might resist to the force induced by the anisotropic strain. The drying and its consequence on simple 3D structure were studied in details in chapter 5.

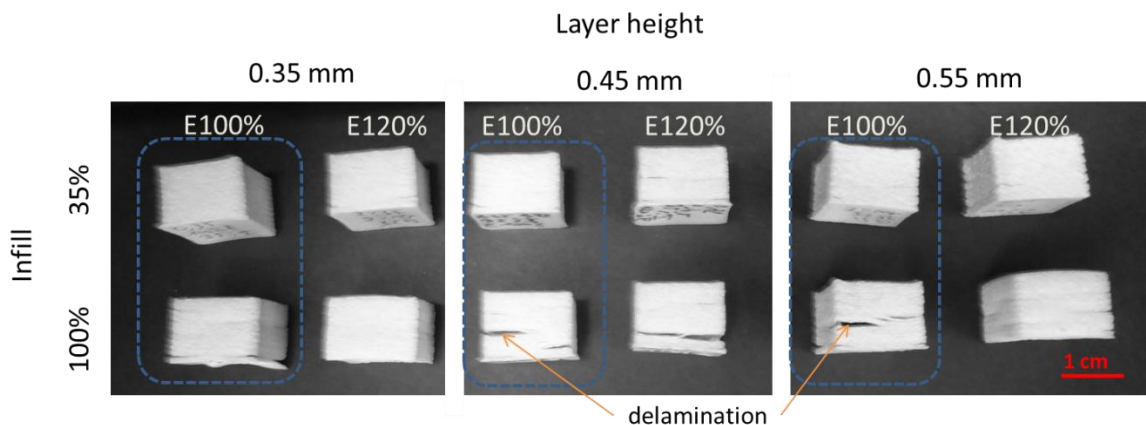


Figure 4-11. Influence of the layer height (0.35, 0.45 and 0.55 mm), the extrusion flow (100% and 120% of the calibrated one) and the infilled percentage (35 and 100%) on the accuracy (absence of damage) of a 2 filaments thick wall cube with edges of 1.5 cm after air drying.

- To print a simple and accurate structure with a solid exterior, a partially hollow part with two filaments thick wall and 4 top solid layers should be a good option.

4.3.2.2 Parallelepipeds with overhang of 35 and 45° to respect with the vertical plane for overhang performance

This part was designed for testing the overhang performance of the developed paste. The accuracy of the top solid layer was not considered anymore. As prescribed previously, the part was printed with a partially hollow structure, at 35% infilled.

Figure 4-12 shows the image of the fresh printed parts with an overhang angle of 35° and 45° to respect with the vertical plane for the three layer heights and the two extrusion rates considered. Only Figure 4-12.F and I show the other side of the printed part. On these images, we can see ripples. These ripples were present on all the printed parallelepipeds. It was due to the printing path that started and finished the outer perimeter at this specific point on each layers.

When overhang angles were printed, the filament was only partially supported by the layer below: one transversal part of the filament is offset (exposed to air) and unsupported. The ratio between the unsupported transversal part of the filament, x , and the filament width, w , increases with the layer height, h , and the overhang angle to respect with the vertical plane, θ , for a define filament width (Figure 4-12.A, B and C). By assuming that the cross section of the deposited filament is a square, this ratio, $\frac{x}{w} = \frac{htan(\theta)}{w}$ varies from 0.34 to 0.76 with the layer height and overhang angles tested. Figure 4-12.E, F, H, I Q and R show good accuracy of the printed part. For these parts, at least 50% of the filament was supported by the previous layer with a layer height of 0.45 and 0.35 mm. Figure 4-12.N and Q show quite good accuracy of the printed part as we can observe a slight sagging of the filament in the overhanging face although only 37% of the filament was supported by the previous layer. These parts were printed with a layer height of 0.45 mm and an extrusion flow about 1.0 to 1.2 times the calibrated one. Figure 4-12.D, G, M and P show sagging and stringy mess on the overhanging face that increase with the height. These parts were printed with a layer height of 0.55 mm and showed an apparent 47 and 24% of filament supported by the previous layer. The sagging of the filament located on the overhanging phase increased when the extrusion flow varies from 100% to 120% of the calibrated one.

When less than 50% of the filament is supported by the previous layer, $\frac{x}{w} < 0.5$, it means that the center of gravity of the filament is still supported by the previous layers which help the extruded filament to turn 90° and be deformed. It should not lead to sagging while the filament itself does not collapse under its own weight. However, when more than 50% of the filament is supported, it does not lead automatically to sagging as shown by Figure 4-12.N and Q. Indeed, before being offset in the

overhanging face, the filament is vertically aligned with the above layers and as a consequence it is stable. Then, the challenges dealing with a quasi-non-supported filament are basically the same as those of bridging presented in the following sub section of this chapter (section 4.3.2.4 p.143). However, unlike bridging, when the filament of one layer starts sagging, the sagging process increases in part damage.

- To conclude, choosing printing parameters such as $\frac{w}{h} > 2\tan(\theta)$ with h the layer height, w , the track width, θ the overhang angle to respect with the vertical plane guarantee an accurate printing of the overhang. However, using parameters that does not respect this inequality is not sufficient to predict the failure of the overhang of the printed part.

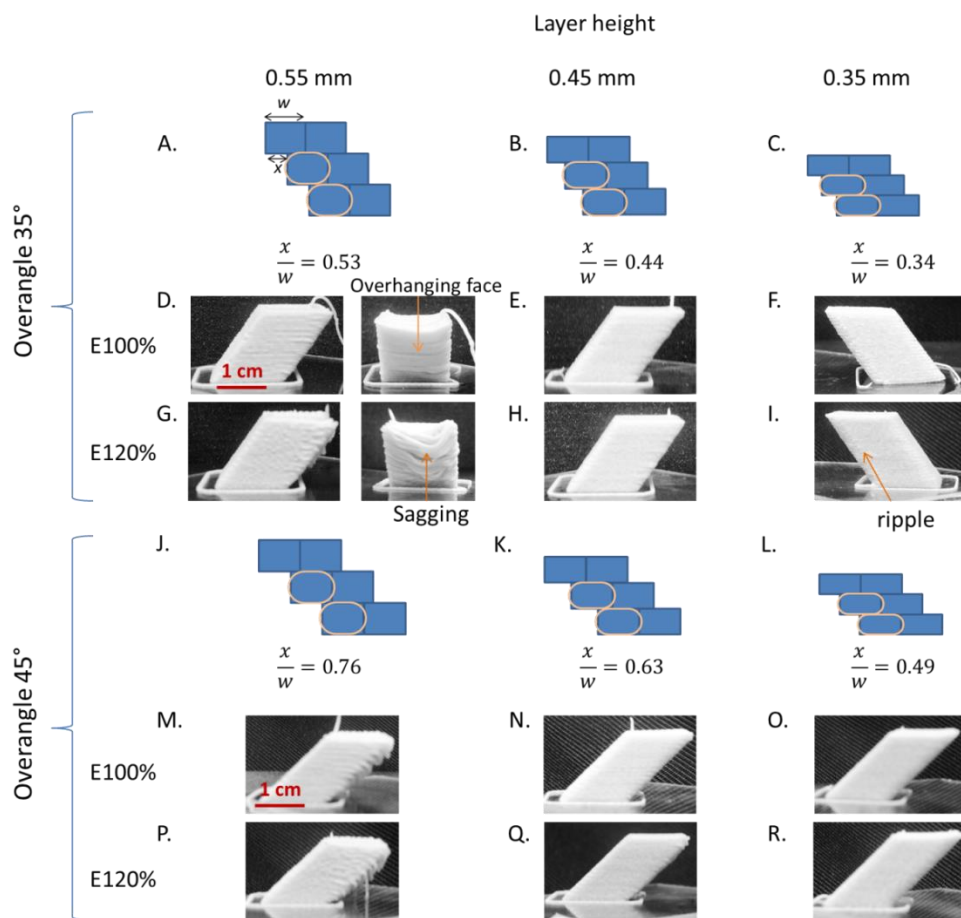


Figure 4-12. Influence of the layer height and the extrusion flow on the accuracy of a 2 filaments thick wall parallelepiped with a 1.5x1.5 cm² base filled at 35% with overhang angle of 35 and 45° to respect with the vertical plane to test the overhang performance – (A, B, C, J, K and L) Schematic view of the cross section of the two filaments that composed the wall of the 3D part in the overhang area with the calculated ratio of unsupported filament due to the overhang. Side grey scale images of 3D parts printed with an extrusion flow of 100% (D, E, F, M, N and O) and 120% (G, H, I, P, Q and R) of the calibrated one.

After air drying, Figure 4-13 shows that almost all the printed parts show delamination except the parallelepipeds with an overhang angle of 35° printed with a layer height of 0.35 mm. Indeed, unlike the filaments that composed the wall of the 35% infilled cube, these filaments do not completely stack on each other. The contact area between two filaments belonging to two successive layers was reduced and maybe its bonding quality. As a consequence, the bonding strength to resist at the force induced by the anisotropic strain was reduced. This lower bonding strength resistance induces delamination for any part that present non straight walls and not only part with overhang. This issue came from the layer by layer in one direction process. To overcome this issue and increase the print quality, software and printer were developed to print on inclined surface (B. Huang et Singamneni, 2012).

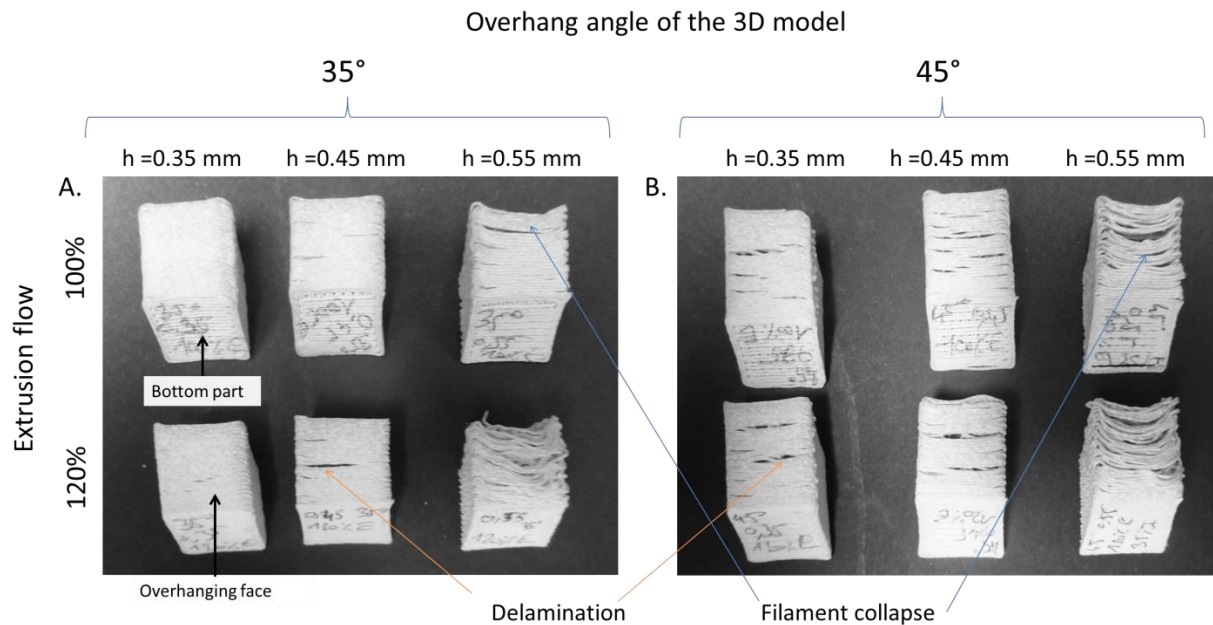


Figure 4-13. Influence of the layer height and the extrusion flow on the accuracy of a 2 filaments thick wall parallelepiped with a $1.5 \times 1.5 \text{ cm}^2$ base filled at 35% with an overhang angle of the initial 3D model of 35° (A) and 45° (B) to respect with the vertical plane after air drying.

- To print an accurate structure with overhang angle, a thin layer height and a thicker wall (3-4 filaments large) should be a good option to increase the area of contact between filaments belonging to two successive layers which contribute to increase the bonding strength between them. Moreover, as the part exhibits height strain after air drying (details in the following chapter), the dried current overhang angle is larger. For example, if the part exhibit a height decrease about 30%, the overhang angle vary from 35° for the 3D model to 45° for the dried part.

4.3.2.3 4 cm high monofilament rectangular cuboid for vertical stacking performance

This part was designed for testing the vertical stacking performance of thin wall. Figure 4-14 shows the images of fresh monofilament rectangular cuboid with different layer heights (0.35, 0.45 and 0.55 mm) and extrusion flows (100 and 120 % of the calibrated one). While there was a low contact surface area (58 mm²) between the build platform and the first layer, there was a good adhesion during printing whereas for the FFF printing of thermoplastics, care must be taken to obtain a good adhesion (such as the temperature of the build platform) (Spoerk, Gonzalez-Gutierrez, et al. 2018). Moreover, all the bottom parts of the printed parts present an accurate stacking of the filaments (Figure 4-15). However, when we looked at the whole 4 cm high part, we can observe that only two parts were accurately printed: the one with a layer height of 0.45 mm and an extrusion flow of 1.2 times the calibrated one (Figure 4-14.E) and the one with a layer height of 0.55 mm and an extrusion flow of 100% of the calibrated one (Figure 4-14.C). The printed part with a layer height of 0.35 mm and a calibrated extrusion flow (Figure 4-14.A) shows a vertical sagging of the structure whereas with a larger layer height (0.45 mm)(Figure 4-14.B) or a larger extrusion flow (1.2 times the calibrated one)(Figure 4-14.D), this sagging was minimized. The part printed with a layer height of 0.55 mm and an extrusion flow of 1.2 times the calibrated one shows filament sagging in the wall and vertically aligned edges (Figure 4-14.F).

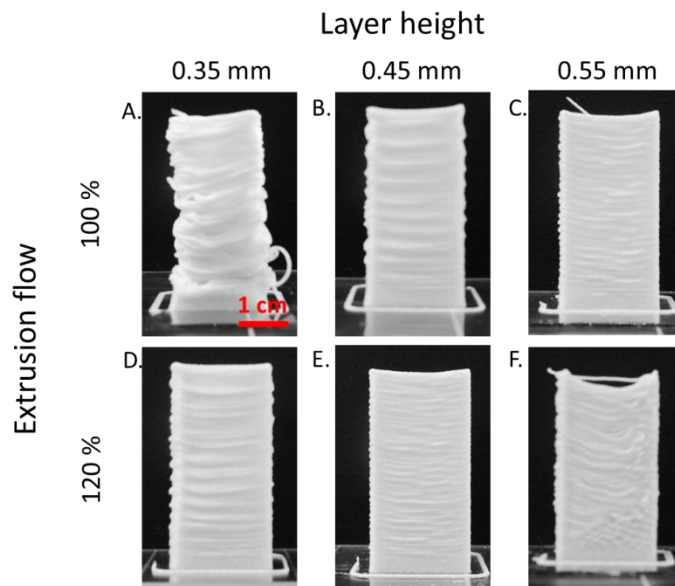


Figure 4-14. Influence of the layer height and the extrusion flow on the accuracy of a 4 cm high monofilament rectangular cuboid to test the vertical stacking performance of thin wall – Side grey scale image of 3D parts printed with an extrusion flow of 100% (A, B and C) and 120% (D, E and F) of the calibrated one.

All these parts should not collapse under their own weights, as the paste presented a yield stress of $\sigma_y = 5.6$ kPa (section 3.3.1 p.107) that could be overcome only if this part was 48 cm high ($L = \frac{\sigma_y}{\rho g}$ with $\rho = 1.2$ kg.m⁻³), which cannot be printed in the build chamber of the printer used.

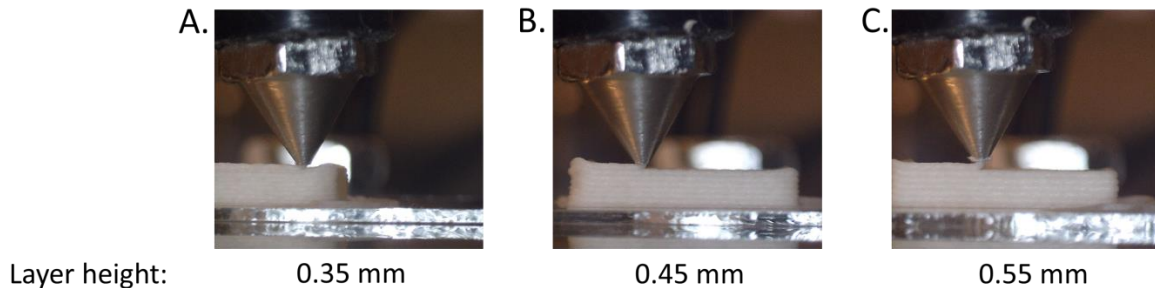


Figure 4-15. 4 cm high monofilament rectangular cuboid during its printing with a layer height of (A) 0.35, (B) 0.45 and (C) 0.55 mm at calibrated extrusion flow rate.

During the printing of parts that show a vertical sagging, a motion of the corners drag by the extruder head during deposition can be noticed as experienced by Alghamdi, Nair, et Neithalath, 2019 and Buswell et al. 2018. This drag force might come from a stretching of the filament. This stretching is initiated by a too large gap between the previous layer and the nozzle that cannot be filled by the paste being extruded as the extrusion flow rate was calibrated to extrude the right amount of paste calculated from the settings (layer height, filament width and printing speed). It can be due to a slight buckling of the thin wall that did not resist to the force applied by the deposition of the filament (Suiker, 2018) or a slight deviation of the extruder head position during the printing of the layers. When the height of the part was small enough, this phenomenon was reduced (Figure 4-15) and the corner might be able to resist to this drag force. Increasing the extrusion flow or the layer height reduce the stretching of the filament caused by the same vertical height loss. However, when the linear extrusion flow rate of the paste through the nozzle exceeds the printing speed without solid foundation, filament sagging in the wall can be observed.

With FFF, the vertical stacking performance is larger due to a rapid solidification of the thermoplastic after its deposition and a possible lower viscosity of the melted thermoplastic in the nozzle that reduce the drag force.

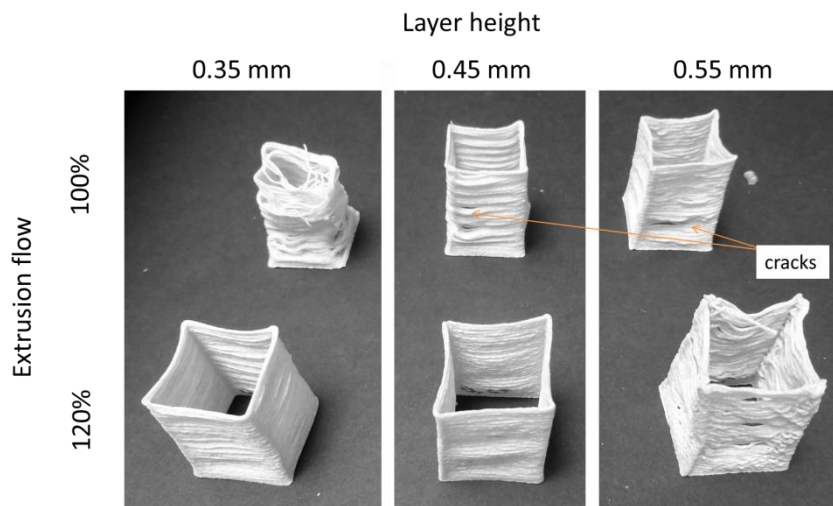


Figure 4-16. Influence of the layer height and the extrusion flow on the accuracy of a 4 cm high monofilament rectangular cuboid after air drying.

After air drying, Figure 4-16 shows that almost all the printed parts present few cracks. Indeed, due to the vertical sagging and filament sagging, it was possible that a part of a layer presents no contact adhesion or a reduced one with the previous layer compared to the above layer leading to crack after drying due to the shrinkage of each filament and a lower drying rate of the corner.

- To print an accurate one filament large thin wall structure, a layer about 60% of the nozzle diameter with a larger extrusion flow to reach almost the same extrusion linear flow as the printing speed should be a good option to avoid filament stretching and its resulting force in case of a slight vertical height deflection and to favour the contact adhesion between layers. A 8 cm high model was accurately printed as well as a 4 cm high model with 4 cm side length with the optimized settings.

It should be noticed that with two filaments large thin wall structure with a 0.5 mm large nozzle diameter, the vertical sagging was minimized.

4.3.2.4 1.5 cm long bridge for bridging performance

This part was designed for testing the bridging performance of the developed paste with only one bridging layer, the most challenging one. Indeed, for the printing of several layers thick bridge, it should be noticed that, only the first layer is suspended in the air. This last one serves as a foundation for the above layers, even in case of a slight sagging, resulting after a certain thickness on good surface finish of the top layers (Fernandez-Vicente, Canyada, et Conejero, 2015). Moreover, the filament was well bonded to the bridge pillars before being suspended in the air.

Figure 4-17 shows the images of fresh 1.5 cm long bridge with different layer heights (0.35, 0.45 and 0.55 mm) and extrusion flow rates (1.0 and 1.2 times the calibrated one). The printed bridges show three different behaviors just after printing for the filaments that compose the unique layer of bridging: breakage (Figure 4-17.A and D), perfectly horizontally aligned (Figure 4-17.B) and vertical sagging (Figure 4-17.C, E and F) mainly due to a flow rate adjustment. Indeed, once the part was completed, the bridge remained in its initial and fresh shape due to the paste characteristics, such as restoring its strength just after exiting the nozzle and a stress level resulting from the part design below the yield stress, $|\sigma_y|$, of the developed paste in its fresh state as measured in chapter 3 (section 3.3.1 p.107). Indeed, by using the Euler-Bernoulli beam theory and assuming that the filament behaves as a straight beam clamped at its extremities under its own weight, the maximal tension-compression stresses in the filament (located at its extremities) was $|\sigma_{max}| = \frac{2\rho g L_f^2}{3d}$ varying from 2.5 to 3.1 kPa, which is below the value of 5.6 kPa, the paste yield stress calculated with the density, $\rho = 1.2 \text{ g.cm}^{-3}$, the standard gravity $g = 9.81 \text{ m.s}^{-2}$, the span distance $L_f = 15 \text{ mm}$ and the diameter of the filament d , ranging from 0.56 to 0.72 mm (due to the layer height variation of the printing settings).

The filament breakage occurred only for the thinner layer height (0.35 mm): in the middle of the bridge for the calibrated extrusion flow rate and near the bridge pillars for only one out of the seven filaments for the bridge printed with over-extrusion parameter. Indeed, the section of the extruded filament was thinner on the pillars as well as on the bridging part. However, on the pillar the filament was turned 90° and squeezed to flatten it on the previous layer whereas on the bridging part, the filament was turned 90° but the cross section of the filament was kept round due to the absence of foundation. As a consequence, the filament was stretched during bridging (during 1 s) at 37% and 25% with the 1.0 and 1.2 times the calibrated extrusion flow rate, respectively. This 37% of stretching was too large for the filament to resist rupturing, whereas at 25%, only one extremities of a bridging filament, transition between squeezed filament at 0.35 mm layer height and stretched one, broke.

The perfectly aligned filament for the bridging occurred only for the 0.45 mm layer height with the calibrated extrusion flow rate. During the bridging, the filament was stretched at 20% which allow a perfectly horizontal transition between the squeezed filament at a layer height of 0.45 mm and the stretched one.

The vertical sagging occurred for the bridge printed with a layer height of 0.45 mm with over extrusion (1.2 times the calibrated extrusion flow) resulting in 4% stretching of the filament and with layer height of 0.55 mm with an extrusion flow rate of 100% and 120% of the calibrated one resulting in 2% and no stretching (17% of extra filament extrusion). The sagging was larger in Figure 4-17.E

than in Figure 4-17.C whereas the stretching was also larger. It might come from a larger pressure in the nozzle due to the over extrusion during the printing of pillars that decrease during the suspended part of the bridge and lead to a larger extrusion flow. However, the slight sagging of Figure 4-17.C was surprising due to the presence of a slight stretching and an enough large yield stress just after deformation. The extrusion flow rate was maybe not perfectly calibrated as the same bridge was perfectly printed at $10 \text{ mm}\cdot\text{s}^{-1}$ with a layer height of 0.4 mm and a filament width of 0.5 mm equal to the nozzle diameter corresponding to equivalence between the cross section area of the nozzle and of the deposited filament leading to no filament stretching (Thibaut et al. 2019).

The bridging performance of the developed paste relies on (i) a good balance of the extrusion flow to avoid rupture and sagging and (ii) a limitation of design (span distance) based on the yield stress value of the paste whereas for the FFF process, the main challenge rely on the rapid solidification of the paste to recover high mechanical properties and avoid dropping (Jiang et al. 2019).

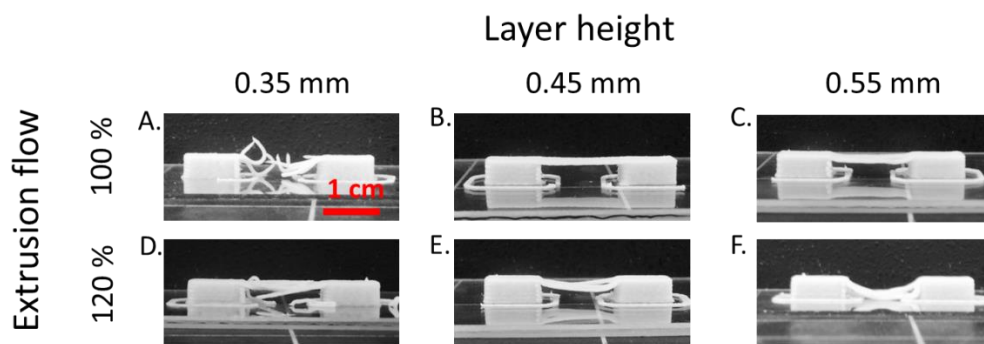


Figure 4-17. Influence of the layer height and the extrusion flow on the accuracy of a 1.5 cm long bridge to test the bridging performance – Side grey scale image of the 3D parts printed with an extrusion flow of 100% (A, B and C) and 120% (D, E and F).

- To print an accurate 1.5 cm long bridge with the developed paste, a filament stretching about 20% or less to avoid filament dropping and a layer height thick enough to resist the stretching without breaking at the weak point between supported and non-supported filament. A 3 cm long bridge was well printed with the optimized settings. However, two out of the seven filaments that constitute the bridge broke during drying.

From the screening and the evaluation of the printing parameters on the main 3D models features, the best practices guideline shows that the printing settings should be adapted for every feature to avoid part damaged with the developed paste. Moreover, few design limitations were point it out due to the rheological paste properties (bridging length, maximum weight on the first

layers linked to the 3D model height for example) provided precise settings (such as for thin wall and bridging performance). However, the drying gradient process and the large anisotropic strain upon drying induced delamination that can lead to design limitation or add design constraints such as a tool path optimization.

4.3.3 Printability of a complex model in the fresh state

To evaluate the printability of the paste with a more complex model that gathers different elementary features (overhang angle, bridging, pillar with small cross section, start and stop of the flowrate) and a larger printing time (over 1 h), we selected the 3D Benchy model (Figure 4-18.A and B). However, only one set of printing settings were chosen to print it as described in chapter 2 (2.3.4 p.79).

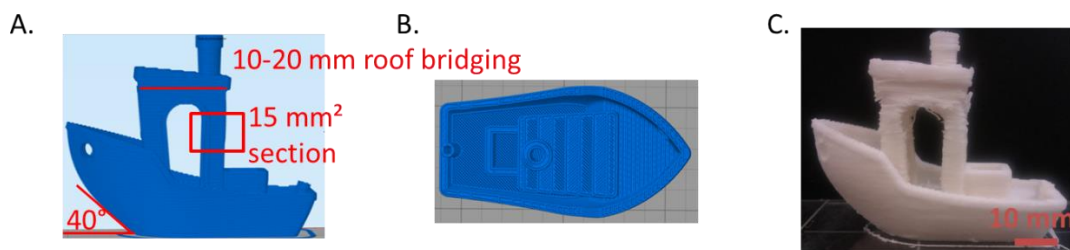


Figure 4-18. 3DBenchy download from (Thingiverse.com, 2018) – (A) Side and (B) top view of the sliced model, (C) Side view of the 3D printed model with fibrous cellulose based paste just after completion.

Figure 4-18.C shows that the 40° overhang angle to respect with the horizontal plane of the 3DBenchy using a nozzle diameter of 0.5 mm, and a layer height of 0.3 mm (i.e. 70% of the width of the filament is unsupported), exhibited no apparent defects besides non optimal parameter. Indeed, this overhang angle was sharp unlike the planar overhang angle of the parallelepiped tested in the previous section which reduces the height of the potential sagging and apparent defect. However, the four 10 cm high pillars with small sections (<math><15\text{ mm}^2</math>) were not printed well. Indeed, the pillars were flexible and moved with the printing head (Figure 4-19), resulting in crooked pillars. The deposition start and stop of the pillar with filament breaking show the maximum deflection that increase with layer height. However, when the 4 pillars were connected, it required several layers (~5) to stiffen the structure and allow printing without defects. Indeed, unlike thermoplastics that become rigid upon cooling, the paste used herein requires drying to become stiffer to resist rapid motion of the nozzle on small surfaces. However, parts that show similar challenge than these 4 pillars were printed with nanocellulose paste without defect (V. C.-F. Li et al. 2017). An optimization of the printing parameters can be performed to reduce this defect. For instance, an optimization of the printing path by printing several layers on one pillar before printing another one to reduce the back and forth of the nozzle on the flexible pillars can be considered. The bridging between the wall

and the roof of the boat cabin shows sagging due to a gap between the perimeter shell (the wall) and the bridging filament (the roof). Indeed, the bridging filament quite bond to the shell and detach due to the back-and-forth pattern leading to sagging. However, after several layers, sagging decrease until it allows printing without defects.

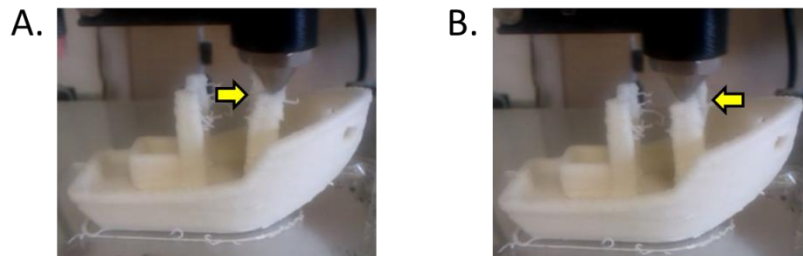


Figure 4-19. Printing of the 3D Benchy model and pillars motion with the print head from right (A) to left (B).

4.4 Conclusion

The present work identified among the printing settings (software) and the available printer technologies (hardware) the main factors that promote or prevent the manufacture of an accurate 3D part. The manufacturing of accurate 3D part can be decomposed in three key steps. The first one has to be mastered to move to the next step:

- Extrusion flow accuracy within the range of utilization: its precise control was provided by (i) the extrusion head based on a screw driven device filled with the fibrous cellulose paste contained in an air-pressurized tank, (ii) a constant extrusion efficiency while the exit flow rate of the tank was large enough, (iii) a calibration factor to measure, (iv) a specific inner shape of the nozzle with a gradual reduction of its section area that ended with a enough long channel with a constant section area to favor the fiber alignment in order to avoid flow disruption and (v) an efficient cleaning of the 3D printing environment (extrusion head, tank, mixing device...) promoted by the water dissolution of the paste to avoid clogging with too large solid particles.
- Precise deposition of the track within the layer: a good calibration of the printer such as the motion of the extruder head and a parallelism between the extruder head and the build platform was achieved.
- Manufacturing 3D parts: the selection of the printing settings such as the layer height, the track width and the extrusion rate to 3D print accurate 2D and 3D forms with simple shape, overhang angle of 35° or 45°, thin features with aspect ratio or bridging features were summarized in Table 4-1. This table synthetize the printing settings guideline and design

limitations such as thin and high elements for manufacturing complex part that can be splitted into different elementary features as described above.

The challenges for reaching part accuracy were linked to the deposited paste properties which were different from thermoplastics ones: (i) the paste harden after drying, a quite long process (see following chapter), (ii) the paste present a brittle behavior even in its fresh states and (iii), the paste present large strain after drying. By applying this guideline, a complex model was printed to illustrate the potential and limitation of the fibrous cellulose paste.

The study of the stop and initiation of the paste flow could be address in a more detailed study. Indeed, during the 3D printing of part, the start-stop events can frequently happen depending on the 3D model.

Likewise, the impact of many other factors on the accuracy of the 3D printed part would have been relevant to study such as the influence of the cellulose paste temperature (from 5° to 30°C for example) and the optimization of the printing path. Likewise, the implementation of a method to evaluate the adhesion in the fresh state between filaments as a function of the printing settings would have been relevant in the printing settings guideline with design limitation.



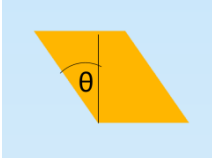

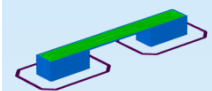

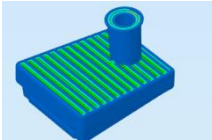
3D features	Printing parameters		Design limitation and comments
	Accurate printing	Dried part without damage	
Dense simple 2D feature 	Layer height: $h < \frac{d\pi}{4}$ Track width: d Extrusion multiplier: $1.0C$ to $1.2C$	-	Dried part not completely dense – porosity between filaments belonging to the same layer
Simple 3D feature 	Layer height : $h < \frac{d\pi}{4}$ Infill %: 35 to 100 Top solid layer: at least 2 Extrusion multiplier: $1.2C$ for layer height $< 0.8 \frac{d\pi}{4}$ $1.0C$ for layer height from $0.8 \frac{d\pi}{4}$ to $\frac{d\pi}{4}$	Limitation of the infill % (ex: 35%) 4 top solid layers (different rectilinear infill angle)	Limited porosity of the top solid layer due to a dense network
Overhang angle, θ 	Layer height: $h < \frac{d}{2 \tan(\theta)}$, for h up to $\frac{d}{\tan(\theta)}$, see bridging parameters Extrusion multiplier: $1.0C$ to $1.2C$ for layer height $< 0.8 \frac{d\pi}{4}$ For larger layer height, favor $1.0C$	Favor layer height: $h < \frac{2d}{3 \tan(\theta)}$	Due to height strain of the part, the dried part exhibit a larger overhang angle
Thin wall 	For 1 filament thick wall Layer height: $h = \frac{\pi d E}{4 C}$ Extrusion multiplier: $E = 1.0C$ to $1.2C$ For 2 filament thick wall see simple 3D feature	Few delamination for 1 filament thick wall, favor a thicker wall or smaller nozzle size	Interesting for printing support structure
Bridging 	Layer height: $h = \frac{\pi d E}{4 C} > h_{min}$ to resist stretching Extrusion multiplier: E about $0.8C$	OK	
Multiple start and stop extrusion events 	To optimized	To optimized	Can cause crooked feature on thin pillars. Addition of a vertical lift of the nozzle
Small contact area on a 3D printed part 	To optimized	To optimized	Printing parameters to study to improve the adhesion between the small feature and the part

Table 4-1. Synthesis of the printing parameters to use for an accurate printing and dried part without damage of the developed high solid content paste – d is the nozzle diameter, h is the layer height, E is the extrusion multiplier and C is the calibration factor

Chapter 5. Study of the drying toward the manufacturing of an accurate dried 3D printed part

5.1	Introduction.....	151
5.2	Toward optimization of ethanol drying conditions	152
5.2.1	Influence of the ethanol concentration during ethanol drying.....	153
5.2.2	Optimization of the immersion time during ethanol drying.....	154
5.2.3	Guideline for ethanol bath.....	157
5.3	Drying of a filament, building block of the 3D printed structure	158
5.3.1	Temporal evolution of the filament	159
5.3.2	Influence of the environmental conditions	164
5.3.3	Temporal evolution of the mechanical properties	168
5.4	Drying of a cube, a simple 3D structure.....	172
5.4.1	Validation of the experimental set up	172
5.4.2	Temporal evolution of the cube at macroscopic scale	174
5.4.3	Temporal evolution of the cube at filament scale.....	182
5.5	Compensation strategy	184
5.6	Conclusion.....	185

5.1 Introduction

One key aspect of the printed parts with the developed paste is that the paste contained more than 50 wt.% of water which is equivalent to almost 70 vol.% and evaporated during drying. Drying plays a major role in the accuracy and the non-damaging of the 3D printed part with aqueous ink or paste made of solid particles (cellulose, ceramic, graphite...) as seen in the “state-of-the art” chapter.

As described in chapter 1, the main drying technologies available for aqueous suspension or paste are air drying, oven drying, solvent exchange drying and freeze-drying. For Additive Manufacturing (AM) by extrusion 100% cellulose based ink, the larger solid content used was about 20 wt.%, (i.e, 14 vol.%) with the objective to produce porous parts with high added values (G. Siqueira et al. 2017; Hausmann et al. 2018; V. C.-F. Li et al. 2017; C. Jia et al. 2017; Klar et al. 2017). Simple air drying of ink with solid content about 20 and 2 wt.% lead to a volume reduction about 1/5 with few damages (Klar et al. 2019) and to a dried part that cannot be recognize in term of 3D structure and dimensions (Håkansson et al. 2016), respectively and few pores. Most often, the cellulose based parts were freeze-dried to preserve the 3D structure and the dimensions at the expense of mechanical properties due to the highly porous part. Solvent exchange with less and less polar solvent preserve the 3D structure with a reduction of the dimensions for a low solid content (2 wt.%) (Håkansson et al. 2016). The ethanol bath was the first bath used over the three.

To overcome the cost of the freeze-drying process, the focus was made on air-dried processes where the water or the solvent undergoes a vaporization process. During the drying by vaporization process of material made of solid particles and liquid, the part is subjected to diffusion of liquid from the inside to the outside by the Darcy’s law in response to the pressure gradient due to large drying strengths (capillarity pressure, osmotic pressure, disjoining pressure and moisture stress) (Scherer 1990). The diffusion and the vaporization of the liquid coexist during drying. However, the ratio between these two rates varies along the drying and allows the identification of at least two drying periods over the four drying periods generally identified for the drying of a material at a larger temperature than the initial one of the material (increase of the wet solid temperature, constant drying rate, first and second falling rate period).

- The constant drying rate period, the vaporization takes place at the surface of the part: liquid diffusion to the surface is larger than the liquid evaporation. It is the vaporization rate that limits the drying rate. During this period, the part shrinks: every unit of volume of liquid that evaporate correspond to a decrease of one unit volume of the part (Scherer 1990). Particles come closer.

- The first falling rate period, the shell is drier than the inside of the part and the vaporization takes place inside the pores: liquid diffusion rate to the surface is smaller than the liquid evaporation rate. Then, it is the diffusion rate that limits the drying rate. During this period, pores develop.

During air drying, the temperature, the relative humidity and the convection affect the vaporization rate. As described previously, an increase of the vaporization rate may shorten the constant drying rate period. Likewise, the addition of a water soluble polymer influences the drying kinetics (Fichot, 2013).

In the particular case of robocasting, the ceramic slurry presents high solid content varying from 40 to 60 vol.% to be printed (Feilden, 2017) with the objective to obtain dense part. Then, air drying processes followed by sintering for debinding and consolidation are implemented. The larger the solid content is, the lower the printed parts are prone to cracks, warping and shrinkage (Peng, Zhang, et Ding 2018). Moreover a slow drying and a low adhesion between the substrate and the part can avoid failure (Cesarano, 1998; Feilden, 2017). The linear shrinkage value of the part may be comprised between 4 to 10% of the initial dimension of the part for solid content from 45 vol.% to 26 vol.%, respectively (Martínez-Vázquez, Pajares, et Miranda, 2018).

In the particular case of 3D printed parts based on cellulose, air-drying process faces the following challenge: cellulose is a hygroscopic material and in the presence of water, the cellulose fiber swells in its diameter (20 to 30%) whereas its length remains the same (1% of expansion) (Wainwright 1976). Moreover, during the mixing of the considered paste components (CMC, cellulose fiber and water), we don't know whether the cellulose fiber swells due to the water contact nor the CMC "absorbs" all the available water.

This chapter aims at studying the different periods of the drying process that can be identified in our particular case and at proposing a compensation strategy to obtain accurate dried 3D printed part. The different periods were studied on the building block of 3D printed structure (section 5.3 p.158) and on a simple 3D printed part (section 5.4 p.172) with two different drying processes: (i) air drying process at ambient temperature (23°C) for relative humidity ranging from 30 to 50% as encounter in everyday life inside a room and (ii) ethanol drying process which was optimized in term of concentration and bath duration (section 5.2 p.152).

5.2 Toward optimization of ethanol drying conditions

The ethanol drying conditions such as the concentration and the immersion time were evaluated by qualitative (image observations) and quantitative (strain measurement and mechanical testing)

analyses to identify the potential impact of the ethanol concentration (section 5.2.1 p.153) on the part quality and optimize the immersion time (section 5.2.2 p.154).

5.2.1 Influence of the ethanol concentration during ethanol drying

The tests were implemented to determine the minimum concentration of ethanol bath from which the efficiency of the ethanol bath is obtained and ensured quality of the part. The influence of the ethanol concentration was evaluated by qualitative analysis of the aspect of ethanol-dried filaments at 23°C and 30%RH as well as by quantitative analysis by studying the relative dry diameter, $\frac{d}{d_{nozzle}}$ after ethanol drying of 3 samples. Each filament was immersed during 30 min in one of these baths with the following weight proportions: [ethanol at 95%/water], 50/50, 70/30, 80/20, 90/10 and 100/0. By considering the water content of a wet filament regarding the size of the ethanol bath, the ethanol mass concentration reduces of about 1%.

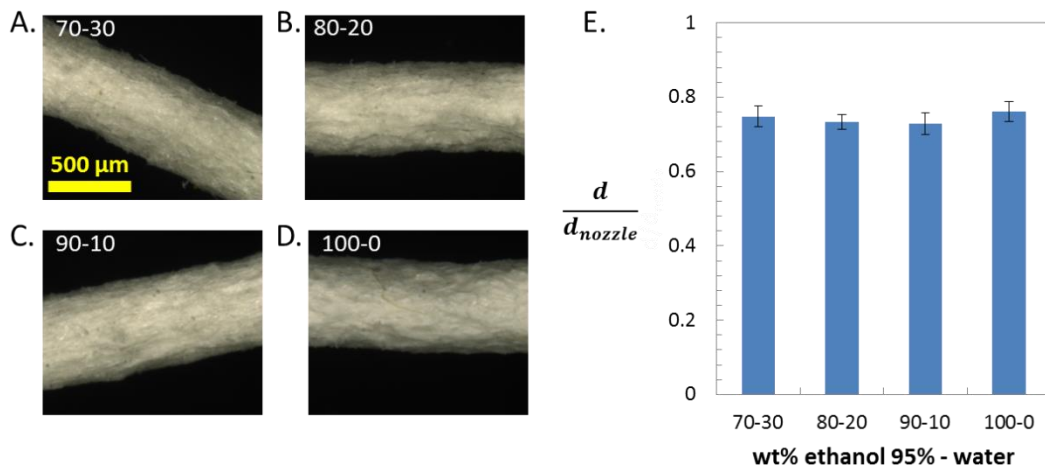


Figure 5-1. Impact of ethanol concentration on filament drying – Images of dry filament after a 30 min in a 10 mL ethanol bath at wt% ethanol 95% - water: 70-30 (A), 80-20 (B), 90-10 (C) and, 100-0 (D). (E) Relative dry diameter as a function of ethanol concentration, the error bars correspond to the mean deviation between the samples values dried in the same condition.

It should be noticed that when the ethanol bath contains more than 50 wt.% of water, the filament partially disintegrates and could not be removed from its bath without breaking it. Therefore these results are not presented in Figure 5-1.

Figure 5-1.A-D show 2D images of the surface of ethanol-dried filament in a 10 mL ethanol bath with concentration of ethanol (95%) ranging from 70 to 100 wt.%. All the filaments presented a well-defined surface without fibers pulling away which could be a harbinger of a partial disintegration of the filament that began. We cannot observe any differences in term of quality between the surfaces of filaments after ethanol drying. Figure 5-1.E shows the mean relative dry diameter of three samples

dried in the same ethanol bath concentration (chapter 2, section 2.3.6.1 p.84). The error bar was about 0.03. The mean values were ranging between 0.73 to 0.76 for filament dried in ethanol bath with concentration of ethanol varying from 70 to 100 wt.%. So the results are not significant.

From 70/30 in weight proportion of ethanol at 95%/water, the influence of the ethanol concentration was negligible. Therefore, maintaining an ethanol bath concentration of 70 wt.% is enough to keep the ethanol bath efficiency as well as the surface quality of the filament.

5.2.2 Optimization of the immersion time during ethanol drying

As in the study of the influence of the ethanol concentration during drying, the tests were implemented to determine the minimum time duration of the ethanol bath at 95% from which the ethanol bath shows efficiency.

The influence of the immersion time in ethanol bath at 95% ranging from 10 min to 24 h was

- Quantitatively analyzed on single filament (section 5.2.2.1): the relative diameter and the Young's modulus were evaluated from image analysis procedures and tensile test performed after the ethanol bath with only 1 min spend in open air, respectively.
- Qualitatively and quantitatively analyzed on H beam (section 5.2.2.2) based on visual inspection as well as on vertical strain measurements.

5.2.2.1 Filament

As mentioned above, diameter measurements and tensile tests were conducted after ethanol bath (10 mL) and 1 min spent in open air. The Young modulus was calculated from the force measurement and the actual filament length during the tensile test as well as the diameter obtained from image analysis on another filament dry in the same conditions.

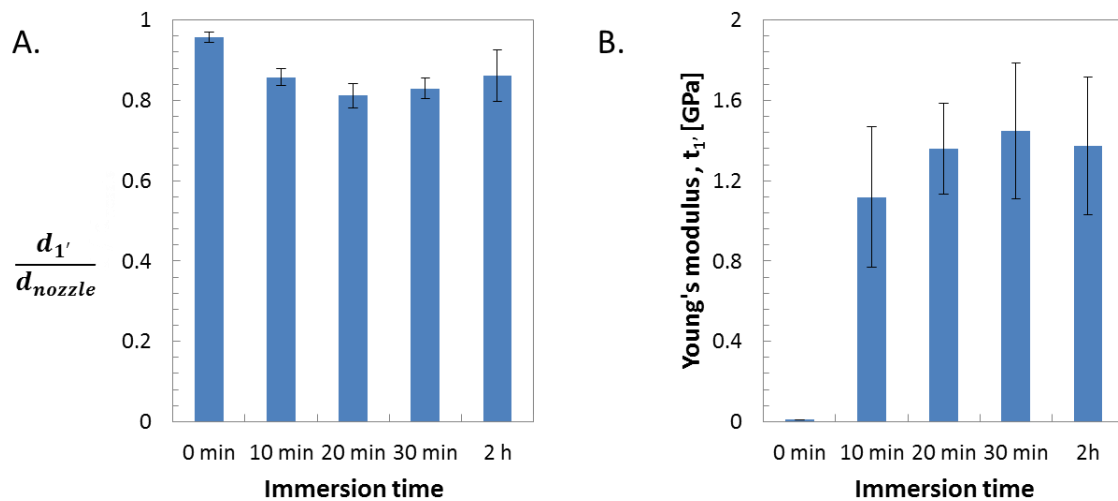


Figure 5-2. Optimization of ethanol immersion time for filament samples – Relative diameter (A) and Young's modulus (B) after the ethanol bath and 1 min spent in open air at 30%RH as a function of their immersion time in ethanol. The error bars correspond to the mean deviation between the samples values dried in the same condition.

Figure 5-2.A shows the relative diameter of the filament for ethanol bath duration varying from 10 min to 2 h and 1 min spent in open air. It was about 0.96 for filaments without ethanol bath immersion whereas it was ranging from 0.81 to 0.86 after an ethanol bath of at least 10 min. These relative diameter values are larger than the ones measured after complete drying as shown in the above section. Indeed, the drying in open air was shorter and the filament might not be completely dried and as a consequence present a larger diameter. After at least 10 min in the ethanol bath, no significant difference in relative diameter was noticed. Likewise, Figure 5-2.B shows the Young's modulus for the same ethanol bath duration. It was about 0.01 GPa for filament without ethanol bath whereas it was comprised between 1.1 and 1.4 GPa for filament tested after an ethanol bath of at least 10 min. The different behavior between filament dry with or without an ethanol bath was studied in the following section (section 5.3).

For a single filament, from 10 min to 2 h of immersion time in ethanol, no significant change was noticed on the diameter strain and the Young's modulus: an efficient ethanol bath can last only 10 min. What about the duration of an efficient ethanol bath for 3D printed part of different thicknesses?

5.2.2.2 H beam

As mentioned previously, the influence of the immersion time in an ethanol bath of 200 mL was evaluated by qualitative analysis of the aspect of the dried H beam (chapter 2, section 2.3.4 p.79) and

by quantitative analysis of its dimensions after ethanol drying in a conditioned room at 50%RH and 23°C.

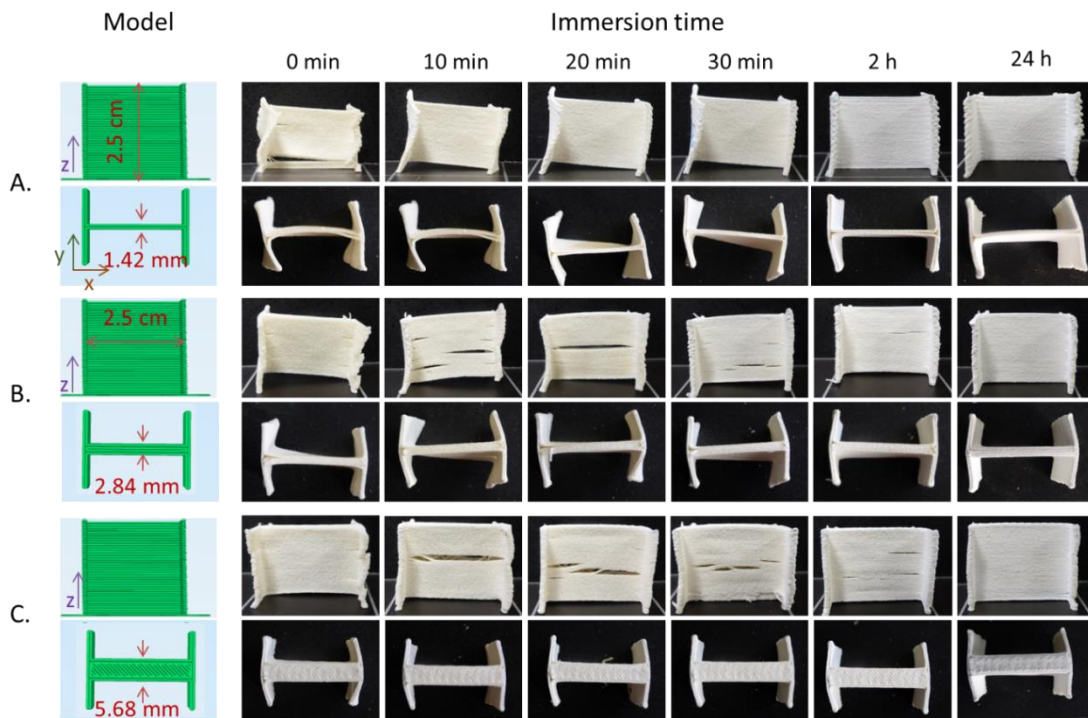


Figure 5-3. Front and top view of model and dried parts after an immersion time in an ethanol bath of 0 min, 10 min, 20 min, 30 min, 2 h and 24 h. Three models were evaluated: 1 perimeter shell model (A), 2 perimeter shell model (B) and 2 perimeter shell model and 50% infill (C).

Figure 5-3 shows dried H beam with different thickness after ethanol drying with a bath duration varying from 0 to 24 h. The thickness of the part was about 2, 4 or 8 times the nozzle diameter and was constituted by 2 to 4 juxtaposed filaments as presented in Figure 5-3.A, B and C.

For all the dried parts, we can notice that the part mainly shrank in the vertical direction. This result was expected due to the large diameter strain of the filament measured previously with (section 5.2.1 p.153) and without ethanol bath (section 3.3.2 p.109). It is the square wall of the H beam that presents interest to evaluate the ethanol bath efficiency influenced by the ethanol diffusion in the part. Yet, the diffusion time of ethanol in the part depends on the shell thickness of the part.

- For the 1 perimeter shell model (two filaments thick H beam) (Figure 5-3.A), the square wall of the H beam dried without ethanol bath presented delamination whereas from 10 min to 24h, no damage of the part was noticed. Moreover, the longer the ethanol bath was, the more stable the dried H beam was. As a

consequence, an efficient ethanol bath can last 10 min as in the case of the single filament.

- For the 2 perimeters shell model (four filaments thick H beam) (Figure 5-3.B), damages were observed for ethanol-dried parts with an immersion time varying from 10 min to 2h. The number of crack and the opening size decrease when the immersion time increases. As for the two filament thick H beam, the part dried without ethanol bath present less stability than the one dried after 24 h of immersion in ethanol bath. As a consequence, an efficient ethanol bath should last about 2 h.
- For the 2 perimeters shell and 50% infill model (Figure 5-3.C), the results were quasi identical to the 2 perimeters shell model, the opened cracks were larger.

Figure 5-4.B shows that the mean relative height of the three parts was about 0.77 after 24 h in ethanol bath whereas it was about 0.67 for air-dried samples highlighting the efficiency of an ethanol bath to reduce the vertical strain of the part.

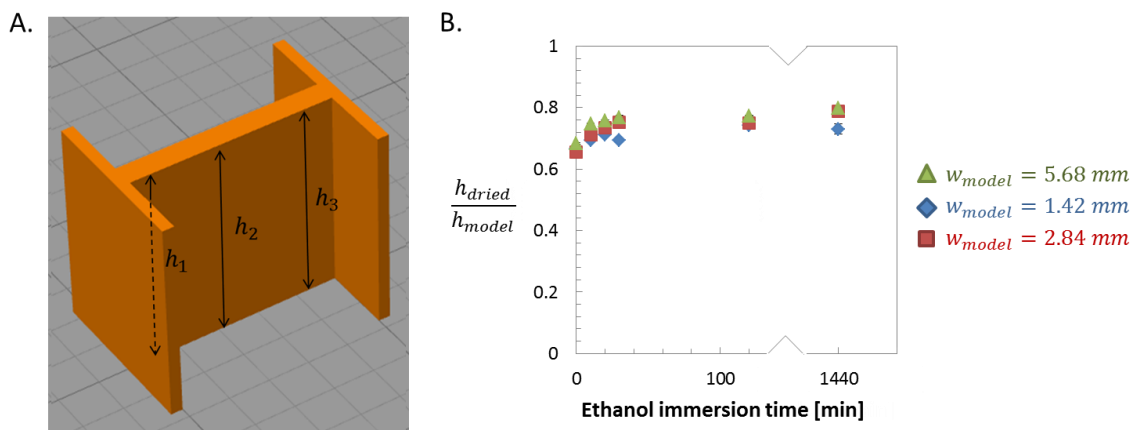


Figure 5-4. Strain of the dried H beam after ethanol drying with different immersion time. (A) Localization of the height measurements. (B) Plots of the relative height of H beam with wall thickness of 1.42mm, 2.84 mm and 5.68 mm as a function of the ethanol immersion time; the error bars correspond to the mean deviation between the three measurements values.

The influence of the immersion time on the part quality (absence of defect) was important. For thin part (two filaments thick part), a short ethanol bath of 10 min was already efficient to improve the dried part quality whereas for thicker part, a longer ethanol bath (more than 2h) is required.

5.2.3 Guideline for ethanol bath

From the results obtained from the experiments performed on the ethanol bath concentration and ethanol bath duration, a guideline for ethanol bath can be implemented.

- Size of the ethanol bath: if we consider that all the water comprised in the fresh part is exchanged with ethanol which is about 60 wt.% of the part, the mass of pure ethanol bath (95%) should weigh at least two times the mass of the fresh part to maintain an ethanol concentration equal or larger than 70 wt.% (the concentration limit found in section 5.2.1 p.153) due to water dilution bring by the wet part.
- Re-use of the ethanol bath: the same ethanol bath can be reuse while the ethanol concentration is maintained at 70 wt.%
- Duration of the ethanol bath:
 - o For single filament or parts with a wall thickness about 1.4 mm made of two juxtaposed filaments, the influence of the ethanol bath is consistent after an immersion time of 10 min.
 - o For larger parts, with 2 perimeters shell and a porous infilled structure, the influence of the ethanol bath is consistent after an immersion time of at least 2 h. More tests should be performed to optimize the immersion time for parts larger than 5 mm printed with a nozzle of 0.7 mm diameter.

5.3 Drying of a filament, building block of the 3D printed structure

To evaluate the influence of the drying conditions of a single filament on its structure, we implemented a monitoring of

- the temporal evolution (chapter 2, section 2.4.6.1 p.89) of the relative Moisture Content (MC) on dry basis compared to the initial one ($\frac{MC_t}{MC_0}$, where MC_t is the Moisture Content at time t and MC_0 , the initial moisture content of the paste),
- the relative diameter compared to the diameter of the nozzle ($\frac{d}{d_{nozzle}}$, where d is the diameter of the filament at time t and d_{nozzle} , the diameter of the nozzle used to extrude the filament),
- the relative length compared to the initial one ($\frac{l}{l_0}$ where l is the length of the filament at time t and l_0 is the initial length of the filament)

with three different drying conditions: air drying at 30 and 50% RH and ethanol drying. The temporal evolution of these structural properties were first evaluated for air drying at 30%RH (section 5.3.1) to present the drying periods and the methods used to describe them and then the results of the three different drying conditions were compared in section 5.3.2 to evaluate their influence on the drying kinetics and their structural properties.

5.3.1 Temporal evolution of the filament

The temporal evolution of the filament during its air drying at 30%RH was evaluated by monitoring its relative moisture content and its main dimensions: diameter and length as explained in chapter 2 (section 2.4.6.2 p.90).

5.3.1.1 Moisture content evolution

Figure 5-5.A shows the temporal evolution of the mass, m_t of two different filaments. The initial mass of a single filament is about 0.08 g and the final mass of the filament is about 0.04 g. These mass measurements are consistent with the accuracy of the scale used. The normalized moisture content can be calculated.

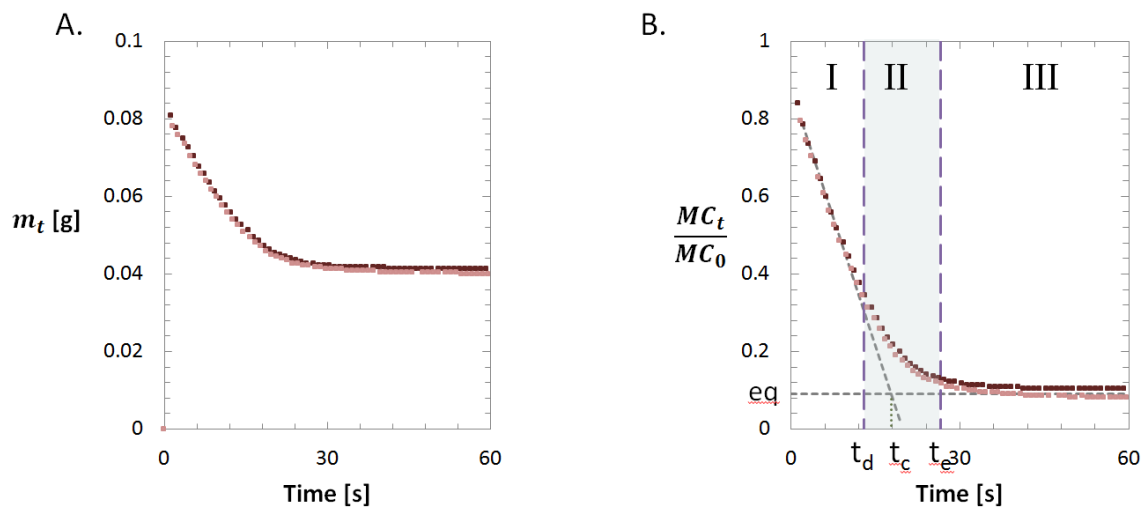


Figure 5-5. Characterization of single filaments during drying at 30%RH and 22°C during 1 h – (A) Temporal evolution of the mass, m_t and (B) temporal evolution of the relative moisture content, $\frac{MC_t}{MC_0}$.

Figure 5-5.B shows the normalized moisture content, $\frac{MC_t}{MC_0}$, for two different filaments where MC_0 was found to be 1.49 kg.kg^{-1} on dry basis and was measured on the fresh paste (see chapter 2, section 2.3.7 p.85). On this graph, we can observe a good reproducibility and the same behavior of the samples: the same initial relative and final moisture contents and the same trend. We can observe three periods: first a linear decrease with time (I), then a transition period (II) and finally a steady state plateau (III). The initial moisture content is about 87% of its initial value and the final moisture content is about 9% of its initial value. It should be noticed that the linear decrease should start around 1 at $t = 0$ min. The scale precision is a key parameter as the weight of the fresh filament was about 0.08 g. Indeed, an error of 2.5% on the dried filament weight measurement (± 0.0010 g) affects the relative humidity of 4%. One of the reasons of error on the weight measurement can be a

fast water uptake before the dried filament was weighted or a partial drying of the paste inside the extruder head.

5.3.1.2 Strain evolution

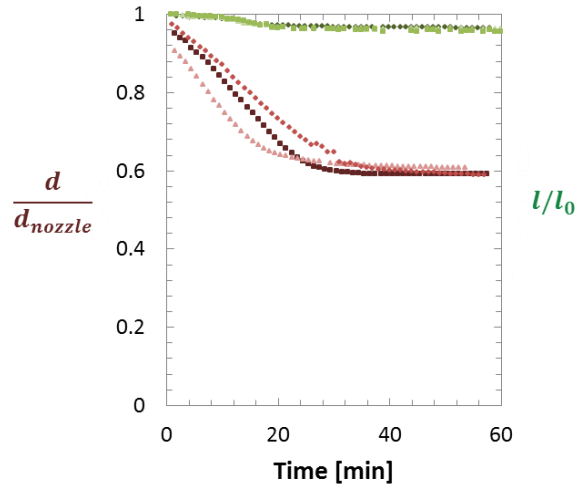


Figure 5-6. Temporal evolution of the normalized diameter, $\frac{d}{d_{nozzle}}$ and length, $\frac{l}{l_0}$ of single filaments during drying at 30%RH and 22°C during 1 h.

Figure 5-6 shows the temporal evolution of the normalized diameter, $\frac{d}{d_{nozzle}}$, and of the normalized length, $\frac{l}{l_0}$, for three different filaments where the nozzle diameter, d_{nozzle} was 0.72 mm and the initial length, l_0 was about 7 cm. For each case, we can observe the reproducibility of the measurements and the three different periods. The decreased of the normalized diameter is about 40%, more than 10 times larger than the decreased of the normalized length which is only 4%. This anisotropic shrinkage behavior is mainly caused by the fiber alignment, their shrinkage and capillarity forces as commented previously in chapter 3 (section 3.3.2 p.109).

5.3.1.3 Identification of the drying periods and temporal adjustment

To quantified the three periods of these graphs (Figure 5-5 and Figure 5-6) and understand the interaction between the moisture content and the dimensional variations, we can in a first approximation define three characteristics times (Figure 5-5.A). The intersection of the linear fitting of the decrease and the linear fitting of the steady state period gives the characteristics time, t_c . The reached 5% deviation between the linear fitting of the decrease and the measured values after their remapped between 0 and 1 gives the decreased time, t_d , that characterized the end of the decrease period (I) and the beginning of the transition period (II). Likewise, the reached 5% deviation between the measured value and the linear fitting of the steady state period after values remapping gives the

equilibrium time, t_e , that characterized the end of the transition period (II) and the beginning of the steady state period (III). These three characteristic times and the fits are reported in Table 5-1.

Structural properties	n° sample	I Equation	III Equation	t_d [min]	t_c [min]	t_e [min]
$\frac{MC_t}{MC_0}$	1	-0.044t + 0.888	0.150	13	17	26
	2	-0.044t + 0.865	0.130	13	17	27
$\frac{d}{d_{nozzle}}$	1	-0.015t + 0.988	0.590	22	26	28
	2	-0.017t + 0.965	0.610	20	21	29
	3	-0.013t + 0.994	0.590	27	31	37
$\frac{l}{l_0}$	1	-0.002t + 1.012	0.970	23	21	27
	2	-0.002t + 1.010	0.965	19	22	51
	3	-0.002t + 1.004	0.960	24	22	32

Table 5-1. Analyze of the three periods of the structural properties of filament during drying at 30%RH and 23°C where t represent the time expressed in minutes.

Table 5-1 presents the equations of fitting as well as the values of the characteristic times for the three defined structural properties. The initial value of the relative filament diameter and length was about 1. As shown in chapter 3 (section 3.2.2.1 p.101), no die swelling was noticed at the exit of the nozzle. Moreover, as the temporal change of the length was small compared to the initial length, the measurements accuracy could influence the linear fitting. Both the relative diameter and the relative length show a similar temporal scale whereas these temporal scales are different compared to the moisture content one. This might be due to a smaller exposed surface area to air of the filament with only 75% of its surface during diameter measurement as the filament was placed on a support for taking pictures. Moreover, this measurement configuration with a quasi-closed containment can result in an increase of the local relative humidity that affect the drying time as shown in later paragraph (section 5.3.2). Indeed, as shown in Figure 5-7.A with an air drying process at 60%RH and 27°C, the optical set up strongly influences the drying kinetic of the diameter strain. The optical set up with the filament on the top of the camera looks like the set up for weight measurement. We can consider that both of the filaments dried in the same condition. As a consequence, the diameter evolution obtained with the camera above the filament at 23°C and 30%RH must be temporally rescaled to use it with data obtained with filament that dry in a suspended condition such as the moisture content. We can notice that the characteristic time of the diameter measurement is lower than the decrease time of the moisture content, a resizing performed by coinciding this two times is not enough precise. However, Figure 5-7.B shows that during the period I, the rate of water evaporation coincide with the rate of strain of the filament section area. Indeed, during a period named constant drying rate period, the water mass losses are equal to the volume decrease. Yet, due

to the anisotropic shrinkage of the filament, the length evolution can be neglected and the volume decrease is driven by the diameter strain. A more precise rescaling can be performed by fitting the rate of water evaporation with the first order term of the strain of the filament section area.

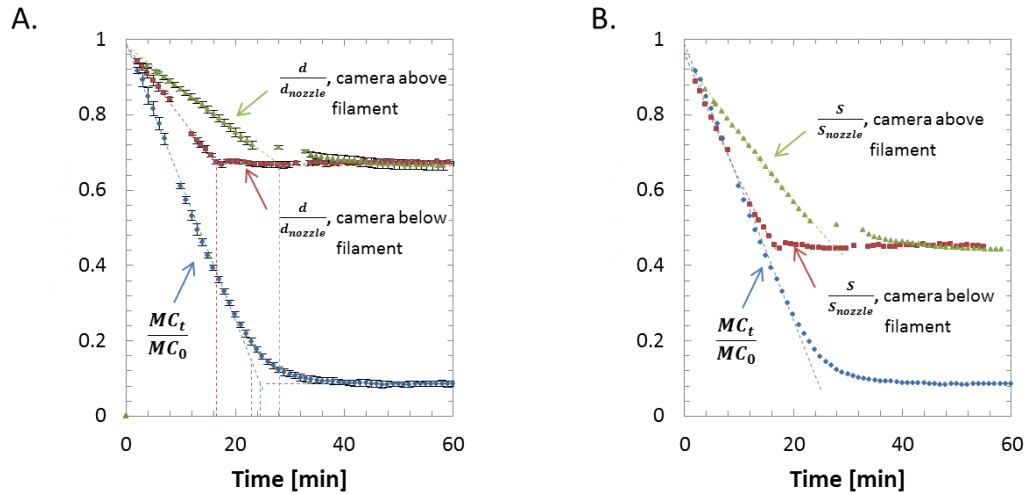


Figure 5-7. Single filament drying curves at 27°C and 60%RH – (A) Temporal evolution of the relative moisture content and of the relative diameter with the two optical set up for the diameter measurement: camera above the filament and filament above camera and (B) Temporal evolution of the relative moisture content and of the normalized filament section area $\frac{s}{s_{nozzle}} = \frac{d^2}{d_{nozzle}^2}$.

5.3.1.4 Drying rate evolution

From the above rescaling, we can plot the drying rate as a function of the time (Figure 5-8.A) and as a function of the relative moisture content (Figure 5-8.B). From these curves (Figure 5-8), we can observe three periods: a quasi-constant drying rate period (I), a falling rate period (II) and a quasi-null drying rate period (III) related to the drying period identified previously (section 5.3.1.3 p.160). The transition between the two first periods is characterized by a critical relative moisture content about 0.4 (Figure 5-8.A) that corresponds to a drying time about 13 min (Figure 5-8.B). These two periods were described in the state of the art (section 1.1.2.4.3.2 p.36).

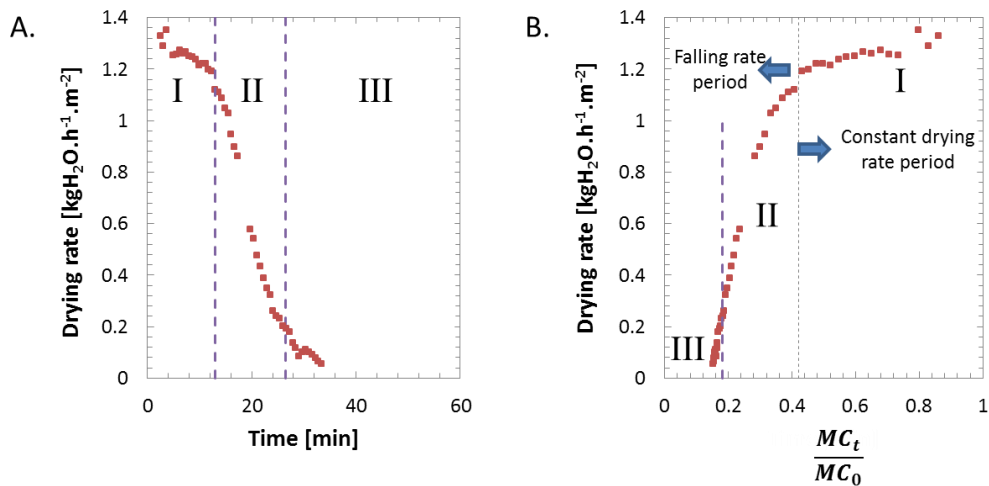


Figure 5-8. Drying rate of the filament ($R = \frac{w_d}{l_t d_t} \frac{MC_{t+1} - MC_t}{\Delta t}$ with w_d , its dry weight, l , its length, d , its diameter, MC_t , its moisture content and Δt , the time step) as a function (A) of time and (B) of relative moisture content.

During the constant drying rate period, the evaporation is the limiting step whereas during the falling rate period, it is the diffusion of liquid toward the surface, which is the limiting step. Moreover, it is during the constant drying rate period that the filament shrinks (Figure 5-9.A, B) whereas it is during the falling rate period that the pores developed and shrinkage stopped (Figure 5-9.B, C) provided it exhibits larger resistance than the drying forces. The pores development cannot be observed on Figure 5-9.

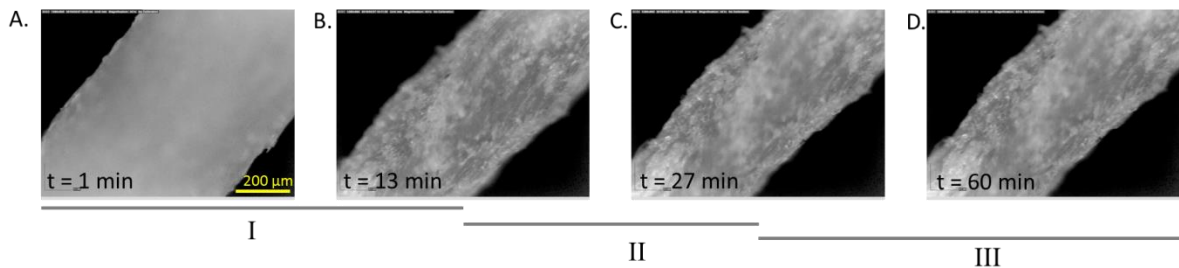


Figure 5-9. Temporal evolution of the filament images corresponding to the beginning and the end of the constant drying rate period (A, B), of the falling rate period (B, C) and of the quasi null drying rate period (C, D).

The evaporation rate, $\frac{dW}{dt}$ is given by equation (13). As mentioned above, during the constant drying rate period, the evaporation rate value coincides with the drying rate value. Therefore the mass transfer coefficient can be calculated. It was found to be around $6 \cdot 10^{-4} \text{ h} \cdot \text{m}^{-1}$ at 23°C and 30%RH with $P_s = 2800 \text{ Pa}$, $\frac{DW}{dt} = 1.2 \text{ kg} \cdot \text{h}^{-1} \cdot \text{m}^{-2}$ whereas for a film of CMC at 3 wt.% ($M_w = 90000 \text{ g} \cdot \text{mol}^{-1}$), it

was found to be around $16 \cdot 10^{-4} \text{ h} \cdot \text{m}^{-1}$ at 25°C and 43%RH with $P_s = 3 \text{ 100 Pa}$, $\frac{dW}{dt} = 2.9 \text{ kg} \cdot \text{h}^{-1} \cdot \text{m}^{-2}$ (Fichot, 2013), about 2 to 3 times the value found for the paste developed in this study where CMC concentration is much larger. Indeed, CMC was known to slow down drying.

$$\frac{dW}{dt} = k_g (P_s - P_w) = k_g P_s \left(1 - \frac{P_w}{P_s}\right) \quad (13)$$

Where $\frac{dW}{dt}$ is the evaporation rate [$\text{kg} \cdot \text{h}^{-1} \cdot \text{m}^{-2}$]

k_g is the mass transfer coefficient [$\text{h} \cdot \text{m}^{-1}$]

P_s is the vapour pressure of water [Pa] and is in function of temperature

P_w is the partial pressure of water [Pa]

$\frac{P_w}{P_s}$ is the relative humidity, RH

To conclude on the temporal evolution of filaments air-dried at 30%RH, we can observe:

- good reproducibility of the results. Therefore, one measurement is consistent and gives the tendency. It also validates the methodological approach that consisted in calculating the mean values for the same drying condition. Moreover, this methodological approach for analysing the results was implemented in the following section for the study of the influence of the drying conditions.
- anisotropy of the shrinkage with a limited longitudinal strain. The longitudinal strain was not studied in the following section.

5.3.2 Influence of the environmental conditions

The Relative Humidity (RH) met in everyday life is between 30 and 50%. It could be interesting to evaluate the influence of these RH on the filament characteristic upon drying. The influence of the drying conditions was evaluated on two these two relative moisture contents (30%RH and 50%RH) and with air or ethanol drying conditions following the same approach than in the previous section (section 5.3.1) which consisted in the monitoring of the moisture content and the diameter of the filament.

Figure 5-10.A and B show the averaged curves of the evolution of the relative moisture content and relative diameter of the filament obtained for three samples dried in the same condition (air drying at 30 or 50%RH or ethanol drying) with the same batch of paste ($MC_0 = 1.49$) and the error bar, their mean deviation. We can observe a similar drying behavior for the three drying conditions as presented in the previous section (section 5.3.1). The correction presented in section 5.3.1.3 p.160 for the 30%RH samples on the time scaling of the evolution of the relative diameter of filaments was

applied except for ethanol drying as presented in Figure 5-10.C due to a rapid drying compared to the time period of measurements.

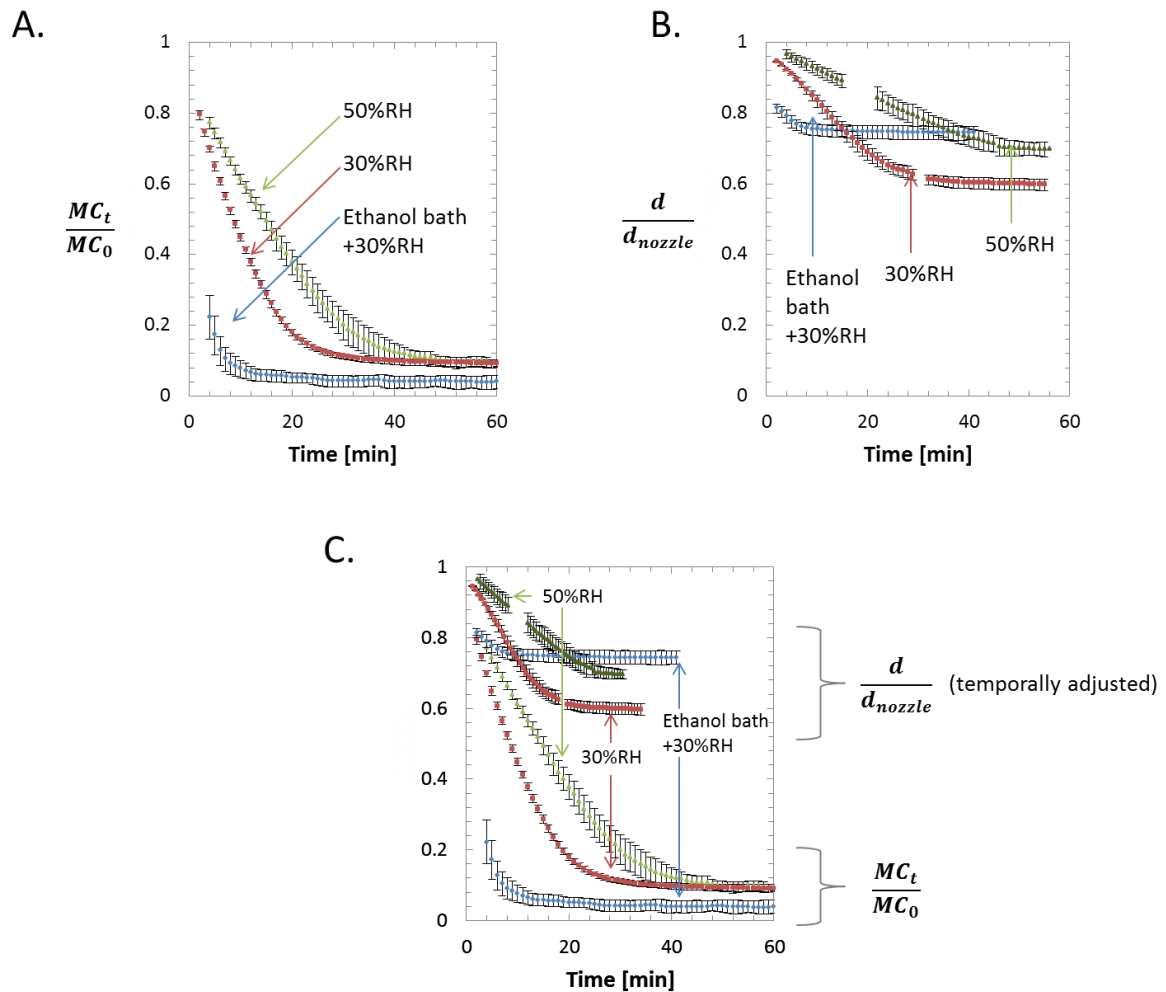


Figure 5-10. Influence of the drying condition – (A) Plots of the averaged relative moisture content versus time and (B) relative diameter versus time combined in (C) with a temporal rescaling of the relative diameter of filament air-dried at 30 and 50%RH and ethanol-dried at 30%RH versus time during 60 min. The error bars correspond to the mean deviation between the samples dried in the same condition.

Figure 5-10.A and C show the temporal evolution of the normalized moisture content for three different drying conditions. Initial moisture content of air-dried filaments and ethanol-dried filaments before their ethanol bath are about 87% and 94% of their initial value (1.49 kg.kg^{-1} dry basis), respectively. After the ethanol bath, the initial moisture content is about 41% of its initial value (see Table 5-2). This means that at least 59% of initial mass of water was exchanged by ethanol in 30 min by assuming that ethanol vaporization is immediate and the initial moisture content was 1.49. The final moisture content for the ethanol-dried and air-dried filaments is about 4% and 9% of its initial

value, respectively which is in the range of the moisture content of the cellulose fiber and the CMC sold by the supplier for the air-dried filament. Although CMC and cellulose fiber are known to be hygroscopic material, after the ethanol bath and the drying, the final value is half of the initial water content of the bulk material, the water uptake might be a long process or the ethanol bath change the water uptake capacity of the cellulose.

Figure 5-10.C shows also the temporal evolution of the normalized diameter for three different drying conditions after time rescaling. The initial diameter is about 99% of the nozzle diameter for air drying process whereas it is about 84% of the nozzle diameter for the ethanol drying process just after the ethanol bath. During the ethanol bath, the filament shrank. The cross section area after ethanol bath is about 70% of the area of the nozzle. Yet, in the previous paragraph, we observed that at least 59% of the initial mass of the water was exchange during the ethanol bath. It corresponds to a volume loss of 41% of its initial volume by using the mixing law for density calculation of the fresh paste assuming that there is no porosity. The water loss converted in volume loss is more than 1.3 times larger than the volume loss obtained by neglected the length strain of the filament and the presence of ethanol which present a density lower than water. So we can consider the presence of at least 30 vol.% of pores inside the filament after the ethanol bath. The ethanol-dried filament exhibits a final relative diameter of 74% whereas the air-dried filament at 30%RH and 50%RH exhibit a final relative diameter of 60 and 70%, respectively. After ethanol drying, the diameter strain is the lowest. Indeed, the advantage of this solvent exchange is the reduction of formation of new hydrogen bond between approaching cellulose fiber and the reduction of capillarity forces that applied during drying leading to less deformation than without solvent exchange. The range of relative humidity that is possible to encounter without conditioned room, 30 to 50%RH, with an ambient temperature around 23°C seems to strongly affects the shrinkage. However, an opposite results was found when 3 samples were dried in a conditioned box with saturated salt solution at 32%RH or 48%RH and each sample were capture at 3 areas. The relative mean diameter for 32%RH and 48%RH were 66 and 64% with a mean deviation up to 3% (results presented in chapter 3 section 3.3.2 p.109). To control deformation during and after drying, a minimization of the impact of the relative humidity on the shrinkage is positive.

Structural properties	Drying condition	I Equation	III equation	t_d [min]	t_c [min]	t_e [min]
$\frac{MC_t}{MC_0}$	30%RH – 23°C	$-0.044t + 0.877$	0.090	13	18	27
	50%RH – 23°C	$-0.024t + 0.861$	0.090	27	32	40
	Ethanol bath – 50%RH – 23°C	$-0.048t + 0.412$	0.040	8	8	11
$\frac{d}{d_{nozzle}}$ adjusted	30%RH – 23°C	$-0.024t + 0.981$	0.600	14	16	31
	50%RH – 23°C	$-0.012t + 0.990$	0.700	23	24	45
	Ethanol bath – 30%RH – 23°C	$-0.011t + 0.838$	0.740	9	9	10

Table 5-2. Characterization of the rescaled drying curves of filaments air-dried at 30 and 50%RH and filament ethanol-dried.

Table 5-2 shows the different times and slopes that characterized the drying behavior. We can easily noticed that with ethanol drying condition, the drying is about 2 times faster than with air drying process as well as a dried air is in favor of a faster drying. These large characteristic times with air drying process are in favor for printing layers that can take few minutes to print without damaging the part or extra settings to optimize. Indeed, a too quick and large strain of the filament can results in poor adhesion between layers and failure of the printed part due to a too large gap to fill between the nozzle and the previous layer.

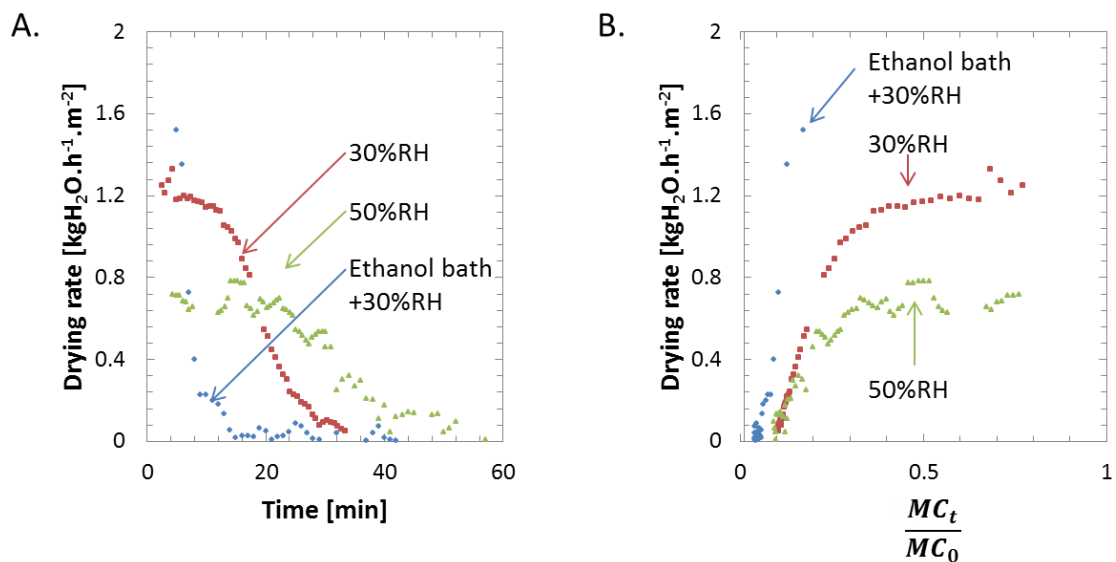


Figure 5-11. The drying kinetics of filament air-dried at 30 and 50%RH or ethanol-dried. The drying rate plotted (A) as a function of time and (B) as a function of the relative moisture content.

Figure 5-11.A shows the drying kinetics of the filament with the 3 drying conditions, the ethanol drying, and air drying at 30 and 50%RH. Both the drying rates of the air-dried filament show a

constant drying rate period (1.2 and $0.7 \text{ kgH}_2\text{O}\cdot\text{h}^{-1}\cdot\text{m}^{-2}$, respectively) and a falling rate period whereas the ethanol drying shows two falling rate periods. For a relative moisture content larger than 0.08 , we can observe a larger drying rate for the ethanol drying compared to air drying at 30 and 50% RH. The strong drying rate decrease of the ethanol-dried sample might be caused by the end of ethanol vaporization and the second slope to evaporation of the water that is still present inside the filament. Yet, beside a lower density, ethanol is a volatile liquid compared to water. Likewise, we can observe that the drying rate of filament dry at 30% RH is larger than the one of filament dry at 50% RH. During the constant drying rate period where the evaporation is the limiting step, the drying rate at 30% RH is 1.7 times larger than the one at 50% RH which is not in agreement with the evaporation rate (equation (13)). The drying rate should have been 1.4 times larger as the two experiments were performed at the same temperature. However, when the falling rate period start, the difference between both drying rates decreases. Indeed, as mentioned in chapter 1 (section 1.1.2.4 p.34), during this period, the diffusion from the inside to the outside of the filament is the limiting step, the relative humidity of the air should not influence the drying rate anymore. This transition between the constant drying rate and the falling drying rate for the filament air-dried seems to be characterized by a moisture content of 0.4 .

The relative humidity met in everyday life is between 30 and 50% . Drying the filament in this range of RH affect the drying rate and as a consequence the drying time of the filament. The ethanol drying condition fasten the drying when dried in open air, after the ethanol immersion and limit the radial strain of the filament.

5.3.3 Temporal evolution of the mechanical properties

To study the stresses developed during the drying, the temporal evolutions of the mechanical properties such as the Young's modulus of a filament and the force resulting from the longitudinal strain of the filament were measured during its drying. To measure it tensile tests on filaments that dried during 2 to 60 min were performed and the force applied by the filament during its drying without displacement of the clamp of a tensile machine during 60 min was monitored.

5.3.3.1 Temporal evolution of the Young's modulus

The Young's modulus of the filament upon drying was extracted from stress strain curves. These curves were obtained by using the tensile force measurements and the actual filament length during the tensile test performed after 2 to 60 min after the beginning of the sample extrusion as well as the diameter corresponding to the drying time measured in the previous section of this chapter (section 5.3.2).

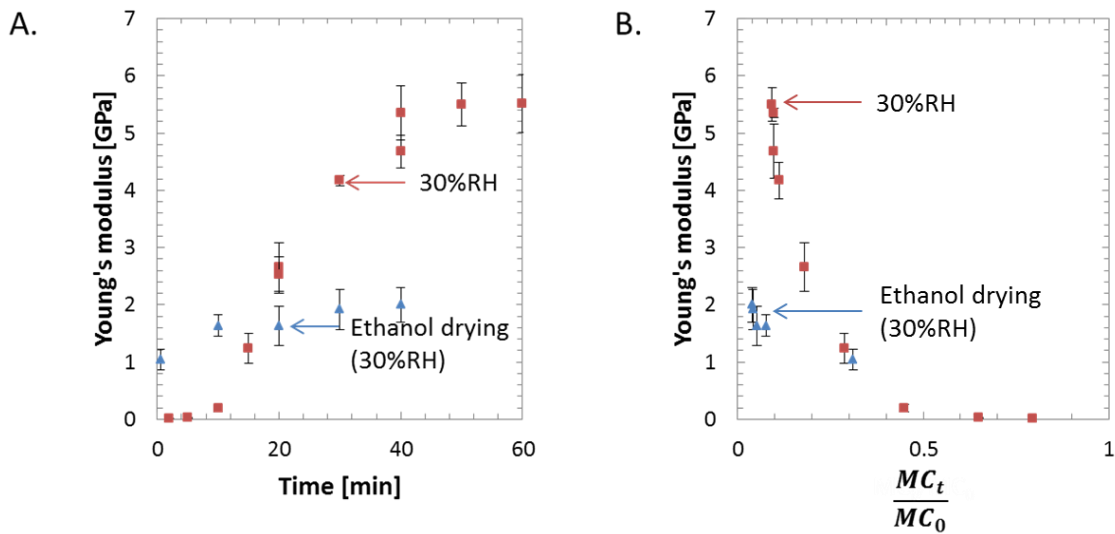


Figure 5-12. Temporal evolution of the mechanical characterizations of filament air-dried at 30%RH and ethanol-dried. (A) Plot of the Young's modulus as a function of time and (B) plot of the Young's modulus as a function of moisture content, the error bars correspond to the mean deviation between the samples values dried in the same condition.

Figure 5-12.A shows the temporal evolution of the Young's modulus of the filament during air drying and ethanol drying at 30%RH.

The temporal evolution of the Young's modulus measured on air drying samples follows a S curve shape with an initial Young's modulus about 0.01 GPa and a plateau at 5.5 GPa after 40 min of air drying.

The temporal evolution of the Young's modulus measured on ethanol drying samples shows a slight increase until reaching a plateau with an initial value about 1.0 GPa and a plateau value about 2.0 GPa after 20 min of drying.

This difference in initial value of the Young's modulus was caused by a filament moisture content of the air-dried filament after exiting the nozzle twice as large than the one of the ethanol-dried filament just after the ethanol bath as previously mentioned (section 5.3.2) and the CMC is not soluble in ethanol. To be able to compare the Young's modulus with the same moisture content, the Young's modulus was plotted as a function of the relative moisture content on Figure 5-12.B. The Young's modulus at its equilibrium moisture content is more than two times larger for the air-dried filament than the ethanol-dried one. This difference in stiffness was due to a larger strain of the air-dried filament that results in less porosity than with the ethanol-dried filament as illustrated by the SEM images of the cross section of air-dried and ethanol-dried filament of Figure 5-13. By neglecting the longitudinal strain of the filament and the presence of pores in the wet state of the paste, the

porosity after drying can be evaluated from the measured radial strain, the initial moisture content and the density of water and cellulose. The ethanol-dried filament presents more porosity (47%) than the air-dried filament (14%). Another tensile test after complete ethanol and air drying in the same condition and diameter measured on each sample show a porosity of 42 and 30% and a Young's modulus of 2.7 ± 0.3 and 5.4 ± 0.5 GPa for the ethanol-dried and air-dried filament, respectively. The difference in Young's moduli cannot only be explained by the difference in porosities and presence of defects below the image resolution. Indeed, if we consider that the ethanol exchange dried filament had the same diameter as the air-dried filament, the Young's modulus was about 3.5 ± 0.5 GPa, which is still lower than the 5.4 ± 0.5 GPa of the air-dried filament. Thus, the ethanol does not only affect the strain during drying, but it also might influence the hydrogen bonding between the cellulose fibers (Przybysz, Dubowik, Kucner, Przybysz, & Buzafa, 2016) or the CMC-cellulose fiber adhesion.

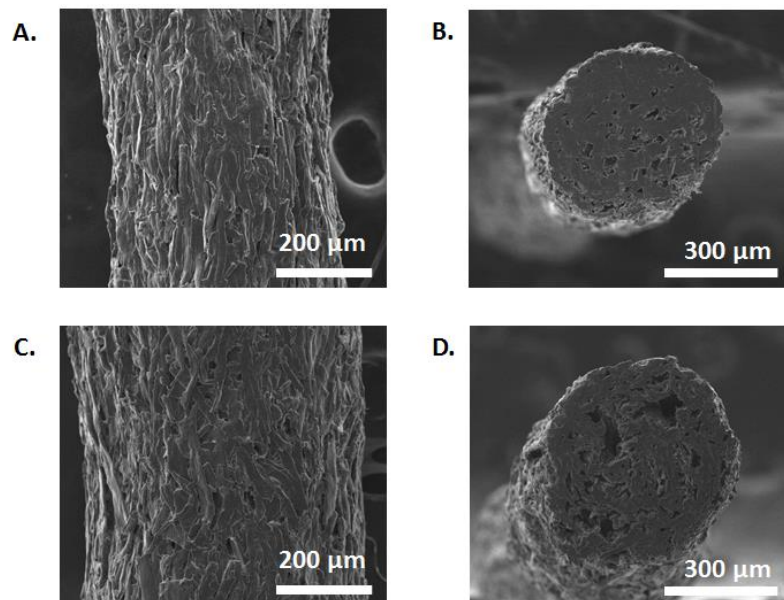


Figure 5-13. SEM images of the surface and cross-section of an (A, B) air-dried filament and (C, D) ethanol-dried filament after complete drying.

Figure 5-12.B shows the evolution of the Young's modulus as a function of the relative moisture content of the filament. We can observe for the air-dried filament that for a relative moisture content larger than 0.4, the Young's modulus is low (< 0.2 GPa) whereas its value increased rapidly when the relative moisture content decreased in particular when the relative moisture content almost reached its equilibrium value due to the presence of few unbonded water which still favors sliding between fibers. Yet, this moisture content of 0.4 was identified as the transition between the constant drying rate period and the falling drying rate period (previous section): the filament

shrinkage almost stop and from the outer surface to the inside, the filament starts to dry (local moisture content lower than the mean value) reinforcing the strength adhesion between fibers.

To conclude, in the wet state, the stiffness of the paste is low compare to the stiffness of the paste in the dry state. Moreover, ethanol drying degrades the stiffness of the filament besides a better dimensional stability upon drying.

5.3.3.2 Temporal evolution of the drying strength

Using a universal tensile testing machine without any displacement of the clamp after a preload (see chapter 2 section 2.4.6.4 p.94), the force F applied by the filament on the clamps during the drying was recorded during 60 min to evaluate the longitudinal drying strength of the filament. This experiment is similar to what happened during the drying of the bridge printed previously (section 4.3.2.4 p.143) as the filament is fixed at its extremities by adhesion to the pillars.

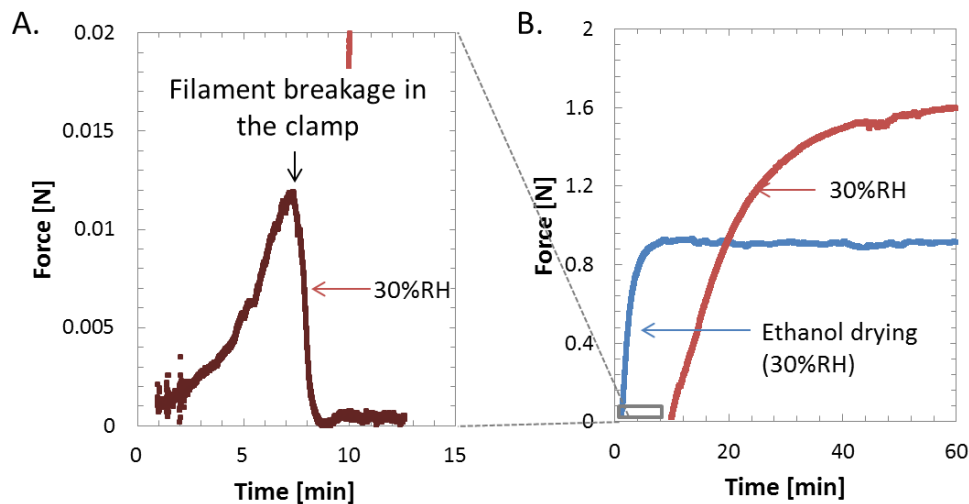


Figure 5-14. Temporal evolution of the tensile force record during drying of filament at 30%RH with ethanol and air drying conditions without any displacement of the clamps for samples tested (A) 1 min after ethanol bath (ethanol drying condition) and 10 min after extrusion (air drying condition) or (B) after 1 min after filament extrusion.

Figure 5-14 shows the force induced by the filament during its drying on the clamp of the tensile machine after preloaded. During the experiment, the air-dried filament broke in the clamps; the force induced by the drying was too large for the wet filament that could not dry in the clamps to resist to the force induced by its drying unlike, in the case of the design of the bridge where the filament that belong to the unsupported part and the one that is above the pillars could dried simultaneously. That is why, no filament breakage was observed during the drying of the bridge. However, after 10 min of drying or with the ethanol drying process, we can observe that the filament

does not break and the drying force increased over time until reaching a plateau about 0.9 and 1.6 N for the ethanol drying and air-dried filament, respectively. This drying force is due to the longitudinal strain of the filament, about 4% for the air drying condition (section 5.3.1 p.159) and 1% for the ethanol dry condition, resulting in a lower force induced by the ethanol drying condition than the air drying condition. The temporal evolution of the drying strength is in accordance with what we observed for the radial strain of the filament (section 5.3.2 p.164).

During the drying, the large strains observed on the filament result from large stresses such as the ones measured in the longitudinal direction of the filament.

5.4 Drying of a cube, a simple 3D structure

To evaluate the influence of the filament strain on a 3D structure, we implemented a monitoring of the temporal evolution of the 3D structure of a cube, the elementary feature that composed any 3D part, by fast laboratory X-ray measurement, for different drying conditions: air drying and ethanol drying both at 30%RH. From these measurements, we obtained the temporal 3D evolution of the inner and outer structure of the cubes.

5.4.1 Validation of the experimental set up

5.4.1.1 Sample description and drying condition

The printed cube consisted in 2 perimeters shell that formed the vertical walls and a rectilinear infill pattern dense at 50% and rotated at 90° every layer. The solid volume of the model to print is about 600 mm³ and present a surface exposed to air of about 1 100 mm². The ratio solid volume over the exposed surface is three times larger than the one of the filament studied previously. Moreover, the surface of the part can be decomposed in two areas:

- The outer surface: it is constituted of the 4 vertical faces of the cube and the surface of the top of the cube. It represents about 400 mm².
- The inner surface: it is constituted of the surface of the inner structure of the part and the inner surface of the vertical wall. It represents about 700 mm².

The temporal monitoring of the cube was performed on air and ethanol drying cubes at 23°C and 30%RH in the tomography equipment room (section 2.4.6.3 p.92). From the results on the optimization of the ethanol bath (section 5.2.2 p.154), the ethanol bath duration of the cube was set at 15 min.

5.4.1.2 Validation of the lab X-ray micro-tomography set up

We monitor the temporal evolution of the relative moisture content on dry basis of the 9 mm side cube to estimate the temporal evolution of the strain of the cube depending of the drying conditions (Figure 5-15). From these results, the set-up of the laboratory X-ray micro-tomography equipment was optimized to monitor the temporal evolution of the strain.

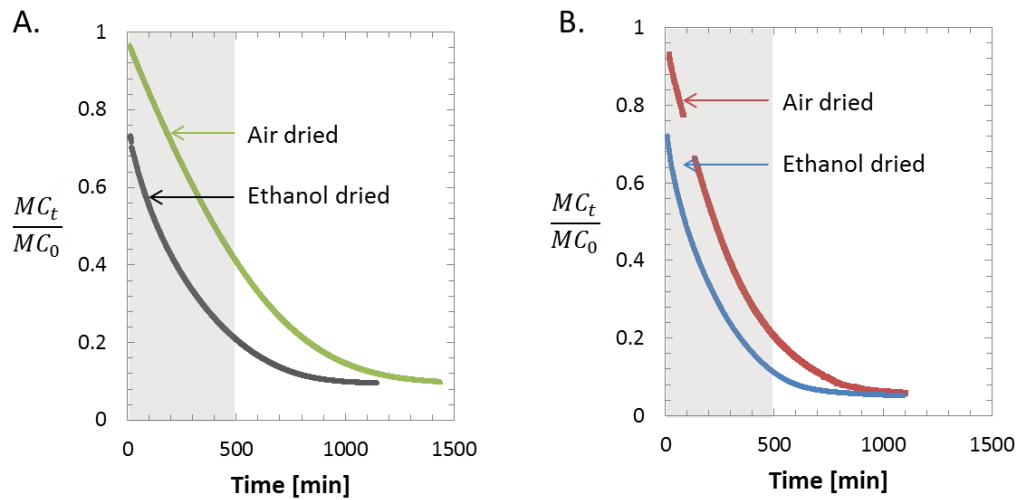


Figure 5-15. Plots of the relative Moisture Content (MC) of a 9 mm side cube for air and ethanol drying conditions (A) at 50%RH and (B) at 30%RH.

The resolution was about $28^3 \mu\text{m}^3/\text{voxels}$. The section of a wet filament or a dried one will be composed of about 520 or 200 pixels, respectively, which allowed an accurate definition of the deposited filament during the drying.

The scanning time was about 36 s. Figure 5-15 shows that the slopes of the temporal evolution of the relative moisture content with different drying conditions is larger for the first hours than the rest of the curve. Their slope values are ranging from -0.0013 to -0.0029 min^{-1} . In one minute, the volume variation can reach 0.3% of the initial solid volume of the cube (volume 3D model, 593 mm^3). So in 36 s, it can reach 0.2% of its initial solid volume which represents a maximum height variation of about $16 \mu\text{m}$, below the resolution of the scan. The volume variation should not influence the quality of the scan.

5.4.1.3 Validation of the monitoring duration

To evaluate the temporal evolution of the 3D structure of the cube, it should be monitored from the beginning of the drying to an advanced stage of the falling rate period to get an overview of the strain.

On Figure 5-15, it can be observed that the time required for reaching the equilibrium moisture with air drying at 50%RH is larger than the one needed for ethanol drying at 30%RH, as previously observed with the drying of a single filament. After 8 h of drying, the moisture content of the air-dried and ethanol-dried cube at 30%RH reached 0.21 and 0.12 of their initial value (1.49), respectively whereas the relative moisture content equilibrium value was about 0.05. As seen previously in this chapter (section 5.3.1 p.159), at this relative moisture content level, the falling rate period already started and the strain rate decreased whereas for the air-dried cube at 50%RH, the moisture content is about 0.42 of its initial value, above the beginning of the falling rate period of the filament.

The drying time of the cube is more than 10 times larger than the drying time of the filament. Indeed, the ratio exposed surface to volume is much smaller for the cube which results in a larger drying time. However, after 8 hours of drying, most of the structural change have occurred for the cube dried at 30%RH and the structural change that are still going to occur after the 8 hours of drying happen below the chosen pixels size and cannot be captured.

5.4.2 Temporal evolution of the cube at macroscopic scale

5.4.2.1 Qualitative analysis

The obtained stack of images can be qualitatively analyzed to provide an overview of the 3D structural changes all along the drying and to compare the ethanol and air drying conditions.

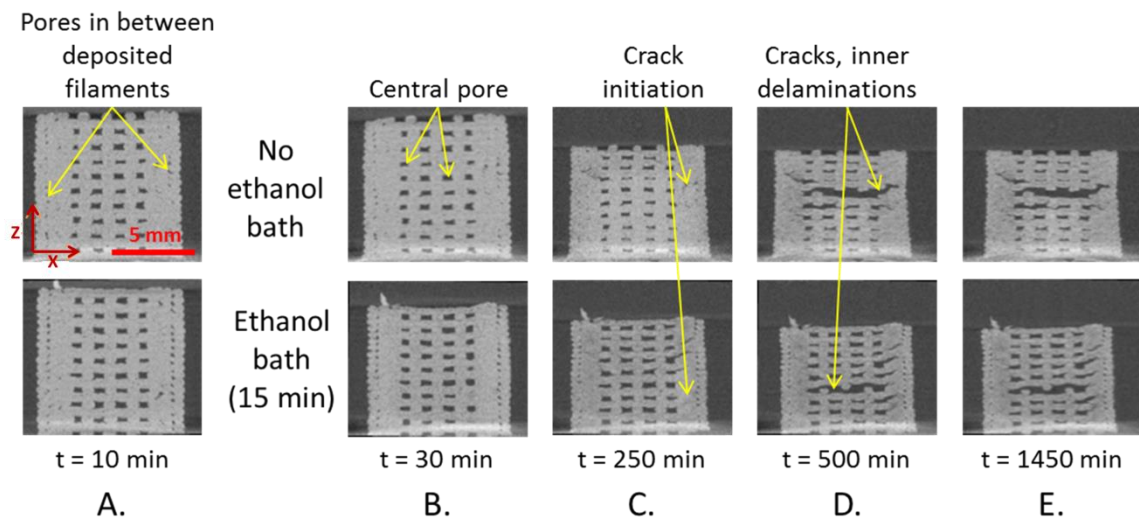


Figure 5-16. Temporal evolution of the 3D structure of the 9 mm side cube - 2D view of X-ray computed tomography scans of the (XZ) cross section belonging to the middle plan of the cube (A) 10 min, (B) 30 min, (C) 250 min, (D) 500 min and (E) 1450 min after the beginning of printing with air and ethanol drying at 30%RH.

Figure 5-16 shows inner slices of the 3D structure of cube during its drying in air or ethanol drying conditions for different times of the drying process. We can observe for example the oval cross section of the filament deposited as already mentioned by Pfister et al. 2004 in the case polyurethane scaffolds fabricated by bioprinting. We can also notice for both drying processes:

- A similar final strain for both drying conditions after a complete drying.
- A global anisotropic shrinkage characterized by a huge height deformation and a tinny thinning of the wall.
- Two drying periods: the first one was characterized by a size reduction of the part from Figure 5-16.A to C and the second one was characterized by cracks initiations and inner delamination from Figure 5-16.C to D.

For the ethanol drying condition, we can observe on Figure 5-16.B that after the ethanol bath, with the same time spent in open air, the cube present a larger vertical shrinkage than the cube that dried with air drying condition as previously showed with the filament drying monitoring.

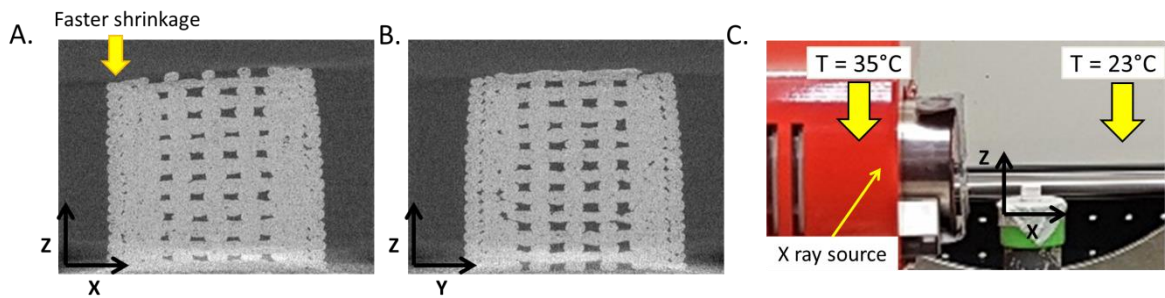


Figure 5-17. 2D views of X-ray computed tomography scans after 90 min of drying of the cross section belonging to the middle plan of the cube (A) (XZ) and (B) (YZ) with air drying condition. (C) Image of the experiment set up with the local temperatures.

A thorough scrutinization of the 3D views shows, as illustrated by Figure 5-17.A and B with the 2D views of X-ray computed tomography scan after 90 min of drying, a faster shrinkage on one side of the cube. This face was the closest one of the X-ray source. This is due to the gradient of temperature close to the cube (Figure 5-17.C): the X-ray source which was not stopped in between scans to obtain high quality images was at 35°C. It constituted a hot spot and heats the air at 23°C by thermal conduction.

5.4.2.2 Quantitative analysis

5.4.2.2.1 Preliminary remarks

The obtained stack of images can be quantitatively analyzed (i) to confirm the qualitative observations, (ii) to compare the temporal evolution of the relative volume of water that composed

the cube with the temporal evolution of the relative weight of water contained in the sample, (iii) to evaluate the evolution of the apparent volume (iv) to obtain an approximation of the drying rate of the cube to compare it with the one of the filament.

Figure 5-18.B and E show that the lower part of the scan was noisy due to the sample holder on which the cube was printed. The noisy part was removed to limit the error due to misinterpretation of the voxels during the segmentation phase. This leads to a volume of study that corresponds to a factor k in height of the 3D model (Figure 5-18.A, C, D and F). For the air-dried and the ethanol-dried cube, k equaled 0.89 and 0.87, respectively. The volume of the study is large enough to be representative of most of the structural changes that took place during the drying.

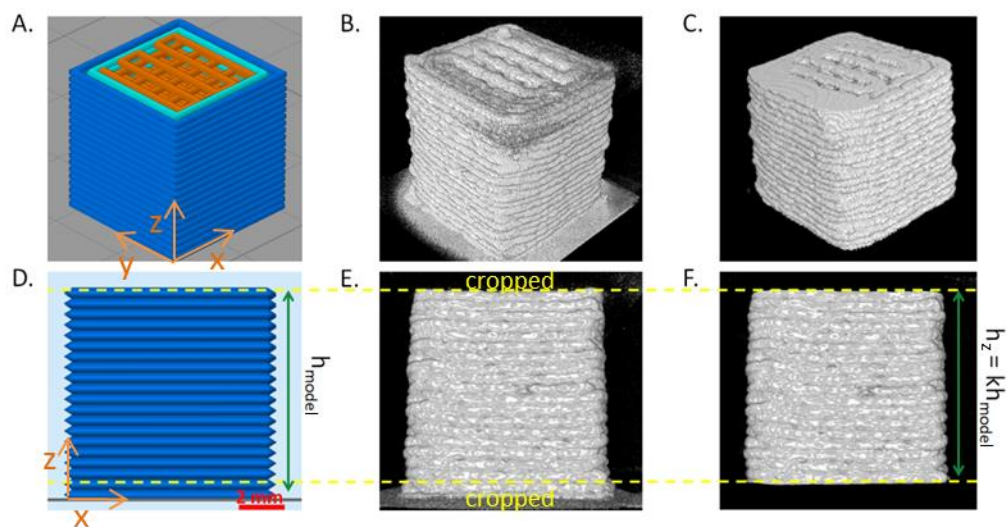


Figure 5-18 Determination of the volume of study. Isometric (A) and side (D) view of the 3D model (G-code). Isometric (B) and side (E) view of the first scan of the cube after binarization with a noisy lower part. Isometric (C) and side (F) view of the volume of study that corresponded to 87-89% in height of the 3D model.

5.4.2.2.2 Solid volume fraction analysis

The global and anisotropic shrinkages observed qualitatively in the previous section for both drying conditions (air and ethanol drying) were quantitatively assessed in this section by temporal monitoring of the relative solid volume of the cube, its relative apparent volume, its relative height and its relative length of its side. Moreover, the volume variation of the cube was compared with the mass variation to validate the 3D structural monitoring.

The anisotropic shrinkage was quantitatively analysed by temporal monitoring of (i) the apparent volume of the cube, V_{at} , that correspond to the volume of the cube defined by the outer surface of the vertical wall and the lower and upper slices considered to constitute the volume of study, (ii) the

height of the cube, h_t and (iii) the apparent length of the sides of the cube, l_{at} , calculated from the apparent surface area in (xy) plane of the cube (Figure 5-19.A).

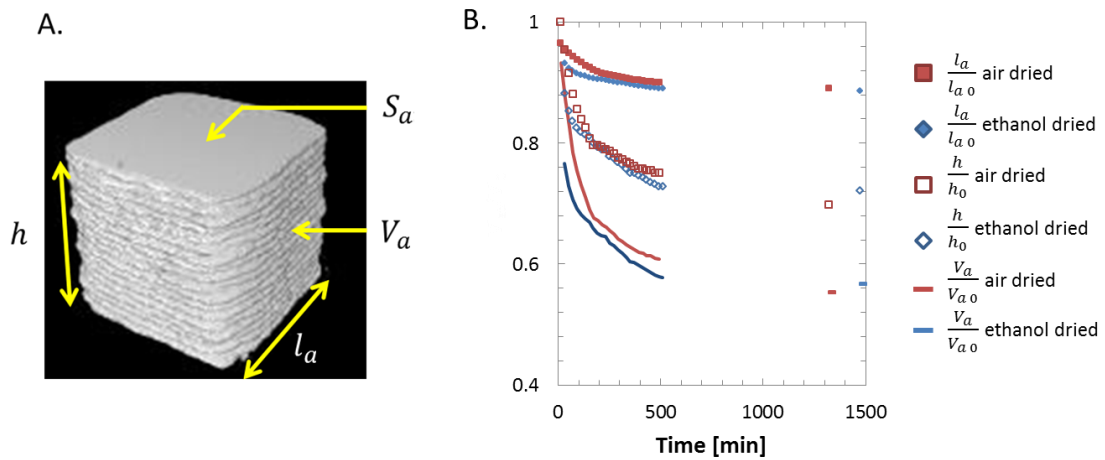


Figure 5-19. The anisotropic shrinkage – (A) 3D view of the scan with holes filled and (B) plot of the temporal evolution of the relative apparent volume of the cube, $\frac{V_a}{V_{a0}}$, the relative height of the cube, $\frac{h}{h_0}$ and the relative length of the sides of the cubes for both drying processes.

Figure 5-19.B shows the temporal evolution of such magnitudes. The initial value of the apparent volume of the cube was about 0.97 and 0.80 of the volume of a cube of 9 mm sides for the air drying and ethanol drying conditions, respectively. The final values were about 0.55 and 0.57. Up to 500 min, we can observe two drying periods that started with a strong decrease of the apparent volume of the cube and followed by a smaller one. Its temporal evolution can be decomposed in a vertical shrinkage that can be monitored by the height temporal evolution and in an horizontal shrinkage that can be monitored by the apparent length of the side of the cube in the horizontal plane. Both of these variables follow the same trend as the apparent volume. As noticed by the qualitative analysis of the drying induced shrinkage of the cube, the relative height of the cube vary from 1 or 0.92 to 0.70 or 0.72 for the air drying and ethanol drying condition whereas the shrinkage is less pronounced for the planar shrinkage with an apparent relative length of the side of the cube that vary from 0.97 or 0.94 to 0.89. Moreover, this planar shrinkage of the cube is partially due to the radial shrinkage of the filament that contributes to the height strain; its contribution represents 0.05 and 0.03 point of the relative length variation of the side of the cube for the air and ethanol drying conditions, respectively.

It should be noticed that unlike the final radial strain of filament (section 3.3.2 p.109), the final strain of the cube is quasi identical for both the air drying and ethanol drying conditions. For the ethanol drying conditions, the cube shows a larger strain than the filament (0.72 vs 0.8-0.75)

whereas for the air drying condition, the cube shows a smaller strain than the filament (0.70 vs 0.60-0.69). It can be explained by a too short ethanol bath duration to remove more water from the part or an inner structure that prevent the height strain during the air drying step due to a delay between the drying of the wall and the inner structure as presented in the following section.

Figure 5-20.A shows the temporal evolution of the relative solid volume, $\frac{V}{V_0}$ with V the solid volume of the volume of study of the cube at time t and V_0 , the solid volume of the 3D model corresponding to the volume of study. For both drying conditions, the decrease of the relative solid volume presents the same trend as the temporal evolution of the diameter of the filament in the previous section (section 5.3.2 p.164) with a sharp decrease followed by a transition before the equilibrium plateau about half of the initial volume as well as an initial relative solid volume after the ethanol bath much lower than the one of the air-dried. Moreover, the final relative solid volume for both drying conditions is in the same ranges of values than the apparent solid volume of the filament, calculated from the diameter strain (section 5.3.2 p.164): for ethanol drying, the value is slightly lower (0.51 vs 0.54) and for air drying, the value is a bit larger (0.48 vs. 0.35-0.43) than the ones measured for the filament. The final relative solid volume of the cube was expected to be lower than the apparent solid volume variation of the filament since the filament inner porosity larger than few voxels of about $28^3 \mu\text{m}^3$ were not taking into account for the solid volume of the cube.

Yet, the temporal evolution of the relative volume of water that composed the printed cube was evaluated on the volume of study defined above and compared to the temporal evolution of the relative weight of water obtained by averaging the values of 3 samples dried at 30%RH and 23°C with air or ethanol drying to validate the results of the 3D structural monitoring.

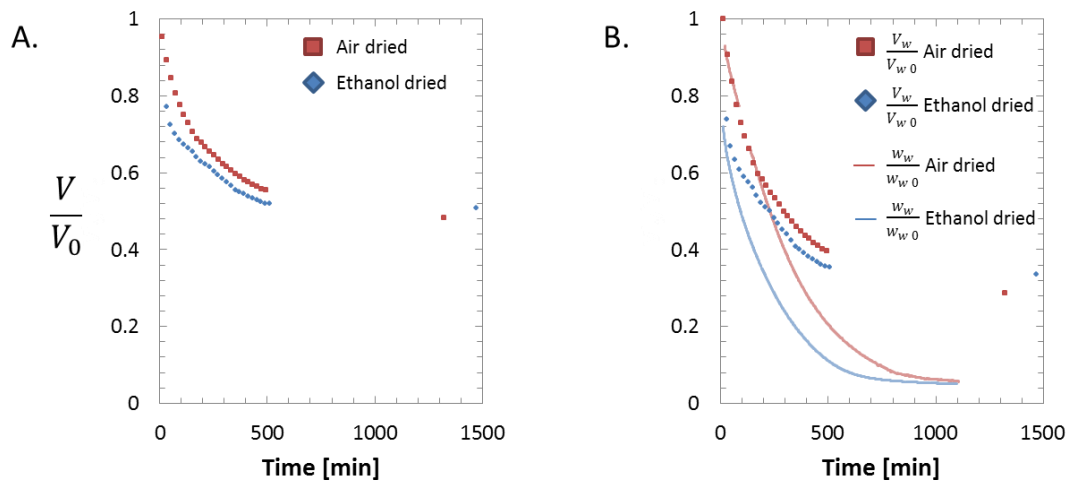


Figure 5-20. (A) Temporal evolution of the relative solid volume of the cube and (B) temporal evolution of the relative volume of water that composed the cube, $\frac{V_w}{V_{w0}}$ and of the relative weight of water in the cube, $\frac{w_w}{w_{w0}}$.

Figure 5-20 shows the temporal evolution of the relative volume of water that composed the cube, $\frac{V_w}{V_{w0}}$ (equation 10) as well as the relative weight of water, $\frac{w_w}{w_{w0}}$.

$$\frac{V_w}{V_{w0}} = \frac{V - V_0 \frac{\frac{DC_0}{\rho_c} + WC_0}{\rho_c + \rho_w}}{V_0 - V_0 \frac{\frac{DC_0}{\rho_c} + WC_0}{\rho_c + \rho_w}} \quad (10)$$

Where, V is the solid volume of the cube at time t obtained from X-ray tomography

$$DC_0 = \frac{w_{d0}}{w_{d0} + w_{w0}} = \frac{1}{MC_0 + 1} \text{ is the initial dried content of the paste}$$

$$WC_0 = \frac{w_{w0}}{w_{d0} + w_{w0}} = \frac{MC_0}{1 + MC_0} \text{ is the initial water content of the paste}$$

$$\rho_c = 1.5 \text{ g.cm}^{-3} \text{ is the cellulose density and } \rho_w = 1.0 \text{ g.cm}^{-3} \text{ is the water density}$$

We can observe as expected a lower relative volume of water and relative weight of water for the cube just after its immersion in ethanol compared to the ones of the cube that dried in open air. However, compared to the results on the filament, it remains a large amount of water in the part after the ethanol bath (71%).

For both drying conditions, we can observe two slopes for the temporal evolution of the relative volume of water during the first 8 h of drying. The first slope of the temporal evolution of the relative volume of water shows a good fitting with the relative weight of water of the cube for both drying conditions. Indeed, every unit volume of water (equivalent to gram) that evaporates should correspond to a decrease of one unit volume of the solid volume of the cube (Scherer 1990). The

space between fibers is filled by CMC and water. The significant difference that occurred for the second slope might correspond to a too low definition of the scan with the formation of micro pores below the resolution ($28^3 \mu\text{m}^3$) that occurred during the falling rate period. This slope change after 3h and 70 min for the air and ethanol drying conditions, respectively, might mark the transition between a global constant drying rate period and a global falling rate period characterized by a diffusion of water from the inside of the part to the surface slower than the evaporation rate. Likewise, both the drying conditions should have presented the same equilibrium point as the equilibrium moisture content was identical. The larger value for the ethanol drying condition might come from a larger number of micro pores that were assimilated with solid volume.

5.4.2.3 Drying kinetics of the cube

5.4.2.3.1 Preliminary remarks

A thorough scrutinization of the 3D views (Figure 5-16) shows a temporal and spatial variations of the grey level of the part. Yet, the grey level relies on the density of the matter: a lighter grey level (value tends to 65 535) corresponds to a more dense matter. Table 5-3 shows the temporal evolution of the grey level of an area about 1200 pixels belonging to the wall of the cube. During drying, the temporal density variation is due to the water evaporation which increases the density ($\rho_{\text{water}} = \frac{2}{3}\rho_{\text{cellulose}}$) and pores creations which decreases the density. We can observe for both drying conditions:

- a global decrease of the grey level (about 15% of the initial grey level) during the drying while the standard deviation remains quasi constant. It means that the part presents numerous small pores below the resolution ($28^3 \mu\text{m}^3$) which emphasis the explanation of the shift between the slope of the relative volume of water and relative weight of water of the previous paragraph.
- A quasi constant grey level at the beginning of the drying (until 250 min for air drying condition and 30 min for ethanol drying condition). Two explanations are possible: the drying of this area had not yet started as it is not directly in contact with air or the volume reduce, fibers became closer and few pores below the resolution appeared which do not affect the local density of the area covered by one pixel.

The final density of the ethanol-dried cube is slightly lower than the air-dried cube which is consistent with the results found on the single filament. Moreover, the density decrease of the ethanol-dried cube started before the one of the air-dried cube.

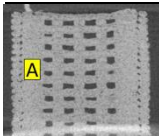
	Time [min]	10	30	250	500	1450
 Mean grey level of area A ($\times 10^3$)	Air drying	44 ± 3	44 ± 3	43 ± 4	38 ± 4	38 ± 4
	Ethanol drying	44 ± 2	43 ± 3	37 ± 2	36 ± 3	36 ± 3

Table 5-3. Temporal evolution of the grey level of a representative area of the wall of the cube.

5.4.2.3.2 Drying rate

The drying rate was calculated as presented in chapter 2, section 2.4.6.1 p.89. The exposed surface area corresponds to the outer surface described previously (section 5.4.1.1) over time calculated from the length and the height multiplied by $\frac{1}{k}$ in order to correspond to the actual height of the cube. To obtain a value of the exposed surface every minute, we calculated the value with a rule of three between the measured values every 20 min.

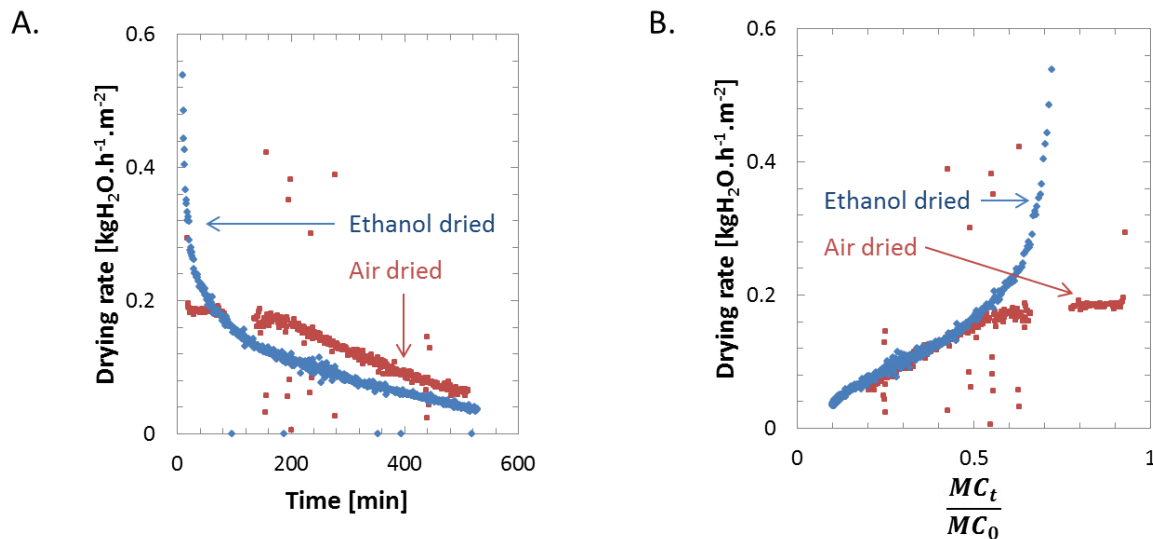


Figure 5-21. The drying kinetics of cube air-dried at 30%RH and ethanol-dried. The drying rate plotted (A) as a function of time and (B) as a function of the relative moisture content.

Figure 5-21 shows the drying kinetics of the cube with the ethanol and the air drying conditions. We can observe the same trend as the drying kinetics of the filament: the drying rate of the air-dried cube shows a constant rate period ($0.2 \text{ kgH}_2\text{O}\cdot\text{h}^{-1}\cdot\text{m}^{-2}$) and a falling rate period whereas the ethanol-dried cube shows two falling rate periods, the second one coincides with the air-dried cube. This overlapping of the two slopes shows that it remains only water in the sample after a while. The ethanol bath should have last longer. The transition between the two periods initiated after 3 h of air drying or a moisture content about 0.6 of the initial value and after only 40 min of ethanol drying or a moisture content of 0.6 of the initial value. These times that marked the transitions correspond to the ones of the transition observe in the section above (section 5.4.2.2). While we only consider the

outer surface of the cube to calculate the drying rate, the constant drying rate value of the air-dried cube is 6 times smaller than the one measured on the filament whereas, this value should only rely on the environmental conditions. This difference might come from an a weight measurement experiment performed at a larger relative humidity in a quasi-close chamber of the weight machine (only the top of the weight machine was open). Indeed, if we consider that the weight machine chamber was completely close, at the beginning of the experiment, at 23°C and 30%RH, the air in the chamber of 0.08 m³ contains about 0.5 g of water. At the end of the experiment, the cube loss about 0.4 g of water, so the air of the chamber contains about 0.9 g of water which corresponds at 23°C to about 55%RH which affect the drying rate. During the experiment, due to the absence of forced convection, the relative humidity close to the sample can even be larger than 50%RH. If we consider the equation (9) and results from Figure 5-11, the relative humidity is about 90%. The presence of a fan during the experiment should help to obtain the same drying rate during the constant drying rate period for the filament and the cube.

5.4.3 Temporal evolution of the cube at filament scale

The temporal evolution of the cube at filament scale was evaluated by monitoring the temporal evolution of the diameter of span filaments along the vertical direction in the middle of the cube and the temporal evolution of the volume of the macro pore of the cube. The objective was to locally study the temporal evolution of the strain during drying.

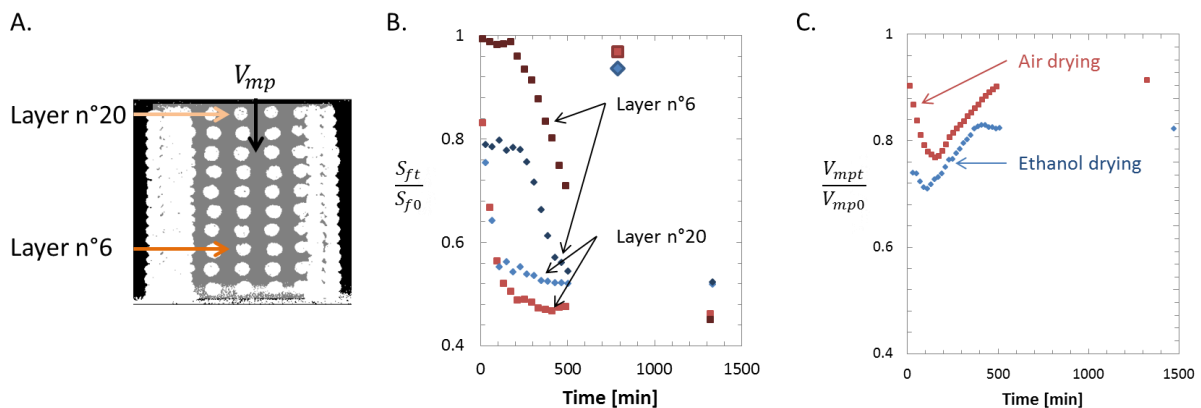


Figure 5-22. Temporal evolution of the cube at filament scale with air and ethanol drying conditions – (A) 2D view of binarized X-ray computed tomography scan (B) Plot of the temporal evolution of the relative cross section area of span filaments $\left(\frac{S_{ft}}{S_{fo}}\right)$ in the middle of the layer n°6 and n°20, the upper layer of the cube. (C) Plot of the temporal evolution of the relative volume of the macro pore $\left(\frac{V_{mpt}}{V_{mp0}}\right)$.

Figure 5-22.B shows the temporal evolution of the relative cross section area of span filaments located in the middle of a layer close to the bottom of the cube and the upper layer (Figure 5-22.A)

for both the studied drying conditions. For both drying conditions, we can observe that the cross section of the filament in the upper part of the cube immediately start to shrink to reach the equilibrium value whereas for the filament in the lower part of the cube, the cross section area was kept constant during the first 200 min before shrinking and reach the same equilibrium value as the one of the upper filament. This can be explained by an increase of the relative humidity inside the cube that can reach 100% and prevent evaporation of the filament in the lower part of the cube. It delays and extends the drying period without affecting the strain value. This also applied for the strength of adhesion between layers.

Figure 5-22.C shows the temporal evolution of the relative volume of the macro pore of the cube. For both the drying conditions, we can observe a first decreased of the volume of the macro pore before its volume increased. The variation of the macro pore is due to (i) the vertical strain of the cube, (ii) the radial strain of the filament inside the cube and (iii) the crack initiation that opened the inner wall of the cube. For the first 150 or 70 min for the air and ethanol drying conditions, respectively, the impact of the vertical strain on the volume of the macro pore is larger than the radial strain of the filament that constitute the inner part of the cube and no cracks are visible. This delay between the two strains limits the vertical strain of the cube as the inner structure must be compressed. Then, it is the radial strain of the inner filament that mainly contributed to the increase of the volume of the macro pore as well as the delamination between layers caused by the large filament strain, the drying gradient and a too low strength adhesion between filaments.

The drying of the cube can be decomposed in three phases:

- The first phase consisted in a strain of the outer structure of the cube mainly driven by a vertical strain of the cube and last from the beginning to about 3 h and 1 h 10 min for air and ethanol drying conditions, respectively.
- The second phase consisted in a strain of filaments that constitute the inner structure of the cube from the top to the bottom. It is during this drying phase that delamination and cracks could occur due to the gradient of strain in the cube and a limited strength adhesion between the filaments. It started after the first phase until at least 8 h.
- The third phase consisted in the stabilization of the strain induced by the drying that start after the 8 hours of monitoring.

It can be noticed that the delamination between layers of the 3D structure study in Chapter 4 were larger for part with a 100% infilled structure than for part with lighter inner structure (35% infill). Indeed, the vertical strain of the outer structure applies a vertical compression on the 3D structure. The resistance of the inner structure to this compression strength is larger the more the

inner structure is dense, reducing the resulting strain and the adhesion between layers. Then, when the inner structure starts to dry, no resistance to the compression is encountered, resulting in a free strain until the strain of the inner structure exceed the strain of the outer structure leading to opening of cracks and delamination.

5.5 Dimensional compensation strategy

The dimensional compensation strategy consists in printing a bigger object than the one with the targeted dimension. This strategy was implemented on two parts: a double spiral vase which is a hollow and high structure that allows an easy and accurate height measurement and a fast printing (about 1 h) and a small cube of 9 mm side for both of the drying conditions studied. The vase was immersed during 2 h in the ethanol bath whereas the cube was only immersed during 15 min.

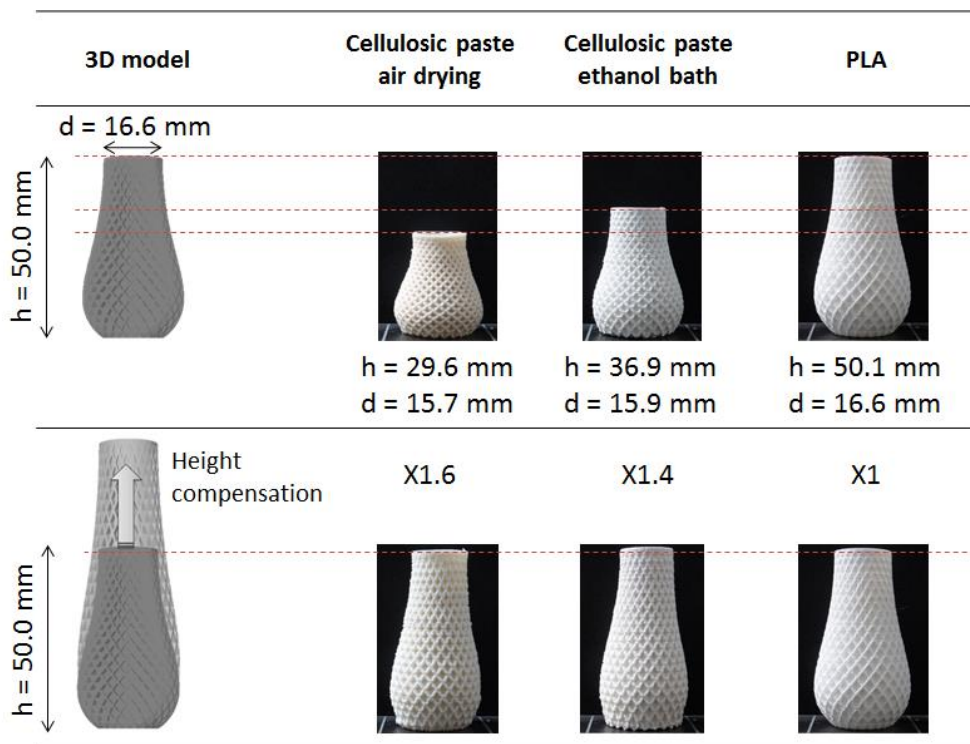


Figure 5-23. 3D printing of a double spiral vase with the optimized formulation dried with or without an ethanol bath or with polylactic acid (PLA). Upper row: 50mm high vase. Lower row: vase with height compensation in the model based on the calculated strain.

Figure 5-23 shows 3D printed solid vases with the optimized paste or with polylactic acid (PLA). The vases in the first row of Figure 5-23 were printed with the same 3D model. As expected, the vase printed with PLA maintained shape fidelity, as it did not exhibit any dimensional variations from the model. When printed with the optimized paste, the air-dried model exhibited height and external

diameter outlet strains of 41% and 5%, respectively. These strains decreased to 26% and 4%, respectively, by the addition of an ethanol bath before air drying. The height strain of the vase was larger than the radial strain measured on a single filament with a radial strain about 33 and 23% for air and ethanol drying respectively and than the cube in the previous section with a height strain about 30 and 28% for air and ethanol drying, respectively. This may have been due to (i) the subsidence of the first layers due to an overhang angle of 45° with almost 60% of the filaments unsupported, (ii) the addition of a load during drying due the weight of the layers pressing down on the lower layer, (iii) a larger drying time due to a smaller surface contact and greater volume compared to those of a filament and, (iv) the absence of an inner structure to partially prevent the strain as in the case of the printed cube. The strain of the external diameter outlet was a combination of longitudinal and radial strains of the filament. These strains, mainly observed in the vertical plan of the part, enable us to devise a strategy to directly compensate for the height change by introducing a vertical compensation in the digital 3D model to obtain a printed and solid (dried) part with the desired height. The results are shown in Figure 5-23. With a multiplier coefficient in height of 1.6, a printed vase similar to the one produced using fused filament fabrication with PLA was achieved whereas a multiplier coefficient in height of 1.5 was sufficient for the cube with the inner structure. This multiplier coefficient in height on the digital model was slightly lower than the calculated strain for the 50 mm high vase (-5%). This may be due to (i) no subsidence of the first layer of the 80 mm high vase due to a lower overhang angle of 32° and (ii) a compensation of the height strain due to slow drying during the printing (printing time $\times \sim 1.6$). However, this dimensional compensation approach becomes less practical for printing larger objects. Therefore, the solvent exchange (water \rightarrow ethanol), which minimized the radial strain of the filament, may be a good option for reducing dimension changes upon drying. Indeed, the 3D printed 50 mm high vase immersed in ethanol after completion showed a significantly lower strain, with only 26% height strain compared to the 41% strain for the non-immersed part. In this case, a multiplier coefficient in height of 1.4 was used to compensate for the drying strain (Figure 5-23).

5.6 Conclusion

In this chapter, the two drying conditions identified (air drying and ethanol drying conditions) were studied in details by monitoring the temporal evolution of the building block of 3D structures (the filament) and of a simple 3D object (the cube).

First, the conditions of ethanol drying were optimized and guidelines regarding the concentration (> 70wt.% of ethanol 95%) and the immersion time (from 10 min to more than 2h depending on the thickness of the printed object) were proposed based on qualitative and quantitative criterion.

Then, the monitoring of the drying of the filament allows first quantifying by image analysis the anisotropic shrinkage observed in chapter 3: the radial strain of the filament (30-40%) was about 10 times larger than the longitudinal one. Moreover, the ethanol dried filaments present less volume variations (radial strain about 20 to 25%), they allow being seized after their ethanol bath and they dry faster ($\times 2.5$ at 23°C and 30%RH). However, the filament presents more porosity and lower mechanical resistance. The choice of the drying conditions is a compromise between a better dimensional stability upon drying and lower mechanical resistance. The study of the drying kinetic of the filament as a function of its moisture content (calculated from the temporal monitoring of its dimensions and its mass) allowed to identify, as described in the literature, a constant drying rate period followed by the falling rate period until a quasi-null drying rate that ends the drying process. Most of the dimensional changes happen during the constant drying rate period. During this drying period, the drying rate can be tailored by the relative humidity for a given temperature and as a consequence, limit the strain that occur during the printing time of one layer that can cause printing failure. Yet, to go further in the understanding of the applied stress during the drying, the Young's modulus and the strain induced by the transversal strain of the filament were monitored.

The drying mechanisms were also studied on a 3D cube of 9 mm side using in situ fast X-ray micro-tomography. This innovative characterization technique allowed us to monitor the temporal evolution of the inner and outer structure of the cube during the first 8h of drying with an accurate resolution to couple the strain mechanism observed with the moisture content of the cube. A qualitative analysis of the obtained scans showed for both drying conditions a first phase that consisted in a vertical strain of the cube followed by a second phase, where, in parallel of the strain of the filament that constitute the inner structure, delamination and cracks occurred due to a competition among the adhesion forces between the filaments and the stresses induced by the strain of the filament. The analysis of the obtained scans allowed us to quantify the volumetric variation of the cube (solid and apparent) as well as the dimensional variation of the filament inside the cube for both drying conditions and confirmed the results of the qualitative analysis. From these results, the global drying kinetics was calculated and showed the same trend as the drying kinetics of the filament with the identification of the different drying periods. Furthermore, the slow drying kinetics confirmed the small volume variation occurring during long printing that should not cause failure during printing.

The experimental vertical compensation strategy implemented show positive results to obtain a dried printed object with the targeted dimensions despite the strain induce by the drying. However, the height multiplier coefficient depends on the presence or absence of an inner structure. This

compensation strategy is even more interesting with the ethanol drying condition as the printing time will be reduced compared to the air drying condition.

General conclusion and perspectives

Conclusions

The main objective of this PhD project was to evaluate the possibility of developing a cellulose-based material to produce complex objects by Additive Manufacturing (AM) by extrusion. Such developments are necessary to extend the choices of printed material for this technology that is in constant evolution.

All the chapters of this manuscript are tightly linked to each other, so that the complete study brings a thorough understanding of the development of an innovative material to produce reasonably complex and accurate 3D parts by AM by extrusion with optimized set up.

In the state of the art, presented in **chapter 1**, a particular attention was paid on the one hand on the process of additive manufacturing by extrusion and on the other hand on cellulosic based materials. This chapter ended with a general overview of the use of cellulose in AM by extrusion with the main strategies implemented to overcome the challenges. It also pointed out the difficulties (i) to formulate paste with large fiber content compatible with AM by extrusion (ii) to use directly commercial printers and (iii) to limit the deformation of 3D printed parts upon drying in a simple and low cost manner. In order to overcome these difficulties, an experimental procedure was developed and proposed in **chapter 2**. It consisted in paste preparation mainly based on short cellulose fibers, CMC and water. These pastes were extruded to form 3D parts thanks to a commercial printer that was upgraded. The 3D printed parts were air-dried using two protocols based on the addition or not of an ethanol bath. These drying protocols were studied in details. Different characterization procedures were developed depending on the aim of the analysis: rheological tools for paste characterization, structural and mechanical testing on wet and dried part. Protocols were also proposed to monitor the evolution of the 3D structure upon drying process.

In **chapter 3**, the development and characterization of cellulose based formulations with strong potential for AM by extrusion was developed. The chapter identified three formulations with strong

potential for AM by extrusion: two inert pastes and a conductive one (0.3 S.m^{-1}). They are composed of (i) fillers that vary in shape, in nature and in concentration in the matrix: cellulose fiber (30 wt.%), cellulose powder (37.5 wt.%) and graphite powder (57 wt.%) and, (ii) a matrix made of CMC at a concentration from 17 to 20 wt.% in water. These formulations were identified based on criteria that should ensure accuracy between the cellulose printed part and the 3D model: (i) filament extrusion, (ii) shape fidelity before drying, and (iii) limiting deformation after drying. To fulfill these criteria, these identified pastes exhibited a pronounced thinning behavior and a yield stress after relaxation, which are critical parameters for 3D printing parts. Moreover, all the printed filaments exhibited an anisotropic shrinkage: a larger radial strain than the longitudinal strain. This radial strain of about 33% in the case of the cellulose based paste lead to porous structures. The fibrous cellulose based filament exhibited high Young's moduli ($\sim 5 \text{ GPa}$) in a dry state. In the following chapters, we only focused on the cellulose fibrous based paste.

The **chapter 4** was dedicated to the optimization of the paste printing conditions. First, the extrusion flow, the printing parameters and the shape of the nozzle were optimized for the customized printer in the case of the fibrous paste identified in chapter 3. Such studies allowed to propose guidelines to print 3D parts that exhibited simple shape, overhang angle of 35° or 45° , thin and high vertical features or bridging features. This guideline was used to AM by extrusion a complex 3D boat. Therefore, this chapter confirmed the 3D printing compatibility of the developed paste.

In **chapter 5**, a detailed characterization of the drying phenomena that occurred in both the filaments and 3D parts was carried out. First, the ethanol drying condition were optimized: immersing the 3D printed part in an ethanol bath of a concentration of at least 66° during at least 10 minutes prevents the deformation upon drying of the 3D printed parts. Then, during different drying conditions (air and ethanol drying), the study of the temporal evolution of the filament such as its dimensions, its moisture content and its mechanical properties has established a large database to better understand the drying mechanism of this paste on the building block of 3D structures. Then, the drying of simple 3D parts such as a small cube was monitored in 3D by fast X-ray tomography scan. This analysis proposed to link the drying kinematics with structural changes such as the apparition of cracks due to delamination effects or filament shrinkage and pores modifications. Finally, a compensation strategy to anticipate the vertical shrinkage of the 3D parts was proposed and validated.

Figure C-1 illustrates the main achievements summarized above.

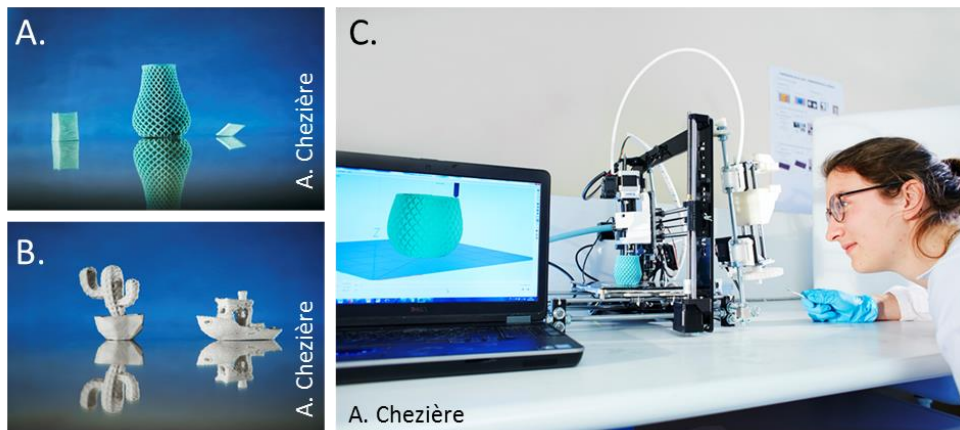


Figure C-1. Pictures of dried 3D printed parts with the optimized fibrous cellulose paste (A) with a dye and (B) without dye. Photography (C): on going AM by extrusion of a 3D structure. (copyright A. Chezière).

The overall conclusion coming from the project is that at the beginning of the project, few studies had shown the compatibility of cellulose as an AM material by extrusion; the use of cellulose as a raw material for AM by extrusion is still in maturation phase. Through this project, cellulose fibers were implemented for the first time into a paste that can be shaped by AM by extrusion to produce complex parts as illustrated in Figure C-1, close to PLA 3D printed part in term of design, mechanical properties and cost. However, the development of a conductive material for 3D pattern or the use of one for 2D pattern for producing a smart object demonstrator is still in development. A first prototype was made during a student project at Pagora's engineering school (Figure C-2).

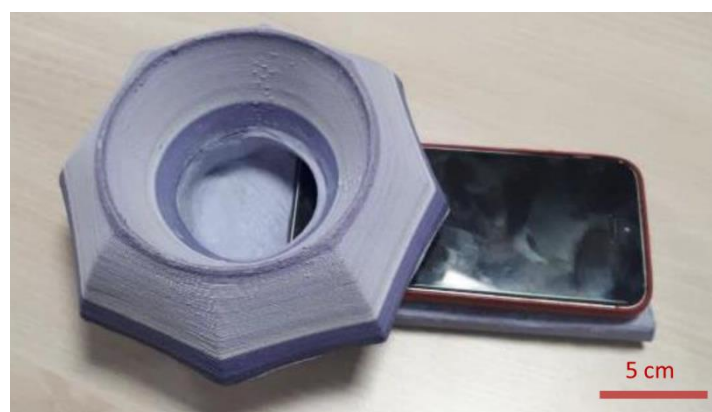


Figure C-2. Preliminary results on a smart object demonstrator.

Scientific productions

The work on development of innovative cellulose based material for AM by extrusion was summed up through a proof of concept publication in a scientific journal and shared through different oral presentations within the academic campus and abroad as listed below.

- 1 Publication in rank A journal: Thibaut, C., A. Denneulin, S. Rolland du Roscoat, D. Beneventi, L. Orgéas, et D. Chaussy. 2019. « A fibrous cellulose paste formulation to manufacture structural parts using 3D printing by extrusion ». *Carbohydrate Polymers*, janvier. <https://doi.org/10.1016/j.carbpol.2019.01.076>.
- 1 Oral presentation in an international conference: H. Murtaza, C. Thibaut, S. Rolland du Roscoat, P. Lhuissier, L. Salvo, A. Denneulin, E. Endo, O. Stamati, L. Orgeas, D. Beneventi, D. Chaussy, “A real-time monitoring of air drying of 3D cellulose printed parts by extrusion with fast lab x-ray micro-tomography”, Euromat2019, Stockholm, Suède.
- 1 Poster presentation in an international conference: C. Thibaut, H. Murtaza, A. Denneulin, S. Rolland du Roscoat, P. Lhuissier, L. Salvo, D. Beneventi, L. Orgéas, D. Chaussy. “A fibrous cellulose water based paste: characterization during drying of 3D printing parts produced by extrusion”, BioPol2019, Stockholm, Suède.

Perspectives

In this work, a methodology was set-up to develop paste made up of short cellulosic fibers fully compatible with Additive Manufacturing by extrusion and to prevent the effect of air-drying on the printed parts. The limitations of such an approach come from:

- the amount of water present in the initial paste that induced the huge anisotropic shrinkage of the 3D printed parts. Developing new formulations and new paste preparation method could prevent this problem by increasing the solid content. For example, additions of mineral charges could increase the solid content. This approach coupled with a twin-screw extruder is an interesting way to scrutinize. Another solution could consist in replacing the water by photo-polymerizable matrix.
- the capacities of the customized printer and software which is limited in terms of (i) the temperature controlled of the extruded paste and (ii) the use of large tank without printing speed limitation and (iii) the choice of the printing path to manufacture the 3D part. Such developments should be completed by the evaluation of the adhesion between layers in the wet state as a function of the printing settings. This should help to propose complete guidelines to define the printer parameters. A customize printers with several extruder head would be judicious for multi-materials printing such as the printing of smart object.
- the absence of a model to predict the local strain, damage of the part and mechanical properties as a function of the part design and the printing parameters selected. The current work settled the experimental protocol necessary to build it and to validate it.

In parallel to these developments, it should also be useful to complete formulation aspects by introducing nanocellulose fibers that would (i) facilitate the paste extrusion through smaller nozzles inducing a high surface resolution of the 3D printed part, (ii) decrease the surface roughness of the filament, which is a key point for advanced strategies of conductive ink deposition. Another point to investigate is the thermal cross linking of CMC on dried parts to delay its disintegration in contact of water without addition of resin or to consider 4D printing with part swelling when immersed in water.

All these developments were necessary to propose strategies to produce centimetric to decimetric size objects as initiated or smart objects with both inert and conductive materials.

Résumé étendu en français

Introduction générale

La fabrication additive (FA) ou impression 3D est reconnue comme une technologie de rupture et trouve des applications dans de nombreux secteurs d'activités comme le secteur automobile, le secteur médical ou le secteur du loisir. Ce procédé, par ajout de matière, est utilisé pour produire des objets 3D à partir de modèles numériques, le plus souvent couche par couche contrairement aux procédés de fabrications soustractifs. Ainsi, la fabrication additive regroupe de multiples procédés d'ajout de matière classifiés et décrits par la norme NF ISO 17296-2 présentant leurs propres avantages et inconvénients. De façon générale, ces procédés offrent de nouvelles opportunités en termes de design et prototypage telles que des pièces aux formes plus complexes ou allégées en matière, des délais de fabrication courts et des modifications de design simplifiées permettant la personnalisation par exemple (Huang, Liu, Mokasdar, & Hou, 2013). De plus, cette technologie est compatible avec de nombreux matériaux tels que les métaux, les polymères, les céramiques, les gels et les matériaux bio-sourcés (Wohlers, Caffrey, & Campbell, 2016). Par ailleurs, l'utilisation de matériaux bio-sourcés et biodégradables est actuellement mis en avant du fait de leurs nombreux avantages environnementaux en plus de leurs caractéristiques intrinsèques, notamment le stockage du carbone contenu dans l'atmosphère, leur disponibilité en tant que matériaux renouvelables, la préservation de ressources non renouvelables telles que les minerais ou les matériaux fossiles et une fin de vie des objets élaborés peu impactant pour les sols ou les océans.

La fabrication additive (FA) par extrusion de matière, l'une des catégories établies par l'ISO, regroupe le plus grand nombre d'imprimantes 3D installées (domestiques ou industrielles) (Wohlers et al. 2016). Ce procédé permet de produire des pièces complexes et allégées par dépose sélective de matière à travers une buse sous forme d'un filament continu présentant des propriétés d'écoulement spécifiques. Il est capable d'élaborer des objets multimatériaux avec des résolutions de l'ordre du demi-millimètre ainsi que des objets fonctionnalisés dits 'intelligents'. L'acide polylactique (PLA), un thermoplastique bio-sourcé produit à partir d'amidon et dégradable dans des composts

industriels, est très utilisé en FA par extrusion dû à sa facilité d'utilisation (Steinle, 2016; Wittbrodt & Pearce, 2015) et sa capacité, en tant que matrice, à être chargée comme par exemple avec des particules de carbone, rendant le PLA conducteur (conductivité de 10^2 à 10^3 S.m⁻¹).

La cellulose sous forme de fibres étant le polymère bio-sourcé le plus abondant dans la nature et présentant d'excellentes propriétés mécaniques (Dufresne, 2013), peut être un matériau prometteur pour la production par FA par extrusion de structures 3D à bas coût, légères, robustes et compostables. Ainsi, elle pourrait être utilisée en tant qu'additif comme renfort mécanique ou bien comme modificateur rhéologique, ou encore en tant que matière première principale (Dai et al., 2019).

Dans ce contexte, ce projet vise à évaluer la possibilité de mettre au point de nouveaux matériaux bio-sourcés cellulosiques qui pourront être mis en forme via le procédé d'impression 3D par extrusion pour produire des objets 3D complexes et multimatériaux. Les résultats de ce projet permettront d'élargir la gamme de matériaux disponibles et compatibles à cette technologie en constante évolution. Il paraît ainsi justifié de se fixer comme référence pour notre travail, les pièces produites en PLA par FA par extrusion au regard de leurs résolutions, des designs possibles, des propriétés mécaniques ainsi que de leur aspect économique.

Au début de ce projet, plus de vingt ans après le développement du procédé de FA par extrusion (US5121329A, 1992), une seule étude portait sur l'utilisation de cellulose comme matière première principale pour la fabrication d'objet 3D par ce procédé (Markstedt, Sundberg, & Gatenholm, 2014). Ce décalage temporel laisse entrevoir les nombreux verrous à lever pour formuler un matériau fibreux tel qu'une suspension ou une pâte compatible avec la FA par extrusion. A la fin du projet, soit 3 ans après, plus d'une douzaine d'études publiées portaient sur la FA par extrusion de formulations composées essentiellement de cellulose montrant le potentiel et l'intérêt portés à la cellulose comme matière première principale pour l'impression 3D. Par ailleurs, ces études balayent de nombreuses possibilités de formulation avec l'utilisation de multiples formes de cellulose, de pourcentages de matière sèche, de résolutions (taille de buse), de formes d'objets imprimés comme preuve de concept, de post traitements (ex : réticulation et/ou séchage) et d'applications (ex : médicale, énergie). Cette variété de formulations proposée provient des nombreux verrous soulevés par la FA par extrusion et des multiples atouts de la cellulose pour répondre à certaines de ces exigences. Pour s'imprimer en 3D par extrusion, la cellulose doit s'écouler de façon homogène à travers la buse puis se figer immédiatement pour assurer le maintien de la forme imprimée (J. A. Lewis, 2006). Ce comportement rhéologique, à la différence des polymères thermoplastiques, ne peut pas s'obtenir par changement de température et donc être utilisé avec le procédé de FA par

extrusion de matière fondue. Un adjuvant liquide doit être ajouté dans un juste équilibre pour obtenir les propriétés d'écoulement spécifique à l'extrusion du matériau et en même temps, être compatible avec l'immobilisation immédiate du matériau après extrusion sans un changement rapide de viscosité dû par exemple à la réticulation, une évaporation rapide ou la coagulation du matériau. De plus, l'évaporation du liquide risque d'engendrer des problèmes tels que le rétrécissement de l'objet imprimé après séchage et de la délamination.

Ainsi, les nombreux obstacles à lever pour accomplir l'objectif principal de ce projet sont en lien direct avec les objectifs visés en termes de design de l'objet, de ses propriétés mécaniques, de sa résolution, de son coût et de ses applications. Notre étude s'est basée sur les paramètres principaux résumés dans le diagramme Ishikawa de la Figure R-1 i.e, la composition du matériau, le design de l'objet 3D, l'imprimante 3D utilisée, les paramètres impression sélectionnés, les facteurs environnementaux et le post traitement de l'objet.

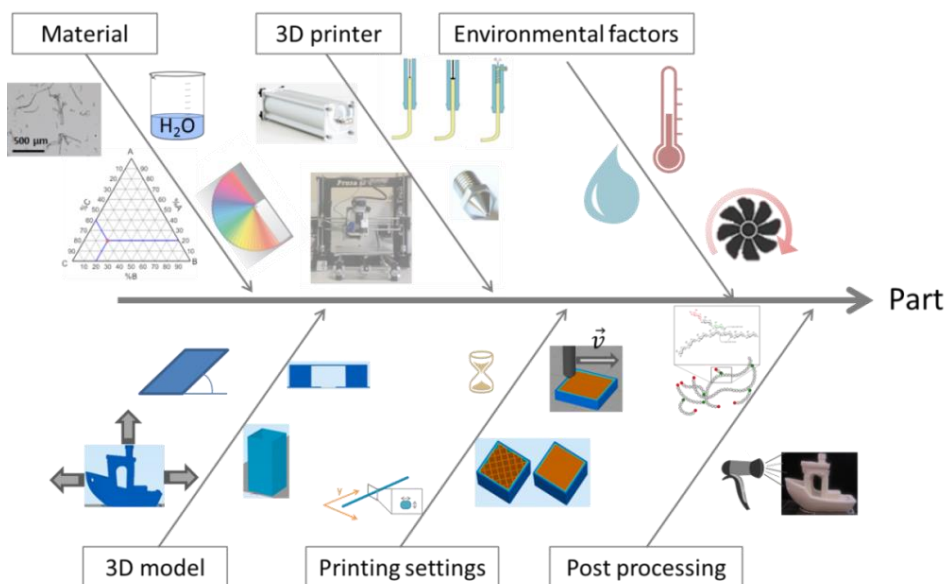


Figure R-1. Synthèse des paramètres principaux de l'étude pour l'obtention d'objet 3D imprimé conforme au cahier des charges.

L'étude de ces paramètres a conduit à un travail multidisciplinaires couvrant différents champs tels que la formulation, la rhéologie, le procédé, la caractérisation de matériaux et le procédé de séchage. Comme montré par la Figure R-2, le manuscrit, rédigé en anglais, est ainsi composé de ces mêmes 5 chapitres dont les résultats principaux sont synthétisés en français dans la suite de ce résumé étendu.

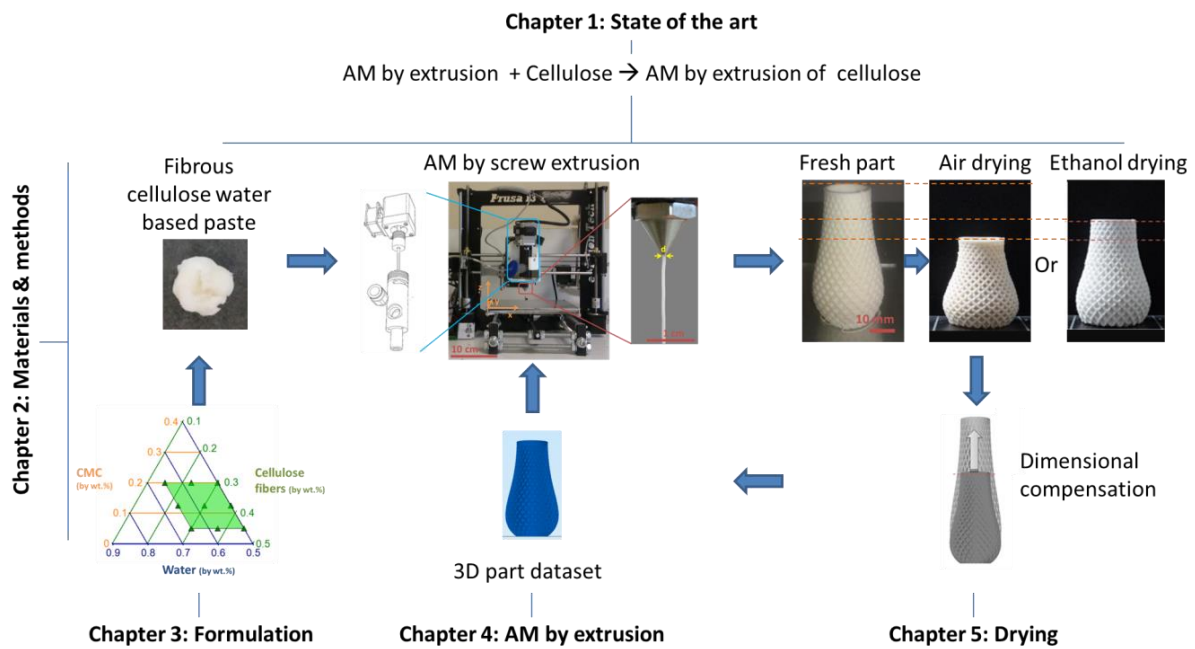


Figure R-2. Représentation schématique de l'organisation du manuscrit.

Etat de l'art

Le chapitre bibliographique s'articule autour de 2 axes majeurs :

- la description de la FA et en particulier du procédé de FA par extrusion
- la description des matériaux cellulosiques existant et de leur utilisation en FA par extrusion

Ce chapitre permet ainsi de conclure sur les motivations du projet et les axes d'études choisis.

Comme décrit précédemment, le terme de FA et les sept catégories de procédés qu'elle comprend ont été définies par la norme NF ISO 17296-2. Chacune de ces catégories se différencie par son principe d'ajout de matière (architecture de machine identique et mécanisme physique de transformation des matériaux similaire (Laverne, Segonds, et Dubois 2016)) conférant des caractéristiques propres aux pièces produites ainsi que par sa gamme de matériaux disponibles compatibles avec le procédé en question. **La FA par extrusion** est un procédé intéressant de par son faible coût, son environnement d'installation peu contraignant type bureau, sa facilité d'utilisation notamment avec un faible post-traitement nécessaire et enfin sa capacité à produire des structures 3D complexes et allégées en matière avec une ou plusieurs têtes d'extrusion (approche multimatières). Cette catégorie de procédés regroupe de nombreuses technologies connus sous différentes appellations telles que le dépôt de fil fondu, la bio-impression, le robo-casting ou encore le liquid deposit modeling (LDM). Tous ces procédés comportent typiquement trois phases comme illustrées Figure R-3: (i) une phase d'extrusion d'un filament de matière, (ii) une phase de dépôt de ce

filament couche par couche pour former une pièce volumique et (iii) une dernière phase qui permet la solidification de la pièce.

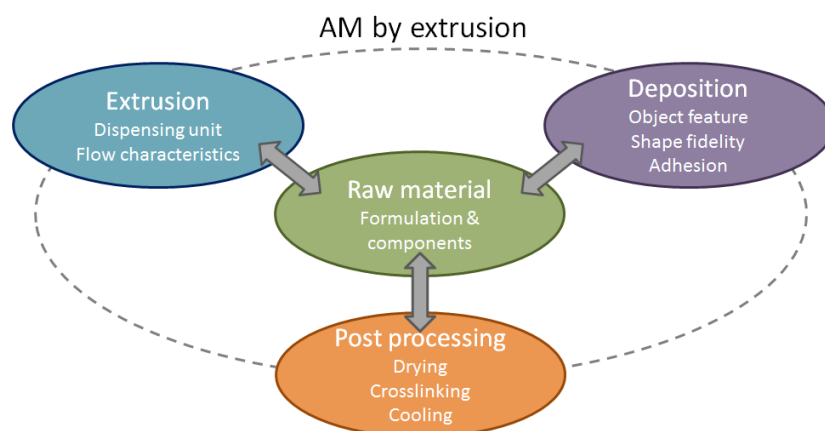


Figure R-3. Dépendance de la matière première avec les étapes clés de la FA par extrusion : extrusion, déposition et post-traitement.

Les matériaux compatibles avec ce procédé répertoriés dans la littérature sont principalement des gels, des suspensions colloïdales, des pâtes très concentrées, des composites ou des thermoplastiques. La plupart étant composé de petites particules solides et sphériques (<1/10 voire 1/100 du diamètre de la buse) avec un adjuvant liquide tel que de l'eau ou une résine thermodurcissable présentant une densité proche de celle des particules afin de favoriser une bonne stabilité colloïdale du matériau ainsi formé (Coussot, 2012) et donc de favoriser une extrusion continue du matériau mélangé préalablement de façon adéquate afin d'éviter tout risque de colmatage (J. Benbow et Bridgwater, 1993). Cet adjuvant liquide abaisse la résistance à la déformation du matériau ainsi constitué pour faciliter la phase d'extrusion mais contribue également à accentuer le phénomène de retrait après séchage. De nombreux auteurs (Jennifer A Lewis et Gratson, 2004; Compton et Lewis, 2014; M'Barki, Bocquet, et Stevenson, 2017; Feilden, 2017 ; G. Siqueira et al. 2017) ont affirmé que ces matériaux développés compatibles avec la FA par extrusion devaient être rhéofluidifiants et posséder une contrainte seuil (modèle de Herschel-Bulkley) avec par exemple des valeurs de viscosité apparentes de 10^4 Pa.s à 0.1 s^{-1} et de 10 Pa.s à 10^2 s^{-1} et une contrainte seuil de 10^2 - 10^3 Pa pour un matériau imprimé en 3D avec un système d'extrusion pneumatique. Ces grandeurs peuvent varier en fonction des spécificités du système d'extrusion choisi, des paramètres d'impression et les spécificités de l'objet 3D imprimé. Pour les matériaux thermoplastiques, leur viscosité varie lors des étapes du procédé de FA par extrusion par changement de température. Notons que le comportement rhéologique des matériaux est un paramètre essentiel pour leur compatibilité au procédé de FA par extrusion.

Lors de **la phase d'extrusion**, le matériau est soumis à

- un écoulement élongationnel à l'entrée de la buse dû à un rétrécissement de section,
- un écoulement sous cisaillement dû aux frottements aux parois dans la buse,
- une recouvrance de la déformation élastique et élongationnelle en sortie de buse.

Ces forces résultantes liées au design de la buse impliquent une poussée du matériau suffisamment élevée pour obtenir un débit suffisant en sortie d'extrusion et conduisent dans certains cas à différents phénomènes comme l'alignement de fibres ou encore un gonflement ou une rupture de surface du filament en sortie de buse. Des dispositifs d'extrusion variés existent. Ils sont caractérisés par leur température de fonctionnement, leur système de transport du matériau, la forme interne de la buse et enfin le diamètre de sortie de la buse. Le choix de ces caractéristiques est lié au matériau sélectionné et en particulier à son comportement rhéologique.

L'objectif lors de **la phase de déposition** du filament est d'obtenir une structure autoportante, fidèle au modèle, présentant une bonne adhésion entre les filaments. Chaque structure 3D pouvant être décomposée en structure 3D élémentaires, des objets modèles reprenant ces structures élémentaires ont été conçus pour évaluer le matériau, l'imprimante 3D utilisée et les paramètres d'impression. Cette stabilité structurelle liée à l'utilisation d'un nouveau matériau peut ainsi être évaluée soit par preuve de concept puis caractérisation rhéologique intensive (valeurs de références) ou bien par modélisation théorique des efforts appliqués sur le matériau donnant ainsi des valeurs numériques de limites de compatibilité du matériau associé à un design particulier. L'adhésion entre les filaments est connue comme étant le point faible des objets imprimé en 3D par extrusion dû à la présence de porosité et une force d'adhésion faible. Cette dernière étant le résultat d'une pression du filament sur la couche précédente et une consolidation à l'interface.

La phase de solidification est le processus qui intervient entre la phase de déposition et la phase de stabilisation de la structure dans le temps. Les phénomènes de solidifications varient en fonction du matériau utilisé. De ces différents phénomènes de solidification résultent l'apparition de contraintes interne au matériau pouvant conduire à des déformations plus ou moins importante de l'objet imprimé. Par exemple, lors de la phase de solidification, les matériaux thermoplastiques cristallisent de façon inhomogènes dans le temps et l'espace conduisant à un retrait dimensionnel limité tandis que pour les matériaux composés d'un adjuvant liquide, la matrice peut réticuler conduisant à un retrait acceptable ou s'évaporer conduisant à un retrait importante possible en fonction du procédé de séchage utilisé (séchage super critique, lyophilisation, séchage à l'air avec ou sans échange de solvant). Le procédé de séchage utilisé influence le retrait dimensionnel, la densité et les propriétés de l'objet ainsi obtenu.

De nombreux défis sont donc à relever pour développer de nouveaux matériaux compatibles avec la FA par extrusion liés aux différentes phases du procédé : préparation du matériau, extrusion, déposition, solidification. Ces exigences relèvent principalement du comportement rhéologique du matériau. De plus ces nouveaux matériaux doivent également être renouvelables et biodégradables pour répondre aux défis environnementaux et espérer avoir un futur.

Or **la cellulose** qui compose la paroi des celluloses végétales est le matériau le plus abondant et disponible à travers le monde. Son organisation moléculaire spécifique et ses multiples procédés d'extraction possibles permettent l'obtention d'un large panel de matériaux avec des propriétés distinctes telles que les fibres papetières de cellulose, les fibres de nanocellulose, les éthers et esters de cellulose (ex : la carboxyméthylcellulose et l'acétate de cellulose).

Deux revues récentes (Dai et al. 2019 ; Q. Wang et al. 2018), recensent **l'utilisation de la cellulose et de ses dérivées dans la composition de matériaux compatibles avec la FA par extrusion** notamment comme additifs. Leurs rôles sont par exemple le renforcement, la modification rhéologique ou encore l'utilisation en tant que matrice, charge de matrice, liant, plastifiant ou excipient. Cependant, la FA par extrusion de cellulose comme matière première principale présente de nombreux défis car la contribution des autres composants des formulations précédentes devra également être apportée par la cellulose elle-même. Cependant, récemment, quelques formulations ont été proposées comme illustrée par le Tableau R-1 avec l'utilisation de multiples formes de cellulose, de pourcentages de matière sèche, de résolutions (taille de buse), de formes d'objets imprimés comme preuve de concept, de post traitements (ex : réticulation et séchage) et d'applications (ex : médicale, énergie).

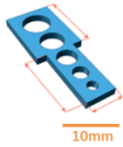





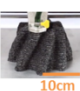








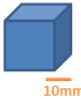









Matériau	Modèle 3D	Objet 3D imprimé	Référence
❖ Thermoplastique Poly(éthylène-2,5-furandicarboxylate) (PEF)		 <p>Retrait thermique négligeable < 3,4%</p> 	Kuchеров et al. (2017)
❖ Cellulose dissoute Acétate de cellulose (AC) - AC ~ 25-35%		 <p>Evaporation quasi immédiate (~1min) de l'acétone</p> 	Pattinson et al. (2017)
❖ Suspension aqueuse Fibres papetières (FP) + liant - FP ~ nd% $d_f \sim 20-50 \mu\text{m}$, $l_f \sim \text{mm}$		<p>Avant séchage</p>  <p>Résolution ~1cm</p>  <p>Séché à l'air</p>  <p>Affaissement</p> 	Holthuis (2018)
Nanocelluloses - % Nanofibrilles < 5% $d_f \sim 5-10 \text{ nm}$, $l_f \sim \mu\text{m}$		<p>Lyophilisation</p>   <p>Echange de solvant</p>  	Håkansson et al. (2016)
- % Nanofibrilles < 5% $d_f \sim 5-10 \text{ nm}$, $l_f \sim \mu\text{m}$		<p>Lyophilisation</p>   <p>Echange de solvant</p>  	Klar et al. (2019)
- % Nanocristaux ~ 20% $d_f \sim 5-10 \text{ nm}$, $l_f \sim 100 \text{ nm}$		<p>Lyophilisation</p>   <p>Echange de solvant</p>  	Li et al. (2017)

Tableau R-1. Résumé des principales études portant sur l'utilisation de la cellulose comme matière première principale pour la FA par extrusion.

Ces formulations mettent en lumière les différents défis à relever ainsi que les stratégies développées pour y répondre partiellement (forte modification de la cellulose, nécessité d'ajout d'un adjuvant liquide, problème d'adhésion entre les couches et procédé d'impression lent pour la formulation de cellulose dissoute, déformation importante avec un séchage à l'air alors que la quantité de matière sèche maximale est atteinte pour les formulations à base de nanocelluloses). Ainsi, les questions suivantes peuvent être soulevées : la cellulose pourra-t-elle concurrencer le PLA et devenir un nouveau matériau peu cher, léger, robuste, renouvelable et biodégradable compatible avec la FA par extrusion ? Sous quelle forme (fibres de cellulose naturelle, nanocellulose, dérivée de cellulose) devra-t-elle être utilisée et avec quel adjuvant liquide ? Quelle quantité de matière sèche devra être ajoutée pour limiter la déformation après séchage et le coût du procédé de séchage tout en restant extrudable ? Existe-t-il des restrictions de design ou de nouvelles opportunités de design par rapport au procédé de dépôt de filament fondu avec les matériaux thermoplastiques comme le PLA ? Un matériau conducteur à base de cellulose peut-il être mis en œuvre comme le composite conducteur PLA/graphène ?

Pour faire face à ces interrogations, **ce projet** propose le développement d'un matériau 100% cellulosique compatible avec la FA par extrusion pour produire des objets complexes et multi-matières (ex : objet fonctionnel conducteur) avec comme cible le PLA et ses capacités d'impression, c'est à dire :

- une résolution de l'ordre de 0.4-0.8 mm
- une vitesse d'impression de 10 à 50 mm.s⁻¹
- une capacité à être imprimée sous forme d'objet complexe
- des propriétés mécaniques avec un module de Young de 2-3 GPa
- une manutention et une utilisation sans danger
- un coût faible ainsi que celui des objets produits (<30€/kg)
- une valeur de conductivité de 10²-10³ S.m⁻¹ sous forme de composite graphène/PLA

Pour atteindre cet objectif, ce travail a porté sur :

- Une formulation de pâte concentrée composée de fibres courtes de cellulose et CMC ou de graphite et CMC,
- L'adaptation d'une imprimante 3D pour être compatible avec les pâtes développées,
- Le séchage à l'air d'objet 3D dense avec la possibilité d'une étape préalable d'échange de solvant pour réduire le retrait après séchage.

Ces trois axes de travail ont été développés dans les chapitres résultats du manuscrit (Chapter 3, Chapter 4 et Chapter 5) et sont résumés ci-dessous.

Développement et caractérisation de formulations cellulosiques compatible avec la FA par extrusion

Comme décrit précédemment, les principales limites des formulations proposées dans la littérature par rapport à notre objectif de développer un matériau cellulosique similaires aux PLA en termes de caractéristiques et processabilité sont :

- l'impression précise d'un objet à l'état humide,
- le procédé onéreux de lyophilisation permettant de garantir les dimensions et la structure de l'objet imprimé à l'état sec bien que l'extrait sec de la formulation soit limité à 20% massique entraînant des propriétés mécaniques et une densité faible,
- un procédé d'impression lent pour permettre l'évaporation de l'adjuvant liquide et la compensation dimensionnelle immédiate due à son évaporation.

Cependant, parmi les formulations développées et les applications visées, il n'a pas été rapporté de formulations utilisant des fibres de cellulose de diamètre micrométrique utilisé pour des impressions présentant des résolutions de l'ordre du demi-millimètre. Or les dimensions moyennes des fibres papetières sont les suivantes : une longueur de 1 à 5 mm, un diamètre de 10 à 50 μm et une épaisseur de paroi de 1 à 5 μm (Niskanen, 1998). Le diamètre de ces fibres est donc bien compatible avec la résolution visée (0.5 mm) : le diamètre de fibre est plus de cent fois inférieur aux valeurs de diamètre de la buse (autour des 500 μm). Cependant, la longueur de ces fibres devra être raccourcie à 0.5 mm pour respecter la résolution visée. L'utilisation de ces fibres de cellulose semble être la plus prometteuse pour produire des structures 3D à bas coût, légères, robustes et recyclables dans l'esprit des objets imprimés en PLA. Des tests préliminaires de formulation avec ce type de fibres réduit en poudre et des nanocelluloses comme modificateur rhéologique ont montré une séparation de phase du matériau pouvant conduire à un bouchage dans la buse notamment quand le pourcentage volumique de poudre de cellulose a été augmenté pour limiter le retrait après séchage. Ainsi, un dérivé de la cellulose, le carboxyméthyl cellulose (CMC), additif reconnu pour son rôle épaississant, ses propriétés hygroscopiques, sa capacité à maintenir des particules en suspension et ses propriétés liantes, a dû être ajouté pour limiter la séparation de phase.

Dans le **chapitre 3** du manuscrit, trois formulations ont pu être identifiées comme ayant un fort potentiel pour la FA par extrusion parmi de nombreuses formulations évaluées en faisant varier leur extrait sec, leurs proportions de CMC et celles des particules micrométriques organiques (cellulose sous forme de fibres courtes ou poudre et poudre de graphite). Comme il lustrée par la Figure R-4, ces formulations ont été identifiées en se basant sur trois critères spécifiques développées par nos soins qui devraient garantir une reproduction la plus fidèle possible du modèle en cellulose après impression :

- extrudabilité d'un filament,
- impression 3D d'un objet précis à l'état humide et,
- limitation (et prévision simple) de la déformation après séchage à l'air.

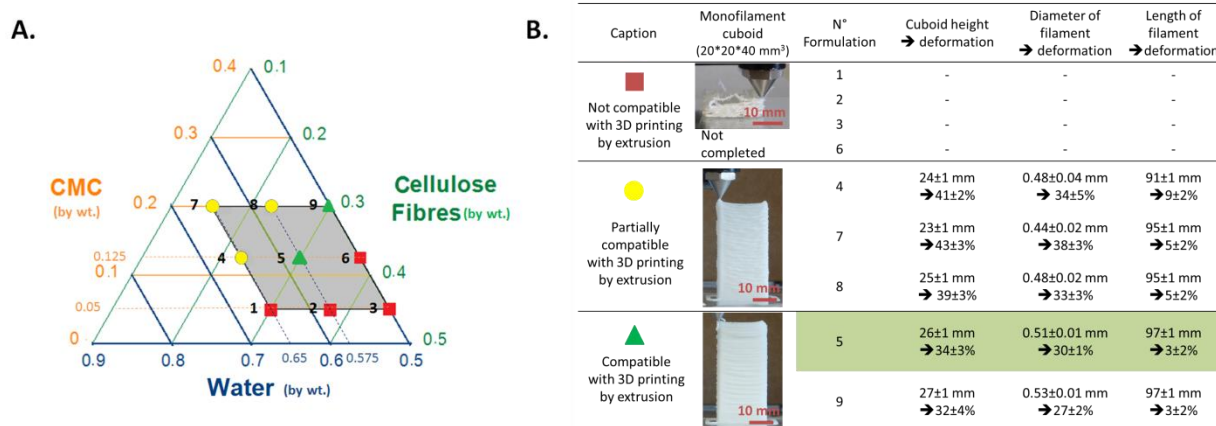


Figure R-4. Diagramme ternaire en fraction massique présentant les formulations évaluées composées de CMC, de fibres de cellulose et d'eau. (B) Caractérisation qualitative et quantitative des 9 formulations élaborées pour évaluer la compatibilité avec la FA par extrusion.

Ces formulations identifiées sont donc composées (i) de particules micrométriques dont leur forme, leur nature et leur concentration varient dans la matrice : fibres de cellulose (30% massique soit 23% volumique), poudre de cellulose (37.5% massique soit 30% volumique) et poudre de graphite (57% massique soit 38% volumique) et (ii) d'une matrice composée de CMC à 17 et 20% massique en « solution » aqueuse. Cette matrice possède :

- une viscosité importante à l'état humide ou la présence d'une contrainte seuil car elle ne semble pas s'écouler dans son flacon à moitié rempli après 5 min lors du changement de sa position verticale à une position horizontale,
- un module de Young de 2.8 GPa, une contrainte maximale de 37 MPa et une élongation à rupture de 1.7% après séchage, résultats obtenus par des tests de traction sur des éprouvettes rectangulaires de CMC d'environ 200 µm d'épaisseur,
- une conductivité à l'état sec d'environ 0.3 S.m⁻¹ lorsque 14 à 33% volumique en base sèche de graphite sont incorporés à la matrice et mis en forme sous l'aspect de filament à l'aide de la tête d'extrusion de l'imprimante 3D utilisée (vis sans fin et buse de 0.7 mm de diamètre).

Le comportement rhéologique de ces pâtes a été caractérisé en adaptant des essais de compression avec une méthode nommée lubricated squeeze flow. Pour chaque pâte cellulosique, les résultats obtenus ont montré un comportement rhéofluidifiant prononcé et une contrainte seuil après relaxation, paramètres essentielles pour l'impression 3D. Par exemple, pour la formulation identifiée à base de fibres courtes de cellulose, la courbe de viscosité a pu être modélisée par une loi puissance d'équation $\eta_{0,3} = 3.5 \cdot 10^4 |\dot{\epsilon}_{0,3}|^{-0.8}$ et la contrainte seuil mesurée était de 6 kPa. De plus, toutes ces pâtes extrudées sous forme de filament homogène présentent une déformation

anisotrope après séchage à l'air : la déformation radiale du filament est plus importante que celle longitudinale. La déformation radiale, $\left| \frac{d_{\text{sec}}}{d_{\text{humide}}} - 1 \right|$, était d'environ 30% pour les pâtes cellulosiques et seulement de 8% pour celle de graphite conduisant à plus ou moins de porosité dans le filament. Les filaments produits à partir de la formulation à base de fibres de cellulose présentent un module de Young élevé (~5 GPa) à l'état sec alors que, immergé dans de l'eau, le filament se délite, ce qui peut permettre la réutilisation de la pâte. Cependant, pour conserver la forme du filament et ainsi augmenter ses propriétés mécaniques à l'état humide, un agent de résistance à l'état humide (Kymene) doit être ajouté à hauteur de 1% massique en base sèche dans la formulation. Une autre possibilité peut être la réticulation de la CMC avec la cellulose à haute température (180°C). Des tests préliminaires ont montré un impact positif de ce traitement à haute température de l'objet imprimé avec la pâte cellulosique fibreuse pour éviter le délitement quasi immédiat de l'objet 3D imprimé.

Pour la suite de l'étude, nous avons retenu la formulation suivante : 30.0% massique de fibre courte de cellulose, 12.5% massique de CMC et 57.5% massique d'eau et nous l'avons utilisée pour optimiser le procédé d'impression 3D et le séchage. Cependant les mêmes études peuvent être menées avec les 2 autres formulations sélectionnées.

Optimisation des paramètres d'impression et de l'imprimante 3D pour produire des objets 3D conformes au cahier des charges avec la formulation optimisée

Pour imprimer en 3D un objet avec le procédé de FA par extrusion, une imprimante 3D et un logiciel de découpage en tranches (slicer) sont utilisés pour garantir un contrôle précis du débit d'extrusion et du chemin de dépose du filament.

- L'imprimante 3D est essentiellement constituée d'une tête d'extrusion adaptée à la rhéologie du matériau, d'un système de déplacement dans les 3 directions (X, Y et Z), d'un plateau d'impression, d'un contrôleur électronique et d'une alimentation électrique.
- Le slicer convertit un modèle 3D sauvegardé sous format STL (données correspondant à la surface de l'objet maillée par des triangles) en Gcode, un langage de programmation permettant de piloter l'imprimante 3D par séquences d'instructions telles que les coordonnées du point à atteindre, la vitesse de déplacement et la quantité de matière à extruder.

Alors qu'à ces débuts, la plupart des imprimantes 3D étaient dites « propriétaire » (ou fermées) ne permettant pas la customisation au niveau du logiciel utilisé, des matériaux utilisés ni des

paramètres d'impression, ce type d'imprimante a laissé place aux imprimantes 3D dites « ouvertes ». La version la plus aboutie de ces imprimantes ouvertes est le projet RepRap (Jones et al. 2011) avec le développement open source du logiciel et du hardware permettant un contrôle complet des différentes options du procédé. Le pendant à cette ouverture est la nécessité de mettre en place de nombreux guides de dépannage et des procédures de maintenance et calibration de l'imprimante (horizontalité du plateau, débit d'extrusion et déplacement de la tête d'extrusion précis...). Ce large panel d'options disponibles touche aussi bien aux paramètres d'extrusion (largeur de filament déposé, multiplicateur d'extrusion, paramètres d'amorce et d'arrêt de l'extrusion), aux paramètres de couche (nombre de périmètre de contour, hauteur de couche), aux paramètres de remplissage de l'objet (le pourcentage de remplissage interne, le motif de remplissage) mais aussi à la température d'impression, à la vitesse d'impression, au positionnement de l'objet à imprimer, à l'ajout de matériaux de support et bien d'autres encore. Ces paramètres n'ont été que peu étudiés lors d'utilisation de matériau sous forme de pâte ou suspension. Le plus souvent, les articles scientifiques traitent de l'élaboration d'une formulation et de ses propriétés rhéologiques avant de conclure sur une impression 3D réussie d'un objet imprimé avec un ensemble de paramètres définis, de façon similaire au chapitre 3 de ce manuscrit.

Ainsi, **le chapitre 4** a permis d'identifier, parmi les paramètres d'impression (logiciel) et les technologies d'impression 3D disponibles (hardware), les principales conditions d'impression favorisant ou limitant la fabrication d'un **objet 3D précis à l'état humide**. L'optimisation de ces conditions d'impression pour la formulation développée s'est décomposée en trois étapes clés liées au procédé de FA par extrusion :

- Contrôle précis du débit d'extrusion dans sa plage d'utilisation assuré par (i) une tête d'extrusion constituée d'une pompe à vis alimentée en continu par la pâte cellulosique, elle-même contenu dans le réservoir pressurisé, (ii) un débit d'extrusion proportionnel à la vitesse de rotation de la vis sur la plage d'utilisation (observation d'un décrochage pour des vitesses de rotation trop élevées dû à un possible reflux lié à une pression de refoulement qui augmente) (iii) une mesure précise du facteur de calibration du débit d'extrusion réel par rapport au débit théorique calculé en fonction de la vitesse de rotation de la vis, (iv) une forme interne de buse spécifique avec une réduction graduelle de la section finissant par un canal d'extrusion de diamètre constant suffisamment long pour permettre l'alignement des fibres et éviter des perturbations de l'écoulement et (v) un nettoyage efficace de l'imprimante 3D et de son environnement (tête d'extrusion, réservoir, robot planétaire de mélange...) facilité par la bonne dispersion de pâte solidifiée au contact de l'eau avec pour objectif d'éviter le bouchage de la buse par un amas de particules solides.

- Déposition précise du filament sur la piste définie au sein d'une couche : la calibration de l'imprimante telle que le déplacement de la tête d'extrusion et le parallélisme entre la tête d'extrusion et le plateau d'impression a été réalisée.
- Fabrication d'un objet 3D : des impressions de structure 3D élémentaires telles qu'un cube, un surplomb de 35 et 45° par rapport à la verticale, un élément haut avec des parois fines ou encore un élément de pontage ont été réalisés en faisant varier la valeur des trois paramètres d'impression : la hauteur de couche, la largeur de piste et le facteur d'extrusion. Le choix des paramètres optimaux s'est basé sur des critères principalement qualitatifs. Ces résultats ont permis de proposer un premier protocole d'impression avec des plages de valeurs de paramètres d'impression à utiliser (Table 4-1 p.149) et l'identification de limites en termes de design d'objet telles que les éléments avec un rapport d'aspect élevé.

En appliquant les résultats obtenus pour la maîtrise de ces 3 étapes clés, un modèle complexe de bateau a été imprimé (Figure R-5). Il illustre ainsi le potentiel et les limites de la formulation sélectionnée.

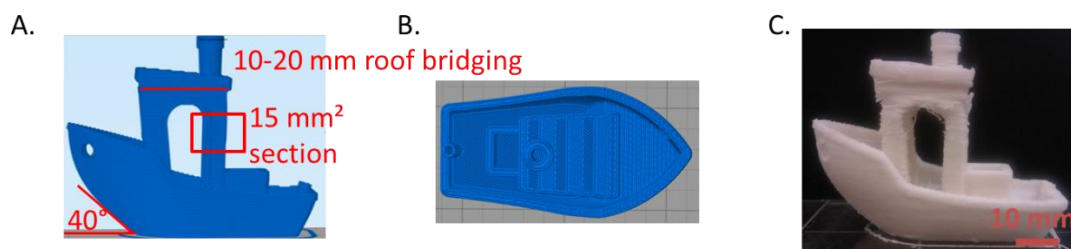


Figure R-5. Modèle complexe téléchargé via Thingiverse.com, 2018, 3DBenchy – Vue de (A) coté et (B) du dessus du modèle slicé, (C) Vue de coté de l'impression 3D du modèle avec la pâte à base de fibres de cellulose à l'état humide.

Notre étude s'est concentrée sur les paramètres d'impression principaux. Cependant, l'étude de l'influence de nombreux autres paramètres semble également intéressante tels que l'amorce et l'arrêt de l'extrusion, la température de la pâte (5° à 30°C), le chemin de dépose du filament. De plus, la mise en place d'une méthode quantitative d'évaluation de l'adhésion entre les filaments en fonctions des paramètres d'impression aurait pu renforcer et compléter le protocole proposé.

Etude du séchage en vue de fabriquer un objet 3D imprimé fidèle au modèle à l'état sec

L'un des aspects majeurs des objets imprimés avec la pâte développée à base de fibres de cellulose est que celle-ci contient plus de 50% massique d'eau, ce qui correspond à presque 70% en volumique et que cette eau s'évapore lorsque l'objet est à l'air libre. Le séchage joue donc un rôle

majeur dans l'objectif d'obtenir un objet sans défauts, fidèle au modèle dans ses dimensions et sa structure. La lyophilisation a fait ses preuves pour des formulations à faible extrait sec (<20% massique de cellulose et >80% massique d'eau). Le séchage par échange de solvant est lui moins performant mais permet tout de même de réduire la déformation par rapport à un séchage à l'air libre (Håkansson et al. 2016). Mais si l'extrait sec de la formulation est plus élevé (40-60% volumique comme pour les céramiques), un séchage lent à l'air permet d'obtenir des objets denses sans déformations ou fissures (Feilden, 2017 ; Peng, Zhang et Ding 2018). Pour éviter donc un coût prohibitif de l'objet après séchage et comme l'extrait sec de la formulation développée est de 30% volumique, nous avons préféré nous concentrer sur un séchage par évaporation de l'eau contenue dans la formulation ou de solvant après une seule étape d'échange de solvant (procédé de séchage simple). L'éthanol est un bon candidat comme solvant car il est miscible dans l'eau, peu cher et sa tension superficielle est trois fois plus faible que celle de l'eau, réduisant ainsi les forces capillaires lors de son évaporation. Lors du séchage, 2 phénomènes interviennent : l'évaporation du solvant et la diffusion du solvant de l'intérieur de l'objet vers sa surface externe en réaction à de nombreuses forces internes telles que la pression capillaire (Scherer 1990). L'évolution de la vitesse relative de ces 2 phénomènes évolue au cours du séchage et permet de définir 2 périodes de séchage distinctes :

- La période de séchage à vitesse constante : la vitesse d'évaporation est l'élément limitant et l'évaporation s'effectue à la surface de l'objet. La vitesse de séchage est donc proportionnelle à l'humidité relative.
- La période de ralentissement : la vitesse de diffusion est l'élément limitant. La teneur en humidité de la partie externe de l'objet est plus faible qu'à l'intérieur.

Dans le **chapitre 5** du manuscrit, les deux procédés de séchage sélectionnés (séchage à l'air précédé ou non d'une immersion dans un bain d'éthanol) ont été étudiés en détails en suivant l'évolution temporelle d'un élément constitutif de n'importe quel objet imprimé (le filament) et d'un objet 3D simple (un cube de 9 mm de côté).

Les conditions d'immersion de l'objet dans l'éthanol (temps d'immersion et concentration du bain) pour permettre un échange de solvant (au moins partiel) ont tout d'abord été optimisé en basant l'étude sur des critères à la fois qualitatifs (aspect de l'objet imprimé) et quantitatifs (mesure de déformation et test de traction) sur différents objets 3D (filament et structure en H de différentes épaisseurs). Les résultats ont conduit aux préconisations suivantes : la concentration du bain d'éthanol doit être supérieure à 66% massique en prenant en compte la dilution partielle du bain due à l'échange de solvant et le temps d'immersion qui doit être supérieur à 10 min ou 2h en fonction de l'épaisseur de l'objet considéré.

L'étude du séchage du filament a permis tout d'abord de quantifier par analyse d'image la déformation anisotrope observée au chapitre 3 : la déformation transversale d'un filament (~30-40%) est presque 10 fois plus élevée que sa déformation longitudinale. De plus, les filaments séchés après avoir été immergés dans l'éthanol ont montré une variation volumique plus faible (variation transversale de 20 à 25%), ils peuvent être manipulés dès que le temps d'immersion dans l'éthanol est écoulé et ils sèchent plus vite ($\times 2.5$ à 23° et 30%RH). Cependant, leur porosité s'accroît et leurs propriétés mécaniques diminuent (module de Young de 2 GPa). Le choix du procédé de séchage est donc un compromis entre une meilleure stabilité dimensionnelle après séchage et des propriétés mécaniques plus faibles. Une étude de la cinétique de séchage du filament en fonction de sa teneur en humidité (obtenue grâce au suivi des variations dimensionnelles et de sa masse au cours du temps) a permis ensuite d'identifier, comme décrit dans la littérature, une première période de séchage à vitesse constante (vitesse proportionnelle à l'humidité relative pour une température donnée) suivie d'une période de ralentissement jusqu'à une vitesse nulle marquant la fin du séchage. L'essentielle des variations dimensionnelles s'opèrent lors de la période de séchage à vitesse constante. Sa vitesse de variation peut donc être ajustée en fonction de l'humidité relative pour une température donnée pour s'adapter au temps d'impression d'une couche de l'objet et ainsi limiter les défauts d'impression. Ainsi, pour aller plus loin dans la compréhension des efforts en jeu lors du séchage, le module de Young et la force longitudinale induite par le séchage ont été mesurés au cours du séchage.

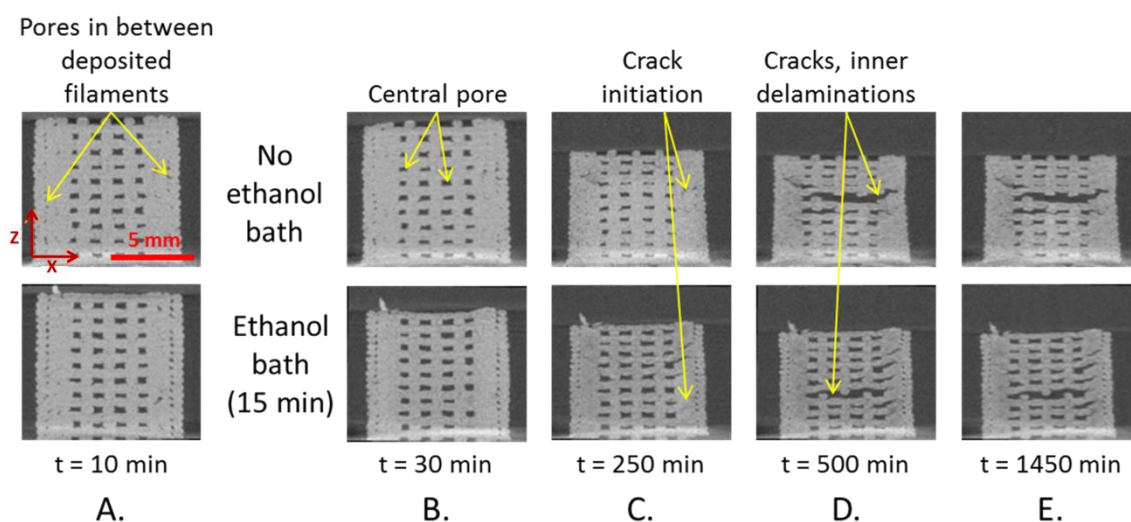


Figure R-6. Evolution de la structure 3D interne d'un cube de 9 mm de côté au cours du séchage – vue 2D de scans de tomographie à rayons X (A) 10 min, (B) 30 min, (C) 250 min, (D) 500 min et (E) 1450 min après le début de l'impression avec un séchage à l'air (23°C-30%RH) précédé ou non d'une immersion dans un bain d'éthanol.

Les mécanismes de séchage ont également été étudiés in situ sur un cube de 9 mm de côté imprimé en 3D en utilisant une technique originale d'acquisition rapide d'image par tomographie à rayon X. Cette technique de caractérisation a permis le suivi de l'évolution de la structure interne et externe d'un cube au cours du séchage pendant les 8 premières heures avec une résolution suffisante et donc de coupler des observations sur l'évolution de la teneur en eau du matériau et les mécanismes de déformation. Nous avons pu observer qualitativement (Figure R-6) une première phase ($t = 0-250$ min) avec un retrait vertical de la structure, puis, dans une seconde phase ($t = 250-1450$ min), où, en parallèle de la déformation des filaments composant la structure interne, apparaît un amorçage de fissures et de délamination, résultat de la compétition entre les forces d'adhésion entre les filaments et les forces de retrait dimensionnelle des filaments. La mise en place d'une méthode de suivi de l'adhésion entre 2 filaments serait intéressante pour définir la vitesse maximale de séchage autorisée pour éviter les fissurations. L'analyse des scans obtenus a également permis de quantifier les variations volumiques du cube (solide et apparent) ainsi que les variations dimensionnelles du filament à l'intérieur du cube pour les 2 conditions de séchage et ainsi confirmer l'analyse qualitative. La cinétique de séchage globale du cube a ainsi pu être obtenue (avec le suivi de la masse) en considérant seulement la surface extérieure du cube comme surface d'échange. Nous avons ainsi pu retrouver la même tendance que pour la cinétique de séchage du filament avec l'identification des différentes périodes de séchage. Par ailleurs, la lenteur de cette cinétique de séchage, confirme la présence de faibles variations dimensionnelles lors d'impression longue ce qui ne devrait pas conduire à l'échec de l'impression.

Une stratégie de compensation verticale empirique (impression d'un objet plus haut que celui désiré) a été mise en place et a montré des résultats positifs permettant de corriger les effets de retrait liés au séchage et donc d'obtenir un objet 3D sec fidèle au modèle CAO. Cependant le coefficient d'agrandissement vertical varie en fonction de la présence ou non de structure interne. Combiner cette stratégie de compensation avec le séchage par échange de solvant est d'autant plus intéressant que le temps d'impression sera réduit par rapport au séchage à l'air.

Conclusions et perspectives

Ce travail portant sur le développement de matériaux cellulosiques pour la production d'objets bio-sourcés imprimés en 3D par extrusion a permis de proposer plusieurs formulations présentant des propriétés adéquates aux exigences de la FA par extrusion (Chapter 3). Pour l'une de ces formulations, le procédé de FA par extrusion (imprimantes et paramètres) a été optimisé pour garantir une fidélité optimum des objets produits à l'état humide en regard des modèles numériques et exempts de défauts prononcés (Chapter 4). Enfin, l'étude du procédé de séchage à l'air (précédé

ou non par une étape d'échange de solvant) par le suivi de l'évolution de structures 3D élémentaires imprimées au cours du séchage a permis de mieux comprendre les mécanismes de séchage d'objets et de proposer une stratégie de compensation dimensionnelle simple de l'objet (agrandissement vertical) afin d'obtenir un objet 3D à l'état sec semblable en dimensions et forme au modèle numérique (Chapter 5). Ainsi, ces résultats ont permis d'aboutir à l'impression 3D de formes complexes en matériau 100% cellulosique avec des propriétés mécaniques comparables aux thermoplastiques habituellement utilisés en impression 3D de fils fondus et ont pu être valorisés sous forme d'un article scientifique et de communication orales.

Bien que ces travaux constituent une base de données importante pour aboutir à la fabrication par extrusion de pièces sans défauts et aux dimensions contrôlées, les résultats de ce projet ouvrent de nombreuses perspectives tant au niveau de la formulation, que du procédé et méthode ainsi que du post-traitement et des applications possibles comme synthétisés dans le tableau ci-dessous.

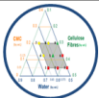

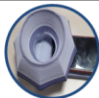
		
Formulation	Procédé et méthode	Post-traitement et applications
<p>Réduction la part d'eau dans la formulation</p> <ul style="list-style-type: none"> - Nouvelle méthode de mélange de la pâte - Ajout de charges minérales dans la composition - Utilisation de matrice photo-polymérisable - Quantification de l'absorption de l'eau par les fibres de cellulose 	<p>Axes d'amélioration de l'imprimante 3D</p> <ul style="list-style-type: none"> - Système d'alimentation de la tête d'extrusion pour ne pas limiter la vitesse d'impression - Deux têtes d'extrusion - Optimisation du design de la buse (résultat de modélisations d'écoulements) 	<p>Fonctionnalisation d'objet conducteur</p> <ul style="list-style-type: none"> - Impact de l'état de surface sur la conductivité (utilisation de nanocellulose pour une surface moins rugueuse ?) - Etude de l'interface entre le matériau inerte et celui conducteur
<p>Compatibilité de la formulation pour des résolution plus faible (~ 200 µm)</p> <ul style="list-style-type: none"> - Utilisation de nanocellulose à haute concentration avec de la CMC 	<p>Etude des paramètres d'impression secondaires</p> <ul style="list-style-type: none"> - Chemin de dépose - Amorce et arrêt de l'extrusion - Température de la pâte <p>Modélisation du séchage</p> <ul style="list-style-type: none"> - Evaluation de l'adhésion entre les filaments - Prédire les déformations locales, l'apparition de défaut et les propriétés mécaniques en fonction du design de l'objet et des paramètres d'impression 	<p>Production d'objets de grande taille (40 cm de haut)</p> <ul style="list-style-type: none"> - Formulation d'un matériaux avec des fibres de cellulose papetières ? - Utilisation de buses plus larges ? <p>Impression 4D</p> <ul style="list-style-type: none"> - Etude du gonflement et du retrait des objets imprimés dont la CMC a été réticulé par traitement thermique par exemple <p>Réutilisation de la pâte après séchage et réhydratation</p>

Tableau R-2. Synthèse des perspectives du projet.

Abbreviations

AFM: Atomic Force Microscopy

AgNW: Silver Nanowire

AM: Additive Manufacturing

ASTM: American Society for Testing and Materials

CaCl₂: Calcium Chloride

CAD: Computed Aided Design

CMC: Carboxymethyl Cellulose

CNC: Cellulose Nanocrystal

CNF: Cellulose Nanofiber

DMSO: Dimethyl sulfoxide

DS: Degree of Substitution

DP: Degree of Polymerization

EmimAc: 1-ethyl-3-methylimidazolium acetate

FFF: Fused Filament Fabrication

FLAM: fungal-like adhesive material

HefCel: High consistency fibrillation method

HRP: horseradish peroxidase

LS: Lignosulfonate

MC: Moisture Content

MCC: Microcrystalline Cellulose

MFC: Micro Fibrillated Cellulose

M_w: Molecular Weight

NFC: Nano Fibrillated Cellulose

Abbreviations

NMMO: N-nethylmorpholine N-oxide

OH-group: hydroxyl groups

PBS: Phosphate-Buffered Saline

PEF: Poly(ethylene-2,5-furandicarboxylate)

PETG: glycol-modified poly(ethylene terephthalate)

PHA: Polyhydroxyalkanoates

PLA: Polylactic Acid

PP: Polypropylene

PVOH: Polyvinyl Alcohol

RH: Relative Humidity

RM: Relative Moisture

SEM: Scanning Electron Microscopy

TCNF: Tempo Oxydized Cellulose Nanofiber

TS: Tensile Strength

WRV: Water Retention Value

XT: modified Xylan with Tyramide

List of figures

Figure I-1. Summary of the main studied parameters of this project to obtain the 3D printed part as accurate as possible.....	10
Figure I-2. Schematic representation of the manuscript organization.....	11
Figure 1-1. The additive manufacturing process steps adapted from (3D Hubs website, 2018).	15
Figure 1-2. Circle chart of the industrial sectors applying additive manufacturing (Wohlers Associates, 2017)..	20
Figure 1-3. Dependence of the raw material with the key steps of AM by extrusion: extrusion, deposition and post processing.	21
Figure 1-4. Rheological behavior of a compatible material for AM by extrusion. (A) the apparent viscosity, (B) the viscoelastic properties and the yield stress (G. Siqueira et al. 2017).....	23
Figure 1-5. Flow defects – Illustration (A) and picture (B) of die swelling phenomena (A. Gold, Strong, et N. Turner 2014; Carrot et Guillet, 2000). Surface fracture phenomenon influenced by the composition (C)and die shape and operating conditions (D) (J. Benbow et Bridgwater, 1993).	26
Figure 1-6. Dispensing devices for additive manufacturing by extrusion. Driven device technology were adapted from (Hölzl et al. 2016) and tips shape adapted from (Billiet et al. 2014).....	27
Figure 1-7. Test models for AM by extrusion: (A) dimensional accuracy, (B) overhang performance, (C) mechanical resonance in XY, (D) mechanical resonance in Z, (E) negative space tolerance, (F) fine positive space features performance, (G) bridging performance. Adapted from (Bastian, 2001).	31
Figure 1-8. Simple bending.....	32
Figure 1-9. Filament bonding – (A) Porosity in AM by extrusion (adapted from Reddy, Reddy, et Ghosh, 2007) and (B) Micrograph of contact between two filaments deposited.(adapted from Shor, Bellini, et Guceri, 2005).....	33
Figure 1-10. 3D printed part with warpage in ABS. According to Simplify 3D troubleshooting guide, ABS material can shrinks up to 1.5%.	34

List of figures

Figure 1-11. The different techniques for drying a wet solid – (A) Wet porous solid, (B) variety of the drying processes and (C) dried porous solid adapted from https://eduscol.education.fr	35
Figure 1-12. Evaporation of water adapted from www.meteobell.com	36
Figure 1-13. Drying steps and drying phenomena coupled inspired from (Scherer, 1990).....	38
Figure 1-14. Schematic process for producing cellulose fiber from wood.	39
Figure 1-15. Schematic illustration of the supramolecular organization of cellulose adapted from (Sixta, 2006).40	
Figure 1-16 : Molecular structure of cellulose adapted from (Moon et al. 2011).....	41
Figure 1-17. Micrograph of sugar beet (A) cell wall (Dufresne, Cavaillé, et Vignon, 1997), (B) microfibrils Dufresne, Cavaillé, et Vignon, 1997) and, (C) nanocrystals (Saïd Azizi Samir et al. 2004).....	43
Figure 1-18. The gel like behavior of nanocellulose adapted from (Klemm et al. 2011) (A) macroscopic image of nanocellulose hydrogel, (B) storage, G' and loss modulus, G'' of nanocellulose suspension of different concentration at a frequency of 6.28 rad.s^{-1} , (C) viscosity of different concentration of nanocellulose suspension as a function of the shear rate.	43
Figure 1-19. Overview of the broad treatments used to produce various type of nanocellulose suspensions (Nechyporchuk, Belgacem, et Bras 2016).	44
Figure 1-20. Molecular structure of cellulose acetate based on its degree of substitution (from Sigma Aldrich).45	
Figure 1-21. Molecular structure of sodium carboxymethyl cellulose based on its degree of substitution (from Sigma Aldrich).....	46
Figure 1-22. Historical review of development of additive manufacturing processes and the first use of cellulose of those processes.....	46
Figure 1-23. 15 wt.% of wood filled PLA: (A) SEM micrograph of a section of the raw filament (Duigou et al. 2016), (B) printed part with WoodFill filament from ColorFabb – 40% of wood filled PLA: (C) Printed part with Laywoo-3D filament from CC-Products (Li T et al. 2016).....	49
Figure 1-24. 4D printing – (A) schematic illustration of the 4D process induced by an anisotropic swelling behavior – (B) Flower 4D printed. (Sydney Gladman et al. 2016).....	51
Figure 1-25. Images of extruded filament and 3D structure with honeycomb before drying, after air drying at 80°C and ambient condition with insert micrograph of the fresh and dried foam. (Voisin et al. 2018).....	52
Figure 1-26. (A) Viscosity curves of MFC at 2 wt.%, lignosulfonate (LS) at 50 wt.% and the blend of the two. (B) 3D printed part with 2 wt.% of MFC blend with 50 wt.% of LS before and after air drying. (Shao et al. 2015).....	53
Figure 1-27. 3D printed part with CNF, modified Xylan with Tyramide (XT) and XT+CNF after crosslinking. (Markstedt et al. 2017).....	54

List of figures

Figure 1-28. (A) 3D printed porous scaffold (B) SEM image of the well-defined cross section after sintering. (Eqtesadi et al. 2013).....	55
Figure 1-29. (A) Schematic overview of the printed electrode with composition of each layer. (B) the 3D printed electrode being 3D printed. (Park, Kim, et Kim 2017).....	56
Figure 1-30. (A) reaction scheme for the synthesis of PEF from cellulose. (B) Model and printed part in PLA, PEF and ABS for thermal shrinkage evaluation. (C) No apparent change between printed part with fresh and 4 time recycled PEF. (Kucherov et al. 2017).....	57
Figure 1-31. (A) Low structure printed with or without coagulation of the dissolved cellulose. (B) side view (C) top view of high structure printed with imperfectly vertical agar gel structure. (D) SEM image of the microstructure of the freeze-dried coagulated part. (Markstedt, Sundberg, et Gatenholm 2014).....	58
Figure 1-32. (A) Illustration of the AM by extrusion process of cellulose acetate and acetone. (B) Optical image of extruded filament during acetone evaporation. (C) 3D model of flower (D) 3D printed flower. (Pattinson et Hart, 2017).....	59
Figure 1-33. (A) Schematic illustration of the wet (up) and dry (down) fungal-like adhesive material. (B) Processing stage of the 3D printed 1.2m long wind turbine blade (1) 3D printing in two parts (2) assembly (3) final part after coating and sanding. (Sanandiya et al. 2018)	60
Figure 1-34. 3D printed part with nanocellulose at low solid content. (A) TEMPO or highly charged nanocellulose with increasing solid content from left to right (Rees et al. 2015; Håkansson et al. 2016; V. C. F. Li et al. 2018) (B) enzymatic nanocellulose (Markstedt et al. 2015) and (C) C_Periodate nanocellulose (Rees et al. 2015).....	61
Figure 1-35. Evaluation of the drying technique on a 1cm ³ grid cube made of 2 wt.% of nanocellulose and 98 wt.% of water. (Håkansson et al. 2016).....	62
Figure 1-36. 3D models printed with high solid content (20wt.%) and dried with (A) freeze-drying without shrinkage (V. C.-F. Li et al. 2017) or (B) air drying with a volume shrinkage by 5 (Klar et al. 2019).64	
Figure 2-1. Optical characterization of cellulose fibers – (A) Image of natural cellulose fibers in suspension taken with an optical microscope. (B) Length distribution of cellulose fibers. (C) Width distribution of cellulose fibers with lengths greater than 100 µm.	70
Figure 2-2. Optical characterization of cellulose powder – (A) Image of microcrystalline cellulose powder in suspension taken with an optical microscope. (B) Diameter distribution of cellulose powder.	70
Figure 2-3. Optical characterization of graphite powder – (A) Image of graphite powder in suspension taken with an optical microscope. (B) Diameter distribution of graphite powder.	71
Figure 2-4. Image of dry sodium carboxymethyl cellulose powder taken with a binocular magnifier.	71

List of figures

- Figure 2-5. Ternary diagrams indicating the weight fractions of CMC, fillers, and water for the tested formulations: (A) global overview; Zoom on (B) cellulose fiber pastes, (C) cellulose powder pastes and (D) graphite powder pastes..... 74
- Figure 2-6. 3D printer Prusa i3 upgraded with a Liquid Deposit Modeling WASP Extruder – (A) Close-up and exploding drawing of the LDM extruder(www.3dwasp.com), (B) Picture of the printer used in this work, (C) Close-up of nozzle with an inner diameter of 0.7 mm and (D) 2D view of an X-ray Computed Tomography (XCT) scan of the nozzle . (1) Cavity, (2) Air pressure syringe, (3) screw-driven device, (4) barrel, and (5) steel nozzle..... 76
- Figure 2-7. Visualization obtained using Simplify 3D of (A) one track, (B) one layer, and (C) two layers of a cube. 77
- Figure 2-8. Screw extruder geometry – (A) Illustration (Vergnes et Puissant 2002) and (B) picture of the screw used without a proper cleaning. 78
- Figure 2-9. Schematic view of the extruder with the three flows: the measured outlet flow of the tank, Q' , the rotation speed of the screw, Ω , and, the experimental flow measured at the outlet of the nozzle, Q_{exp} (inspired from www.3dwasp.com). 79
- Figure 2-10. Side and top view of 3D model sliced with their printing parameters – (A) Single filament with various lengths, (B) rectangular 2D form, (C) cube, (D) parallelepiped with overhang angles to respect to the vertical plane and (E) H beam. 80
- Figure 2-11. Side and top view of 3D model sliced with their printing parameters – (A) 4 cm high monofilament rectangular cuboid, (B) 1.5 cm long bridge, (C) 5 cm high double spiral vase and (D) 3DBenchy. 82
- Figure 2-12. Automatic procedure for diameter measurement: (A) 8 bit grey scale image, (B) Selection of the upper and lower thresholds on the grey scale image zoom in (C), (D) Histogram of the 8 bit grey scale image and (E) the obtained binarized image. 85
- Figure 2-13. Lubricated squeeze flow testing – (A) Cylindrical sample preparation by casting, (B) Contact of the two compression plates with the sample for initial height, h_0 , measurement, (C) Sample positioning before compression started and (D) Plot of the measured data: plate position and force as a function of time. 86
- Figure 2-14. Tensile test – (A) Filament positioning with the 10 cm gage length before (B) the beginning of the tensile test. (C) The plotted curve with the record data: force and displacement of the clamp and (D) the strain-stress curve with the Young's Modulus, E , the tensile strength, TS , and the strain at break, ϵ_b , represented. 89
- Figure 2-15. Monitoring of the temporal weight evolution – (A) Top view of the weight machine during filament drying and (B) the plotted recorded weight data as a function of time. 90
- Figure 2-16. Optical set up to monitor the temporal evolution of the filament – (A) Sample holder (B) Positioning of the camera on the top of the filament and (C) side and (D) top view of the positioning of the filament on the top of the camera during images acquisitions..... 91

Figure 2-17. Temporal evolution of the filament images focus with (A) the first snapped image, (B), (C) and (D), snapped images after 20, 40 and 60 min, respectively. 91

Figure 2-18. Length measurement – (A) Test implementation and (B) skeleton of the binarized image. 91

Figure 2-19. (A) Experimental set up with a laboratory X-ray micro-tomography to monitor the inner and outer modifications of the cube during drying. (B) Zoom in of the cube fixed on the platform. (D) Stack of slices composed of whether Z slices (C) or Y slices (E). 92

Figure 2-20. Threshold determination of the scans of the cube – (A) 16 bits slice, (B) histogram of the 16 bits stack and (C) binarized slice. 93

Figure 2-21. 2D and 3D views of a X-ray Computed Tomography (XCT) scan of the 3D printed cube (upper row) and the same XCT scan filled by image processing to extract apparent data (lower row). (A and E) 3D view of the whole scan, (B and F) 3D view of the scan cropped horizontally in (xy) plane, (C and G) 3D view of the scan cropper vertically in (yz) plane and, (D and H) 2D view of a cross section in (yz) plane. 94

Figure 3-1. Images of CMC at different concentrations (5 to 25 wt.%) in water in a upright jar and in a laying jar after 5 min in that position 98

Figure 3-2. Mechanical properties of CMC films – Strain-stress curves of samples with dimensions ($L \times W \times D$) of (A) $50 \times 15 \times 0.22 \text{ mm}^3$ and (B) $100 \times 15 \times 0.16 \text{ mm}^3$ and (C) picture of a tensile specimen after fracture. 100

Figure 3-3. (A) Ternary diagram indicating the weight fractions of CMC, cellulose fibers, and water for the tested formulations. (B) Qualitative and quantitative characterization of the nine different tested formulations for compatibility with AM by extrusion. 101

Figure 3-4. (A) Ternary diagram indicating the weight fractions of CMC, cellulose powder, and water for the tested formulations. (B) Qualitative and quantitative characterization of the nine different tested formulations for compatibility with AM by extrusion. 104

Figure 3-5. (A) Ternary diagram indicating the weight fractions of CMC, graphite powder, and water for the tested formulations. (B) Qualitative and quantitative characterization of the nine different tested formulations for compatibility with AM by extrusion. 105

Figure 3-6. Rheological properties of the optimized cellulose based formulations (30 wt.% cellulose fiber, 12.5 wt.% carboxymethyl cellulose (CMC), 57.5 wt.% distilled water and 37 wt.% of cellulose powder, 12.5 wt.% CMC and 50 wt.% of distilled water). Three lubricated squeeze flow tests (compression at constant speed followed by 2 min of relaxation) were performed at an initial compression strain rate of 0.033 s^{-1} . (A) Stress-strain curves. (B) Stress during the lubricated squeeze flow test. During the relaxation time, the stress reached a plateau, which corresponds to the yield stress σ_y . (C) Viscosity curve fit with a power law, $\eta = k\epsilon_0 n - 1$. (D) Yield stress, σ_y as a function of the initial strain rate. 107

List of figures

- Figure 3-7. Plot of the diameter strain of the lower and upper part of the dry filament as a function of its extrusion length, L_{fresh} , for the optimized fiber cellulose paste. The diameter engineering strain was calculated as followed: $\frac{d_{dried} - d_{nozzle}}{d_{nozzle}} \times 100$ and the errors bars represent the standard deviation between the 5 tested samples for each extrusion length.109
- Figure 3-8. SEM images of the surface and cross-section of air-dried filament with (A, B) short cellulose fiber, (C, D) cellulose powder and (E, F) graphite powder.112
- Figure 3-9. SEM images of a fractured air-dried filament extruded through a 0.7 mm nozzle diameter: (A) surface and (B) cross-section. (C) Typical stress-strain curve obtained for a tested air-dried filament.113
- Figure 3-10. Influence of the wet strength agent (Kymene) on the dry properties: (A) diameter, (B), Young's modulus, (C) Tensile strength and (D) Strain at break.114
- Figure 3-11. Filament made of cellulose fiber paste after 30 min in water with a dry Kymene concentration of (A) 0 wt.%, (B) 0.5 wt.% and (C) 5 wt.%.115
- Figure 3-12. Influence of the wet strength agent (Kymene) on the wet properties: (A) Young's modulus, (B) Tensile strength and (C) Strain at break.116
- Figure 4-1. Influence of the rotation velocity on the outlet flow of the extruder for a given outlet flow of the tank – (A) Schematic view of the extruder with the outlet flow of the tank, Q' , the rotation velocity of the screw, Ω , and, the experimental flow measured at the outlet of the nozzle, Q_{exp} (www.3dwasp.com). (B) Plot of Q_{exp} as a function of Ω for a given Q'122
- Figure 4-2. Influence of the nozzle (diameter and inner shape) on the extrusion efficiency, nozzle with diameter of 0.9, 0.7 or 0.5 mm – (A) Plot of Q_{exp} as a function of Ω for the three nozzles, (B) Plot of the extrusion flow through the three nozzles as a function of the main pressure loss in the nozzle and plot of Q_{th} and Q_{exp} through different nozzles for different rotation speeds as a function of the pressure loss in the nozzle.124
- Figure 4-3. Influence of the outlet flow of the tank, Q' for different rotation speeds, Ω on the extrusion flow of the nozzle, Q_{exp} – (A) Plot of Q_{exp} as a function of Ω for different Q' and (B) plot of $Q_{exp}Q'$ as a function of $Q_{th}Q'$125
- Figure 4-4. Influence of the inner shape of the nozzle and the extrusion flow on the aspect of the filament – (A) 2D view of a X-ray Computed Tomography (XCT) scan of the 3 tested nozzle: 0.9, 0.7 and 0.5 mm large nozzle. SEM images and snapped images with a binocular magnifier (x25 and x100) of the surface of a dried filament extruded through the 3 nozzles at a linear extrusion flow of (B) 5 $\text{mm}\cdot\text{s}^{-1}$ (C) 15 $\text{mm}\cdot\text{s}^{-1}$ and (D) 30 $\text{mm}\cdot\text{s}^{-1}$127
- Figure 4-5. Influence of the nozzle shape and the linear extrusion flow on the diameter deformation of the dried filament. The error bars represent the standard deviation between the 15 diameters measurements performed on 5 tested samples for each condition.129

Figure 4-6. Influence of the extrusion flow rate and the inner shape of the nozzle on the mechanical properties – (A) Tensile strength, TS, (B) strain at break, ϵb and (C) Young’s modulus, E.....129

Figure 4-7. Influence of the filament width and extrusion flow on tensile test specimens: aspect and mechanical properties – (A) Whole fresh tensile test specimen ($1.4 \times 15.0 \times 0.1 \text{ cm}^3$) with longitudinal infill pattern and zoom of the sample printed with a filament width of 0.65 mm, 90% of the nozzle diameter (B,C) and 0.72 mm, the nozzle diameter (D,E) and an extrusion flow of 100% (B, D) and 120% (C and E). Plots of the tensile strength (F), elongation at break (G) and Young’s modulus (H) obtained from tensile test on 3 dried specimens for each filament width (0.65 and 0.72 mm) and extrusion flow (100 and 120% of the calibrated one). Images of the specimen after performing the tensile test: filament width of 0.65 mm (I, J) and 0.72 mm (K, L) and extrusion flow of 100% (I, K) and 120% (J, L).132

Figure 4-8. Influence of the layer height on the mechanical properties of 2 layers high tensile specimens ($1.4 \times 15 \text{ cm}^2$) with a filament width of 0.72 mm and an extrusion flow about 120% of the calibrated one – Plot of the tensile strength (A), elongation at break (B) and Young’s modulus (C) obtained from tensile tests on 3 dried specimen for each layer height tested ranging from 0.35 to 0.55 mm. ..134

Figure 4-9. Influence of the extrusion flow on the accuracy of a 2 filaments thick wall cube with edges of 1.5 cm filled at 35 and 100% with a layer height of 0.45 mm to test printability of simple object – Side and top grey scale images of 3D parts printed with an extrusion flow of 100% (A and B) and 120% (C and D) of the calibrated one.136

Figure 4-10. Influence of the layer height and the extrusion flow on the accuracy of a 2 filaments thick wall cube with edges of 1.5 cm filled at 35% to test printability of simple object – Top grey scale images of 3D parts printed with an extrusion flow of 100% (A, B and C) and 120% (D, E and F) of the calibrated one.....137

Figure 4-11. Influence of the layer height (0.35, 0.45 and 0.55 mm), the extrusion flow (100% and 120% of the calibrated one) and the infilled percentage (35 and 100%) on the accuracy (absence of damage) of a 2 filaments thick wall cube with edges of 1.5 cm after air drying.137

Figure 4-12. Influence of the layer height and the extrusion flow on the accuracy of a 2 filaments thick wall parallelepiped with a $1.5 \times 1.5 \text{ cm}^2$ base filled at 35% with overhang angle of 35 and 45° to respect with the vertical plane to test the overhang performance – (A, B, C, J, K and L) Schematic view of the cross section of the two filaments that composed the wall of the 3D part in the overhang area with the calculated ratio of unsupported filament due to the overhang. Side grey scale images of 3D parts printed with an extrusion flow of 100% (D, E, F, M, N and O) and 120% (G, H, I, P, Q and R) of the calibrated one.139

Figure 4-13. Influence of the layer height and the extrusion flow on the accuracy of a 2 filaments thick wall parallelepiped with a $1.5 \times 1.5 \text{ cm}^2$ base filled at 35% with an overhang angle of the initial 3D model of 35 (A) and 45° (B) to respect with the vertical plane after air drying.140

List of figures

- Figure 4-14. Influence of the layer height and the extrusion flow on the accuracy of a 4 cm high monofilament rectangular cuboid to test the vertical stacking performance of thin wall – Side grey scale image of 3D parts printed with an extrusion flow of 100% (A, B and C) and 120% (D, E and F) of the calibrated one.....141
- Figure 4-15. 4 cm high monofilament rectangular cuboid during its printing with a layer height of (A) 0.35, (B) 0.45 and (C) 0.55 mm at calibrated extrusion flow rate.142
- Figure 4-16. Influence of the layer height and the extrusion flow on the accuracy of a 4 cm high monofilament rectangular cuboid after air drying.....143
- Figure 4-17. Influence of the layer height and the extrusion flow on the accuracy of a 1.5 cm long bridge to test the bridging performance – Side grey scale image of the 3D parts printed with an extrusion flow of 100% (A, B and C) and 120% (D, E and F).145
- Figure 4-18. 3DBenchy download from (Thingiverse.com, 2018) – (A) Side and (B) top view of the sliced model, (C) Side view of the 3D printed model with fibrous cellulose based paste just after completion. 146
- Figure 4-19. Printing of the 3D Benchy model and pillars motion with the print head from right (A) to left (B). 147
- Figure 5-1. Impact of ethanol concentration on filament drying – Images of dry filament after a 30 min in a 10 mL ethanol bath at wt% ethanol 95% - water: 70-30 (A), 80-20 (B), 90-10 (C) and, 100-0 (D). (E) Relative dry diameter as a function of ethanol concentration, the error bars correspond to the mean deviation between the samples values dried in the same condition.....153
- Figure 5-2. Optimization of ethanol immersion time for filament samples – Relative diameter (A) and Young's modulus (B) after the ethanol bath and 1 min spent in open air at 30%RH as a function of their immersion time in ethanol. The error bars correspond to the mean deviation between the samples values dried in the same condition.....155
- Figure 5-3. Front and top view of model and dried parts after an immersion time in an ethanol bath of 0 min, 10 min, 20 min, 30 min, 2 h and 24 h. Three models were evaluated: 1 perimeter shell model (A), 2 perimeters shell model (B) and 2 perimeters shell model and 50%infill (C).156
- Figure 5-4. Strain of the dried H beam after ethanol drying with different immersion time. (A) Localization of the height measurements. (B) Plots of the relative height of H beam with wall thickness of 1.42mm, 2.84 mm and 5.68 mm as a function of the ethanol immersion time; the error bars correspond to the mean deviation between the three measurements values.....157
- Figure 5-5. Characterization of single filaments during drying at 30%RH and 22°C during 1 h – (A) Temporal evolution of the mass, mt and (B) temporal evolution of the relative moisture content, $M CtMC0$.159
- Figure 5-6. Temporal evolution of the normalized diameter, dd_{nozzle} and length, $ll0$ of single filaments during drying at 30%RH and 22°C during 1 h.....160
- Figure 5-7. Single filament drying curves at 27°C and 60%RH – (A) Temporal evolution of the relative moisture content and of the relative diameter with the two optical set up for the diameter measurement:

camera above the filament and filament above camera and (B) Temporal evolution of the relative moisture content and of the normalized filament section area $SS_{nozzle} = d^2 d_{nozzle}^2$ 162

Figure 5-8. Drying rate of the filament ($R = \frac{wd}{l} \frac{dM}{dt} + 1 - M$ with w , its dry weight, l , its length, d , its diameter, M , its moisture content and Δt , the time step) as a function (A) of time and (B) of relative moisture content.163

Figure 5-9. Temporal evolution of the filament images corresponding to the beginning and the end of the constant drying rate period (A, B), of the falling rate period (B, C) and of the quasi null drying rate period (C, D).163

Figure 5-10. Influence of the drying condition – (A) Plots of the averaged relative moisture content versus time and (B) relative diameter versus time combined in (C) with a temporal rescaling of the relative diameter of filament air-dried at 30 and 50%RH and ethanol-dried at 30%RH versus time during 60 min. The error bars correspond to the mean deviation between the samples dried in the same condition.165

Figure 5-11. The drying kinetics of filament air-dried at 30 and 50%RH or ethanol-dried. The drying rate plotted (A) as a function of time and (B) as a function of the relative moisture content.167

Figure 5-12. Temporal evolution of the mechanical characterizations of filament air-dried at 30%RH and ethanol-dried. (A) Plot of the Young’s modulus as a function of time and (B) plot of the Young’s modulus as a function of moisture content, the error bars correspond to the mean deviation between the samples values dried in the same condition.....169

Figure 5-13. SEM images of the surface and cross-section of an (A, B) air-dried filament and (C, D) ethanol-dried filament after complete drying.170

Figure 5-14. Temporal evolution of the tensile force record during drying of filament at 30%RH with ethanol and air drying conditions without any displacement of the clamps for samples tested (A) 1 min after ethanol bath (ethanol drying condition) and 10 min after extrusion (air drying condition) or (B) after 1 min after filament extrusion.....171

Figure 5-15. Plots of the relative Moisture Content (MC) of a 9 mm side cube for air and ethanol drying conditions (A) at 50%RH and (B) at 30%RH.173

Figure 5-16. Temporal evolution of the 3D structure of the 9 mm side cube - 2D view of X-ray computed tomography scans of the (XZ) cross section belonging to the middle plan of the cube (A) 10 min, (B) 30 min, (C) 250 min, (D) 500 min and (E) 1450 min after the beginning of printing with air and ethanol drying at 30%RH.174

Figure 5-17. 2D views of X-ray computed tomography scans after 90 min of drying of the cross section belonging to the middle plan of the cube (A) (XZ) and (B) (YZ) with air drying condition. (C) Image of the experiment set up with the local temperatures.....175

List of figures

- Figure 5-18 Determination of the volume of study. Isometric (A) and side (D) view of the 3D model (G-code). Isometric (B) and side (E) view of the first scan of the cube after binarization with a noisy lower part. Isometric (C) and side (F) view of the volume of study that corresponded to 87-89% in height of the 3D model.....176
- Figure 5-19. The anisotropic shrinkage – (A) 3D view of the scan with holes filled and (B) plot of the temporal evolution of the relative apparent volume of the cube, $VaVa0$, the relative height of the cube, $hth0$ and the relative length of the sides of the cubes for both drying processes.....177
- Figure 5-20. (A) Temporal evolution of the relative solid volume of the cube and (B) temporal evolution of the relative volume of water that composed the cube, $VwVw0$ and of the relative weight of water in the cube, $www0$179
- Figure 5-21. The drying kinetics of cube air-dried at 30%RH and ethanol-dried. The drying rate plotted (A) as a function of time and (B) as a function of the relative moisture content.181
- Figure 5-22. Temporal evolution of the cube at filament scale with air and ethanol drying conditions – (A) 2D view of binarized X-ray computed tomography scan (B) Plot of the temporal evolution of the relative cross section area of span filaments $SftSf0$ in the middle of the layer n°6 and n°20, the upper layer of the cube. (C) Plot of the temporal evolution of the relative volume of the macro pore $VmptVmpt0$ 182
- Figure 5-23. 3D printing of a double spiral vase with the optimized formulation dried with or without an ethanol bath or with polylactic acid (PLA). Upper row: 50 mm high vase. Lower row: vase with height compensation in the model based on the calculated strain.....184
-
- Figure C-1. Pictures of dried 3D printed parts with the optimized fibrous cellulose paste (A) with a dye and (B) without dye. Photography (C): on going AM by extrusion of a 3D structure. (copyright A. Chezière).....190
-
- Figure R-1. Synthèse des paramètres principaux de l'étude pour l'obtention d'objet 3D imprimé conforme au cahier des charges.....196
- Figure R-2. Représentation schématique de l'organisation du manuscrit.197
- Figure R-3. Dépendance de la matière première avec les étapes clés de la FA par extrusion : extrusion, déposition et post-traitement.198
- Figure R-4. Diagramme ternaire en fraction massique présentant les formulations évaluées composées de CMC, de fibres de cellulose et d'eau. (B) Caractérisation qualitative et quantitative des 9 formulations élaborées pour évaluer la compatibilité avec la FA par extrusion.....204

List of figures

- Figure R-5. Modèle complexe téléchargé via Thingiverse.com, 2018, 3DBenchy – Vue de (A) coté et (B) du dessus du modèle slicé, (C) Vue de coté de l’impression 3D du modèle avec la pâte à base de fibres de cellulose à l’état humide.....207
- Figure R-6. Evolution de la structure 3D interne d’un cube de 9 mm de côté au cours du séchage – vue 2D de scans de tomographie à rayons X (A) 10 min, (B) 30 min, (C) 250 min, (D) 500 min et (E) 1450 min après le début de l’impression avec un séchage à l’air (23°C-30%RH) précédé ou non d’une immersion dans un bain d’éthanol.....209

List of tables

Table 1-1. The seven categories of additive manufacturing processes according to the American Society for Testing and Materials (ASTM).	16
Table 1-2. Examples of material compatible with AM by extrusion	21
Table 1-3. Non exhaustive list of materials compatible with 3D printing by extrusion with their working temperature required to allow extrusion.	28
Table 1-4. Structural properties of cellulose fiber with an image of kraft pulp fibers of Spruce (Niskanen, 1998)41	
Table 1-5. Overview of a panel of example that highlight the wide range of materials compatible with AM by extrusion, the use of different structures of cellulose (text bold) and derivatives with their solid content, the different roles of cellulose in the formulation as well as the shapes of the printed parts. AgNW: silver nanowire, CMC: carboxymethyl cellulose, CNC: cellulose nanocrystal, CNF: cellulose nanofiber MCC: microcrystalline cellulose, MFC: micro fibrillated cellulose, NFC: nano fibrillated cellulose, PHA: Polyhydroxyalkanoates , PLA: polylactic acid, PP: polypropylene, PVOH: polyvinyl alcohol	48
Table 1-6. Overview of the studies published on formulations compatible with AM by extrusion based on cellulose as the main building block.....	65
Table 2-1. Fibrous cellulose formulations in weight and volume contents of water, CMC and cellulose fiber.....	72
Table 2-2. Powder cellulose formulations in weight and volume contents of water, CMC and cellulose powder.	73
Table 2-3. Graphite formulations in weight and volume content of water, CMC and graphite.	73
Table 2-4. Formulations to evaluate the influence of the wet strength agent from 0 to 10 wt.% of the dry content.	75
Table 2-5. The Main 3D printing settings of the tested printed parts where C is the calibration factor.....	82
Table 2-6. The main 3D printing settings of the tested printed parts where C is the calibration factor.....	83
Table 3-1. Mechanical properties of two batches of CMC films and results from literatures.	100
Table 4-1. Synthesis of the printing parameters to use for an accurate printing and dried part without damage of the developed high solid content paste – d is the nozzle diameter, h is the layer height, E is the extrusion multiplier and C is the calibration factor.	149

List of tables

Table 5-1. Analyze of the three periods of the structural properties of filament during drying at 30%RH and 23°C where t represent the time expressed in minutes.....	161
Table 5-2. Characterization of the rescaled drying curves of filaments air-dried at 30 and 50%RH and filament ethanol dried	167
Table 5-3. Temporal evolution of the grey level of a representative area of the wall of the cube.	181
Tableau R-1. Résumé des principales études portant sur l'utilisation de la cellulose comme matière première principale pour la FA par extrusion.	201
Tableau R-2. Synthèse des perspectives du projet.	211

References

- 3D Hubs. 2018. « What is 3D Printing ? The Definitive Guide ». <https://www.3dhubs.com/guides/3d-printing/>.
- A. Gold, Scott, Robert Strong, et Brian N. Turner. 2014. « A Review of Melt Extrusion Additive Manufacturing Processes: I. Process Design and Modeling ». *Rapid Prototyping Journal* 20 (3): 192-204. <https://doi.org/10.1108/RPJ-01-2013-0012>.
- Aeschelmann, F, et M Carus. 2017. « Bio-based Building Blocks and Polymers – Global Capacities and Trends 2016 - 2021" ». http://www.bio-based.eu/market_study/.
- Alghamdi, Hussam, Sooraj A. O. Nair, et Narayanan Neithalath. 2019. « Insights into Material Design, Extrusion Rheology, and Properties of 3D-Printable Alkali-Activated Fly Ash-Based Binders ». *Materials & Design* 167 (avril): 107634. <https://doi.org/10.1016/j.matdes.2019.107634>.
- Alsoufi, Mohammad, et Abdulrhman El-Sayed. 2017. « Warping Deformation of Desktop 3D Printed Parts Manufactured by Open Source Fused Deposition Modeling (FDM) System ». *International Journal of Mechanical & Mechatronics Engineering* 17 (août): 7-16.
- Arnoul Jarriault, Benoît. 2015. « Extraction des Hémicelluloses de Pâtes Papetières pour la Production de Pâte à Dissoudre ». Thesis, Grenoble Alpes. <http://www.theses.fr/2015GREAI123>.
- ASTM International. 2012. *Standard Terminology for Additive Manufacturing Technologies: Designation F2792-12a*. West Conshohocken, PA: ASTM International.
- Bastian, Andreas. 2001. « How to Evaluate the 2015 Make: 3DP Test Probes | Make »: Make: DIY Projects and Ideas for Makers. 30 novembre 2001. <https://makezine.com/2014/11/07/how-to-evaluate-the-2015-make-3dp-test-probes/>.
- Benbow, J.J., S. Blackburn, et H. Mills. 1998. « The Effects of Liquid-Phase Rheology on the Extrusion Behaviour of Paste ». *Journal of Materials Science* 33 (24): 5827-33. <https://doi.org/10.1023/A:1004458217898>.
- Benbow, John, et J Bridgwater. 1993. *Paste Flow and Extrusion*. Oxford; New York: Clarendon Press ; Oxford University Press. <http://books.google.com/books?id=KMBTAAAMAAJ>.
- Benchabane, Adel, et Bekkour Karim. 2008. « Rheological Properties of Carboxymethyl Cellulose (CMC) Solutions ». *Colloid and Polymer Science* 286 (septembre): 1173-80. <https://doi.org/10.1007/s00396-008-1882-2>.
- Billiet, Thomas, Elien Gevaert, Thomas De Schryver, Maria Cornelissen, et Peter Dubruel. 2014. « The 3D Printing of Gelatin Methacrylamide Cell-Laden Tissue-Engineered Constructs with High Cell Viability ». *Biomaterials* 35 (1): 49-62. <https://doi.org/10.1016/j.biomaterials.2013.09.078>.
- Billiet, Thomas, Mieke Vandenhaute, Jorg Schelfhout, Sandra Van Vlierberghe, et Peter Dubruel. 2012. « A Review of Trends and Limitations in Hydrogel-Rapid Prototyping for Tissue

- Engineering ». *Biomaterials* 33 (26): 6020-41. <https://doi.org/10.1016/j.biomaterials.2012.04.050>.
- Bonazzi, Catherine, et Jean-Jacques Bimbenet. 2003. « Séchage des Produits Alimentaires Principes ». *Techniques de l'ingénieur Opérations unitaires du génie industriel alimentaire* base documentaire : TIB430DUO. (ref. article : f3000). <https://www.techniques-ingenieur.fr/base-documentaire/procedes-chimie-bio-agro-th2/operations-unitaires-du-genie-industriel-alimentaire-42430210/sechage-des-produits-alimentaires-f3000/>.
- Boulos, Vincent, Vincent Fristot, Dominique Houzet, Luc Salvo, et P. Lhuissier. 2012. « Investigating Performance Variations of an Optimized GPU-ported Granulometry Algorithm ». In *Design and Architectures for Signal and Image Processing (DASIP), 2012 Conference on*, 1-6. Karlsruhe, Germany. <https://hal.archives-ouvertes.fr/hal-00787861>.
- Buswell, R. A., W. R. Leal de Silva, S. Z. Jones, et J. Dirrenberger. 2018. « 3D Printing Using Concrete Extrusion: A Roadmap for Research ». *Cement and Concrete Research*, SI : Digital concrete 2018, 112 (octobre): 37-49. <https://doi.org/10.1016/j.cemconres.2018.05.006>.
- Cai, Kunpeng, Benito Román-Manso, Jim E. Smay, Ji Zhou, María Isabel Osendi, Manuel Belmonte, et Pilar Miranzo. 2012. « Geometrically Complex Silicon Carbide Structures Fabricated by Robocasting ». *Journal of the American Ceramic Society* 95 (8): 2660-66. <https://doi.org/10.1111/j.1551-2916.2012.05276.x>.
- Carrot, Christian, et Jacques Guillet. 2000. « Viscoélasticité Non Linéaire des Polymères Fondus ». Text. Ref : TIP100WEB - « Plastiques et composites ». 10 avril 2000. <https://www-techniques-ingenieur-fr.gaelnomade-1.grenet.fr/base-documentaire/42152210-proprietes-generales-des-plastiques/download/am3630/viscoelasticite-non-lineaire-des-polymeres-fondus.html>.
- Cataldi, A., D. Rigotti, V. D. H. Nguyen, et A. Pegoretti. 2018. « Polyvinyl Alcohol Reinforced with Crystalline Nanocellulose for 3D Printing Application ». *Materials Today Communications* 15 (juin): 236-44. <https://doi.org/10.1016/j.mtcomm.2018.02.007>.
- Cesarano, Joseph. 1998. « A Review of Robocasting Technology ». *MRS Online Proceedings Library Archive* 542. <https://doi.org/10.1557/PROC-542-133>.
- Chalencou, F., L. Orgéas, P. J. J. Dumont, G. Foray, J. -Y. Cavallé, E. Maire, et S. Rolland du Roscoat. 2010. « Lubricated Compression and X-Ray Microtomography to Analyse the Rheology of a Fibre-Reinforced Mortar ». *Rheologica Acta* 49 (3): 221-35. <https://doi.org/10.1007/s00397-009-0393-5>.
- Champetier, Georges. 1954. *Dérivés Cellulosiques*. 2me éd. Paris: Dunod.
- Chinga-Carrasco, Gary, Nanci V. Ehman, Jennifer Pettersson, María E. Vallejos, Malin W. Brodin, Fernando E. Felissia, Joakim Håkansson, et María C. Area. 2018. « Pulping and Pretreatment Affect the Characteristics of Bagasse Inks for Three-dimensional Printing ». *ACS Sustainable Chemistry & Engineering* 6 (3): 4068-75. <https://doi.org/10.1021/acssuschemeng.7b04440>.
- Cloitre, Michel, et Roger T. Bonnecaze. 2017. « A Review on Wall Slip in High Solid Dispersions ». *Rheologica Acta* 56 (3): 283-305. <https://doi.org/10.1007/s00397-017-1002-7>.
- Compton, Brett G., et Jennifer A. Lewis. 2014. « 3D-Printing of Lightweight Cellular Composites ». *Advanced Materials (Deerfield Beach, Fla.)* 26 (34): 5930-35. <https://doi.org/10.1002/adma.201401804>.
- Coussot, Philippe. 2012. *Rhéophysique, la Matière dans tous ses États*.
- Curmi, Hélène. 2018. « Etude de l'Impact de l'Autohydrolyse sur les Constituants du Bois et sur le Déroulement du Procédé de Production de Cellulose Pure ». Thesis, Grenoble Alpes. <http://www.theses.fr/2018GREAI089>.

- Dai, Lei, Ting Cheng, Chao Duan, Wei Zhao, Weipeng Zhang, Xuejun Zou, Joseph Aspler, et Yonghao Ni. 2019. « 3D Printing using Plant-derived Cellulose and its Derivatives: A Review ». *Carbohydrate Polymers* 203 (janvier): 71- 86. <https://doi.org/10.1016/j.carbpol.2018.09.027>.
- Dey, Arup, et Nita Yodo. 2019. « A Systematic Survey of FDM Process Parameter Optimization and Their Influence on Part Characteristics ». *Journal of Manufacturing and Materials Processing* 3 (3): 64. <https://doi.org/10.3390/jmmp3030064>.
- Drisch, Nicolas, et Marcel Chêne. 1967. *La Cellulose: par Marcel Chêne, ... et Nicolas Drisch, ...* Presses universitaires de France.
- Dufresne, Alain. 2015. « Nanomatériaux Cellulosiques ». Text. Ref : TIP155WEB - « Nanosciences et nanotechnologies ». 10 juin 2015. <https://www-techniques-ingenieur-fr.gaelnomade-1.grenet.fr/base-documentaire/42635210-nanomateriaux-proprietes/download/nm3490/nanomateriaux-cellulosiques.html>.
- Dufresne, Alain. 2017. *Nanocellulose: From Nature to High Performance Tailored Materials*. Walter de Gruyter GmbH & Co KG.
- Dufresne, Alain, Jean-Yves Cavailié, et Michel R. Vignon. 1997. « Mechanical Behavior of Sheets Prepared from Sugar Beet Cellulose Microfibrils ». *Journal of Applied Polymer Science* 64 (6): 1185-94. [https://doi.org/10.1002/\(SICI\)1097-4628\(19970509\)64:6<1185::AID-APP19>3.0.CO;2-V](https://doi.org/10.1002/(SICI)1097-4628(19970509)64:6<1185::AID-APP19>3.0.CO;2-V).
- Duigou, A. Le, M. Castro, R. Bevan, et N. Martin. 2016. « 3D Printing of Wood Fibre Biocomposites: From Mechanical to Actuation Functionality ». *Materials & Design C* (96): 106-14. <https://doi.org/10.1016/j.matdes.2016.02.018>.
- Dumas, Jérémie, Jean Hergel, et Sylvain Lefebvre. 2014. « Bridging the Gap: Automated Steady Scaffoldings for 3D Printing ». *ACM Trans. Graph.* 33 (4): 98:1–98:10. <https://doi.org/10.1145/2601097.2601153>.
- Edali, Mohamed, M. Nabil Esmail, et Goergios H. Vatistas. 2001. « Rheological Properties of High Concentrations of Carboxymethyl Cellulose Solutions ». *Journal of Applied Polymer Science* 79 (10): 1787- 1801. [https://doi.org/10.1002/1097-4628\(20010307\)79:10<1787::AID-APP70>3.0.CO;2-2](https://doi.org/10.1002/1097-4628(20010307)79:10<1787::AID-APP70>3.0.CO;2-2).
- Einarsrud, Mari-Ann. 1998. « Light Gels by Conventional Drying ». *Journal of Non-Crystalline Solids* 225 (Supplement C): 1- 7. [https://doi.org/10.1016/S0022-3093\(98\)00002-7](https://doi.org/10.1016/S0022-3093(98)00002-7).
- Eqtesadi, Siamak, Azadeh Motealleh, Pedro Miranda, Alexandra Lemos, Avito Rebelo, et José M. F. Ferreira. 2013. « A Simple Recipe for Direct Writing Complex 45S5 Bioglass® 3D Scaffolds ». *Materials Letters* 93 (février): 68- 71. <https://doi.org/10.1016/j.matlet.2012.11.043>.
- Feilden, Erza. 2017. « Additive Manufacturing of Ceramics and Ceramic Composites via Robocasting ». Imperial College London. https://www.google.com/url?sa=t&rct=j&q=&esrc=s&source=web&cd=1&cad=rja&uact=8&ved=2ahUKEwjziPGvtcrkAhXJBWMBHbdzAkwQFjAAegQIABAC&url=https%3A%2F%2Fspiral.imperial.ac.uk%2Fbitstream%2F10044%2F1%2F55940%2F3%2Ffeilden-E-2017-PhD-Thesis.pdf&usg=AOvVaw2f6HrXz5KD_ubXIYbu4R2c.
- Fernandez-Vicente, Miguel, Miquel Canyada, et Andres Conejero. 2015. « Identifying Limitations for Design for Manufacturing with Desktop FFF 3D Printers ». *International Journal of Rapid Manufacturing* 5 (1): 116- 28. <https://doi.org/10.1504/IJRAPIDM.2015.073551>.
- Feygin, Michael, et Brian Hsieh. 1991. « Laminated Object Manufacturing (LOM): A Simpler Process ». In . <https://doi.org/10.15781/T2PV6BQ54>.
- Fichot, Julie. 2013. « Propriétés de Séchage de Textures Complexes Appliquées à La Cosmétologie », janvier. <https://tel.archives-ouvertes.fr/tel-00859622>.

- Ganster, Johannes, et Hans-Peter Fink. 2013. « Cellulose and Cellulose Acetate ». In *Bio-Based Plastics*, 35- 62. Wiley-Blackwell. <https://doi.org/10.1002/9781118676646.ch3>.
- Gao, Hui, Jun Rao, Ying Guan, Wen-qi Li, Mao-chao Zhang, Ting Shu, et Zi-wen Lv. 2018. « Investigation of the Thermo-Mechanical Properties of Blend Films Based on Hemicelluloses and Cellulose ». Research article. *International Journal of Polymer Science*. 2018. <https://doi.org/10.1155/2018/9620346>.
- Gardan, Julien, Duy Cuong Nguyen, Roucoules Lionel, et Guillaume Montay. 2016. « Characterization of Wood Filament in Additive Deposition to Study the Mechanical Behavior of Reconstituted Wood Products ». *Journal of engineered fibers and fabrics* 11 (décembre): 56. <https://doi.org/10.1177/155892501601100408>.
- GARDAN, Julien, et Lionel Roucoules. 2010. « Characterization of Beech Wood Pulp towards Sustainable Rapid Prototyping ». In *IDMME - Virtual Concept 2010*, 3:6p. France: Springer verlag. <https://hal.archives-ouvertes.fr/hal-00958172>.
- Gharehkhani, Samira, Emad Sadeghinezhad, Salim Newaz Kazi, Hooman Yarmand, Ahmad Badarudin, Mohammad Reza Safaei, et Mohd Nashrul Mohd Zubir. 2015. « Basic Effects of Pulp Refining on Fiber Properties—A Review ». *Carbohydrate Polymers* 115 (janvier): 785-803. <https://doi.org/10.1016/j.carbpol.2014.08.047>.
- Golecha, Rajdeep, et Jianbang Gan. 2016. « Cellulosic Biorefinery Portfolio and Diversification: Strategies to Mitigate Cellulosic Biorefinery Risks in US Corn Belt ». *Energy Strategy Reviews* 13- 14 (novembre): 147- 53. <https://doi.org/10.1016/j.esr.2016.09.003>.
- Gordeev, Evgeniy G., Alexey S. Galushko, et Valentine P. Ananikov. 2018. « Improvement of Quality of 3D Printed Objects by Elimination of Microscopic Structural Defects in Fused Deposition Modeling ». *PLOS ONE* 13 (6): e0198370. <https://doi.org/10.1371/journal.pone.0198370>.
- Gurralla, Pavan Kumar, et Srinivasa Prakash Regalla. 2014. « Part strength evolution with bonding between filaments in fused deposition modelling ». *Virtual and Physical Prototyping* 9 (3): 141- 49. <https://doi.org/10.1080/17452759.2014.913400>.
- Håkansson, Karl M. O., Ida C. Henriksson, Cristina de la Peña Vázquez, Volodymyr Kuzmenko, Kajsa Markstedt, Peter Enoksson, et Paul Gatenholm. 2016. « Solidification of 3D Printed Nanofibril Hydrogels into Functional 3D Cellulose Structures ». *Advanced Materials Technologies* 1 (7): n/a-n/a. <https://doi.org/10.1002/admt.201600096>.
- Hausmann, Michael K., Patrick A. Rühs, Gilberto Siqueira, Jörg Läger, Rafael Libanori, Tanja Zimmermann, et André R. Studart. 2018. « Dynamics of Cellulose Nanocrystal Alignment during 3D Printing ». *ACS Nano* 12 (7): 6926- 37. <https://doi.org/10.1021/acsnano.8b02366>.
- Haworth, W. N. 1940. « Structure of Cellulose and Other Polymers Related to Simple Sugars* ». *Journal of the Society of Dyers and Colourists* 56 (2): 49- 58. <https://doi.org/10.1111/j.1478-4408.1940.tb02090.x>.
- Hölzl, Katja, Shengmao Lin, Liesbeth Tytgat, Sandra Van Vlierberghe, Linxia Gu, et Aleksandr Ovsianikov. 2016. « Bioink Properties before, during and after 3D Bioprinting ». *Biofabrication* 8 (3): 032002. <https://doi.org/10.1088/1758-5090/8/3/032002>.
- Huang, B., et S. Singamneni. 2012. « Alternate Slicing and Deposition Strategies for Fused Deposition Modelling of Light Curved Parts ». *Journal of Achievements in Materials and Manufacturing Engineering* Vol. 55 (nr 2). <http://yadda.icm.edu.pl/baztech/element/bwmeta1.element.baztech-8064e0c9-f70f-4447-8963-3c2f3ca7f10d>.
- Huang, Chu Yin. 2018. « Extrusion-Based 3D Printing and Characterization of Edible Materials », janvier. <https://uwspace.uwaterloo.ca/handle/10012/12899>.

- Hubbe, Martin A., Pegah Tayeb, Michael Joyce, Preeti Tyagi, Margaret Kehoe, Katarina Dimic-Misic, et Lokendra Pal. 2017. « Rheology of Nanocellulose-Rich Aqueous Suspensions: A Review ». *BioResources* 12 (4): 9556-9661-9661. <https://doi.org/10.15376/biores.12.4.9556-9661>.
- INRS. 2018. « Fibres de cellulose (FT 282). Caractéristiques - Fiche toxicologique - ». 2018. http://www.inrs.fr/publications/bdd/fichetox/fiche.html?refINRS=FICHETOX_282§ion=caraacteristiques.
- ISO 23714. 2014. « Pulps — Determination of Water Retention Value (WRV) ». 2014. <https://www.iso.org/obp/ui/#iso:std:iso:23714:ed-2:v1:en>.
- Jia, Chao, Huiyang Bian, Tingting Gao, Feng Jiang, Iain Michael Kierzewski, Yilin Wang, Yonggang Yao, et al. 2017. « Thermally Stable Cellulose Nanocrystals toward High-Performance 2D and 3D Nanostructures ». *ACS Applied Materials & Interfaces* 9 (34): 28922-29. <https://doi.org/10.1021/acsami.7b08760>.
- Jia, Xuejuan, Yingwen Chen, Chong Shi, Yangfan Ye, Muhammad Abid, Saqib Jabbar, Peng Wang, Xiaoxiong Zeng, et Tao Wu. 2014. « Rheological Properties of an Amorphous Cellulose Suspension ». *Food Hydrocolloids* 39 (août): 27-33. <https://doi.org/10.1016/j.foodhyd.2013.12.026>.
- Jiang, Jingchao, Guobiao Hu, Xiao Li, Xun Xu, Pai Zheng, et Jonathan Stringer. 2019. « Analysis and Prediction of Printable Bridge Length in Fused Deposition Modelling based on Back Propagation Neural Network ». *Virtual and Physical Prototyping* 14 (3): 253-66. <https://doi.org/10.1080/17452759.2019.1576010>.
- Jiang, Jingchao, Jingjun Lou, et Guobiao Hu. 2019. « Effect of Support on Printed Properties in Fused Deposition Modelling Processes ». *Virtual and Physical Prototyping* 14 (4): 308-15. <https://doi.org/10.1080/17452759.2019.1568835>.
- Jones, Rhys, Patrick Haufe, Edward Sells, Pejman Iravani, Vik Olliver, Chris Palmer, et Adrian Bowyer. 2011. « RepRap – the Replicating Rapid Prototyper ». *Robotica* 29 (1): 177-91. <https://doi.org/10.1017/S026357471000069X>.
- Kamide, Kenji, et Masatoshi Saito. 1985. « Thermal Analysis of Cellulose Acetate Solids with Total Degrees of Substitution of 0.49, 1.75, 2.46, and 2.92 ». *Polymer Journal* 17 (8): 919-28. <https://doi.org/10.1295/polymj.17.919>.
- Kaynak, Baris, Martin Spoerk, Anuja Shirole, Wolfgang Ziegler, et Janak Sapkota. 2018. « Polypropylene/Cellulose Composites for Material Extrusion Additive Manufacturing ». *Macromolecular Materials and Engineering* 303 (5): 1800037. <https://doi.org/10.1002/mame.201800037>.
- Klar, Ville, Pyy Kärki, Hannes Orelma, et Petri Kuosmanen. 2017. « Analysis of Drying Deformation of 3D Printed Nanocellulose Structures ». In *Cellulose Materials Doctoral Students Conference 2017*. Graz University of Technology, TUG. [https://research.aalto.fi/en/publications/analysis-of-drying-deformation-of-3d-printed-nanocellulose-structures\(447440d2-bf95-47bb-98ab-f9984beb3f4a\).html](https://research.aalto.fi/en/publications/analysis-of-drying-deformation-of-3d-printed-nanocellulose-structures(447440d2-bf95-47bb-98ab-f9984beb3f4a).html).
- Klar, Ville, Jaakko Pere, Tuomas Turpeinen, Pyy Kärki, Hannes Orelma, et Petri Kuosmanen. 2019. « Shape Fidelity and Structure of 3D Printed High Consistency Nanocellulose ». *Scientific Reports* 9 (1): 3822. <https://doi.org/10.1038/s41598-019-40469-x>.
- Klemm, Dieter, Brigitte Heublein, Hans-Peter Fink, et Andreas Bohn. 2005. « Cellulose: Fascinating Biopolymer and Sustainable Raw Material ». *Angewandte Chemie International Edition* 44 (22): 3358-93. <https://doi.org/10.1002/anie.200460587>.
- Klemm, Dieter, Friederike Kramer, Sebastian Moritz, Tom Lindström, Mikael Ankerfors, Derek Gray, et Annie Dorris. 2011. « Nanocelluloses: A New Family of Nature-Based Materials ».

- Angewandte Chemie International Edition* 50 (24): 5438-66. <https://doi.org/10.1002/anie.201001273>.
- Kucherov, Fedor A., Evgeny G. Gordeev, Alexey S. Kashin, et Valentine P. Ananikov. 2017. « Three-Dimensional Printing with Biomass-Derived PEF for Carbon-Neutral Manufacturing ». *Angewandte Chemie (International Ed. in English)* 56 (50): 15931-35. <https://doi.org/10.1002/anie.201708528>.
- Kumar, Sandeep, Manfred Hofmann, Bettina Steinmann, E. Johan Foster, et Christoph Weder. 2012. « Reinforcement of Stereolithographic Resins for Rapid Prototyping with Cellulose Nanocrystals ». *ACS Applied Materials & Interfaces* 4 (10): 5399-5407. <https://doi.org/10.1021/am301321v>.
- Kuznetsov, Vladimir E., Azamat G. Tavitov, et Oleg D. Urzhumtcev. 2019. « Hardware Factors Influencing Interlayer Bonding Strength of Parts Obtained by Fused Filament Fabrication », mai. <https://doi.org/10.20944/preprints201905.0108.v1>.
- Laurencin, T., L. Orgéas, P. J. J. Dumont, S. Rolland du Roscoat, P. Laure, S. Le Corre, L. Silva, R. Mokso, et M. Terrien. 2016. « 3D Real-Time and In Situ Characterisation of Fibre Kinematics in Dilute Non-Newtonian Fibre Suspensions during Confined and Lubricated Compression Flow ». *Composites Science and Technology* 134 (octobre): 258-66. <https://doi.org/10.1016/j.compscitech.2016.09.004>.
- Laureto, John J., et Joshua M. Pearce. 2018. « Anisotropic Mechanical Property Variance Between ASTM D638-14 Type I and Type IV Fused Filament Fabricated Specimens ». *Polymer Testing* 68 (juillet): 294-301. <https://doi.org/10.1016/j.polymertesting.2018.04.029>.
- Laverne, Floriane, Frédéric Segonds, et Patrice Dubois. 2016. « Fabrication additive - Principes généraux ». Text. Ref : TIP153WEB - « Travail des matériaux - Assemblage ». 10 février 2016. <https://www.techniques-ingenieur.fr/base-documentaire/mecanique-th7/procedes-de-fabrication-additive-42633210/fabrication-additive-bm7017/>.
- Lee, Jin-Hyon, Ungyu Paik, Vincent A. Hackley, et Young-Min Choi. 2005. « Effect of Carboxymethyl Cellulose on Aqueous Processing of Natural Graphite Negative Electrodes and Their Electrochemical Performance for Lithium Batteries ». *Journal of The Electrochemical Society* 152 (9): A1763-69. <https://doi.org/10.1149/1.1979214>.
- Leppiniemi, Jenni, Panu Lahtinen, Antti Paajanen, Riitta Mahlberg, Sini Metsä-Kortelainen, Tatu Pinomaa, Heikki Pajari, Inger Vikholm-Lundin, Pekka Pursula, et Vesa P. Hytönen. 2017. « 3D-Printable Bioactivated Nanocellulose-Alginate Hydrogels ». *ACS Applied Materials & Interfaces* 9 (26): 21959-70. <https://doi.org/10.1021/acsami.7b02756>.
- Lewis, J. A. 2002. « Direct-Write Assembly of Ceramics From Colloidal Inks ». *Current Opinion in Solid State and Materials Science* 6 (3): 245-50. [https://doi.org/10.1016/S1359-0286\(02\)00031-1](https://doi.org/10.1016/S1359-0286(02)00031-1).
- Lewis, J. A. 2006. « Direct Ink Writing of 3D Functional Materials ». *Advanced Functional Materials* 16 (17): 2193-2204. <https://doi.org/10.1002/adfm.200600434>.
- Lewis, J. A, et Gregory M Gratson. 2004. « Direct Writing in Three Dimensions ». *Materials Today* 7 (7): 32-39. [https://doi.org/10.1016/S1369-7021\(04\)00344-X](https://doi.org/10.1016/S1369-7021(04)00344-X).
- Li, Lei, Yufang Zhu, et Junhe Yang. 2018. « 3D Bioprinting of Cellulose with Controlled Porous Structures from NMMO ». *Materials Letters* 210 (janvier): 136-38. <https://doi.org/10.1016/j.matlet.2017.09.015>.
- Li T, Aspler J, Kingsland A, Cormier LM, et Zou X. 2016. « 3D Printing—a Review of Technologies, Markets, and Opportunities for the Forest Industry. *J Sci Technol For Prod Process* 5(2):30–37 ».
- Li, Vincent C. F., Arie Mulyadi, Conner K. Dunn, Yulin Deng, et H. Jerry Qi. 2018. « Direct Ink Write 3D Printed Cellulose Nanofiber Aerogel Structures with Highly Deformable, Shape Recoverable,

- and Functionalizable Properties ». *ACS Sustainable Chemistry & Engineering* 6 (2): 2011-22. <https://doi.org/10.1021/acssuschemeng.7b03439>.
- Li, Vincent Chi-Fung, Conner K. Dunn, Zhe Zhang, Yulin Deng, et H. Jerry Qi. 2017. « Direct Ink Write (DIW) 3D Printed Cellulose Nanocrystal Aerogel Structures ». *Scientific Reports* 7 (1): 8018. <https://doi.org/10.1038/s41598-017-07771-y>.
- Li, Wenbin, Amir Armani, Ming Leu, et Robert G. Landers. 2017. « Extrusion-On-Demand Methods for High Solids Loading Ceramic Paste in Freeform Extrusion Fabrication ». <https://doi.org/10.1080/17452759.2017.1312735>.
- Lipton, Jeffrey, Dave Arnold, Franz Nigl, Nastassia Lopez, Dan Cohen, Nils Norén, et Hod Lipson. 2010. « Multi-Material Food Printing with Complex Internal Structure Suitable for Conventional Post-Processing », janvier.
- Liu, Jun, Lushan Sun, Wenyang Xu, Qianqian Wang, Sujie Yu, et Jianzhong Sun. 2019. « Current Advances and Future Perspectives of 3D Printing Natural-Derived Biopolymers ». *Carbohydrate Polymers* 207 (mars): 297-316. <https://doi.org/10.1016/j.carbpol.2018.11.077>.
- Lopez, Carlos G, Sarah E Rogers, Ralph H Colby, Peter Graham, et João T Cabral. 2015. « Structure of Sodium Carboxymethyl Cellulose Aqueous Solutions: A SANS and Rheology Study ». *Journal of Polymer Science. Part B, Polymer Physics* 53 (7): 492-501. <https://doi.org/10.1002/polb.23657>.
- Mason, Michael S., Tieshu Huang, Robert G. Landers, Ming C. Leu, et Gregory E. Hilmas. 2009. « Aqueous-based extrusion of high solids loading ceramic pastes: Process modeling and control ». *Journal of Materials Processing Technology* 209 (6): 2946-57. <https://doi.org/10.1016/j.jmatprotec.2008.07.004>.
- Markstedt, Kajsa, Alfredo Escalante, Guillermo Toriz, et Paul Gatenholm. 2017. « Biomimetic Inks Based on Cellulose Nanofibrils and Cross-Linkable Xylans for 3D Printing ». *ACS Applied Materials & Interfaces* 9 (46): 40878-86. <https://doi.org/10.1021/acsmi.7b13400>.
- Markstedt, Kajsa, Athanasios Mantas, Ivan Tournier, Héctor Martínez Ávila, Daniel Hägg, et Paul Gatenholm. 2015. « 3D Bioprinting Human Chondrocytes with Nanocellulose-Alginate Bioink for Cartilage Tissue Engineering Applications ». *Biomacromolecules* 16 (5): 1489-96. <https://doi.org/10.1021/acs.biomac.5b00188>.
- Markstedt, Kajsa, Johan Sundberg, et Paul Gatenholm. 2014. « 3D Bioprinting of Cellulose Structures from an Ionic Liquid ». *3D Printing and Additive Manufacturing* 1 (3): 115-21. <https://doi.org/10.1089/3dp.2014.0004>.
- Martínez-Vázquez, Francisco J., Antonia Pajares, et Pedro Miranda. 2018. « A Simple Graphite-Based Support Material for Robocasting of Ceramic Parts ». *Journal of the European Ceramic Society* 38 (4): 2247-50. <https://doi.org/10.1016/j.jeurceramsoc.2017.10.016>.
- Martoia, F., C. Perge, P. J. J. Dumont, L. Orgéas, M. A. Fardin, S. Manneville, et M. N. Belgacem. 2015. « Heterogeneous Flow Kinematics of Cellulose Nanofibril Suspensions under Shear ». *Soft Matter* 11 (24): 4742-55. <https://doi.org/10.1039/c5sm00530b>.
- Mason, Michael S., Tieshu Huang, Robert G. Landers, Ming C. Leu, et Gregory E. Hilmas. 2009. « Aqueous-Based Extrusion of High Solids Loading Ceramic Pastes: Process Modeling and Control ». *Journal of Materials Processing Technology* 209 (6): 2946-57. <https://doi.org/10.1016/j.jmatprotec.2008.07.004>.
- M'Barki, Amin, Lydéric Bocquet, et Adam Stevenson. 2017. « Linking Rheology and Printability for Dense and Strong Ceramics by Direct Ink Writing ». *Scientific Reports* 7 (1): 6017. <https://doi.org/10.1038/s41598-017-06115-0>.

- Meijer, H. E. H., et C. P. J. M. Verbraak. 1988. « Modeling of Extrusion with Slip Boundary Conditions ». *Polymer Engineering & Science* 28 (11): 758-72. <https://doi.org/10.1002/pen.760281108>.
- Merchant, Morris V. 1957. « A Study of Certain Phenomena of the Liquid Exchange of Water-Swollen Cellulose Fibers and Their Subsequent Drying from Hydrocarbons », janvier. <https://smartech.gatech.edu/handle/1853/5681>.
- Meyer, Kurt H., et Lore Misch. 1937. « Positions des Atomes dans le Nouveau Modèle Spatial de la Cellulose ». *Helvetica Chimica Acta* 20 (1): 232-44. <https://doi.org/10.1002/hlca.19370200134>.
- Michaeli, Walter. 2003. «Extrusion Dies for Plastics and Rubber: Design and Engineering Computations».
- Moon, Robert J., Ashlie Martini, John Nairn, John Simonsen, et Jeff Youngblood. 2011. « Cellulose Nanomaterials Review: Structure, Properties and Nanocomposites ». *Chemical Society Reviews* 40 (7): 3941. <https://doi.org/10.1039/c0cs00108b>.
- Moteleb, Mohamed M. Abdel. 1992. « Electrical Conductance of Some Cellulose Derivatives ». *Polymer Bulletin* 28 (6): 689-95. <https://doi.org/10.1007/BF00295974>.
- Murphy, CA. 2018. « Microcrystalline Cellulose Reinforced Polylactic Acid Biocomposite Filaments for 3D Printing ». *Polymer Composites*, 2018. <https://onlinelibrary-wiley-com.gaelnomade-2.grenet.fr/doi/full/10.1002/pc.24069>.
- Nechyporchuk, Oleksandr, Mohamed Naceur Belgacem, et Julien Bras. 2016. « Production of Cellulose Nanofibrils: A Review of Recent Advances ». *Industrial Crops and Products*, Nanocellulose: production, functionalisation and applications, 93 (décembre): 2-25. <https://doi.org/10.1016/j.indcrop.2016.02.016>.
- Nechyporchuk, Oleksandr, Mohamed Naceur Belgacem, et Frédéric Pignon. 2016. « Current Progress in Rheology of Cellulose Nanofibril Suspensions ». *Biomacromolecules* 17 (7): 2311-20. <https://doi.org/10.1021/acs.biomac.6b00668>.
- Nishiyama, Yoshiharu, Paul Langan, et Henri Chanzy. 2002. « Crystal Structure and Hydrogen-Bonding System in Cellulose I β from Synchrotron X-ray and Neutron Fiber Diffraction ». *Journal of the American Chemical Society* 124 (31): 9074-82. <https://doi.org/10.1021/ja0257319>.
- Niskanen, Kaarlo. 1998. *Paper physics*. 2nd edition. Papermaking Science and Technology, book 16. Fapet Oy.
- Orgéas, L., J.-P. Gabathuler, Th Imwinkelried, Ch Paradies, et M. Rappaz. 2003. « Modelling of Semi-Solid Processing Using a Modified Temperature-Dependent Power-Law Model ». *Modelling and Simulation in Materials Science and Engineering* 11 (4): 553. <https://doi.org/10.1088/0965-0393/11/4/309>.
- Orgéas, Laurent, Pierre J. J. Dumont, Thai-Hung Le, et Denis Favier. 2008. « Lubricated Compression of BMC, a Concentrated and Fibre-Reinforced Granular Polymer Suspension ». *Rheologica Acta* 47 (5): 677. <https://doi.org/10.1007/s00397-008-0276-1>.
- Palaganas, Napolabel B., Joey Dacula Mangadlao, Al Christopher C. de Leon, Jerome O. Palaganas, Katrina D. Pangilinan, Yan Jie Lee, et Rigoberto C. Advincula. 2017. « 3D Printing of Photocurable Cellulose Nanocrystal Composite for Fabrication of Complex Architectures via Stereolithography ». *ACS Applied Materials & Interfaces* 9 (39): 34314-24. <https://doi.org/10.1021/acsami.7b09223>.
- Park, Jae Sung, Taeil Kim, et Woo Soo Kim. 2017. « Conductive Cellulose Composites with Low Percolation Threshold for 3D Printed Electronics ». *Scientific Reports* 7 (1): 3246. <https://doi.org/10.1038/s41598-017-03365-w>.

- Passas, Raphaël, Voillot C, Tarrajat G, Khélifi B, et Guy Tourtollet. 2001. « MorFi : Analyseur Morphologique des Fibres. (2001),SFGP, », In .
- Pattinson, Sebastian W., et A. John Hart. 2017. « Additive Manufacturing of Cellulosic Materials with Robust Mechanics and Antimicrobial Functionality ». *Advanced Materials Technologies* 2 (4): n/a-n/a. <https://doi.org/10.1002/admt.201600084>.
- Peng, Erwin, Danwei Zhang, et Jun Ding. 2018. « Ceramic Robocasting: Recent Achievements, Potential, and Future Developments ». *Advanced Materials* 30 (47): 1802404. <https://doi.org/10.1002/adma.201802404>.
- Perrin, Jordan. 2016. « Production De Cellulose Pure à Partir de Bois par un Procédé d'Épuration et de Blanchiment Propre à Base d'Ozone, en Vue d'une Valorisation Textile ou Chimique ». Thesis, Grenoble Alpes. <http://www.theses.fr/2016GREAI088>.
- Pfister, Andreas, Rüdiger Landers, Andres Laib, Ute Hübner, Rainer Schmelzeisen, et Rolf Mülhaupt. 2004. « Biofunctional Rapid Prototyping for Tissue-Engineering Applications: 3D Bioplotting versus 3D Printing ». *Journal of Polymer Science Part A: Polymer Chemistry* 42 (3): 624- 38. <https://doi.org/10.1002/pola.10807>.
- Pham, D. T, et R. S Gault. 1998. « A Comparison of Rapid Prototyping Technologies ». *International Journal of Machine Tools and Manufacture* 38 (10): 1257- 87. [https://doi.org/10.1016/S0890-6955\(97\)00137-5](https://doi.org/10.1016/S0890-6955(97)00137-5).
- Reddy, B. V., N. V. Reddy, et A. Ghosh. 2007. « Fused Deposition Modelling Using Direct Extrusion ». *Virtual and Physical Prototyping* 2 (1): 51- 60. <https://doi.org/10.1080/17452750701336486>.
- Rees, Adam, Lydia C. Powell, Gary Chinga-Carrasco, David T. Gethin, Kristin Syverud, Katja E. Hill, et David W. Thomas. 2015. « 3D Bioprinting of Carboxymethylated-Periodate Oxidized Nanocellulose Constructs for Wound Dressing Applications ». Research article. BioMed Research International. 2015. <https://doi.org/10.1155/2015/925757>.
- Sachs, E., M. Cima, P. Williams, D. Brancazio, et J. Cornie. 1992. « Three Dimensional Printing: Rapid Tooling and Prototypes Directly from a CAD Model ». *Journal of Engineering for Industry* 114 (4): 481- 88. <https://doi.org/10.1115/1.2900701>.
- Saïd Azizi Samir, My Ahmed, Fannie Alloin, Michel Paillet, et Alain Dufresne. 2004. « Tangling Effect in Fibrillated Cellulose Reinforced Nanocomposites ». *Macromolecules* 37 (11): 4313- 16. <https://doi.org/10.1021/ma035939u>.
- Sampson, W. W., et J. Yamamoto. 2011. « The Drying Shrinkage of Cellulosic Fibres and Isotropic Paper Sheets ». *Journal of Materials Science* 46 (2): 541- 47. <https://doi.org/10.1007/s10853-010-5006-2>.
- Sanandiya, Naresh D., Yadunund Vijay, Marina Dimopoulou, Stylianos Dritsas, et Javier G. Fernandez. 2018. « Large-Scale Additive Manufacturing with Bioinspired Cellulosic Materials ». *Scientific Reports* 8 (1): 8642. <https://doi.org/10.1038/s41598-018-26985-2>.
- Scherer, George W. 1990. « Theory of Drying ». *Journal of the American Ceramic Society* 73 (1): 3- 14. <https://doi.org/10.1111/j.1151-2916.1990.tb05082.x>.
- Schumacher, Christian, Volker Schöppner, et Camilla Fels. 2019. « A Method to Evaluate the Process-Specific Warpage for Different Polymers in the FDM Process ». *AIP Conference Proceedings* 2065 (1): 030057. <https://doi.org/10.1063/1.5088315>.
- Serdeczny, Marcin P., Raphaël Comminal, David B. Pedersen, et Jon Spangenberg. 2018. « Experimental Validation of a Numerical Model for the Strand Shape in Material Extrusion Additive Manufacturing ». *Additive Manufacturing* 24 (décembre): 145- 53. <https://doi.org/10.1016/j.addma.2018.09.022>.
- Shao, Ying, Didier Chaussy, Philippe Grosseau, et Davide Beneventi. 2015. « Use of Microfibrillated Cellulose/Lignosulfonate Blends as Carbon Precursors: Impact of Hydrogel Rheology on 3D

- Printing ». *Industrial & Engineering Chemistry Research* 54 (43): 10575-82. <https://doi.org/10.1021/acs.iecr.5b02763>.
- Shor, Lauren, Anna Bellini, et Selcuk I. Guceri. 2005. « New Developments in Fused Deposition Modeling of Ceramics ». *Rapid Prototyping Journal* 11 (4): 214-20. <https://doi.org/10.1108/13552540510612901>.
- Siqueira, Eder José. 2012. « Polyamidoamine Epichlorohydrin-Based Papers : Mechanisms of Wet Strength Development and Paper Repulping », juin. <https://tel.archives-ouvertes.fr/tel-00952991>.
- Siqueira, Gilberto, Dimitri Kokkinis, Rafael Libanori, Michael K. Hausmann, Amelia Sydney Gladman, Antonia Neels, Philippe Tingaut, Tanja Zimmermann, Jennifer A. Lewis, et André R. Studart. 2017. « Cellulose Nanocrystal Inks for 3D Printing of Textured Cellular Architectures ». *Advanced Functional Materials* 27 (12): n/a-n/a. <https://doi.org/10.1002/adfm.201604619>.
- Sixta, Herbert. 2006. *Handbook of Pulp, 2 Volume Set*. Wiley.
- Smay, James E., Joseph Cesarano, et Jennifer A. Lewis. 2002. « Colloidal Inks for Directed Assembly of 3-D Periodic Structures ». *Langmuir* 18 (14): 5429-37. <https://doi.org/10.1021/la0257135>.
- Spoerk, Martin, Florian Arbeiter, Ivan Raguz, Gerhard Traxler, Stephan Schuschnigg, Ludwig Cardon, et Clemens Holzer. 2018. « The Consequences of Different Printing Chamber Temperatures in Extrusion-Based Additive Manufacturing ». In *International Conference on Polymers and Moulds Innovations - PMI 2018*. Institute of Polymers and Composites, University of Minho, Portugal. <http://hdl.handle.net/1854/LU-8587605>.
- Spoerk, Martin, Joamin Gonzalez-Gutierrez, Janak Sapkota, Stephan Schuschnigg, et Clemens Holzer. 2018. « Effect of the Printing Bed Temperature on the Adhesion of Parts Produced by Fused Filament Fabrication ». *Plastics, Rubber and Composites* 47 (1): 17-24. <https://doi.org/10.1080/14658011.2017.1399531>.
- Sponser, et Dore. 1926. « The Structure of Ramie Cellulose as Derived from X-ray Data ». In .
- Suderman, Norafidah, Norizah Sarbon, et Mohd Ikmar Nizam Mohamad Isa. 2016. « Effect of Drying Temperature on the Functional Properties of Biodegradable CMC-Based Film for Potential Food Packaging ». *International Food Research Journal* 23 (janvier): 1075-84.
- Suiker, A. S. J. 2018. « Mechanical Performance of Wall Structures in 3D Printing Processes: Theory, Design Tools and Experiments ». *International Journal of Mechanical Sciences* 137 (mars): 145-70. <https://doi.org/10.1016/j.ijmecsci.2018.01.010>.
- Sun, Jie, Weibiao Zhou, Liangkun Yan, Dejian Huang, et Lien-ya Lin. 2018. « Extrusion-based food printing for digitalized food design and nutrition control ». *Journal of Food Engineering, 3D Printed Food – Design and Technology*, 220 (mars): 1-11. <https://doi.org/10.1016/j.jfoodeng.2017.02.028>.
- Sydney Gladman, A., Elisabetta A. Matsumoto, Ralph G. Nuzzo, L. Mahadevan, et Jennifer A. Lewis. 2016. « Biomimetic 4D Printing ». *Nature Materials* 15 (janvier): 413.
- Takahashi, Haruki, et Homei Miyashita. 2017. « Expressive Fused Deposition Modeling by Controlling Extruder Height and Extrusion Amount ». In *Proceedings of the 2017 CHI Conference on Human Factors in Computing Systems*, 5065–5074. CHI '17. New York, NY, USA: ACM. <https://doi.org/10.1145/3025453.3025933>.
- Tao, Yubo, Honglei Wang, Zelong Li, Peng Li, et Sheldon Q. Shi. 2017. « Development and Application of Wood Flour-Filled Polylactic Acid Composite Filament for 3D Printing ». *Materials* 10 (4): 339. <https://doi.org/10.3390/ma10040339>.
- Thibaut, C., A. Denneulin, S. Rolland du Roscoat, D. Beneventi, L. Orgéas, et D. Chaussy. 2019. « A Fibrous Cellulose Paste Formulation to Manufacture Structural Parts Using 3D Printing by Extrusion ». *Carbohydrate Polymers*, janvier. <https://doi.org/10.1016/j.carbpol.2019.01.076>.

- Thingiverse.com. s. d. « Thingiverse - Digital Designs for Physical Objects ». Consulté le 13 septembre 2018. <https://www.thingiverse.com/>.
- Tricot, F., C. Venet, D. Beneventi, D. Curtil, D. Chaussy, T. P. Vuong, J. E. Broquin, et N. Reverdy-Bruas. 2018. « Fabrication of 3D Conductive Circuits: Print Quality Evaluation of a Direct Ink Writing Process ». *RSC Advances* 8 (46): 26036-46. <https://doi.org/10.1039/C8RA03380C>.
- Truby, Ryan L., et Jennifer A. Lewis. 2016. « Printing Soft Matter in Three Dimensions ». *Nature* 540 (7633): 371-78. <https://doi.org/10.1038/nature21003>.
- Vergnes, Bruno, et Stéphan Puissant. 2002. « Extrusion - Extrusion Monovis (partie 1) ». Text. Ref : TIP100WEB - « Plastiques et composites ». 10 octobre 2002. <https://www-techniques-ingenieur-fr.gaelnomade-1.grenet.fr/base-documentaire/42150210-plasturgie-procedes-d-extrusion/download/am3650/extrusion.html>.
- Voisin, Hugo P., Korneliya Gordeyeva, Gilberto Siqueira, Michael K. Hausmann, André R. Studart, et Lennart Bergström. 2018. « 3D Printing of Strong Lightweight Cellular Structures Using Polysaccharide-Based Composite Foams ». *ACS Sustainable Chemistry & Engineering* 6 (12): 17160-67. <https://doi.org/10.1021/acssuschemeng.8b04549>.
- Wainwright, Stephen A. 1976. « Mechanical Design in Organisms ». Princeton University Press. 1976. <https://press.princeton.edu/titles/2123.html>.
- Wang, Lu, Douglas J. Gardner, et Douglas W. Bousfield. 2017. « Cellulose Nanofibril-Reinforced Polypropylene Composites for Material Extrusion: Rheological Properties ». *Polymer Engineering & Science*, mai, n/a-n/a. <https://doi.org/10.1002/pen.24615>.
- Wang, Qianqian, Jianzhong Sun, Qian Yao, Chencheng Ji, Jun Liu, et Qianqian Zhu. 2018. « 3D Printing with Cellulose Materials ». *Cellulose* 25 (8): 4275-4301. <https://doi.org/10.1007/s10570-018-1888-y>.
- Wang, Sun, Peng, Luo, Wang, et Zhang. 2015. « Transitional Suspensions Containing Thermosensitive Dispersant for Three-Dimensional Printing ». *ACS Applied Materials & Interfaces* 7 (47): 26131-36. <https://doi.org/10.1021/acsam.5b07913>.
- White, D. 2001. « Rapid Prototyping Processes ». In *Encyclopedia of Materials: Science and Technology*, édité par K. H. Jürgen Buschow, Robert W. Cahn, Merton C. Flemings, Bernhard Ilshner, Edward J. Kramer, Subhash Mahajan, et Patrick Veysi re, 8003-9. Oxford: Elsevier. <https://doi.org/10.1016/B0-08-043152-6/01439-X>.
- Wohlers Associates. 2017. *Wohlers Report 2017: 3D Printing and Additive Manufacturing State of the Industry : Annual Worldwide Progress Report*. Wohlers Associates, Incorporated.
- Wohlers, Terry T., Wohlers Associates, R. Ian Campbell, et Tim Caffrey. 2016. *Wohlers Report 2016: 3D Printing and Additive Manufacturing State of the Industry : Annual Worldwide Progress Report*. Wohlers Associates.
- Xiquan, Lin, Qu Tingzhu, et Qi Shaoqui. 1990. « Kinetics of the Carboxymethylation of Cellulose in the Isopropyl Alcohol System ». *Acta Polymerica* 41 (4): 220-22. <https://doi.org/10.1002/actp.1990.010410406>.
- Xu, Wenyang, Xiaoju Wang, Niklas Sandler, Stefan Willf r, et Chunlin Xu. 2018. « Three-Dimensional Printing of Wood-Derived Biopolymers: A Review Focused on Biomedical Applications ». *ACS Sustainable Chemistry & Engineering* 6 (5): 5663-80. <https://doi.org/10.1021/acssuschemeng.7b03924>.
- Yang, Li, et Md Ashabul Anam. 2014. « An Investigation of Standard Test Part Design for Additive Manufacturing ». In *Proceeding of the Solid Free Form Fabrication Symposium, August*.
- Young, Raymond A. 2002. « Chapter VII - Cross-Linked Cellulose and Cellulose Derivatives ». In *Textile Science and Technology*, édité par P. K. Chatterjee et B. S. Gupta, 13:233-81. Absorbent Technology. Elsevier. [https://doi.org/10.1016/S0920-4083\(02\)80010-X](https://doi.org/10.1016/S0920-4083(02)80010-X).

References

- Zhang, Di, Baihong Chi, Bowen Li, Zewen Gao, Yao Du, Jinbao Guo, et Jie Wei. 2016. « Fabrication of Highly Conductive Graphene Flexible Circuits by 3D Printing ». *Synthetic Metals* 217 (juillet): 79-86. <https://doi.org/10.1016/j.synthmet.2016.03.014>.
- Zhang, T. Y., et C. Y. Suen. 1984. « A Fast Parallel Algorithm for Thinning Digital Patterns ». *Commun. ACM* 27 (3): 236–239. <https://doi.org/10.1145/357994.358023>.

Résumé

Ce projet vise à développer de nouveaux matériaux bio-sourcés cellulosiques qui pourront être mis en forme via le procédé d'impression 3D par extrusion pour produire des objets 3D complexes et multi-matériaux. Ce travail a consisté tout d'abord à formuler des pâtes aqueuses à fort taux de matière sèche présentant des propriétés adéquates aux exigences de l'impression 3D par extrusion. Des mélanges associant des particules micrométriques organiques (cellulose sous forme de fibres courtes ou poudre, poudre de graphite, etc.) et des dérivés de celluloses (carboxyméthylcellulose) ont été étudiés et ont permis l'obtention d'une pâte homogène, compatible avec le procédé d'impression 3D par extrusion qui présente des déformations limitées lors de la phase de séchage de l'objet imprimé. Une seconde phase du projet s'est ensuite concentrée sur l'adaptation et l'optimisation du système d'impression 3D par extrusion ainsi que des paramètres associés afin de garantir une fidélité optimum des objets produits en regard des modèles numériques. Les limitations de ce nouveau matériau au niveau du design des pièces produites ainsi que des paramètres d'utilisation ont été déterminées. Pour caractériser les objets produits, plusieurs approches de caractérisations innovantes comme le suivi du séchage d'une pièce imprimée par tomographie ont été mises en œuvre. Ces résultats ont permis d'aboutir à l'impression 3D de formes complexes en matériau 100% cellulosique avec des propriétés mécaniques comparables aux thermoplastiques habituellement utilisés en impression 3D de fils fondus.

Mots-clés : *Impression 3D, cellulose, extrusion, matériaux bio-sourcés, structure 3D*

Abstract

This project aims at developing new cellulosic bio-based materials for additive manufacturing (AM) by extrusion to produce complex and multi-materials 3D parts. First, this project has evaluated the compatibility of aqueous and high solid content formulations with AM by extrusion. Formulations composed of micrometric organics fillers (cellulose fibers or powder and graphite powder) and cellulose derivatives (carboxymethyl cellulose) were investigated and results in a selection of homogeneous pastes with strong potential for AM by extrusion and limited deformation of the printed part upon air drying. The second stage of this project focused on adjustment and optimization of AM by extrusion equipment and the related settings to guarantee an optimum shape accuracy of 3D printed parts compared to the 3D numerical model. A printing setting guideline and design limitations adapted to the developed paste were suggested. To characterize the printing parts, different innovative methods such as the temporal monitoring by X-ray tomography of a printed part upon drying were implemented. The results of this project lead to the AM by extrusion of complex part 100% cellulose based with mechanical properties close to thermoplastic materials commonly used with fused filament fabrication process.

Key-words: *3D printing, cellulose, extrusion, bio-based material, 3D structure*